Adaptive meshless point collocation methods: investigation and application to geometrically non-linear solid mechanics

LEI FAN

Adaptive meshless point collocation methods: investigation and application to geometrically non-linear solid mechanics

Lei Fan

Submitted as partial consideration towards
the degree of Doctor of Philosophy

Sustainable Infrastructure Research Challenge
Department of Engineering
University of Durham
United Kingdom

June 2019

This thesis is dedicated to

my parents.

Adaptive meshless point collocation methods: investigation and application to geometrically non-linear solid mechanics

Lei Fan

Abstract

Conventional mesh-based methods for solid mechanics problems suffer from issues resulting from the use of a mesh, therefore, various meshless methods that can be grouped into those based on weak or strong forms of the underlying problem have been proposed to address these problems by using only points for discretisation. Compared to weak form meshless methods, strong form meshless methods have some attractive features because of the absence of any background mesh and avoidance of the need for numerical integration, making the implementation straightforward. The objective of this thesis is to develop a novel numerical method based on strong form point collocation methods for solving problems with geometric non-linearity including membrane problems. To address some issues in existing strong form meshless methods, the local maximum entropy point collocation method is developed, where the basis functions possess some advantages such as the weak Kronecker-Delta property on boundaries. r- and h-adaptive strategies are investigated in the proposed method and are further combined into a novel rh-adaptive approach, achieving the prescribed accuracy with the optimised locations and limited number of points. The proposed meshless method with h-adaptivity is then extended to solve geometrically non-linear problems described in a Total Lagrangian formulation, where h-adaptivity is again employed after the initial calculation to improve the accuracy of the solution efficiently. This geometrically non-linear method is finally developed to analyse membrane problems, in which the out-of-plane deformation for membranes complicates the governing PDEs and the use of hyperelastic materials makes the computational modelling of membrane problems challenging. The Newton-Raphson arc-length method is adopted here to capture the snap-through behaviour in hyperelastic membrane problems. Several numerical examples are presented for each proposed algorithm to validate the proposed methodology and suggestions are made for future work leading on from the findings of this thesis.

Declaration

The work in this thesis is based on research carried out in the Sustainable Infrastructure Research Challenge, Department of Engineering, Durham University. No part of this report has been submitted elsewhere for any other degree or qualification and it is all my own work unless referenced to the contrary in the text. Parts of this work have been published in the following:

Acknowledgements

The research work of this thesis would not be possible without the financial support from the China Scholarship Council and Durham University.

Foremost, I am heartily thankful to my main supervisor Prof. Charles Augarde for offering me the PhD opportunity. His endless patience, warm encouragement, thoughtful guidance, immense knowledge and enthusiasm keep me always stay positive during the past three and half years. I could not have imagined having a better supervisor for my PhD study. He is my teacher FOREVER. I am very lucky to be his student. I must also thank my second supervisor Dr. Will Coombs, who offers me support and guidance throughout my research, valuable advice and detailed but important comments on my thesis. Although both of them usually have very busy schedules, they always take time to supervise me, comment my report and have discussions on my research. I have learned a great deal from the enjoyable discussions and interacting with them. I would like to thank Prof. Jon Trevelyan and Dr. Stefano Giani, who are my reviewers. The review meetings with them are very helpful, at which I gained lots of useful suggestions.

Thanks all my colleagues: Dino, Dom, Rob, El, Tim, KZ, Lei and Jianye for their assistance. They always provide me with good suggestions and encourage me when my work does not go smoothly. It has been a pleasure to work with them all. Thanks all my friends in Durham: Ting, Dan, Yi, Steve, CX, Ge, SZ and Kayla for making my life enjoyable and colourful. Living abroad is not easy, but all of them make me feel at home. I will never forgot the great time I spent with my colleagues and my friends in Durham.

Finally, I am deeply thankful to my Mum and Dad for their support, care and boundless love. No matter how far away I am from them, I can always feel their love with all their hearts. I owe them too much for too little time with them but such experience helps me to be independent.

Publications

Parts of work in this thesis have been published, accepted, presented:

- **L. Fan**, W. M. Coombs, C. E. Augarde, The point collocation method with a local maximum entropy approach, Computers & Structures 201(C) (2018) 1-14.

- **L. Fan**, C. E. Augarde, W. M. Coombs, The local maximum entropy point collocation approach for membrane analyses, UK Association for Computational Mechanics Conference 2019. London, UK, City, University of London.

- **L. Fan**, W. M. Coombs, C. E. Augarde, A combined rh-adaptive strategy for the local maximum entropy point collocation method, 6th European Conference on Computational Mechanics (Solids, Structures and Coupled Problems) & 7th European Conference on Computational Fluid Dynamics, Glasgow, UK, 2018.

- **L. Fan**, W. M. Coombs, C. E. Augarde, The point collocation method with a local maximum entropy approach, Young Investigators Conference, Milan, Italy, 2017.

- **L. Fan**, C. E. Augarde, W. M. Coombs, The point collocation method with a local maximum entropy approach, 25th UK Association for Computational Mechanics Conference. Birmingham, UK, University of Birmingham, 232-235.

Contents

List of Figures

List of Tables

Acronyms

ALE	arbitrary Lagrangian-Eulerian
BEM	boundary element method
CPM	cracking particles method
DEM	diffuse element method
EFGM	element-free Galerkin method
FECM	free element collocation method
FEM	finite element method
FMM	free mesh method
FPM	finite point method
FVM	finite volume method
GRKCM	gradient reproducing kernel collocation method
HCM	hermite collocation method
HPC	*hp*-cloud
IGA	isogeometric analysis
IGA-C	isogeometric collocation
LBIE	local boundary integral equation
LRPIM	local radial point interpolation method

max-ent maximum entropy

MEPCM maximum entropy point collocation method

MLPG meshless local Petrov-Galerkin method

MLS moving least squares

MLSCM moving least squares collocation method

MPS moving particle semi-implicit

NEM natural element method

PCMs point collocation methods

PDEs partial differential equations

PIM point interpolation method

PPU particle partition unity

PU partition of unity

PUFEM partition of unity finite element method

RBF radial basis function

RK reproducing kernel

RBCM radial basis collocation method

RKCM reproducing kernel collocation method

RKPM reproducing kernel particle method

RKM reproducing kernel method

SPH smoothed particle hydrodynamics

WLS weighted least-squares

XEFGM extended element-free Galerkin method

Nomenclature

Scalars

$\bar{J}$	error term in the MLS
$\bar{t}^p$	prescribed value on Neumann boundaries for Poisson problems
$\bar{u}^p$	prescribed value on Dirichlet boundaries for Poisson problems
δv_s	nodal volume associated with the sth node inside the support
ϵ	shape parameter
η	tolerance number in the Newton-Raphson method
η_r	relative residual in r-adaptivity
η_t	permissible error
Γ	problem boundary
Γ_t	Neumann boundaries
Γ_u	Dirichlet boundaries
κ	Kolosov constant
λ_1,λ_2,λ_3	principal stretches
λ_m	load factor
μ,α_p	hyperelastic material constants
ν	Poisson's ratio
Ω	problem domain
Ω_s	local domain associated with the sth node inside the support
ϕ_s	basis function value at the sth node (source point) in the support
ψ	free-energy function
θ	effectiveness index
A	deformed area
A_0	undeformed area
A_t	area of Delaunay triangle
d_m	radius of support
d_x	distance between a collocation point and the nearest source point
d_{max}	scaling parameter of support
dV	infinitesimal volume in the current configuration
dV_0	infinitesimal volume in the reference configuration
E	Young's modulus of elasticity
E_g	global error estimator for large deformations
e_g	global error estimator in small deformations
E_t	local error estimator for large deformations
e_t	local error estimator in small deformations
e_{max}	maximum local error estimator
f^p	known value in Poisson problems
G	shear modulus
g_s	radial basis function value at the node in the support
h	thickness of membrane

I_1,I_2,I_3	invariants
J	volume ratio
k	predefined local refinement coefficient
n	number of nodes in the local support
N_c	number of collocation points
N_s	number of source points
N_s^*	number of source points inside the support domain
r	normalised radius of support domain in one dimension
r_s	distance between the point and a node in its support
s	nodal index
V_c	a volume (area or length) associated with a collocation point
W	strain energy
w_s	weight function

Vectors

$\{\bar{\lambda}_s\}$	Lagrange multipliers vector
$\{\bar{p}\}$	pressure vector
$\{\bar{t}\}$	prescribed traction vector for small deformations
$\{\bar{t}^0\}$	prescribed traction vector for large deformations
$\{\bar{t}^{PCM}\}$	prescribed value vector on Neumann boundaries
$\{\bar{u}\}$	prescribed field variable vector for small deformations
$\{\bar{u}^0\}$	prescribed field variable vector for large deformations
$\{\bar{u}^{PCM}\}$	prescribed value vector on Dirichlet boundaries
$\{\bar{X}\}$	coordinates in the reference configuration
$\{\bar{x}\}$	coordinates in the current configuration
$\{\bar{x}^{pre}\}$	coordinates in the initial configuration
$\{\Delta d\}$	the incremental displacement vector
$\{\delta d\}$	the iterative displacement vector
$\{\Psi\}$	test function vector
$\{\Sigma\}$	Eshelby stress vector
$\{\sigma\}$	Cauchy stress vector
$\{\tau\}$	Kirchhoff stress vector
$\{\varepsilon\}$	(logarithmic) strain vector
$\{a\}$	unknown variable vector
$\{C\}$	correction function vector
$\{d\}$	field variable vector at nodes (source points)
$\{d_s\}$	field variable vector at sth source point inside the support
$\{e\}$	a non-zero vector of error residuals
$\{f\}$	right hand side vector in the linear system of PCMs
$\{f^b\}$	body force vector
$\{F^{ext}\}$	external variable vector
$\{F^{int}\}$	internal variable vector
$\{f^{PCM}\}$	right hand side vector in PCMs
$\{f_g\}$	right-hand side vector
$\{G\}$	non-linear system vector
$\{K\}$	kernel function vector
$\{p\}$	polynomial basis vector

$\{R\}$ residual vector of the Newton-Raphson method

$\{u\}$ field variable vector

$\{u^e\}$ exact solution vector

$\{u^h\}$ approximation vector

$\{x_s\}$ coordinates of the sth node (source point) inside the support

$\{\phi\}$ basis function values associated with all nodes in the support

$\{d\bar{x}^{pre}\}$ infinitesimal length in the initial configuration

$\{d\bar{X}\}$ infinitesimal length in the reference configuration

$\{d\bar{x}\}$ infinitesimal length in the current configuration

$\{x\}$ coordinates of any point

Matrices

$[\bar{C}]$ in-plane right Cauchy-Green strain matrix

$[\Delta V]$ nodal volume matrix associated with the sth source point inside the support

$[\phi_s]$ matrix of basis functions associated with the sth node

$[A]$ moment matrix in MLS

$[B]$ matrix term in MLS

$[b]$ the left Cauchy-Green strain matrices

$[C]$ the right Cauchy-Green strain matrices

$[D]$ elastic stiffness matrix

$[E]$ the Green-Lagrangian strain matrix

$[F]$ deformation gradient

$[H]$ Hessian matrix

$[I]$ identity matrix

$[K]$ coefficient matrix in PCMs

$[M]$ moment matrix in RK

$[N]$ resultant force

$[n]$ matrix of the outer normals for small deformation

$[n^0]$ matrix of the outer normals for large deformation

$[n^0_m]$ matrix of the outer normals for membrane problems

$[P(\{x_s\})]$ a matrix of polynomial basis functions

$[P]$ the first Piola-Kirchhoff stress matrix

$[R']$ Jacobian

$[R]$ the local rotation matrix

$[S]$ the second Piola-Kirchhoff stress matrix

$[U]$ the right stretch matrices

$[v]$ the left stretch matrices

$[W]$ weight function matrix

Operators

$(\cdot)_{,x}$ the first partial derivative of $(\cdot)$ with respect to x

$(\cdot)_{,xx}$ the second partial derivative of $(\cdot)$ with respect to x

$(\cdot)^T$ transpose

$[\cdot_0]$ $[\cdot]$ in terms of the reference configuration

$[\cdot_n]$	$[\cdot]$ in terms of the current configuration
$[L]$	differential operators for small deformations
$[L^{NL}]$	differential operators for large deformations
$\Delta(\cdot)$	increment of $(\cdot)$
$\delta(\cdot)$	iterative of $(\cdot)$
$\det(\cdot)$	determinant of $(\cdot)$
$\mathscr{L}$,$\mathscr{L}_u$,$\mathscr{L}_t$	differential operators in PCMs
$\mathscr{L}_g$	any differential operators for PDEs
diag$[\cdot]$	values from leading diagonal of $[\cdot]$
tr$[\cdot]$	trace of $(\cdot)$
$\varphi(\cdot)$	motion

Chapter 1

Introduction

1.1 Overview

Most physical phenomena in nature can be described by a set of partial differential equations (PDEs), an example being the underlying mechanical behaviour of a structure subjected to externally applied loads and boundary conditions [2,3]. However, only limited cases with simple geometry and boundary conditions have analytical solutions and due to the mathematical complexities, the majority cannot be solved analytically. Therefore, numerical methods become indispensable tools to provide approximated solutions for a wide range of problems. As only computer programs are required, numerical analyses could be regarded as more environmentally friendly as compared to experimental studies.

The solution of the problem numerically starts by turning a set of PDEs into some more amenable formulation, e.g. a weak form. A problem domain needs to be discretised first, and the governing PDEs and boundary conditions are imposed to formulate the system of equations. A solution of this system is calculated, which is verified and comparisons with theoretical and experimental results can serve to validate the numerical method.

Plenty of numerical methods, which are generally composed of mesh-based and meshless methods, have been proposed for solving solid mechanics problems. The finite element method (FEM) proposed in [4] is by far the most popular mesh-based method

which has been applied to solve a variety of problems. To implement the FEM, a continuum domain is represented by discrete nodes which are connected together to form small volumes, known as elements. Within each element, simple rules are set on variation of the field variable, using shape (or basis) functions. Interpolations in this method rely on the connectivity of the nodes or a mesh [5–7]. The governing PDEs and boundary conditions are applied to elements, assembling into a system of equations spanning the entire domain. The resulting system is then solved for the unknown field variables which are the nodal displacements in the case of solid mechanics. The approximations of displacement are then reused to obtain stresses and strains at any point in the problem domain. Significant contributions have been made using the conventional FEM with applications to a very wide range of solid mechanics fields, including static linear elasticity [8], vibration [9], hydrostatic and hydrodynamics [10], non-linear (both material non-linear [11] and geometrically non-linear [12]) problems, multi-material analysis [13] and biomechanics [14].

The FEM is a robust and well-established technique, however, as a wider range of phenomena have been simulated, the limitations of this conventional computational method have become apparent [15, 16]. There are many problems of industrial and academic interest, which cannot be easily treated by the classical FEM because the reliance of the method on a mesh leads to complications for certain problems with special properties, e.g. large deformation analysis is an area which presents a tough challenge to researchers in terms of accuracy, resulting from mesh distortion. The dependence on a mesh in the FEM has been partly dealt with by using the boundary element method (BEM) that has some advantages over the FEM. The BEM first appeared for solving elasticity, where the accurate mathematical description of the physics provides highly accurate solutions [17]. All elements are used at only boundaries, so volume integrals are converted to boundary integrals, making the BEM more computationally efficient than the FEM. In spite of the wide applications on certain fields of problems, the BEM still suffer from some drawbacks. As the resulting coefficient matrix in the final system of equations is full and non-symmetric, the computational cost for three-dimensional problems or large scale problems increases, which reduces the efficiency of the BEM [18, 19]. Then, isogeometric analysis (IGA) proposed in [20] represents a recently developed technology in computa-

tional mechanics where element shapes match physical geometries (derived from CAD for instance) exactly. The use of highly smooth B-spline basis functions in IGA methods (which have been largely applied in the FEM) provides accurate solutions to non-linear problems. However, for complicated geometries, additional efforts are still required to construct elements, which restricts its applications.

Conventional numerical methods, relying on a mesh for the discretisation of a continuum therefore have some issues with meshing and remeshing and meshless methods attract much attention, in which the approximation of a solution is entirely based on nodes (particles or points) without any necessity of forming elements [21]. Although various meshless methods have been proposed, they remain to be fully developed for commercial use and possible to be widely applied and compete with mesh-based methods. The goal of this thesis is the investigation of a certain type of meshless method, which enable efficient simulations of some challenging engineering problems involving large deformations. This topic will be dealt with in detail in the following chapters.

1.2 Thesis outline

This thesis is concerned with the theoretical derivation, numerical development and subsequent implementation of meshless methods. The research work can be split into two major parts. The first part, including Chapter 3 and 4, concerns the investigation and development of a novel meshless method and adaptive strategies. The second part, including Chapter 5 and 6, is an application of the proposed novel method to some problems with geometric non-linearity. The contents of each chapter are detailed in the following.

- Chapter 1 presents an overview of research background and a general description of the thesis with an indication of notation.
- Chapter 2 provides a literature review of meshless methods for solid mechanics problems. Meshless basis functions are introduced and some representative examples are reviewed. The history and development of meshless methods are covered followed by their classification, together with corresponding advantages and

disadvantages. Some research challenges in meshless methods and more detailed motivations of this thesis are discussed.

- Chapter 3 starts with the setting up of the governing PDEs and boundary conditions in strong form for both Poisson and linear elasticity problems. Then the basic formulations and numerical implementation of the classical strong form-based reproducing kernel collocation method (RKCM) are described. As the RKCM suffers from some issues, a local maximum entropy basis function is employed for the first time in the author's paper, yielding the local maximum entropy point collocation method (MEPCM) which can facilitate those problems. The influence domains, weight functions and the first and second derivatives of this novel method are introduced followed by a discussion of implementation issues. Some numerical examples including two-dimensional Poisson problems and one- and two-dimensional linear elasticity problems, are analysed to demonstrate the performance of the conventional RKCM and the proposed MEPCM. Comparisons in terms of accuracy, computational time and floating point operations of using these two methods are made.

- In Chapter 4, various adaptive strategies are developed for the MEPCM. After a literature review of error estimation and refinement strategies, pure r- and h-adaptive strategies in the MEPCM are developed to improve the accuracy of the solution. Since the use of a pure adaptive strategy cannot achieve the prescribed accuracy efficiently, these two individual adaptivities are combined to produce a novel rh-adaptivity approach. The implementation issues in terms of determining the number of the source points in the local support domain are discussed. The one- and two-dimensional numerical examples are studied using uniform refinement, r-, h- and combined rh-adaptivities. Comparisons in terms of accuracy and computational cost using different strategies are accomplished to validate the proposed method and their efficiency.

- Chapter 5 analyses geometrically non-linear problems using the MEPCM with h-adaptivity for the first time. The kinematics of large deformation and stress and strain measures used in this chapter are first reviewed. The governing PDEs and

boundary conditions for large deformation mechanics are then described using the Total Lagrangian formulation with the MEPCM and the formed non-linear system of equations is solved by the Newton-Raphson method, where the choice of the stopping criterion is discussed. In large deformation analysis, h-adaptivity is employed after the initial calculation, where the error estimators used for small deformations are extended to large deformation cases. Some one- and two-dimensional numerical examples are analysed to demonstrate the proposed methods, where h-adaptivity is adopted in selected examples.

- In Chapter 6 the geometrically non-linear analysis using the MEPCM developed in Chapter 5 is extended to membrane problems. The configurations together with corresponding kinematics for membrane problems are introduced. Strain and stress measures for both linear elastic and hyperelastic material models are presented. The governing equations and boundary conditions for membrane problems are described using the Total Lagrangian formulation. After that, the numerical implementation using the MEPCM is given, where the Newton-Raphson arc-length method is employed for solving the non-linear system with instability. Numerical examples of prestretched membrane problems using different material models are studied to validate the performance of the proposed formulations.

- Chapter 7 summarises all the research work mentioned above and provides an outlook for future directions in terms of the investigation of meshless methods and their applications.

In this thesis, some novel numerical techniques are developed for solving solid mechanics problems from Chapter 3 to Chapter 6, which is the main contribution. A strong form-based MEPCM is proposed (for the first time in the author's paper) for Poisson and elasticity problems, having some advantages by comparisons with existing methods. As there is a lack of study on various adaptive strategies in strong form-based meshless methods, a novel combined rh-adaptivity is developed in the MEPCM based on the single r- and h-adaptivities. Large deformation problems are modelled by this newly proposed MEPCM with h-adaptivity and membrane problems are analysed using the MEPCM.

1.3 Notation

For clarity and consistency, matrix/vector notation is used for both theoretical derivation and numerical implementation throughout all thesis chapters. In Appendices A and D, matrix/vector notation is adopted and index notation is used in Appendices B-C for derivations, which are more appropriate there.

The numerical algorithms used in this thesis were developed using MATLAB m-script. All programs were run in MATLAB R2015b using an Intel(R) Core(TM) i7-4790 CPU @ 3.60 GHZ. The CPU times stated in the numerical examples are the average times over 10 measurements.

Chapter 2

Meshless methods for solid mechanics - a review

2.1 Introduction

Meshless methods, since their inception almost 40 years ago, have become a major research focus as alternatives to mesh-based methods, achieving remarkable progress in the field of solid mechanics [22]. Before reviewing the literature on meshless methods, it is necessary to clarify the concept of "meshless". As the name suggests, the term "meshless" or "meshfree" indicates the ability of an approximation or interpolation approach to be constructed entirely from discrete points (nodes) without the use of a predefined mesh. In contrast, the connectivity of points is required in conventional mesh-based approximations. Meshless methods possess some advantages over mesh-based methods as explained in [23].

- The reliance on a mesh is removed, thus issues associated with mesh generation for complicated geometries in three dimensions are addressed, which reduces the computational cost for constructing a mesh.
- Local refinement as part of an adaptivity-based method is straightforward to implement, improving the accuracy of the approximations without mesh regeneration.
- Problems with discontinuities or interfaces can be directly treated with minor cost

and accuracy degradation as there is no need for tedious and time consuming remeshing.

- Mesh distortion is not an issue in large deformation analyses.

Meshless methods form a group of numerical methods for solving PDEs in a discrete way, where a continuum is divided into a set of discrete points without connectivity and the unknown field variables are discretised at these points. The PDEs can be written in terms of basis functions and their derivatives, assembling into a system of equations in a weak or strong formulation. Some background on meshless basis functions is introduced in the next section followed by the development and classification of meshless methods. Finally, some of the research challenges in meshless methods are discussed as motivation for this thesis.

2.2 Basis functions

In this section, the fundamentals of basis functions are introduced and four commonly used meshless basis functions are reviewed. In numerical methods, a basis function is used together with unknown field variables (i.e. values at surrounding nodes) to approximate an unknown vector of continuous field $\{u\}$ in two dimensional elasticity problems as

$$\{u\} \approx \{u^h\} = \sum_{s=1}^{n} [\phi_s]\{d_s\} \tag{2.1}$$

where $\{u^h\}$ is a 2×1 vector of the approximation of the solution, s is the nodal index with $s = 1, 2, ..., n$, n is the number of surrounding nodes (as will be described in mesh-based and meshless basis functions separately in the following), $[\phi_s]$ is a 2×2 matrix of basis function values associated with the sth node and $\{d_s\}$ represents a 2×1 vector of the unknown field variables at the sth node. A key difference between mesh-based and meshless methods is the construction of the basis functions so some background of mesh-based and meshless basis functions will now be given.

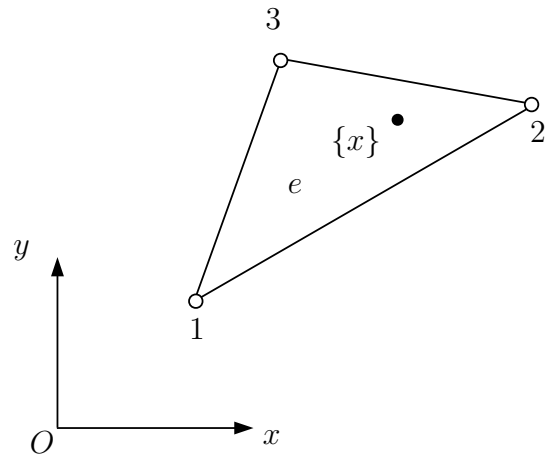

Figure 2.1: A two-dimensional element.

2.2.1 Finite element basis functions

In the mesh-based FEM, element e as shown in Figure 2.1, is defined by nodes 1, 2, 3 and straight line boundaries, so the approximation at any point $\{x\}$ in this element can be calculated by Eq. (2.1), where n is known to be 3 (number of surrounding nodes mentioned above), and the matrix of basis function values $[\phi_s]$ and the vector of field variables $\{d_s\}$ are associated with these three nodes of a element [2]. The construction of finite element basis functions relies on the connectivity of these three nodes, where the basis function value associated with a node is unity at the node itself and zero at the other nodes connected to it.

2.2.2 Meshless basis functions

In meshless methods, the problem domain and boundaries are discretised by a set of arbitrarily scattered nodes as shown in Figure 2.2. In order to calculate the approximation at any point $\{x\}$ by Eq. (2.1), n has to be determined by searching in a predefined local support domain which is given in Figure 2.2 (n=5 is chosen here). The basis function values and the field variables associated with these n surrounding nodes are used in Eq. (2.1). The construction of meshless basis functions is based on those individual nodes which fall in the local support domain (detailed choices of the local support domain will be discussed in Chapter 3).

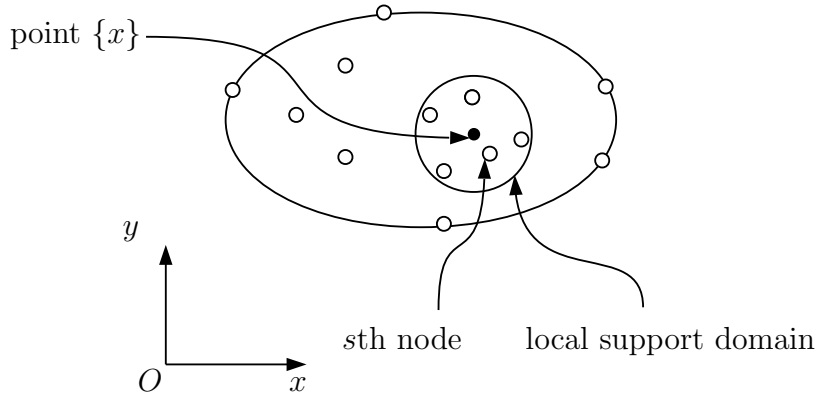

Figure 2.2: A two-dimensional problem domain discretised by a set of nodes.

A large number of basis functions have been employed in meshless methods so far, but it is important to note that meshless basis functions should ideally have the following properties as set out in [24]:

- Points distribution should be arbitrary.
- A complete polynomial basis up to a certain order should be guaranteed.
- The partition of unity (PU) property is required which can be written as

$$\sum_{s=1}^{n} \phi_s(\{x\}) = 1. \tag{2.2}$$

  $\{x\}$ is the location of a point, $\phi_s(\{x\})$ is the meshless basis function value associated with the sth node in the local support domain and n is the total number of nodes in the local support domain.

- The requirement of consistency (reproducing condition), which is the highest polynomial order can be exactly represented with the numerical solution, should be satisfied, e.g. a linear consistency is

$$\sum_{s=1}^{n} \phi_s(\{x\})\{x_s\} = \{x\} \tag{2.3}$$

  where $\{x_s\}$ is the position of the sth node in the local support domain, $\{x\}$ is the

position of any point, $\phi_s(\{x\})$ is the basis function value associated with the sth node in the local support and n is the total number of nodes in the local support domain.

- The Kronecker delta property is a preferable condition in meshless basis functions, as

$$\phi_i(\{x_j\}) = \begin{cases} 1, & i = j \\ 0, & i \neq j \end{cases}, \quad i, j = 1, 2, ..., n \tag{2.4}$$

where $\phi_i(\{x_j\})$ is the value of basis function associated with the ith node in the local support domain at $\{x_j\}$.

It is seen that mesh-based and meshless basis functions share some common properties, e.g. the PU property. However, meshless basis functions are constructed based on points only and exhibit some attractive features as discussed in [23].

- The choice of meshless basis functions is more flexible than in the mesh-based FEM.

- The polynomial-based meshless basis functions can be easily built to have any desired order.

The positive aspects of meshless methods have been listed above, which mainly result from the use of meshless basis functions. The origins, development, detailed formulations and numerical implementation of meshless basis functions can be found in review papers and books e.g. [21, 24–31]. Four representative examples are selected to be reviewed in the following.

The fundamentals of meshless basis functions have been introduced in this section. A wide variety of meshless methods can be developed by employing various basis functions. A classification of meshless methods is provided in the next section, which includes some historical perspective and current development.

2.3 Classification

Meshless methods seem to offer some advantages over mesh-based methods for solid mechanics problems, and it is no surprise therefore that variety of meshless approaches

have been investigated (for a comprehensive review, refer to [27]). Here, a classification of meshless methods is presented to provide a clear picture of the relation between meshless methods in general and the point collocation method which is the subject of the later parts of this thesis. Meshless methods for solid mechanics can be broadly categorised according to whether or not they use integration as discussed in [32, 33], i.e.

- weak form-based meshless methods in which numerical integration is required;
- strong form-based meshless methods, which use no integration, and are therefore truly meshless methods;
- combined weak and strong form meshless methods.

2.3.1 Weak form meshless methods

PDEs, such as the governing equations of linear elasticity can be written as follows

$$[\mathscr{L}_g]^T\{u\} = \{f_g\} \tag{2.5}$$

where g means general cases, $[\mathscr{L}_g]$ is a matrix of any differential operators, $\{u\}$ is a vector of field variables and $\{f_g\}$ is the system's right hand side. It is in general impossible to fulfill a set of governing PDEs in Eq. (2.5) exactly based on a vector of the field variables $\{d\}$ at discrete nodes and a non-zero vector of error residuals $\{e\}$ is given as

$$[\mathscr{L}_g]^T\{d\} - \{f_g\} = \{e\}. \tag{2.6}$$

Therefore, a vector of test functions $\{\Psi\}$ is used in the integral over the problem domain Ω as

$$\int \{\Psi\}^T\{e\}d\Omega = \int \{\Psi\}^T([\mathscr{L}_g]^T\{d\} - \{f_g\})d\Omega. \tag{2.7}$$

The integral expression in Eq. (2.7) is a weak form of the PDE, where the PDE can be satisfied averagely over a domain instead of at discrete nodes, making the numerical results stable and accurate.

One of the earliest meshless approaches, smoothed particle hydrodynamics (SPH), was proposed in 1977 [34–37]. The approximation of a solution $\{u^h\}$ at a point $\{x\}$ using

SPH can be given as

$$\{u^h(\{x\})\} = \int_\Omega [K(\{x\} - \{x_s\})]\{d\} d\Omega \tag{2.8}$$

where s is nodal index of the particles inside the local support domain, $\{x_s\}$ is the coordinate of the sth particle, $\{d\}$ is a vector of the unknown field variables associated with all particles inside the support domain, Ω is the integral domain and $[K(\{x\}-\{x_s\})]$ is a matrix of the smoothed kernel function. The smoothed kernel function in SPH plays the same role as the basis function in Eq. (2.1). As discussed in §1.2, the PU property should be satisfied by the smoothed kernel function as

$$\int [K(\{x\} - \{x_s\})] d\Omega = \{1\} \tag{2.9}$$

where $\{1\} = \{1, 1\}^T$ in two dimensions. This method has been applied to a wide range of applications, e.g. fluid dynamics [38] and heat conduction [39]. However, SPH suffers from some drawbacks such as the lack of consistency (explained in §1.2.1) near boundaries and tension instability [40–42]. The sums of SPH basis function values are not exactly one near boundaries or in areas of non-uniform discretisation. The tension instability is that the motion of particles becomes unstable where particles are under a certain tension stress state. The tension instability in SPH is related to the lack of consistency [43]. More recently, substantial progress has been made by introducing some variations of SPH such as corrected SPH [44] and moving least squares SPH [45].

The diffuse element method (DEM) was developed in 1992, where a local weighted least-squares (WLS) approach is employed to construct basis functions, preserving the local character of approximations. The DEM offers some advantages for calculating the approximation gradients directly, but they are highly dependent on the choice of weight function. In the 1990s, the element-free Galerkin method (EFGM) was introduced in [22, 46–49], where the moving least squares (MLS) approach is used to construct basis functions. The EFGM has since become one of the most popular meshless methods and has been effective for solving crack propagation problems, which cannot be easily addressed by the standard FEM [50,51], achieving better rates of convergence than those

of using the FEM [22]. As the MLS basis function does not possess the Kronecker-delta property, Lagrange multipliers are employed to enforce Dirichlet boundary conditions in the EFGM, which complicates the calculation process as additional unknowns must be determined. Somewhat later, the reproducing kernel particle method (RKPM) was introduced being based on the reproducing kernel (RK) basis function [52]. This basis function offers favourable properties over SPH basis functions as a correction function is applied to the SPH kernel function.

The meshless local Petrov-Galerkin method (MLPG) was proposed in [53], which uses MLS basis functions as in the EFGM. The MLPG is a local weak form-based meshless method as the integral is calculated over a local domain which is chosen to coincide with the support domain of weight functions. Therefore, a background mesh used in the EFGM is not required in the MLPG. A penalty method is employed to facilitate Dirichlet boundary conditions in this approach. The cracking particles method (CPM) is a meshless method, designed to model crack propagation problems [54, 55]. In this method, a set of discontinuous segments are generated associated with the so-called cracking particles to describe crack paths. The support domains of normal particles are cut by these segments. Another weak form-based meshless method is the Galerkin method with local maximum entropy (max-ent) basis functions where Dirichlet boundary conditions can be imposed directly as the max-ent basis function satisfies the weak Kronecker-delta property on boundaries [56]. In addition, the *hp*-cloud method in [47] has been developed where MLS basis functions are enriched by adding additional degrees of freedom to build the PU property with higher order complete polynomial basis. The partition of unity finite element method (PUFEM) has been presented in [48] where the concept of the PU property is used for constructing the approximation.

Table 2.1 summarises the attributes of selected weak form-based meshless methods using different basis functions, which are ordered by the dates when the first versions of these methods were proposed.

The classification of SPH is a subject of debate. The expression of SPH basis functions is calculated by the integral of the product of the particle volume and the kernel function. As integration is used in constructing kernel basis functions, SPH is grouped with weak form meshless methods. Another viewpoint is that SPH is in general a representative of

Method	Year	Researcher(s)	Basis functions
SPH	1970	Lucy	Smooth kernel
DEM	1992	Nayroles	Diffuse MLS/RK
EFGM	1994	Belytschko	Direct MLS
NEM[a]	1995	Braum	Natural neighbour
RKPM	1995	Liu	RK
PUFEM	1996	Melenk	Local polynomials
HPC [b]	1996	Duarte et al.	Enriched MLS/RK
FMM [c]	1996	Yagawa et al.	Local polynomials
MLPG	1998	Atluri et al.	MLS/RK or smooth kernel
LBIE [d]	1998	Zhu et al.	MLS
PPU[e]	2000	Griebel et al.	Enriched MLS/RK
PIM[f]	2001	Liu et al.	Polynomials
max-ent	2004	Sukumar	max-ent
XEFGM[g]	2006	Rabczuk	Enriched MLS

[a] natural element method (NEM)
[b] *hp*-cloud (HPC)
[c] free mesh method (FMM)
[d] local boundary integral equation (LBIE)
[e] particle partition unity (PPU)
[f] point interpolation method (PIM)
[g] extended element-free Galerkin method (XEFGM)

Table 2.1: Weak form-based meshless methods.

a strong form collocation approach since the use of interpolation kernel allows smoothed approximations to be calculated from the particle information rather than using a weak form [24].

A compact integration domain, which is required in weak form for numerical integration, can be constructed globally or locally, therefore weak form meshless methods can be further split to

- global weak forms which involve integrals over the global domain;
- local weak forms in which integration is calculated over local subdomains.

Local domains can be chosen to coincide with local support domains of weight functions. Any shape of local domain can be selected but usually a regular and simple shape is preferable such as circles or rectangles in two dimensions and spheres or cubes in three dimensions. Some global and local weak form-based meshless methods are categorised as in Table 2.2.

Global weak form	DEM [57] EFGM [22, 58] PIM [32]
Local weak form	MLPG [59, 60] NEM, PUFEM, LBIE

Table 2.2: Global and local weak form-based meshless methods.

In spite of the potential benefits of using weak form meshless methods (as mentioned above), there are also some drawbacks. For example, large computational cost can be incurred by numerical integration scheme as a number of integration points are normally needed for accurate solution, posing considerable complexities [61]. The term "meshless" only indicates that no mesh for the approximation of the field variables. Most weak form meshless methods have been criticised for not actually being truly meshless as global or local background meshes have to be created to integrate the governing PDEs. Numerical integration seems to be the most significant issue which reduces the efficiency of weak form-based meshless methods as compared to the standard FEM for instance [62, 63].

To address this drawback, attempts have been made to develop more efficient and accurate integration techniques for weak form meshless methods. These have included direct nodal integration [26], stabilised nodal integration [64], stabilised conforming (not separated nor overlapped) approach [65] and non-conforming scheme [66]. Some of these proposed numerical integration techniques can provide accurate and stable integration schemes but it is known that much computational cost is required, especially for irregular discretisations. Therefore, other strategies have to be investigated to address this problem.

2.3.2 Strong form meshless methods

An alternative approach, the strong form-based point collocation method, has been developed, which eliminates the use of numerical integration in weak form meshless methods. A background mesh for numerical integration, therefore, is not required in point collocation methods (PCMs), which offers the possibility of meshless methods and have in the past been labelled as "truly meshless". In PCMs, a set of collocation points are distributed in the problem domain and on the boundaries. The governing PDEs and corresponding boundary conditions are discretised at collocation points directly to formulate the final system of equations in terms of the unknown field variables at a different

set of points (called source points). The approximation of solution at any point can be obtained by using the basis function values and the field variables associated with source points inside the local support domain (explained in Figure 2.2). Collocation methods necessitate the employment of higher order derivatives of basis functions as the strong form governing equations are imposed at collocation points directly. Compared with weak form meshless methods, strong form meshless methods possess some advantages as given in [30].

- They can be discretised arbitrarily in theory using a regular or a random points distribution.
- They are straightforward to implement.
- They can be computationally efficient as a background mesh is not required for numerical integration.
- They can handle adaptive strategies directly without the use of a mesh.
- They can be applied to applications with large deformations directly as mesh distortion does not exist.

In the context of meshless methods, some strong form-based methods have been investigated. The origin of meshless collocation methods can be tracked back to the pioneer work done by Kansa [67,68] where the radial basis function (RBF) is adopted in a PCM, named the radial basis collocation method (RBCM). In the RBCM, the construction of the final system of equations is direct, especially for three-dimensional problems with complicated geometries. Recently, the RBCM has been applied to solve two-dimensional non-linear boundary value problems [69, 70] and a domain decomposition technique was used in the RBCM for fracture mechanics [71]. However, this method may lead to ill-conditioning matrices when RBF basis functions are constructed globally, which has an effect on the accuracy of the solution. MLS and RK basis functions can be used in PCMs, yielding the moving least squares collocation method (MLSCM) [72, 73] and the RKCM [74, 75], respectively. Since both MLS and RK basis functions have localities, the sparse coefficient matrices in the equation systems can be obtained using both methods.

The RKCM has been applied to solve heat conduction problems in [74] and the stability analysis of the RKCM was discussed in [76]. The finite point method (FPM) was proposed in [77, 78], where a WLS approach is used to construct basis functions and the governing PDEs and boundary conditions are imposed at individual points. A stability analysis of using the FPM was studied, in which the unstable results are caused by the arrangement of points [79]. The Method of Fundamental Solutions (MFS) which belongs to the group of boundary collocation methods, is used to approximate the solution of the problem [80]. In this procedure, a set of single layer source points are distributed outside the solution domain. The boundary conditions are satisfied by simple boundary collocation or a least square fitting of the boundary data. In this procedure, one avoids the problem of evaluation of the singular integrals needed in the BEM. One of the main drawbacks of the MFS is that it is difficult to determine the position of source points for accurate results.

Some strong form-based meshless methods are categorised in Table 2.3. There are exceptions to this classification as some basis functions can be used in both strong and weak form discretisations.

Method	Year	Researcher(s)	Basis functions
RBCM	1990	Kansa	Local RBF
MPS[a]	1996	Koshizuka et al.	WLS
FPM	1996	Oñate	WLS
RKCM	2000	Aluru	RKPM
MLSCM	2001	Zhang	MLS
HCM[b]	2003	Li	Enriched MLS
GRKCM[c]	2013	Chi	Diffuse RKPM
MEPCM	2018	Fan et.al	Mex-ent

[a] moving particle semi-implicit (MPS)
[b] hermite collocation method (HCM)
[c] gradient reproducing kernel collocation method (GRKCM)

Table 2.3: Strong form-based meshless methods.

Other developments include weak and strong form-based meshless methods, which incorporate their formulations in subdomains as proposed in [29, 81–83] for solving incompressible linear elasticity [84, 85]. PCMs have also been further modified to develop an isogeometric collocation (IGA-C) method in [86] where superconvergence theory is adopted to choose the locations for collocation points, achieving similar convergence rates

in energy norms as that of the Galerkin method. Superconvergence theory provides an idea for discretisation, using which the numerical solution converges to the exact solution at a faster rate than that of using arbitrary distributions. More recently, the direct interpolation of the first smoothed gradients of meshless basis functions has been investigated using the IGA-C method. The second derivatives can be computed by differentiating the first derivatives. Using this technique to generate basis function derivatives, the second smoothed basis function derivatives can satisfy the consistency condition and the numerical results can converge to the exact solution at a faster rate than using the analytical derivatives [87]. The free element collocation method (FECM) [88] has recently been presented where the FEM basis function is used in PCMs. This method can provide stable results which are not affected by slightly varying the discretisations.

The classification of meshless methods has been given in this section. Weak and strong formulations formulate the system of equations in different ways. Some remaining research challenges are discussed in the following section.

2.4 Discussion of research challenges

Despite the considerable research efforts to date involving meshless methods, some issues remain before meshless methods can be widely and robustly applied in substantial applications.

As mentioned above in §1.3, higher order derivatives of basis functions, i.e. second order basis function derivatives for elasticity, are required in strong form-based PCMs. The direct differentiation of basis functions such as in MLS and RK is time-consuming because the calculation of the inversion of matrix terms is required in their expressions, which is computationally expensive and further affects the efficiency of overall analyses. In order to overcome this disadvantage, approaches such as the gradient RK basis function, in which the derivatives are approximated directly, have been proposed to improve the analytical differentiation technique [89]. However, it remains to be an interest to explore more available strategies.

The imposition of Dirichlet boundary conditions in the mesh-based FEM is straightforward as finite element basis functions automatically possess the Kronecker-delta prop-

erty. However, due to the lack of this property in most meshless basis functions, such as in MLS and RK basis funcitons, the direct imposition of Dirichlet boundary conditions is impossible. Additional techniques such as using Lagrange multipliers, penalty methods, Nitsche-like methods and coupling with the FEM basis function, have to be used to address this issue [90]. However, these strategies bring more complexities and computational cost. Therefore, exploring an efficient method to impose Dirichlet boundary conditions accurately is necessary.

Stability behaviour, which is vital in numerical analyses, can be studied by either analysing the conditioning number of the coefficient matrix or by perturbing the predefined parameters. Weak form-based meshless methods are usually stable because the governing PDEs and boundary conditions can be applied averagely over a global or local domain in numerical integrations. However, PCMs are criticised because these methods suffer from instabilities, which affects the numerical accuracy. It has been suggested that the negative values of basis functions could be the possible reason [40]. Theoretically, basis functions can be constructed with either random or regular discretisation. However, using an arbitrary distribution of points may fail to get convergent results in some cases.

Meshless methods present some apparent advantages in adaptive processes as the use of a mesh is removed. Some efforts for accurate numerical integration are not required. In meshless h-adaptivity, local regions with relative high errors need to be refined by adding more points directly. Alternatively, points distribution can be optimised by relocating points in r-adaptive meshless methods, preserving the same number of degrees of freedom. Combined rh-adaptivity could provide a more efficient way to improve the accuracy. Up to date, h-adaptivity has been employed in meshless methods (more applications in weak form-based than strong form meshless methods) to improve the accuracy of the solution. However, there is no available literature on meshless r- and combined rh-adaptivities, which can be a future research interest.

The study of geometric non-linearity is of great importance in the field of solid mechanics. Mesh-based methods usually experience difficulties in dealing with large deformation analyses because of mesh distortion that may degrade the accuracy. Meshless methods are therefore well-suited to handle the applications with extremely large defor-

mations robustly because meshless approximation functions are not constructed based on elements. In particular, removed with a PCM is the computational cost for numerical integration which is presented in weak form methods.

Structural analyses of geometrically non-linear membrane problems remain challenging in computational mechanics. Other than the strong non-linearity, the geometry of membranes result in unstable equilibrium. Numerical simulations for membrane problems are often modelled with hyperelastic materials for which the constitutive models are more complicated than linear elastic materials. Mesh-based FEM has been used for membrane analyses in which continuous remeshing is required to address mesh distortion. However in large deformation analyses, meshless methods are excepted to show some attractive advantages here for modelling membrane structures without considering mesh regeneration.

The research challenges in the development of meshless methods in particular for strong form meshless methods, have been given above. As compared to weak form meshless methods, much less study on strong form meshless methods has been conducted in previous research and there are still many issues remaining to be addressed, therefore, the investigation of strong form-based meshless methods for solid mechanics problems becomes the research interest in the following chapters of this thesis.

Chapter 3

The local maximum entropy point collocation method

3.1 Introduction

In the previous chapter, a detailed literature review on meshless methods has been given and it has been shown that strong form-based collocation methods possess some attractive features. In this chapter, the formulations and numerical implementation issues of meshless point collocation methods, especially those based on reproducing kernel (RK) and maximum entropy (max-ent) basis functions, are described in detail. The conventional point collocation method with RK basis functions is introduced. However, due to the lack of the Kronecker-delta property in RK basis functions, the direct imposition of Dirichlet boundary conditions by enforcing prescribed displacement values at individual points is impossible. Therefore, alternative approaches must be used. Lagrangian multipliers can be employed to enforce boundary conditions weakly but a set of additional unknowns are added to the linear system [22]. Dirichlet boundary conditions can be imposed by the penalty method, where a penalty parameter is required [53]. However, using this approach, the solution may not converge optimally as the numerical results are sensitive to the choice of the penalty parameter. Nitsche's method can be considered as an improvement of the penalty method. That is, rather than adding one term to the weak form, a number of terms is added, which is determined by the spe-

cific problem. Using this technique, the solution is stable and accurate with the proper selection of the penalty parameter. In addition, a combination of the basis functions used in Galerkin-based methods and the finite element method (FEM) was employed in [91–95] but the difficulty is caused by addressing the interface between mesh-based and meshless domains. One solution to overcome these issues is to use local max-ent basis functions [56]. Max-ent basis functions were originally derived from information theory and the max-ent principle in [96–99], and have been used to couple finite element and meshless methods [56, 100]. Local max-ent basis functions have been further developed into higher order approximants as described in [101, 102] which have been applied to solve incompressible media problems in [103], elastoplastic geotechnical analysis in [104], three-dimensional crack propagation in [105] and other applications in [106–113]. Compared to RK basis functions, max-ent basis functions are non-negative and possess a weak Kronecker-delta property, which can facilitate the imposition of Dirichlet boundary conditions directly in meshless methods.

Considering these properties in max-ent basis functions, a point collocation method with the local max-ent basis function is developed in this chapter, which is largely based on the published paper by the author [114]. The governing equations for two-dimensional Poisson and elasticity problems are summarised, and strong form-based point collocation methods are reviewed. After that, the formulations for two different basis functions including the conventional RK and the local max-ent are provided. Some numerical implementation issues including the choice of support domain and distribution of points are discussed. Two-dimensional Poisson problem and one- and two-dimensional linear elastic problems are presented. A comparative study in terms of accuracy and run time of the RK and the max-ent based point collocation methods is performed. Another comparison in terms of efficiency between the proposed method and the isogeometric collocation method reviewed in §2.3.2 is discussed. Finally, concluding remarks are given.

3.2 Governing equations

The structural responses of a majority of problems under externally applied loads are commonly characterised by a discrete formulation using governing PDEs in the field of computational solid mechanics [25, 115]. Both two-dimensional Poisson and one- and two-dimensional elasticity problems are studied in this chapter, so their governing PDEs are summarised in this section for the ease of use.

Firstly, for two-dimensional Poisson problems, their governing equations and boundary conditions are given as

$$\frac{\partial^2 u}{\partial x^2} + \frac{\partial^2 u}{\partial y^2} = f^p \quad \text{in} \quad \Omega \tag{3.1a}$$

$$u = \bar{u}^p \quad \text{on} \quad \Gamma_u \tag{3.1b}$$

$$\frac{\partial u}{\partial n} = \bar{t}^p \quad \text{on} \quad \Gamma_t \tag{3.1c}$$

where u is the field variable, f^p is the value of source term , $\bar{u}^p$ and $\bar{t}^p$ are the prescribed values on the Dirichlet and Neumann boundaries, Γ_u and Γ_t, respectively.

Secondly, the governing equations for two-dimensional elasticity are studied. Problems with both small and large deformations are investigated in this thesis, but the problems being considered in this chapter are modelled only under static equilibrium condition for linear elastic homogeneous materials with small deformations.

A two-dimensional solid with domain Ω and boundary $\Gamma(\Gamma_u \cup \Gamma_t)$ is considered as shown in Figure 3.1. This domain is subjected to a vector of external tractions $\{\bar{t}\} = \{\bar{t}_x, \bar{t}_y\}^T$ acting over the Neumann boundary Γ_t and a vector of prescribed displacements $\{\bar{u}\} = \{\bar{u}_x, \bar{u}_y\}^T$ over the Dirichlet boundary Γ_u, where overbars are used as constraints on boundaries and the subscripts associated with the two components in each vector indicate their directions in the Cartesian coordinate system. The vector term $\{f^b\} = \{f^b_x, f^b_y\}^T$ is the body force per unit volume. The governing equations and two different

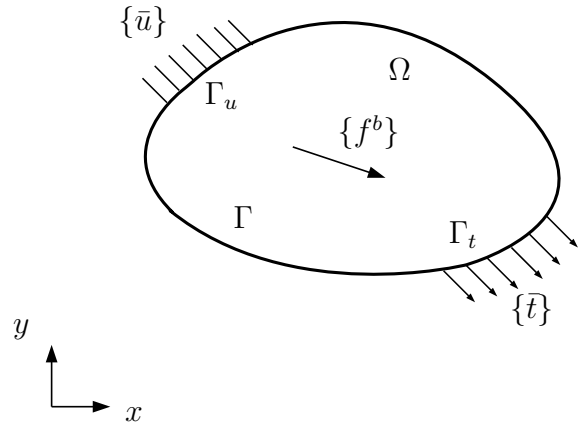

Figure 3.1: A two-dimensional problem domain subjected to the body force and boundary conditions.

boundary conditions are given as

$$[L]^T\{\sigma\} = \{f^b\} \quad \text{in} \quad \Omega \tag{3.2a}$$

$$\{u\} = \{\bar{u}\} \quad \text{on} \quad \Gamma_u \tag{3.2b}$$

$$[n]^T\{\sigma\} = \{\bar{t}\} \quad \text{on} \quad \Gamma_t \tag{3.2c}$$

where $[L]$ is a matrix of differential operators as

$$[L] = \begin{bmatrix} \frac{\partial}{\partial x} & 0 \\ 0 & \frac{\partial}{\partial y} \\ \frac{\partial}{\partial y} & \frac{\partial}{\partial x} \end{bmatrix} \tag{3.3}$$

in two dimensions. The Cauchy stress vector $\{\sigma\}$ is given as

$$\{\sigma\} = \{\sigma_{xx}, \sigma_{yy}, \sigma_{xy}\}^T \tag{3.4}$$

where the two subscripts for each component indicate the surface and the direction respectively. In Eq. (3.4), σ_{xx} and σ_{yy} are normal stresses and σ_{xy} is a shear stress. The

vector $\{u\}$ is the field variable described as

$$\{u\} = \{u_x, u_y\}^T \tag{3.5}$$

and $[n]$ is a matrix of the outer normals of a point lying on the boundary, which can be written as

$$[n] = \begin{bmatrix} n_x & 0 \\ 0 & n_y \\ n_y & n_x \end{bmatrix}. \tag{3.6}$$

When a stress is applied to a solid, this solid will undergo a strain. The linear elastic relationship between stress and strain can be expressed as

$$\{\sigma\} = [D]\{\varepsilon\}. \tag{3.7}$$

$[D]$ is the elastic material stiffness matrix given as

$$[D] = \frac{E}{(1+\nu)(1-2\nu)} \begin{bmatrix} 1-\nu & \nu & 0 \\ \nu & 1-\nu & 0 \\ 0 & 0 & \frac{1-2\nu}{2} \end{bmatrix} \tag{3.8}$$

and

$$[D] = \frac{E}{(1-\nu^2)} \begin{bmatrix} 1 & \nu & 0 \\ \nu & 1 & 0 \\ 0 & 0 & \frac{1-2\nu}{2} \end{bmatrix} \tag{3.9}$$

for plane strain and plane stress respectively, in which E is Young's Modulus and ν is Poisson's ratio. In plane stress cases, all stress components in z direction are zero. In latter plane strain cases, all strain components in z direction are zero. In Eq. (3.7), $\{\varepsilon\}$ is the strain vector which can be written as

$$\{\varepsilon\} = \{\varepsilon_{xx}, \varepsilon_{yy}, \gamma_{xy}\}^T. \tag{3.10}$$

Similarly to the stress vector, ε_{xx} and ε_{yy} are normal strains, γ_{xy} is an engineering shear strain. For small deformation cases, the relation between displacement and strain is

given as

$$\{\varepsilon\} = [L]\{u\}. \tag{3.11}$$

Substituting Eqs. (3.7) and (3.11) into Eq. (3.2), the governing equations and boundary conditions can be written as

$$[L]^T[D]([L]\{u\}) = \{f^b\} \quad \text{in} \quad \Omega \tag{3.12a}$$

$$[n]^T[D]([L]\{u\}) = \{\bar{t}\} \quad \text{on} \quad \Gamma_t \tag{3.12b}$$

$$\{u\} = \{\bar{u}\} \quad \text{on} \quad \Gamma_u. \tag{3.12c}$$

The basic formulations of the governing PDEs and boundary conditions for two-dimensional Poisson and elasticity problems have been provided in this section. In the following section, strong form-based point collocation methods are explained.

3.3 Point collocation methods

The point collocation method is a strong form-based method for solving PDEs and is at the heart of the research developed in this thesis. The theoretical background now presented is based on a two-dimensional spatial domain but it is straightforward to modify for other dimensionalities.

Collocation points and source points (numbering N_c and N_s respectively) are distributed in the domain Ω and on the boundaries Γ as shown in Figure 3.2. In this figure, a support domain of the collocation point is defined and the source points with a number N_s^* are located in this support. The approximation at this collocation point is determined by the basis function values and the field variables associated with those N_s^* source points inside that local support domain. Collocation points are the locations at which the strong form governing PDEs and corresponding boundary conditions are enforced. Therefore the numerical integration used in weak form meshless methods is not required and a background mesh is not needed. The enforcement of the governing equations and boundary conditions at collocation points is written in terms of the field variable values at source points weighted by basis functions associated with the same

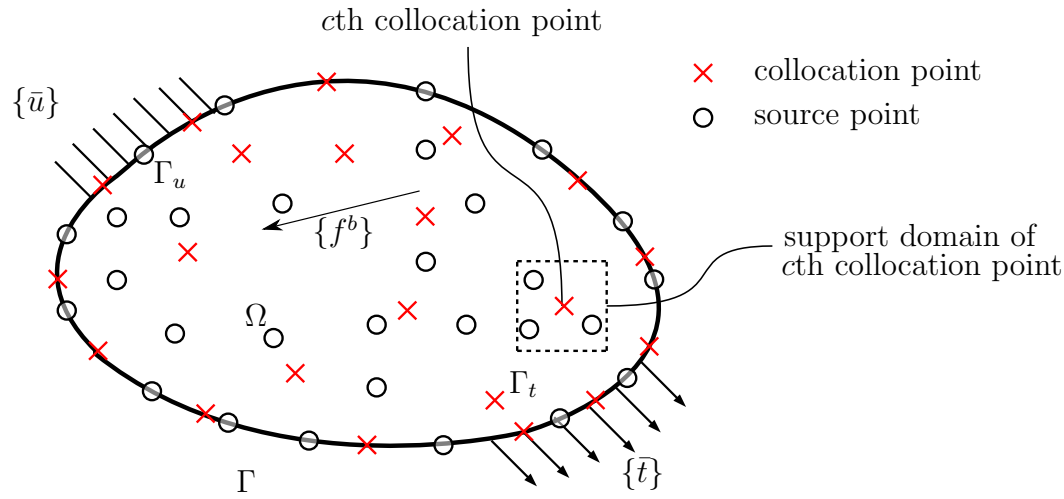

Figure 3.2: A two-dimensional problem domain subjected to the body force and boundary conditions with points discretisation.

source points. The governing PDEs and the two types of boundary conditions can be written as

$$\mathscr{L}\{u\} = \{f^{PCM}\} \quad \text{in } \Omega, \tag{3.13a}$$

$$\mathscr{L}_u\{u\} = \{\bar{u}^{PCM}\} \quad \text{on } \Gamma_u \text{ and } \mathscr{L}_t\{u\} = \{\bar{t}^{PCM}\} \quad \text{on } \Gamma_t, \tag{3.13b}$$

where $\mathscr{L}$ is the differential operator for the governing PDEs in Ω, $\mathscr{L}_u$ and $\mathscr{L}_t$ are the differential operators for Dirichlet and Neumann boundary conditions respectively and $\{u\}$ is the field variable. $\{f^{PCM}\}$, $\{\bar{u}^{PCM}\}$ and $\{\bar{t}^{PCM}\}$ can be reduced to f^p, $\bar{u}^p$ and $\bar{t}^p$ respectively for Poisson problems while they are $\{f^b\}$, $\{\bar{u}\}$ and $\{\bar{t}\}$ for elasticity. Since both Poisson and elasticity problems are demonstrated in the following numerical examples, the differential operators for both are given in Table 3.1 where D is

$$D = \frac{E(1-\nu)}{(1+\nu)(1-2\nu)} \tag{3.14}$$

under plane strain condition. The differential operators for plane strain cases can be derived from Eq. (3.8).

To implement the PCM one imposes the appropriate condition from Eqs. (3.13) at

	Poisson	Elasticity
$\mathscr{L}$	$\frac{\partial^2}{\partial x^2}+\frac{\partial^2}{\partial y^2}$	$D\begin{bmatrix} \frac{\partial^2}{\partial x^2}+\frac{1-2\nu}{2(1-\nu)}\frac{\partial^2}{\partial y^2} & \frac{1}{2(1-\nu)}\frac{\partial^2}{\partial x\partial y} \\ \frac{1}{2(1-\nu)}\frac{\partial^2}{\partial x\partial y} & \frac{\partial^2}{\partial y^2}+\frac{1-2\nu}{2(1-\nu)}\frac{\partial^2}{\partial x^2} \end{bmatrix}$
$\mathscr{L}_u$	1	$\begin{bmatrix} 1 & 0 \\ 0 & 1 \end{bmatrix}$
$\mathscr{L}_t$	$\frac{\partial}{\partial x}+\frac{\partial}{\partial y}$	$D\begin{bmatrix} \frac{\partial}{\partial x}n_x+\frac{1-2\nu}{2(1-\nu)}\frac{\partial}{\partial y}n_y & \frac{\nu}{1-\nu}\frac{\partial}{\partial y}n_x+\frac{1-2\nu}{2(1-\nu)}\frac{\partial}{\partial x}n_y \\ \frac{1-2\nu}{2(1-\nu)}\frac{\partial}{\partial y}n_x+\frac{\nu}{1-\nu}\frac{\partial}{\partial x}n_y & \frac{1-2\nu}{2(1-\nu)}\frac{\partial}{\partial x}n_x+\frac{\partial}{\partial y}n_y \end{bmatrix}$

Table 3.1: The differential operators for two-dimensional Poisson and elasticity problems.

each collocation point in the interior of the domain and on the boundaries, leading to a discrete set of N_c equations for the field variables at source points, $\{d\}$ of the form

$$[K]\{d\} = \{f\} \tag{3.15}$$

where $[K]$ is the coefficient matrix and $\{f\}$ is a vector of known values. The unknown field variables at source points $\{d\}$ are to be solved for determining the approximation of the field variables $\{u\}$ which are made in summation expressions of basis function values and the unknown field variables at source points $\{d\}$. The expanded form of Eq. (3.15) is

$$\begin{bmatrix} [K_{l1}] & [K_{l2}] & ... & [K_{lN_s}] \\ ... & ... & ... & ... \\ [K_{m1}] & [K_{m2}] & ... & [K_{mN_s}] \\ ... & ... & ... & ... \\ [K_{n1}] & [K_{n2}] & ... & [K_{nN_s}] \\ ... & ... & ... & ... \end{bmatrix} \begin{Bmatrix} \{d_1\} \\ \{d_2\} \\ ... \\ \{d_{N_s}\} \end{Bmatrix} = \begin{Bmatrix} \{f_l^{PCM}\} \\ ... \\ \{\bar{u}_m^{PCM}\} \\ ... \\ \{\bar{t}_n^{PCM}\} \\ ... \end{Bmatrix} \tag{3.16}$$

where l is the number of collocation points in the interior of the domain satisfying the governing equations, m and n are the remaining numbers of collocation points on boundaries carrying Dirichlet and Neumann boundary conditions respectively. The total number of collocation points covering the domain is $l + m + n = N_c$. Row i of $[K]$ represents a condition enforced at collocation point i, which is written in terms of the source points in support of that collocation point. Note that $[K]$ is generally non-symmetric. For one- and two-dimensional Poisson problems, $[K]$ in Eq. (3.16) is a matrix with size $N_c \times N_s$. In two-dimensional elasticity, $[K]$ is a $2N_c \times 2N_s$ matrix, the

unknown $\{d\}$ is a $2N_s \times 1$ vector and the right hand side vector is $2N_c \times 1$. The linear system of equations can be solved by either direct or iterative methods (the former is used throughout this thesis). Although the distributions of collocation and source points are independent to each other, N_c must equal or be greater than N_s to obtain the solution. When $N_c = N_s$, a square system is formed which has a unique solution if $[K]$ is not singular. However, when $N_c > N_s$, an over-determined system is obtained and a suitable solver (e.g. the least squares method) must be employed to obtain the source point values. Once $\{d\}$ has been determined, the approximation at any point of a two-dimensional problem domain can be interpolated from source points inside the support domain of this point using the basis functions associates with these source points as

$$\{u^h(\{x\})\} = \sum_{s=1}^{N_s^*} [\phi_s(\{x\})]\{d_s\}, \tag{3.17}$$

where $\{u^h(\{x\})\}$ is a 2×1 vector of approximation of the solution at any point, $[\phi_s(\{x\})]$ is a 2×2 matrix of basis functions and $\{d_s\}$ is a 2×1 vector of the unknown field variables associated with the sth source point inside the domain of support, and N_s^* is the number of source points inside the support.

3.4 Basis functions

Detailed formulations for point collocation methods have been introduced and the reproducing kernel (RK) and the local maximum entropy (max-ent) basis functions are described in this section.

3.4.1 Moving least squares basis functions

The MLS basis function, which was first introduced by Lancaster and Salkauskas in [50] for curve and surface fitting, is a very important member of the family of meshless basis functions. The objective of the MLS approach is to obtain basis functions in a bounded

domain. In one dimension, the MLS approximation at any point u^h is

$$u^h(x) = \sum_{s=1}^{n} \phi_s d_s \tag{3.18}$$

where x is the point's location, s is the nodal index, n is the total number of nodes in the local support domain. In this equation, ϕ_s and d_s are the MLS basis function value and the field variable associated with the sth node in the local support, respectively. The approximation $u^h(x)$ at any point x in one dimension can also be expressed in terms of a polynomial basis via

$$u^h(x) = \{p(x)\}^T \{a(x)\} \tag{3.19}$$

where $\{p(x)\}$ is a polynomial basis i.e. a linear basis in one dimension is $\{p(x)\} = \{1, x\}^T$, and $\{a(x)\}$ is a vector of unknown coefficient at x. A weighted residual error $\bar{J}$ is formed being the difference between the approximations and the unknown field variables, as

$$\bar{J} = \sum_{s=1}^{n} w_s(x) \Big(\{p(x_s)\}^T \{a(x)\} - d_s \Big)^2 \tag{3.20}$$

where x_s is the coordinate of the sth node and w_s is the weight function value at the sth node. Weight functions are used to guarantee the locality of MLS basis functions. That is, the weight function values at the nodes in the compact support domain of a point are non-zero and zero everywhere outside the support domain. Weight functions are required to be non-negative, monotonically decreasing, continuous and differentiable, making the approximation stable and smooth with arbitrary order consistency in basis functions. The unknown vector $\{a\}$ is determined by minimising the weighted residual error $\bar{J}$ in Eq. (3.20), i.e. $\frac{\partial \bar{J}}{\partial \{a\}} = 0$. The unknown vector can be obtained as

$$\{a\} = [A(x)]^{-1} [B(x)] \{d\} \tag{3.21}$$

where

$$[A(x)] = \sum_{s=1}^{n} w_s(x) \{p(x_s)\} \{p(x_s)\}^T, \tag{3.22}$$

$$[B(x)] = \Big[w_1(x)\{p(x_1)\}, \quad \cdots, w_n(x)\{p(x_n)\} \Big] \tag{3.23}$$

and the vector $\{d\}$ is

$$\{d\} = \{d_1, d_2, \cdots, d_n\}^T. \tag{3.24}$$

Eq. (3.19) becomes

$$u^h(x) = \{p(x)\}^T [A(x)]^{-1} [B(x)]\{d\} \tag{3.25}$$

and a $1 \times n$ vector collecting together the MLS basis function values associated with n nodes in the local support can be obtained by comparison with Eq. (3.18) as

$$\{\phi\} = \{p(x)\}^T [A(x)]^{-1} [B(x)]. \tag{3.26}$$

The MLS approach is distinguished from the other least squares approaches by a moving weight function so a standard least squares method is formed if all weight function values are constants. The imposition of Dirichlet boundary conditions using MLS basis functions however has to be indirect as the MLS approximations do not possess the Kronecker delta property, i.e. $u^h(x_s) \neq d_s$ (see Figure 3.3 for one-dimensional case). Extra techniques are therefore needed to impose Dirichlet boundary conditions. The inversion of a matrix term $[A]$ is required in the calculation of MLS basis functions and the derivatives of the inversion of the matrix term is needed in MLS basis function derivatives, which makes the calculation computationally expensive. MLS basis functions can be used in both weak and strong form-based methods.

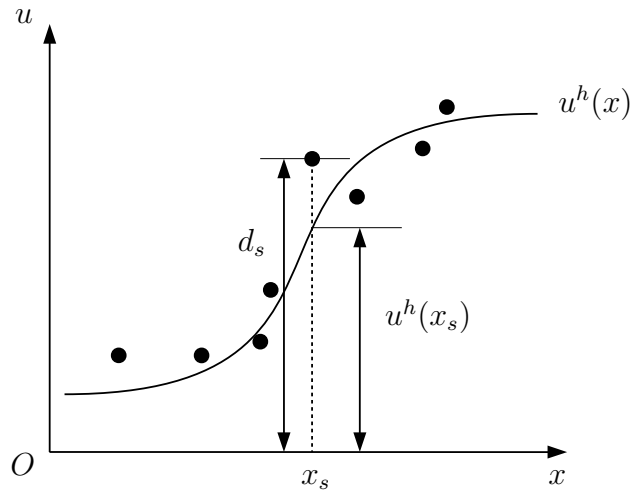

Figure 3.3: Moving least squares approximations in one dimension.

3.4.2 Radial basis functions

The radial basis function (RBF) was first introduced for interpolation by satisfying some known conditions as explained in [116]. An early example of employing RBFs in meshless methods for solving PDEs is due to Kansa [67, 68] and in later work, the RBF-based meshless method was used to address singularity [117] and higher order problems [118]. The theoretical foundation of the RBF for solving PDEs can be found in [119]. For scattered data, the RBF $g_s(r_s)$ at one point $\{x\}$ is dependent on the distance r_s between that point $\{x\}$ and a node $\{x_s\}$ in the local support domain as

$$r_s = ||\{x\} - \{x_s\}|| = \sqrt{(\{x\} - \{x_s\})^T \cdot (\{x\} - \{x_s\})}. \tag{3.27}$$

A few commonly used RBFs are given in Table 3.2. The constant ϵ in Table 3.2 is known as the shape parameter of a RBF, which can be used to control the bandwidth of the coefficient matrix and the locality of a local RBF. The RBF value associated with a node in the support domain tends to be zero or infinity as the distance r_s increases. These three types of RBFs with different values of ϵ are plotted in Figure 3.4. It can be observed in Figure 3.4(c)-3.4(d), the values of ϵ affect the shapes of RBFs.

Name	$g_s(r_s)$
Multiquadric	$(1 + (\epsilon r_s)^2)^{\frac{1}{2}}$
Inverse multiquadric	$(1 + (\epsilon r_s)^2)^{-\frac{1}{2}}$
Gaussian	$e^{-(\epsilon r_s)^2}$

Table 3.2: Three commonly used radial basis functions.

The RBF is usually constructed globally so that the coefficient matrix in the discrete system is formed as a full matrix which sometimes suffer from ill-conditioning problems. Local RBFs have been presented, in which the bandwidth of the coefficient matrix can be reduced by varying the shape parameter ϵ. However, the optimal choice of the shape parameter ϵ is unknown, which needs to be determined by numerical experiments [120]. The use of domain decomposition has also been suggested to reduce the conditioning number of the coefficient matrix [121, 122]. Similarly to MLS basis functions, RBFs can also be used in weak and strong form meshless methods, yielding the local radial point interpolation method (LRPIM) [123] and the RBCM [124], respectively.

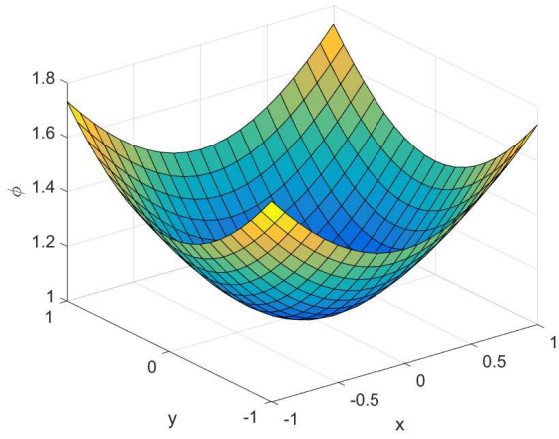

(a) Multiquadric with $\epsilon = 1$.

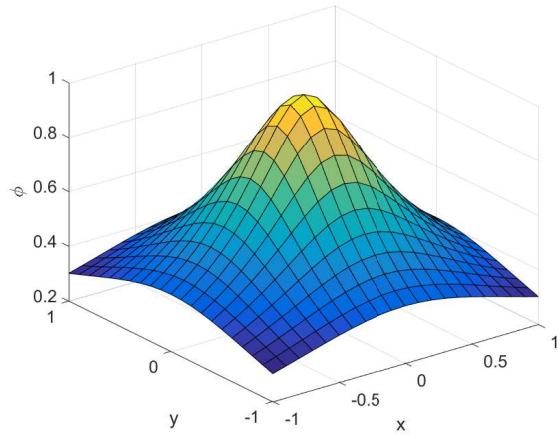

(b) Inverse multiquadric with $\epsilon = 5$.

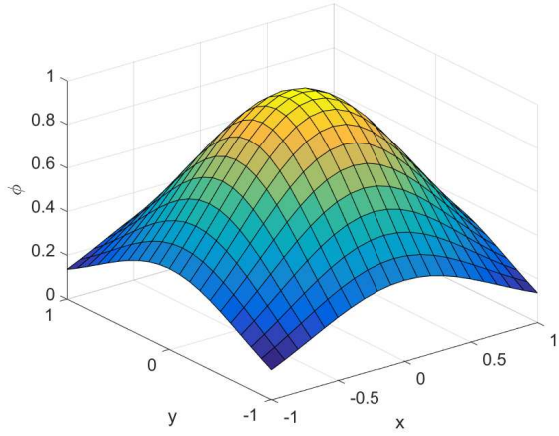

(c) Gaussian with $\epsilon = 1$.

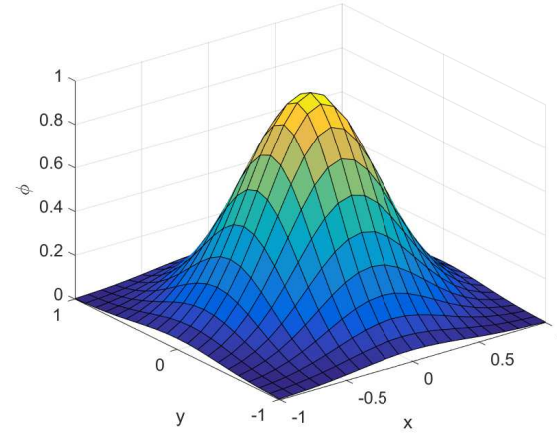

(d) Gaussian with $\epsilon = 3$.

Figure 3.4: Three commonly-used RBFs at $\{x\} = \{0, 0\}^T$ over a two-dimensional domain.

3.4.3 Reproducing kernel basis functions

The RK basis function is a very attractive basis function used in meshless methods for numerical solutions and has been adopted in the EFGM, however, the implementation of a Galerkin-based reproducing kernel particle method faces several challenges such as the calculation of nodal volumes and efficient imposition of boundary conditions [52]. The point collocation method with RK basis functions was presented in [74], which made the implementation straightforward. The detailed formulation of the RK basis function is given in this subsection.

Basis functions

In strong form meshless point collocation methods, the RK basis function has become one of the most often used basis functions for the approximation of the field variables (i.e. displacements in the case of solid mechanics) [52, 125]. Assuming that the support domain at a point $\{x\}$ is represented by N_s^* source points, a vector of RK basis functions associated with N_s^* source points is

$$\{\phi(\{x\})\} = \{K(\{x\})\}[\Delta V] \tag{3.28}$$

where $\{K(\{x\})\}$ is a vector of the kernel function with size $1 \times N_s^*$ and $[\Delta V]$ is a matrix of the nodal volume Δv_s (or area in two dimensions) assigned to the sth source point inside the support domain as

$$[\Delta V] = [\text{diag}((\Delta v_1), ..., (\Delta v_{N_s^*}))]. \tag{3.29}$$

If the kernel function equals the Dirac delta function $\delta_i(\{x_j\})$, where i and j are the indices of the source and collocation points, the field variables at source points can be reproduced exactly and the required consistency (discussed in Chapter 2) can be fulfilled [126]. In RK basis functions, a correction function with a certain consistency is introduced to the kernel function which can reproduce polynomials exactly, and be written as

$$\{K(\{x\})\} = \{C(\{x\})\}[W(\{x\})]. \tag{3.30}$$

In Eq. (3.30), $\{C(\{x\})\}$ is a correction function with size $1 \times N_s^*$ and $[W(\{x\})]$ is a diagonal matrix of weight function values with size $N_s^* \times N_s^*$ (in the context of the RK it is also called a window function) which is given as

$$[W(\{x\})] = [\text{diag}(w(\{x\} - \{x_1\}), ..., w(\{x\} - \{x_{N_s^*}\}))]. \tag{3.31}$$

$w(\{x\} - \{x_s\})$ is the weight function value centred at the sth source point that is used to guarantee the locality of the basis function. As the correction function plays an important role on boundaries and almost has no effect on domain far away from boundaries, it is also referred to as a boundary correction term [52, 126]. The correction function can be derived by several approaches including moving least squares in [127, 128] and Taylor series in [129], but they all give the same results as

$$\{C(\{x\})\} = \{p(\{x\})\}^T [M(\{x\})]^{-1} [P(\{x_s\})] \tag{3.32}$$

where $\{p(\{x\})\}$ is a polynomial basis function, $[M(\{x\})]$ is the discrete moment matrix and $[P(\{x_s\})]$ is a matrix of polynomial basis functions at N_s^* source points as

$$[P(\{x_s\})] = [p(\{x_1\}), ..., p(\{x_{N_s^*}\})]. \tag{3.33}$$

The polynomial basis $\{p(\{x\})\}$ is built from, triangle and Pascals pyramid for two- and three-dimensional problems respectively. Linear and quadratic basis functions are given as

$$\{p(\{x\})\} = \{p(x)\} = \{1, x\}^T \tag{3.34a}$$

$$\{p(\{x\})\} = \{p(x)\} = \{1, x, x^2\}^T \tag{3.34b}$$

in one dimension and

$$\{p(\{x\})\} = \{p(x, y)\} = \{1, x, y\}^T \tag{3.35a}$$

$$\{p(\{x\})\} = \{p(x, y)\} = \{1, x, y, x^2, xy, y^2\}^T \tag{3.35b}$$

in two dimensions. The moment matrix is given as

$$[M(\{x\})] = [P(\{x_s\})][W(\{x\})][P(\{x_s\})]^T. \tag{3.36}$$

The vector of RK basis functions in Eq. (3.28) is now given as

$$\{\phi(\{x\})\} = \{p(\{x\})\}^T[M(\{x\})]^{-1}[P(\{x_s\})][W(\{x\})][\Delta V] \tag{3.37}$$

which includes basis function values associated with N_s^* source points in the support domain. One certain basis function $\phi_s(\{x\})$ associated with the sth source point can be expressed as

$$\phi_s(\{x\}) = \{p(\{x\})\}^T[M(\{x\})]^{-1}\{p(\{x_s\})\}w(\{x\} - \{x_s\})\Delta v_s. \tag{3.38}$$

The RK basis function in Eq. (3.37) is almost the same as the MLS formulation with the choice $\Delta v_s = 1$ but they are deduced from different areas. The RK has its roots in wavelet theory and the MLS has its origin in data fitting [24].

Weight functions

As indicated in Eq. (3.30), weight functions which connect the source points in a collocation point's support domain, are used to obtain a certain locality in constructing basis functions. Weight functions are directionally independent. The functional form of a weight function has some influence on the convergence behaviour of an approximation but this is difficult to predict [126]. The choice of a weight function is to some extent arbitrary since there is no rigorous mathematical proof available to judge which type of weight function is better than another but there are some basic requirements for the selection of a weight function [52]:

- compact support;
- non-negative values;
- monotonically decreasing values with increasing distance;

- continuous and differentiable function.

There exist various possible choices of weight functions but typically, exponential (Gaussian) functions or spline functions with different orders are most often used [130]. The support domains produced differ in size and shape, depending on the choice of basis functions. The size of the support is controlled by the so-called dilatation parameter or smoothing length d_m. The shape of the support domain used in previous research e.g. [130] is usually circular or rectangular in two dimensions and a rectangular support is selected throughout this thesis. It is because that the basis function used in this thesis is expressed in Cartesian coordinates, where a product of two terms in x and y directions is included in two dimensions.

For the problems covered in this thesis, the second derivatives of weight functions are required so an appropriate choice here for the the weight function is a cubic spline which is given in one dimension as

$$w(x-x_s) = w(r) = \begin{cases} \frac{2}{3} - 4r^2 + 4r^3 & 0 < r \leq \frac{1}{2} \\ \frac{4}{3} - 4r + 4r^2 - \frac{4}{3}r^3 & \frac{1}{2} < r \leq 1 \\ 0 & r > 1 \end{cases}, \tag{3.39}$$

where

$$r(x-x_s) = \frac{\|x-x_s\|}{d_m}, \tag{3.40}$$

is the normalised radius of the support domain and $||x-x_s||$ is the distance between the sth source point and collocation point of interest x. d_m is user-defined as

$$d_m = d_{max}\ ds. \tag{3.41}$$

The scaling parameter d_{max} is typically 2.0−4.0 e.g. [131] and in terms of point collocation methods ds is the distance between the collocation point and the nearest source point in its support domain. Sufficient source points are required in the domain to avoid matrix singularity problems, and the accuracy of the approximation at any point also depends on the scaling parameter d_{max} [132]. Besides, the locations of the points also have an effect on the stability of the approximation. Since the weight function is dimensionally

independent, a two-dimensional weight function can be produced from a tensor product, i.e. for the sth source point $\{x_s\}$ in two dimensions is

$$w(\{x - x_s\}) = w(x - x_s)w(y - y_s). \tag{3.42}$$

As stated above, the weight function derivatives with respect to the spatial coordinates are also required and given as follows

$$\frac{dw(x - x_s)}{dx} = \frac{dw}{dr}\frac{dr}{dx} = \begin{cases} (-8r + 12r^2)\ \text{sign}(x - x_s) & 0 < r \leq \frac{1}{2} \\ (-4 + 8r - 4r^2)\ \text{sign}(x - x_s) & \frac{1}{2} < r \leq 1 \\ 0 & r > 1 \end{cases} \tag{3.43}$$

in one dimension and

$$\frac{\partial w(\{x - x_s\})}{\partial x} = \frac{dw(x - x_s)}{dx} w(y - y_s) \tag{3.44a}$$

$$\frac{\partial w(\{x - x_s\})}{\partial y} = w(x - x_s)\frac{dw(y - y_s)}{dy} \tag{3.44b}$$

in two dimensions.

First and second derivatives of RK basis functions

In PCMs, depending on the PDEs to be solved, higher order derivatives are needed (as compared to weak form approaches). These have been derived analytically in [74]. The first derivatives of the RK basis function associated with the sth source point are

$$\begin{aligned} \left\{\frac{\partial \phi_s}{\partial x_k}\right\} &= \Big(\Big[\frac{\partial p}{\partial x_k}\Big]^T [M]^{-1}\{p_s\}w + \{p\}^T\Big[\frac{\partial M}{\partial x_k}\Big]^{-1}\{p_s\}w \\ &+ \{p\}^T[M]^{-1}\{p_s\}\Big\{\frac{\partial w}{\partial x_k}\Big\}\Big)\Delta v_s \end{aligned} \tag{3.45}$$

where k denotes the coordinate index, $\left[\frac{\partial M}{\partial x_k}\right]^{-1} = -[M]^{-1}\left[\frac{\partial M}{\partial x_k}\right][M]^{-1}$ and $\{p_s\}$ is the polynomial basis associated with the sth source point $\{p(x_s)\}$ in short. The second

derivatives are

$$\begin{aligned}\Big[\frac{\partial \phi_s}{\partial x_k \partial x_l}\Big] &= \Big(\Big[\frac{\partial p}{\partial x_k \partial x_l}\Big]^T [M^{-1}]\{p_s\}w + \Big[\frac{\partial p}{\partial x_l}\Big]^T \Big[\frac{\partial M}{\partial x_k}\Big]^{-1}\{p_s\}w \\ &+ \Big[\frac{\partial p}{\partial x_k}\Big]^T [M]^{-1}\{p_s\}\Big\{\frac{\partial w}{\partial x_l}\Big\} + \Big[\frac{\partial p}{\partial x_l}\Big]^T \Big[\frac{\partial M}{\partial x_k}\Big]^{-1}\{p_s\}w \\ &+ \{p\}^T\Big[\frac{\partial M}{\partial x_k \partial x_l}\Big]^{-1}\{p_s\}w + \{p\}^T\Big[\frac{\partial M}{\partial x_k}\Big]^{-1}\{p_s\}\Big\{\frac{\partial w}{\partial x_l}\Big\} \\ &+ \Big[\frac{\partial p}{\partial x_l}\Big]^T [M]^{-1}\{p_s\}\Big\{\frac{\partial w}{\partial x_k}\Big\} + \{p\}^T\Big[\frac{\partial M}{\partial x_l}\Big]^{-1}\{p_s\}\Big\{\frac{\partial w}{\partial x_k}\Big\} \\ &+ \{p\}^T[M]^{-1}\{p_s\}\Big[\frac{\partial w}{\partial x_k \partial x_l}\Big]\Big)\Delta v_s \end{aligned} \tag{3.46}$$

with $\Big[\frac{\partial M}{\partial x_k \partial x_l}\Big]^{-1} = [M]^{-1}\Big[\frac{\partial M}{\partial x_l}\Big][M]^{-1}\Big[\frac{\partial M}{\partial x_k}\Big][M]^{-1} - [M]^{-1}\Big[\frac{\partial M}{\partial x_k \partial x_l}\Big][M]^{-1} + [M]^{-1}\Big[\frac{\partial M}{\partial x_k}\Big][M]^{-1}\Big[\frac{\partial M}{\partial x_l}\Big][M]^{-1}$ where l is the coordinate index. Although RK basis functions are smooth, determining the higher derivatives of basis functions can be quite time-consuming, especially in computing the inversion of the moment matrix $[M(\{x\})]$ and the derivatives of the inversion of the moment matrix. Deriving the derivatives directly using traditional mathematics is unwise. In order to accelerate the computational speed of derivatives, some other methods such as the gradient RKPM proposed in [89] have been developed using derivative approximating techniques to improve the computational efficiency.

3.4.4 Maximum entropy basis functions

MLS and RK basis functions are employed in most early strong form-based meshless approaches but they are not strictly positive and do not possess the Kronecker-delta property, which makes the direct imposition of Dirichlet boundary conditions impossible [90]. A local max-ent scheme is used to construct the basis functions in point collocation methods, which first appeared in the published paper by the author of this thesis, to overcome some of these difficulties. Max-ent basis functions are strictly valid on convex domains (but function well on non-convex domains in many cases [96, 133, 134]).

A local max-ent basis function formulation

The maximum entropy idea arises from probability theory where a set of mutually independent events $\{A_1, A_2, ..., A_n\}$ with unknown probabilities $\{p_1, p_2, ..., p_n\}$, respectively,

are considered. The least biased probability distribution can be obtained by maximising the informational entropy $P(\cdot)$ (the specific description of uncertainty) as

$$\text{maximise}\Big(P(A_1, A_2, ..., A_n) = P(p_1, p_2, ..., p_n) = -\sum_{a=1}^{n} p_a \log p_a\Big). \tag{3.47}$$

If one replaces the probabilities by basis functions in a given defined domain then it is easy to see that the partition of unity property is obtained. The basis functions are obtained by combining the max-ent constraint expressed in Eq. (3.47) with the required linear reproducing conditions [56] and a weight function w_s to give compact support, i.e. maximising

$$P(\phi, w) = -\sum_{s=1}^{N_s^*} \phi_s \log\left(\frac{\phi_s}{w_s}\right) \tag{3.48}$$

subject to (in the one-dimensional case)

$$\sum_{s=1}^{N_s^*} \phi_s = 1 \quad \text{and} \quad \sum_{s=1}^{N_s^*} \phi_s x_s = x. \tag{3.49}$$

The local max-ent basis functions derived in this way can be written as

$$\phi_s(\{x\}) = \frac{Z_s}{Z} \tag{3.50}$$

where

$$Z_s = w_s e^{-\{\bar{\lambda}_s\}^T(\{x_s\}-\{x\})} \tag{3.51}$$

and

$$Z = \sum_{s=1}^{N_s^*} Z_s. \tag{3.52}$$

$\{\bar{\lambda}\}$ denotes the unique Lagrange multiplier associated with the constraints in Eq. (3.49) which can be found via a Newton-Raphson method [135] as

$$\{\bar{\lambda}\} = \arg\min \ \log Z(\{x\}, \{\bar{\lambda}\}). \tag{3.53}$$

A detailed explanation of max-ent basis functions and their implementation can be found in [136].

First and second derivatives of max-ent basis functions

As indicated above, PCMs usually require expressions for derivatives of higher order than required in weak form-based methods. The first derivatives of the max-ent basis functions [136] can be expressed as

$$\begin{aligned}\Big\{\frac{\partial \phi_s}{\partial x_p}\Big\} &= \phi_s\Big\{(\{x_s\}-\{x\})^T\Big[[H]^{-1}-[H]^{-1}\sum_{k=1}^{N_s^*}\frac{\phi_k}{w_k}(\{x_k\}-\{x\})\otimes\Big\{\frac{\partial w_k}{\partial x_p}\Big\}\Big] \\ &+ \Big\{\frac{\partial w_s}{\partial x_p}\Big\}\frac{1}{w_s}-\sum_{j=1}^{N_s^*}\phi_j\Big\{\frac{\partial w_j}{\partial x_p}\Big\}\frac{1}{w_j}\Big\} \end{aligned} \tag{3.54}$$

where $[H]$ is the Hessian matrix given by

$$[H]=\sum_{k=1}^{N_s^*}(\{x_k\}-\{x\})\otimes(\{x_k\}-\{x\})\phi_k, \tag{3.55}$$

where $\otimes$ is the dyadic product of two vectors, for example, for any two vectors $\{x\}\otimes\{y\} = \{x\}\{y\}^T$. Similarly the second derivatives of the max-ent basis functions are

$$\begin{aligned}\Big[\frac{\partial \phi_s}{\partial x_p \partial x_q}\Big] &= \Big(\Big\{\frac{\partial \phi_s}{\partial p}\Big\}\otimes\Big\{\frac{\partial \phi_s}{\partial q}\Big\}\Big)\frac{1}{\phi_s} \\ &+ \phi_s\Big\{-[H]^{-1}+(\{x_s\}-\{x\})\cdot\Big[\frac{\partial H}{\partial x_q}\Big]^{-1} \\ &+ \Big[\sum_{k=1}^{N_s^*}\frac{\phi_k}{w_k}\Big((\{x_k\}-\{x\})\otimes\Big\{\frac{\partial w}{\partial x_p}\Big\}\Big)\Big]^T[H]^{-1}\Big\} \\ &- \phi_s\Big\{(\{x_s\}-\{x\})\cdot\Big[\frac{\partial H}{\partial x_q}\Big]^{-1}\Big[\sum_{k=1}^{N_s^*}\frac{\phi_k}{w_k}\Big((\{x_k\}-\{x\})\otimes\Big\{\frac{\partial w_k}{\partial x_p}\Big\}\Big)\Big] \\ &+ \Big[(\{x_s\}-\{x\})^T[H]^{-1}\Big]\cdot\Big[\partial\Big(\sum_{k=1}^{N_s^*}\frac{\phi_k}{w_k}(\{x_k\}-\{x\})\otimes\Big\{\frac{\partial w_k}{\partial x_p}\Big\}\Big)/\partial x_q\Big]\Big\} \\ &+ \phi_s\Big\{\Big[\partial\Big(\Big\{\frac{\partial w_s}{\partial x_p}\Big\}\frac{1}{w_s}\Big)/\partial x_q\Big]-\sum_{j=1}^{N_s^*}\Big(\Big\{\frac{\partial w_j}{\partial x_p}\Big\}\frac{1}{w_j}\Big)\otimes\Big\{\frac{\partial \phi_j}{\partial x_q}\Big\} \\ &- \sum_{j=1}^{N_s^*}\phi_j\Big[\partial\Big(\Big\{\frac{\partial w_j}{\partial x_p}\Big\}\frac{1}{\partial x_j}\Big)/\partial x_q\Big] \end{aligned} \tag{3.56}$$

The derivation of the second derivatives is given in Appendix A.

In Figure 3.5(a) and 3.5(b), the max-ent and RK basis functions are plotted over a one-dimensional domain with the same sizes of supports, where 6 points are located at $x = 0, 0.2, 0.4, \ldots, 1.0$. It can be seen that the max-ent and RK basis functions possess non-negativity at all points. Besides max-ent basis functions in Figure 3.5(a) satisfy the Kronecker-delta property at the two boundary points, which makes direct imposition of Dirichlet boundary conditions possible. However, the RK basis function values at $x = 0$ and $x = 1.0$ are less than one as shown in Figure 3.5(b). The first and the second derivatives of the max-ent basis functions at each point in the domain are shown in Figure 3.5(c) and 3.5(d). Of note is the fact that the first and second derivatives of the max-ent basis functions are sensitive to the position of the points. One consequence of this for PCMs is that distributing the collocation points and source points at the same positions may lead to serious defects with the numerical results because of the obtained values of basis function first and second derivatives. For instance in Eq. (3.56) the term $(\{x_s - x\})$ is zero when $\{x_s\} = \{x\}$, which results in a zero value for the first and second derivative of basis function. Hôpital's rule was used to obtain the expressions for the derivatives of the max-ent basis functions [137]. Here, the positions for collocation and source points are adjusted to avoid this problem. In this one-dimensional domain, the number of collocation points is one greater than the number of source points. Using a uniform distribution, the problem caused by the coincident distributions of two sets of points can be addressed. But the collocation and source points at two boundaries are located at the same positions, the numerical first derivatives of basis functions at these two boundary points have to be used for imposing Neumann boundary conditions.

In Figure 3.6, the second basis function derivative components at point $(0.5, 0.5)$ in two dimensions are plotted. For this two-dimensional domain, the number of collocation points in each direction is one greater than the number of source points in the same direction, getting rid of the coincident distribution of points. If $N_s = N_c$ is required, a scaling factor can be defined to vary the point distributions (used in the example in Chapter 4). The formulations of the RK and local max-ent basis functions have been described in this section and the performance of these basis functions are compared in the next section.

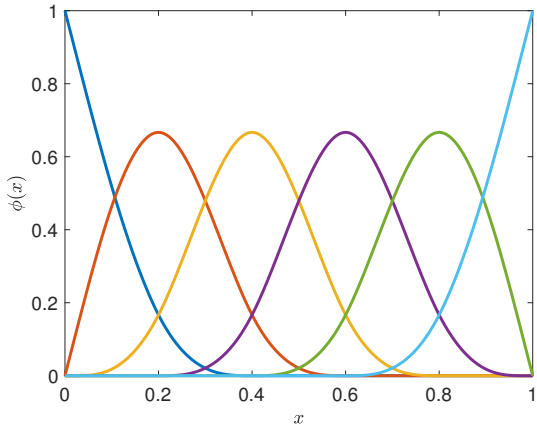

(a) Max-ent basis functions.

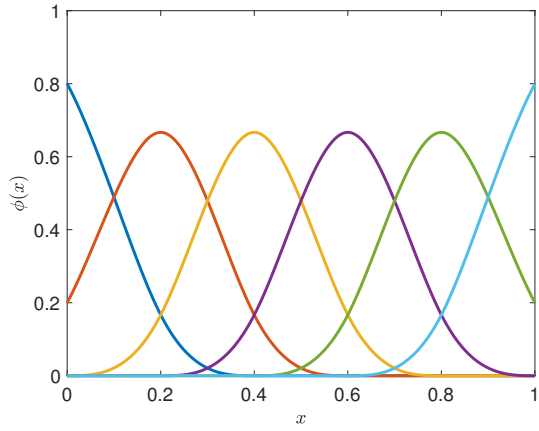

(b) RK basis functions.

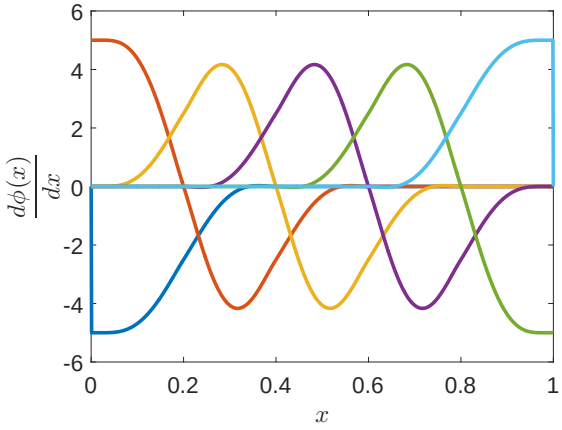

(c) First derivatives of max-ent basis functions with respect to x.

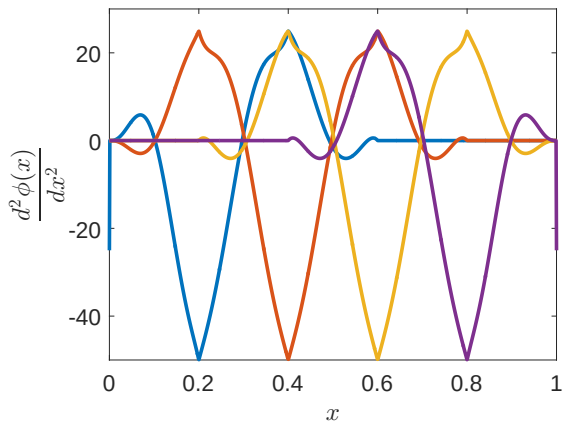

(d) Second derivatives of max-ent basis functions with respect to x.

Figure 3.5: Max-ent and RK basis functions and first and second max-ent basis function derivatives over a one-dimensional domain.

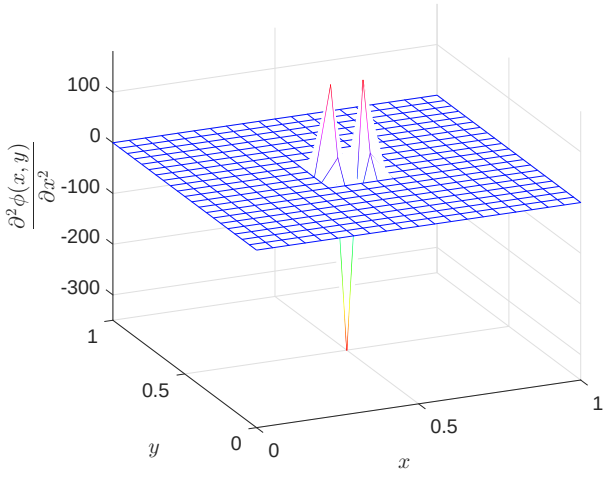

(a) Second partial derivatives with respect to x.

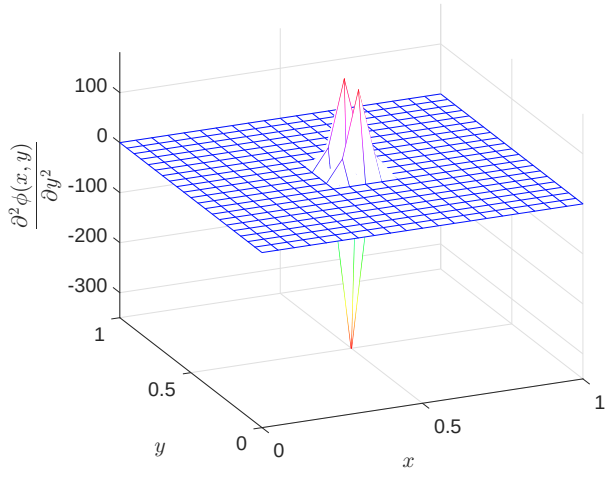

(b) Second partial derivatives with respect to y.

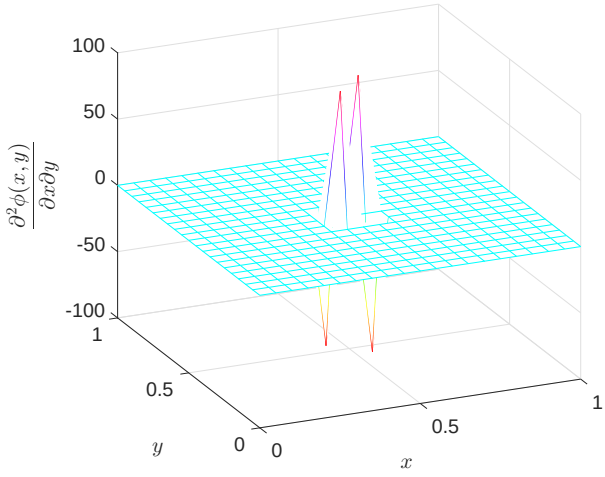

(c) Cross partial derivatives with respect to x and y.

Figure 3.6: The second derivatives of max-ent basis functions at (0.5, 0.5) over a two-dimensional domain.

3.5 Numerical examples

In this section, some numerical examples are analysed to validate the efficiency and accuracy of the conventional reproducing kernel collocation method (referred to the RKCM) and the proposed local max-ent point collocation method (MEPCM). In order to study the performance of the weak Kronecker-delta property on the boundary points, only Dirichlet boundary conditions are considered in the following examples. All examples presented in this chapter have exact solutions so that clear error norms can be calculated to show convergence rates and computational performance. In the results presented below the L_2 norm of relative error on displacement $||e||_{L_2}$ is used to assess error (being an appropriate measure for the types of problems considered, as discussed in [86]) and is evaluated as

$$||e||_{L_2} = \frac{\sqrt{\{u^h - u^e\}^T\{u^h - u^e\}}}{\sqrt{\{u^e\}^T\{u^e\}}}, \tag{3.57}$$

where $\{u^h\}$ denotes the approximation to the field variable and $\{u^e\}$ is the exact solution. In the following examples, plots of $||e||_{L_2}$ in the primary variable of solution versus degrees of freedom are employed to demonstrate the rate of convergence of the method. The efficiency of the proposed method will be shown compared to the point collocation method with RK basis functions, since computational cost is clearly of great importance for numerical methods applied to challenging real world problems in terms of reducing the error [74].

3.5.1 One-dimensional bar problem

The first problem is a one-dimensional linear elastic bar of unit length fixed at a point $x = 0$ and subjected to a linear body force $f^b = x$. The geometry of this problem is shown in Figure 3.7. For the one-dimensional problem, the linear system was set up so that Dirichlet boundary conditions were applied to the collocation points at two ends and the governing equations were imposed at all collocation points inside the problem domain. For this example, Dirichlet boundary conditions are applied at two ends in order to test the accuracy of the MEPCM at Dirichlet boundaries. The analytical solutions

for the displacement and stress field of this one-dimensional bar problem are

$$u(x) = \frac{1}{E}\left(\frac{x}{2} - \frac{x^3}{6}\right) \quad \text{and} \quad \sigma(x) = \frac{1 - x^2}{2}, \tag{3.58}$$

where here, $E = 1.0$.

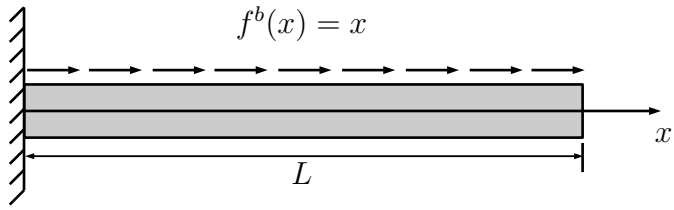

Figure 3.7: The geometry model of the one-dimensional bar.

The unit length bar was discretised by a uniform distribution of 11 collocation points with 10 source points located between each pair of collocation points as shown in Figure 3.8. The figure shows two different sizes of the support domains for $d_{max} = 2.0$ and $d_{max} = 4.0$, so different numbers of source points are included in the support domain. To demonstrate the effect of the choice of d_{max} on accuracy, the problem has been

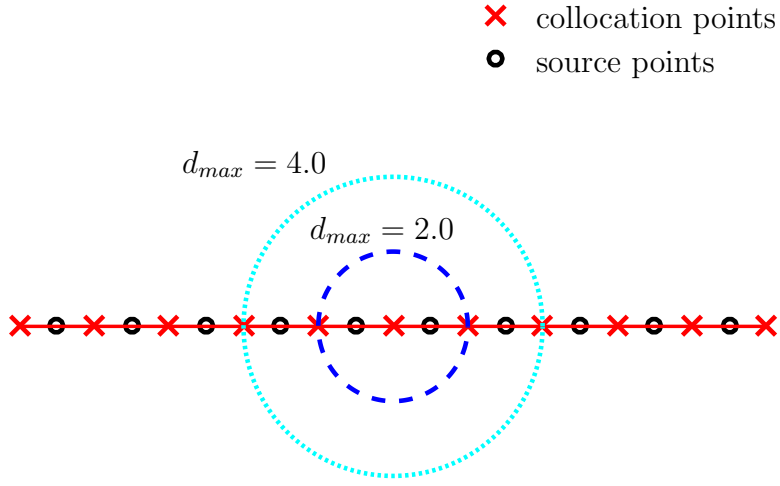

Figure 3.8: A portion of the one-dimensional bar with points distribution and different sizes of support domain.

solved using the MEPCM with a range of different values of this parameter, for varying discretisations (N_s values), and the results are plotted in Figure 3.9. In the analyses with

$d_{max} = 1.5, 2.0, 2.5$, each collocation point has two source points in the local support, however the accuracy and convergence properties differ between analyses due to the effect of d_m in Eq. (3.41) on the weighting functions embedded in the basis functions in Eq. (3.39). In this problem the optimum d_{max} is around 2.0 with close to quadratic convergence characteristics for all three analyses. When d_{max} increases to 3.5, 4.0 and 8.0 the accuracy and rate of convergence deteriorate, likely due to the loss of locality of the approximation (as seen in MLS as it moves towards LS). It is particularly noticeable that the convergence rate for $d_{max} = 8.0$ is very poor. From this discussion, it clearly remains difficult to predict *a priori* optimum value of d_{max} although the max-ent basis function satisfies the linear reproducing conditions, the minimum number of source points in support is 2, which provides a lower bound value for d_{max}. As discussed in §3.5, source points and collocation points should not be distributed at the same positions. When analyses are carried out with coincident points, $||e||_{L_2}$ were recorded as 0.4929, 0.4936, 0.4942, 0.4943, 0.4936, 0.7581 with N_c=N_s=119, 172, 287, 341, 1000, 2000, respectively. It is clear that $||e||_{L_2}$ does not converge using coincident source points and collocation points.

Figures 3.10(a) and 3.10(b) compare the MEPCM results from the "best" choice of $d_{max} = 2.0$, using $N_s = 200$ and $N_c = 201$, with the analytical solution, showing close agreement (note that for clarity only 11 MEPCM results have been plotted from the 201 total values).

The absolute displacement errors at 11 selected collocation points using the MEPCM and the RKCM are shown in Figure 3.11 for different refinements. It is clear that the boundary conditions can always be imposed accurately in the MEPCM due to the Kronecker-delta property at boundaries of the max-ent basis functions, while in the RKCM, the direct imposition of Dirichlet boundary conditions makes the displacement errors on two edge points are greater than 0.005, which has a major effect on the total $||e||_{L_2}$ for the overall accuracy. Since the problem is non-symmetric, it is reasonable that the errors at two ends using the RKCM are different.

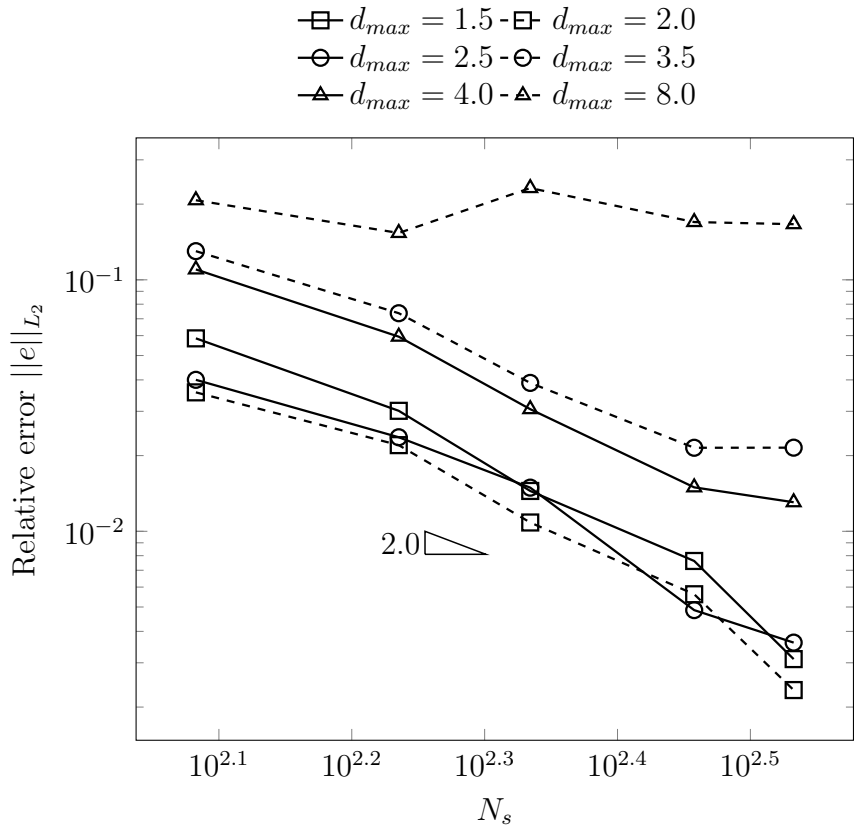

Figure 3.9: Convergence rate of $||e||_{L_2}$ of the one-dimensional bar problem using the MEPCM with different d_{max}.

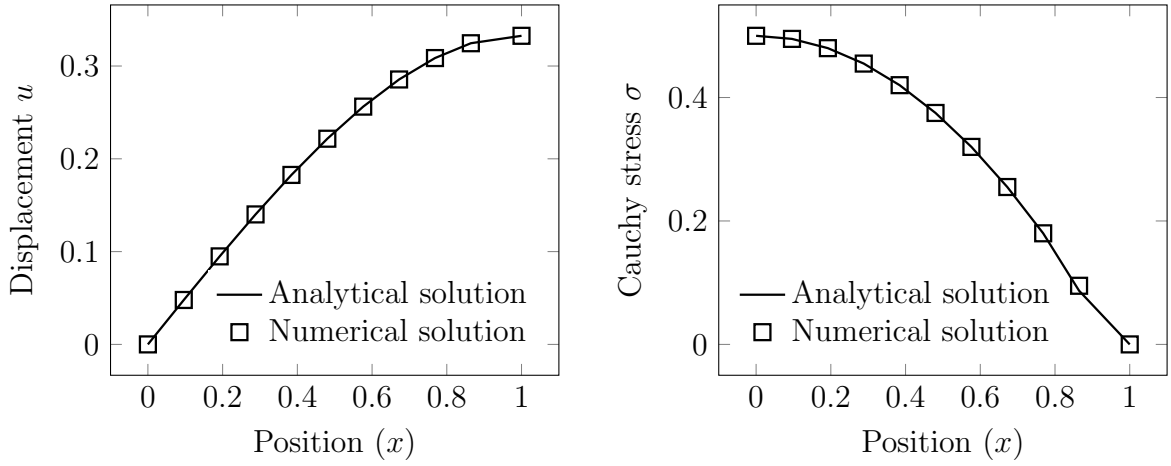

(a) Displacement results against positions.

(b) Stress results against positions.

Figure 3.10: Displacement and stress results of the one-dimensional bar problem using the MEPCM.

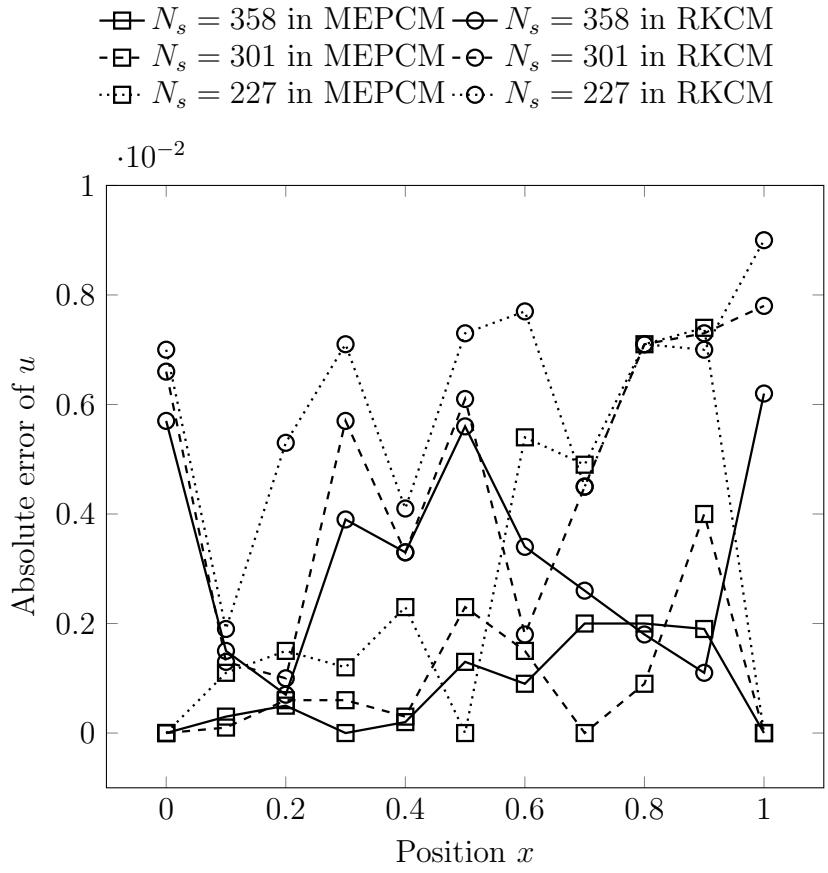

Figure 3.11: The displacement errors of the one-dimensional bar problem using the MEPCM and the RKCM with different N_s.

The convergence rates of $||e||_{L_2}$ using both the MEPCM and the RKCM are shown in Figure 3.12(a) in which N_s denotes degrees of freedom in the one-dimensional bar problem. It is clear that the decrease of $||e||_{L_2}$ in the MEPCM is greater as compared to the RKCM. In PCMs, errors can be attributed to boundary errors and domain errors. For the RKCM, the combination of the two effects mentioned above leads to the total error, while the error on the boundaries in the MEPCM is considerably reduced leading to better convergence rates. In Figure 3.12(a), the errors at boundary points and in the domain are split out and $||e||_{L_2}$ in the domain for refinements are presented. In the MEPCM, the convergence rates for the whole problem and for the domain alone match because of the accurate imposition of the boundary conditions. Using the RKCM, $||e||_{L_2}$ for the problem domain alone is smaller than $||e||_{L_2}$ for the whole problem and keeps the same convergence rate as the whole problem. This is a clear demonstration of the major improvement the max-ent approach gives to the MEPCM in terms of reducing

the error associated with imposing Dirichlet boundary conditions. In Figure 3.12(b), the L_2 norms of strain energy using both the MEPCM and the RKCM are compared. Comparing Figure 3.12(a) with Figure 3.12(b), a similar trend is obtained for $||e||_{L_2}$ and the L_2 norm of strain energy. For the one-dimensional bar problem, using the MEPCM can achieve better convergence rate as in the weak form-based meshless method [136]. With "strong" and "weak" form-based methods, the fundamental difference lies in the approximation. In strong formulations, all the provided information is located at the discrete collocation points and connectivities between points are avoided to decrease the complexities. In weak form approximation the linear system is formulated through numerical integration. In this case, only a number of collocation and source points are distributed in the interior of the problem domain and on boundaries using the MEPCM to study the convergence performance. The information at each collocation point only represents the collocation point itself rather than the average value over its integral domain.

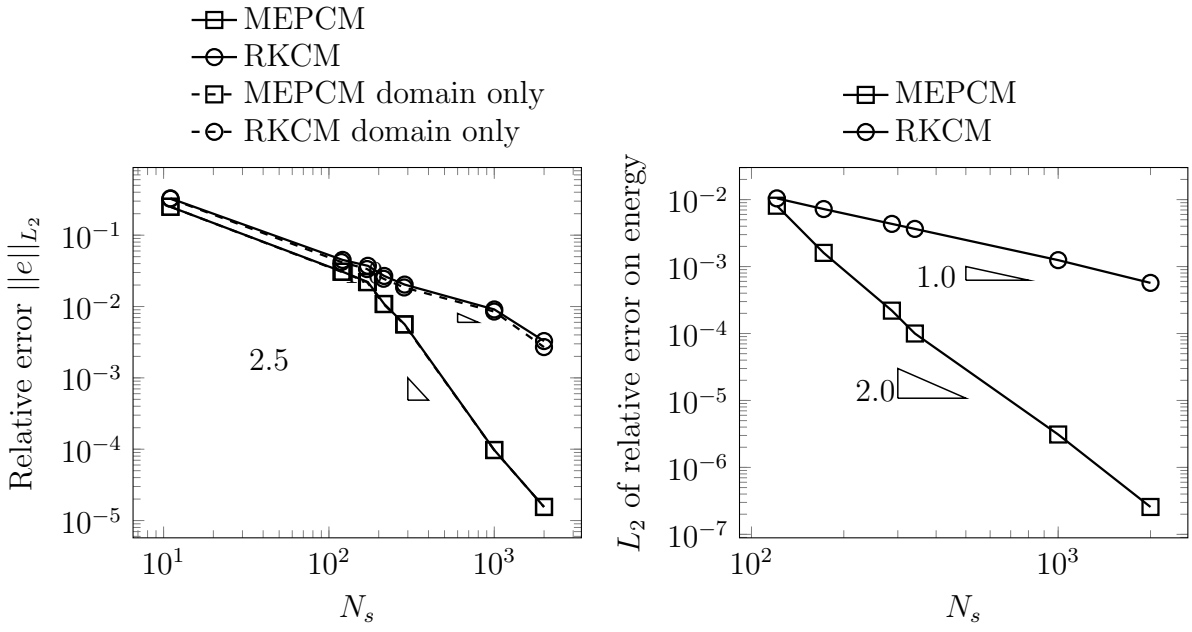

(a) Convergence rate of $||e||_{L_2}$.

(b) The L_2 norm of energy.

Figure 3.12: Convergence rate of $||e||_{L_2}$ and energy norm of the one-dimensional bar problem using the MEPCM and the RKCM .

In addition to the comparison in terms of accuracy, computational cost is important. Table 3.3 gives CPU times using both the RKCM and the MEPCM methods for selected

analyses with varying discretisations. The results show that for a given discretisation, the MEPCM leads to lower CPU times than the RKCM in all cases, and from the results discussed above concerned with convergence, it can be concluded that the MEPCM gives greater accuracy in a lower CPU time. Further support for this point can be shown by plotting error against CPU time as in Figure 3.13 where the advantage of the MEPCM is obvious. The computational cost of the two methods is principally concentrated in the construction of the basis functions and derivatives, and in the solution of the linear system. Both the MEPCM and the RKCM have similar overheads for the latter and the source of the significant difference in CPU time is due to the former. In the RKCM, the calculation of the inversion of the moment matrix in the basis function derivatives are time-consuming. However, these calculations are totally avoided with max-ent basis functions, and the only potential issue is the determination of the Lagrange multipliers $\{\bar{\lambda}\}$ in Eq. (3.53) by the Newton-Raphson method because the derivatives of max-ent basis functions are derived analytically. In this elasticity example on which the proposed MEPCM has been tested, the max-ent schemes have better accuracy for a given discretisation than those based on RK methods.

N_s	MEPCM (s)	RKCM (s)	Speed up
172	1.492×10^{-2}	2.144×10^{-1}	14.4
216	2.672×10^{-2}	3.274×10^{-1}	12.3
287	3.324×10^{-2}	5.744×10^{-1}	17.3
357	4.373×10^{-2}	8.778×10^{-1}	20.1
1000	2.532×10^{-1}	6.764×10^{0}	26.7
2000	7.506×10^{-1}	2.726×10^{1}	36.3

Table 3.3: CPU times for analyses using the MEPCM and the RKCM of the one-dimensional bar problem.

Another useful metric in comparisons of numerical algorithms is floating point operations (flops). Ideally one should be able to make clear comparisons of methods, such as between the MEPCM and the IGA-C methods in [86] (which have been reviewed in Chapter 2). In some cases it is possible to break down a complex algorithm to provide neat expressions for the order of flop counts related to the discretisation (e.g. the number of elements in the IGA-C methods), dimensionality and order of basis (e.g. Table 2 in [86]). Both the MEPCM and the RKCM form the linear system of equations at collocation points in the same way as the IGA-C method of [86] so it is expected that

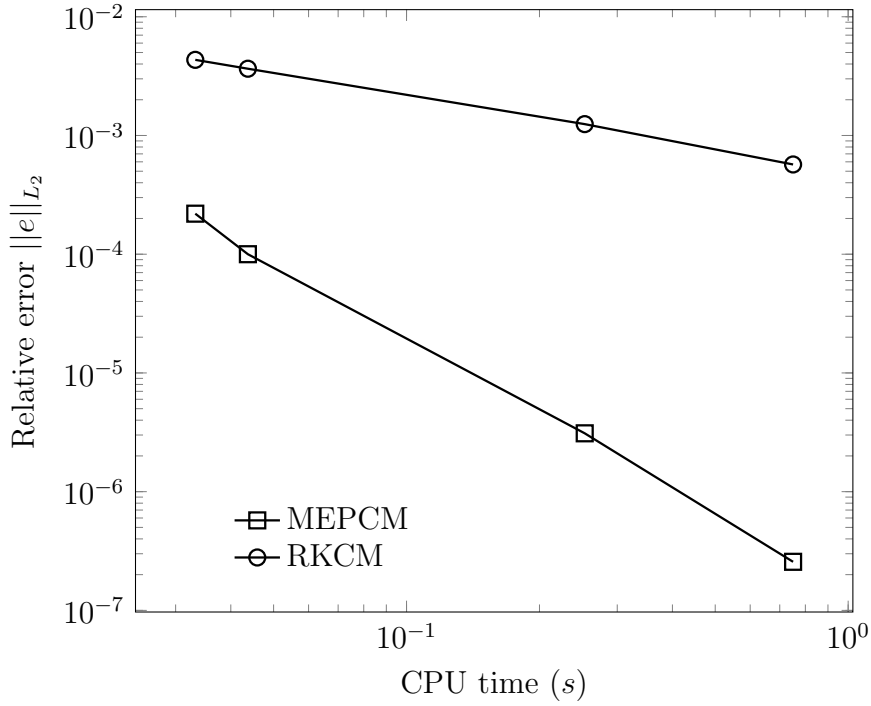

Figure 3.13: Convergence rate of $||e||_{L_2}$ against CPU time of the one-dimensional bar problem using the MEPCM and the RKCM.

flop counts for those operations to be similar here. However, attempting to go further with the MEPCM and the RKCM methods, encounters problems in that there is no clear link between the underlying basis (which is linear here) and the order of the computed basis functions developed via the max-ent procedure (for MEPCM at least) which is undefined. Instead numerical results are presented to indicate trends as regards flop counts based on numerical experiments.

The total flops required for instances of the one-dimensional problem, with different discretisations, are plotted in Figure 3.14. The figure shows that for the same number of collocation points, N_c, the flop count using the MEPCM is smaller than the RKCM. For this one-dimensional problem, the total cost (if taken proportional to flop count) for both the MEPCM and the RKCM is $O(N_c^3)$. It is hard to determine the role of the dimensionality here and, for the reasons outlined above, not possible to include the order of a basis.

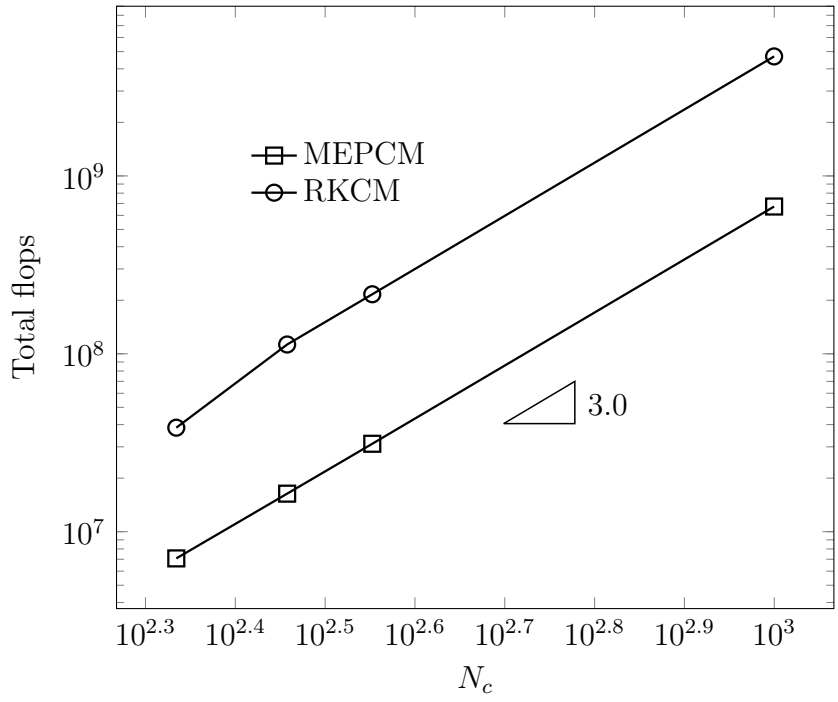

Figure 3.14: Total flops for analysis against N_c of the one-dimensional bar problem using the MEPCM and the RKCM.

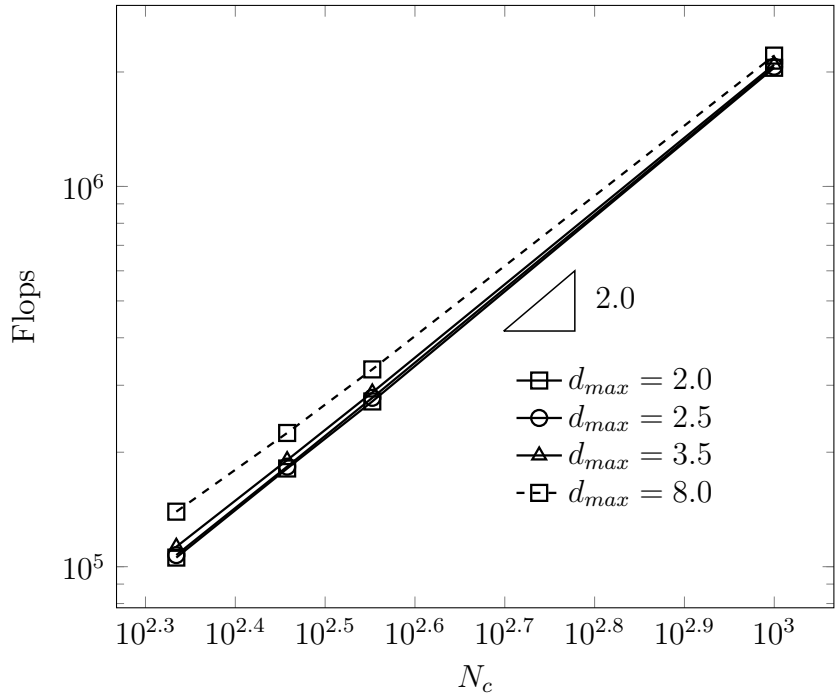

Figure 3.15: Flops of max-ent basis functions with different d_{max} of the one-dimensional bar problem.

Maintaining interest in flop counts but now focussing on comparison of the MEPCM

with the RKCM it is instructive to consider the cost of forming the basis functions in each method. In the formation of the max-ent basis functions, the flops per Newton iteration are the same for each collocation point in the same discretisation although the number of iterations is not known in advance. The cost of constructing max-ent basis functions with varying d_{max} is shown in Figure 3.15 in which the gradients of all the lines are close to 2 for different d_{max}.

The costs of constructing the max-ent and RK basis functions and derivatives are shown in Figure 3.16 where it is clear that the flop counts for max-ent basis functions are less than RK basis functions. It is also observed that the cost of calculating RKPM basis functions derivatives is more expensive than max-ent basis functions derivatives because some variables calculated in max-ent basis functions can be reused in the calculation of max-ent derivatives. The cost of calculating the max-ent and RK basis functions in terms of the number of collocation points is seen to be $O(N_c^2)$.

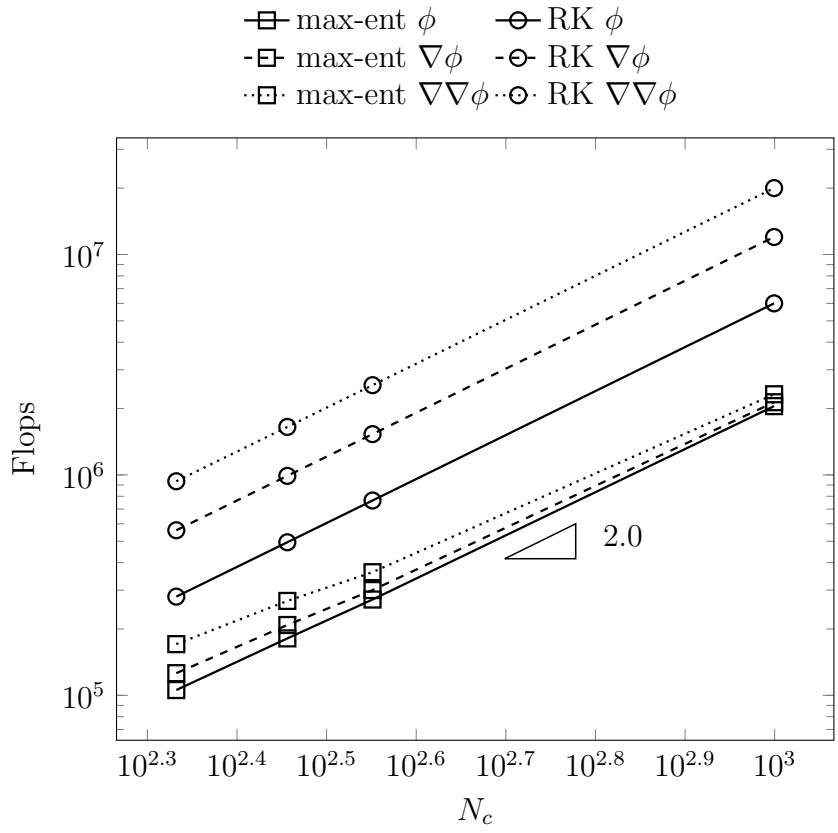

Figure 3.16: Flops of max-ent and RK basis functions and derivatives in one dimension.

3.5.2 Two-dimensional Poisson problem

The second example is a two-dimensional Poisson problem with Dirichlet boundary conditions on a unit square domain. The governing equation is

$$\nabla^2 u(x,y) = 4, \quad \Omega \in (0,1) \times (0,1) \tag{3.59}$$

with the following Dirichlet boundary conditions

$$u_{x=0} = y^2 \tag{3.60a}$$

$$u_{x=1} = 1 + y^2 \tag{3.60b}$$

$$u_{y=0} = x^2 \tag{3.60c}$$

$$u_{y=1} = x^2 + 1, \tag{3.60d}$$

where the analytical solution is

$$u(x,y) = x^2 + y^2, \quad \Omega \in (0,1) \times (0,1). \tag{3.61}$$

All collocation and source points were distributed in x and y directions and the scaling parameter of the support domain d_{max} for each collocation point was 2.0. Note that for a two-dimensional Poisson problem, there is a single degree of freedom in the field variable at each collocation point and also that the PDE contains no mixed derivatives, which simplifies the formation of the differential operators as given in Table 3.1, as compared to two-dimensional elastic problems.

For this example, four different refinements are used (N_s=121, N_c=144; N_s=441, N_c=484; N_s=1681, N_c=1764; N_s=2601, N_c=2704) and N_s is the number of degrees freedom. Figure 3.17 shows convergence rates of the L_2 norm of relative error on the field variable using the MEPCM and the RKCM for this problem, in which the MEPCM clearly performs better convergence rate with lower errors than the RKCM. The differential operators for two-dimensional Poisson problems are simpler than those for two-dimensional elastic problems as given in Table 3.1 and independent in x and y components without the coupling effect, which reduces the relative error.

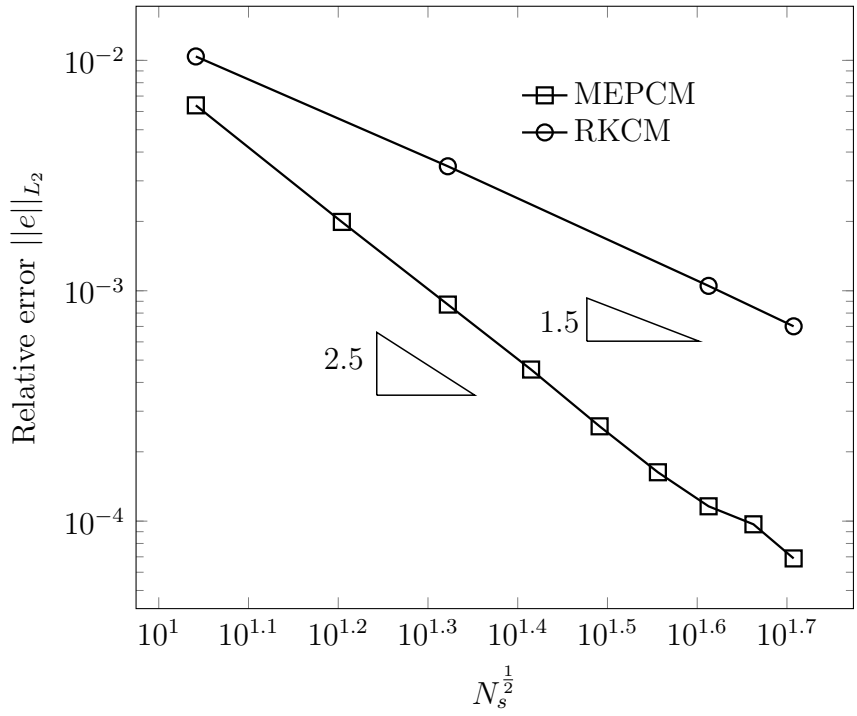

Figure 3.17: Convergence rate of $||e||_{L_2}$ of the two-dimensional Poisson problem using the MEPCM and the RKCM.

Table 3.4 gives the computational times of the MEPCM and the RKCM analyses for this problem, and again, the advantage of the former is clear. The corresponding ratios for CPU time vary from 2.7 ($N_s = 121$) to 10.8 ($N_s = 2601$). Compared to the one-dimensional bar problem, these simulations take longer since the calculation of basis functions and derivatives in two directions are required and the linear solver is also consuming more CPU time than the one-dimensional problem, despite the change in PDEs. The speed up is lower than in the first example which may also be explained by the discretisation. In a two-dimensional domain, the distribution of points is known to have an effect on the iteration times in the calculation of the Lagrange multipliers $\{\bar{\lambda}\}$ and hence the overall computational time. Although this speed up is not as significant as seen in the one-dimensional bar problem, it is nevertheless the case that the MEPCM is more efficient than the RKCM for this problem and that the speed up increases with refinement.

In this two-dimensional domain, considering again just the flops for the formation of basis functions, Figure 3.18 is equivalent to Figure 3.16 for one-dimensional domain and indicates the same relation for two-dimensional problems, implying that the basis

N_s	MEPCM (s)	RKCM (s)	Speed up
121	5.467×10^{-2}	1.476×10^{-1}	2.7
441	2.290×10^{-1}	7.755×10^{-1}	3.4
1681	2.100×10^{0}	1.329×10^{1}	6.3
2601	6.295×10^{0}	6.794×10^{1}	10.8

Table 3.4: CPU times for analyses using the MEPCM and the RKCM of the two-dimensional Poisson problem.

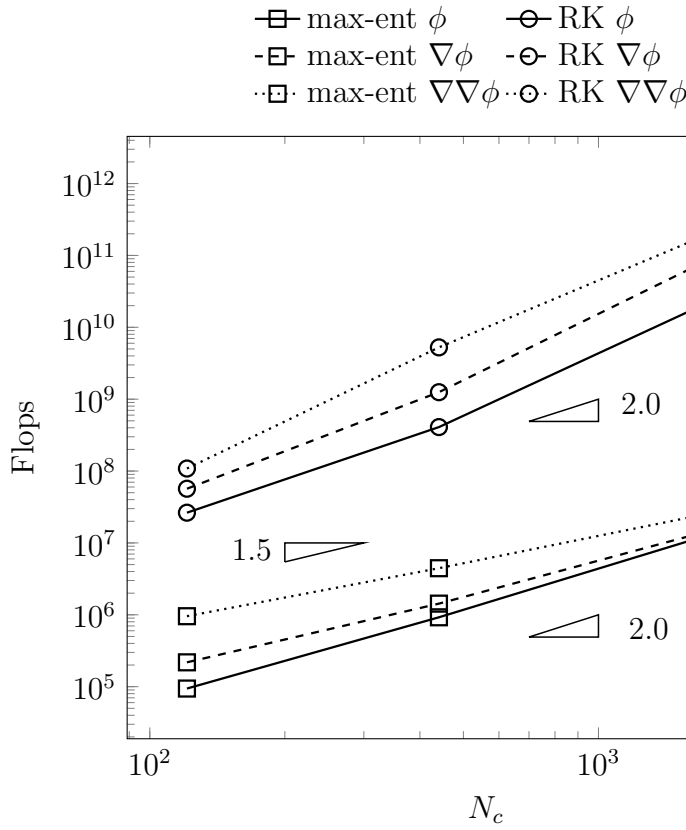

Figure 3.18: Flops of max-ent and RK basis functions and derivatives in two dimensions.

function formation is not controlled by dimensionality. It is noted that the flops for mixed second derivatives of basis functions are included in the plot although they are not used for solving Poisson problems. A further plot of flops against the reciprocal of distance h between two nearest collocation points for a regular distribution (in Figure 3.19) gives gradients close to 4.0. As for the one-dimensional problem, the flop counts in terms of N_c is equivalent to the flops in terms of $\frac{1}{h}$ considering the proportional relation between N_c and $\frac{1}{h}$ in one dimension. Therefore, the cost for constructing the max-ent and the RK basis functions is conjectured to be $O((\frac{1}{h})^{2d})$ where d is the dimension of the physical problem.

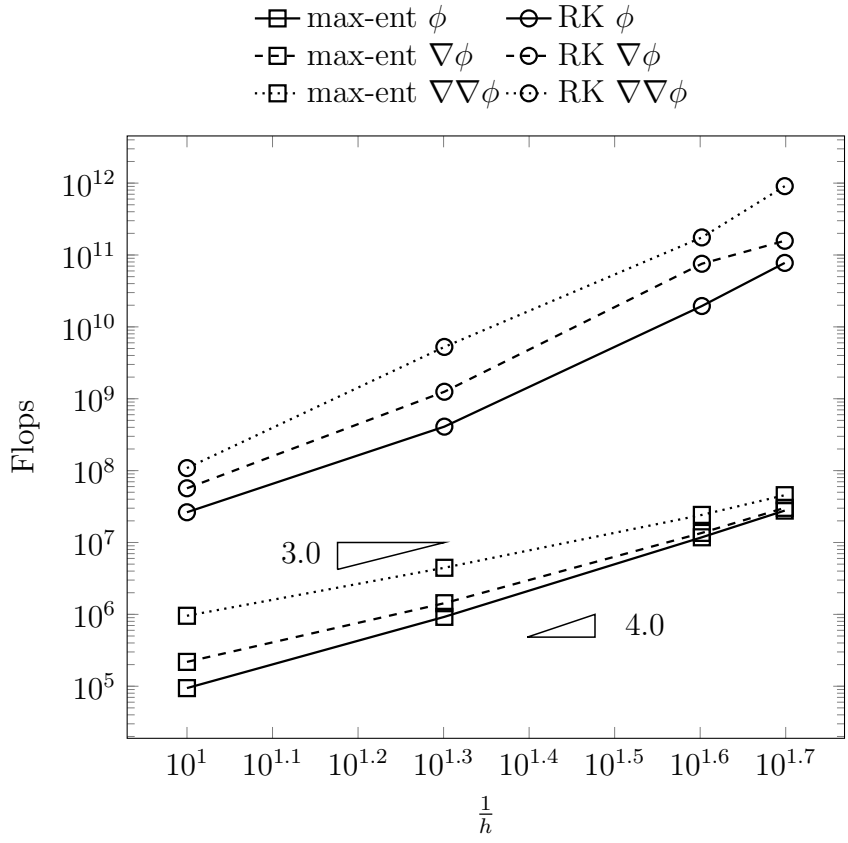

Figure 3.19: Flops of max-ent and RK basis functions and derivatives against $1/h$ in two dimensions.

3.5.3 A two-dimensional elasticity problem: a confined square domain

The third example is a linear elastic unit square domain, subjected to roller boundary conditions on three sides and a prescribed displacement $\bar{u}_y$ on the fourth as shown in Figure 3.20. The purpose of this example is to study the performance of the two-dimensional elasticity problem with convex and symmetric geometry and boundary conditions using the MEPCM. The analytical solution for the displacement field for this problem under plane stress condition is simply given as

$$u_x = 0 \quad \text{and} \quad u_y = \frac{1-\nu^2}{E} y \ . \tag{3.62}$$

The differential operators for two-dimensional linear elasticity are used where the field variables are displacements for elasticity. The material properties used were Young's modulus $E = 1000$ and Poisson's ratio $\nu = 0.25$.

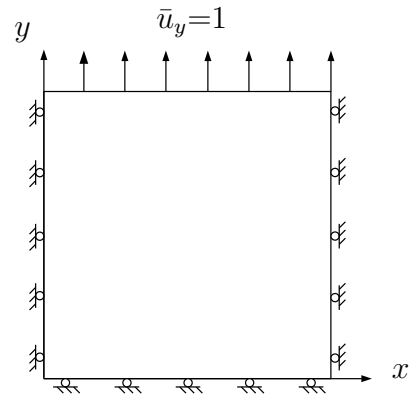

Figure 3.20: An elasticity problem: a confined square domain subjected to a displacement $\bar{u}_y = 1$ in y direction.

All collocation and source points were distributed uniformly in this regular domain and the corresponding errors for different refinements of points are used to plot the convergence rates in Figure 3.21. For two-dimensional elasticity problems, $(2 \times N_s)^{1/2}$ denotes the density of points given that the approximation of displacement is a 2×1 vector. The results again demonstrate that, for a given level of discretisation, the error in the MEPCM is less than that in the RKCM. In addition, the convergence rate in the MEPCM is better than using the RKCM. In this example, the differential operators for

elasticity problems are more complicated than for the two-dimensional Poisson problem. Another feature in this two-dimensional elasticity problem is that the mixed second derivatives of the basis functions $\frac{\partial^2 \phi}{\partial x \partial y}$ are required in the differential operators thus x and y directions are coupled. In this example, the geometry and boundary conditions are symmetric and the body force for this elasticity problem is zero which simplifies the numerical implementation.

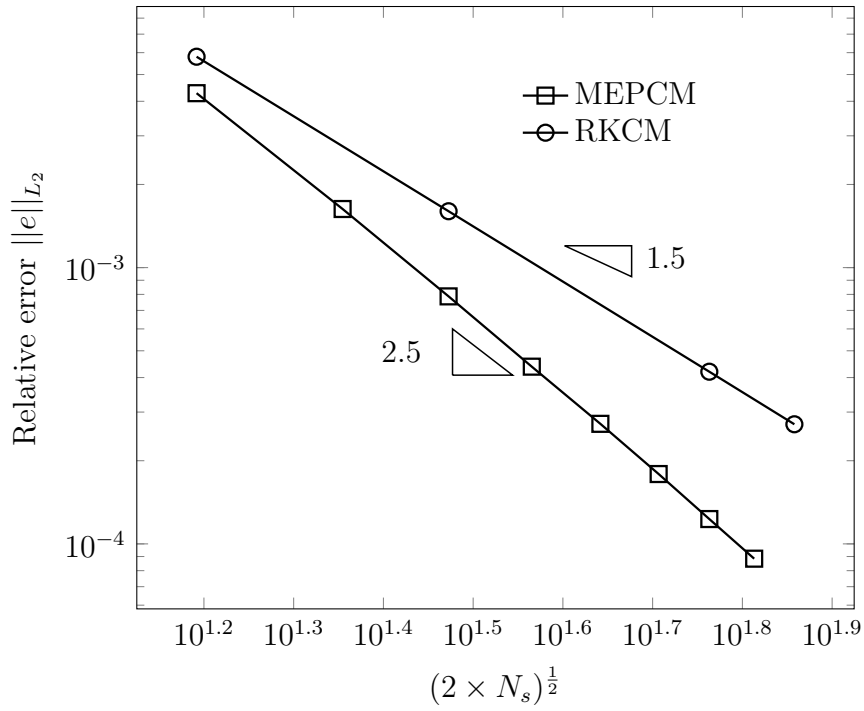

Figure 3.21: Convergence rate of $||e||_{L_2}$ in the two-dimensional elasticity problem: a confined square domain using the MEPCM and the RKCM.

The CPU times for solutions using both the MEPCM and the RKCM are given in Table 3.5 and again there appear to be clear benefits using the MEPCM. The speed up increases with an increasing number of source and collocation points. At the same time, however, the overall computational time in this two-dimensional elasticity problem is longer than that for the previous two-dimensional Poisson problem, for similar discretisations. The explanation for this is the need for calculation of mixed derivatives of max-ent basis functions, assembly of the larger final coefficient matrix and the least squares solver for the over-determined system in this example, all of which take more time than the two-dimensional Poisson problem.

N_s	MEPCM (s)	RKCM (s)	Speed up
121	8.200×10^{-2}	2.010×10^{-1}	2.5
441	3.392×10^{-1}	1.176×10^{0}	3.5
1681	3.150×10^{0}	2.553×10^{1}	8.1
2601	9.099×10^{0}	8.560×10^{1}	9.4

Table 3.5: CPU times for analyses using the MEPCM and the RKCM of the two-dimensional elasticity problem: a confined square domain.

3.5.4 An infinite plate with a circular hole

The final example is another classic elasticity problem: an infinite plate with a circular hole under a far field traction $p = 10$ in x direction. This numerical example is included to study the performance of max-ent basis functions in a non-convex problem domain. Due to symmetry, only the upper right quarter of the infinite plate, with $b = 5$, was taken for analysis as shown in Figure 3.22. Roller boundary conditions were imposed at

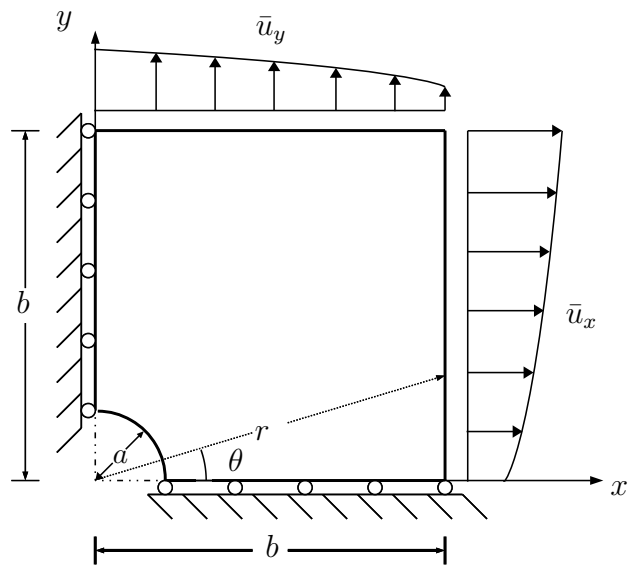

Figure 3.22: A portion of the infinite plate with a circular hole.

the collocation points on the bottom and left edges, the prescribed displacement $\bar{u}_x$ and $\bar{u}_y$ were applied on the right and top edges and the rest collocation points are required to satisfy the equilibrium equations. This problem has been widely used for validation

in the past and has an analytical solution [138] which can be expressed as

$$u_x = \frac{10a}{8G}\left\{\frac{r}{a}(\kappa+1)\cos\theta + \frac{2a}{r}[(1+\kappa)\cos\theta + \cos(3\theta)] - \frac{2a^3}{r^3}\cos(3\theta)\right\} \tag{3.63a}$$

$$u_y = \frac{10a}{8G}\left\{\frac{r}{a}(\kappa-3)\sin\theta + \frac{2a}{r}[(1-\kappa)\sin\theta + \sin(3\theta)] - \frac{2a^3}{r^3}\sin(3\theta)\right\} \tag{3.63b}$$

where G is the shear modulus

$$G = \frac{E}{2(1+\nu)} \tag{3.64}$$

and κ is the Kolosov constant

$$\kappa = \begin{cases} 3-4\nu & \text{plane strain} \\ \frac{3-\nu}{1+\nu} & \text{plane stress.} \end{cases} \tag{3.65}$$

r and θ are the polar coordinates as defined in Figure 3.22. Here, the problem was solved with the plane stress condition and E=100000, ν=0.3 in compatible units.

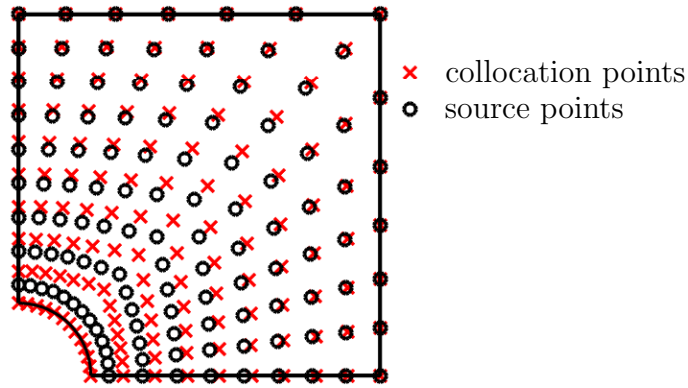

Figure 3.23: The discretisation of points of the infinite plate with a circular hole.

In this example the domain and boundaries are not as regular as in the previous examples so the influence of the discretisation is more noticeable. The (non-convex) problem domain and corresponding boundaries were discretised by 117 source points and 130 collocation points, as shown in Figure 3.23. In order to avoid the coincident

distributions of collocation and source points, source points were distributed at different positions to the collocation points except on the top and right edges, since the second derivatives are not required for imposing Dirichlet boundary conditions on these two edges. The singularity problem (highlighted in §3.5.2) has to be avoided by adjusting the numbers and positions of points. Since both collocation and source points in this example are distributed non-uniformly, the distances between collocation points and their nearest source points in support are different. The scaling parameter d_{max} is therefore adjusted to guarantee sufficient source points in the support domain of each collocation point. This also has an effect on the iteration number for the Lagrange multipliers required in max-ent basis functions, and for these combined reasons in these analyses, the scaling parameter for the support domain was set to 3.5 which is higher than used in the previous numerical examples.

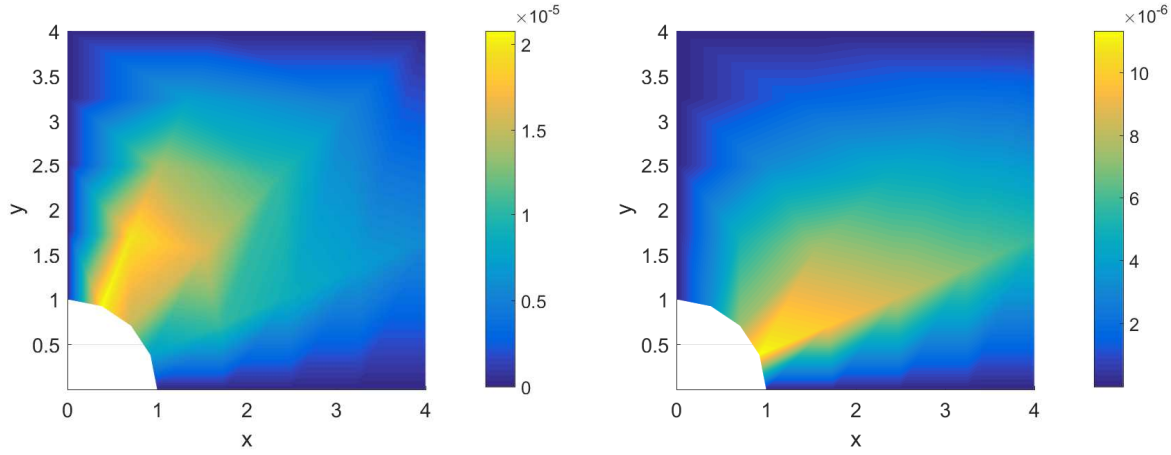

(a) Displacement error of u_x.

(b) Displacement error of u_y.

Figure 3.24: Absolute errors of displacement in x and y directions of the infinite plate with a circular hole problem using the MEPCM.

The distribution of absolute errors between the approximation of displacements and the theoretical solutions in x component and y component is shown in Figure 3.24. The maximum x-displacement for this problem at (5,0) provided by Eq. (3.63)(a) is 5.5248×10^{-4}. As expected, errors on the Dirichlet boundaries are very low, and the most significant source of error is linked to strain gradients in the interior of the domain, and around the circular hole because of the stress concentration. Comparing the errors in x and y directions, the maximum value of error for u_x is higher than in y component

linked to the fact that the far field stress is applied to x direction. The example also shows that the MEPCM works for this non-convex geometry with Dirichlet boundary conditions however, on the circular edge the weak Kronecker-delta property is lost.

To study the convergence properties, the problem is solved with different discretisations using both the MEPCM and the RKCM. It is clear from the results shown in Figure 3.25 that the accuracy for a given discretisation and rate of convergence of the MEPCM is higher than the equivalent RKCM. With an increasing number of degrees of freedom, the convergence using RKCM degrades while the proposed method shows good performance in this irregular geometry as the errors on the Dirichlet boundaries using the RKCM also increase which affects the convergence performance. Compared with a regular domain problem (e.g. Example 3 above), different numbers of source points inside the support domain of collocation points in this example generate different number of basis functions for each collocation points, which has an effect on the value of $||e||_{L_2}$ and the bandwidth of the final coefficient matrix.

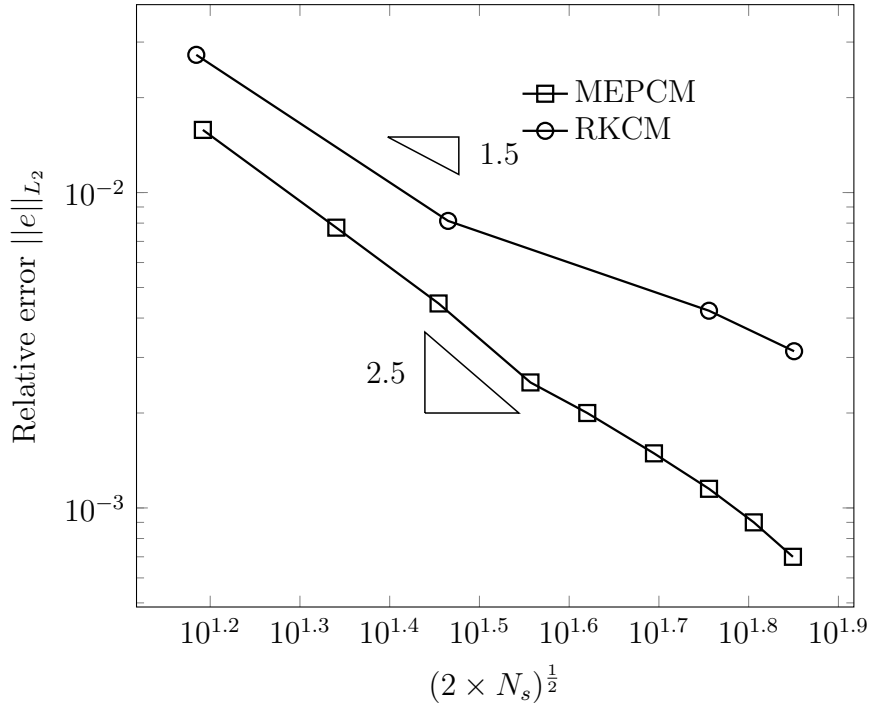

Figure 3.25: Convergence rate of $||e||_{L_2}$ of an infinite plate with a circular hole problem using the MEPCM and the RKCM.

This elastic plate with a circular hole problem has also been studied in [86] and the $||e||_{L_2}$ using the IGA-C with varying order of basis functions has been demonstrated. It

was observed in [86] that the convergence rate using the IGA-C with the second and third order basis function was close to 2. However Figure 3.25 shows a higher rate of convergence using the MEPCM plotted in terms of the number of degrees of freedom, i.e. delivering a rate of convergence which is higher than using the third order IGA-C. As indicated above the major differences in the basis functions and the discretisations probably invalidates a direct and reliable comparison without further study.

Table 3.6 compares the computational times for analyses using the MEPCM and the RKCM for this problem. As can be seen, when the number of degrees of freedom is small, the speed up using these two methods is 1.9 , and the speed up increases as the discretisations get finer. As stated above, the varying number of source points in support at collocation points results from the non-uniform distribution of source points and collocation points in the geometry, and increases the computational burden in both the MEPCM and the RKCM as compared to the previous two-dimensional examples. However, the speed up is not seen to increase as fast as in the other two-dimensional examples as the discretisations get finer. This appears to be due to the non-uniform distribution of points which has more effect on the MEPCM than the RKCM. In this example, the percentage of computational time used in calculating the max-ent basis functions and their derivatives is larger than the previous two-dimensional problems. Using the MEPCM improves the computational efficiency but the effect caused by non-uniform distribution of points cannot be ignored and may be a significant issue for real world geometries, although that investigation is beyond the scope of this chapter. In all cases studied to date however, an increased speed up can be seen with refinement when comparing the MEPCM and the RKCM.

N_s	MEPCM (s)	RKCM (s)	Speed up
117	2.060×10^{-1}	3.845×10^{-1}	1.9
426	9.996×10^{-1}	3.530×10^{0}	3.5
1681	8.009×10^{0}	3.085×10^{1}	3.9
2601	2.072×10^{1}	1.166×10^{2}	5.6

Table 3.6: The CPU times for analyses using the MEPCM and the RKCM of the infinite plate with a circular hole problem.

3.6 Concluding remarks

This chapter has presented for the first time a point collocation method based on the local maximum entropy basis functions. These functions have two properties that make them ideal for the use with point collocation methods: (i) non-negativity and (ii) a weak Kronecker delta for convex domains. Both of these properties improve the convergence rate of the method, in particular the latter removes errors associated with the imposition of Dirichlet boundary conditions which have been shown to limit the convergence rate of other point collocation methods. The performance of the proposed method was explored in the chapter using four numerical examples which included one-dimensional and two-dimensional problems with linear elasticity and Poisson PDEs on both convex and non-convex domains. In all cases the proposed max-ent point collocation method (MEPCM) showed lower errors with higher rates of convergence compared to an existing RKCM. The MEPCM also had an increasingly lower computational cost, with speed-ups of over 20 times for one-dimensional problems and around 5.6 times for two-dimensional elasticity solutions. A numerical study of cost in terms of flop counts further confirms that the MEPCM is more efficient than the RKCM and the proposed approach has been compared to the IGA-C of [86] for one problem solved in both this chapter and that paper. The key improvement of the MEPCM over the RKCM is that for the same number of degrees of freedom, the computational time in calculating the second derivatives of the basis functions is reduced. The performance of max-ent basis functions on non-convex domains with non-uniform point distributions was also investigated and, although lower speed gains were realised, the method still outperformed the RKCM on all simulations in terms of errors and CPU time.

Chapter 4

Error estimation and adaptive strategies

4.1 Introduction

The numerical solution for a continuum problem is obtained by conversion to a discrete formulation in which discretisation errors due to imbalance of the governing equations and boundary conditions at individual points are introduced [26]. The discretisation errors can be split into sources arising from improper distribution of points, an inadequate number of degrees of freedom and inadequacy of the solution space [28]. Uniform h-refinement in which the distances between any two nearest points are reduced uniformly is the easiest way to reduce the error but it is not efficient because it might lead to unnecessary additional computational cost as new points are introduced to regions with very low errors.

An adaptive process is defined as one that has error assessment and then a refinement strategy. There are three types of adaptive strategies such as r-, h- and p- adaptivities, depending on the refinement strategy chosen (similar error measure might be used). The main idea of h-adaptivity is to increase the number of degrees of freedom by refining the mesh in mesh-based methods or simply inserting additional nodes in meshless methods locally to reduce the discretisation errors in the solution [139, 140]. r-adaptivity means maintaining the same number of degrees of freedom and the order of the field variable

approximation, but altering their locations [141–143]. p-adaptivity works by changing the order of the basis functions [144–146].

As the point collocation method with local maximum entropy basis functions proposed in Chapter 3 is implemented only based on individual points, the problems caused by the use of a mesh in adaptive strategies such as the requirement of remeshing can be avoided, which reduces the computational cost. Therefore, r-, h- and combined rh-adaptive strategies with the local maximum entropy point collocation method (MEPCM) for linear elasticity problems are developed in this chapter. Since the arbitrary higher order of max-ent basis functions are unavailable, p-adaptivity is not considered. In this chapter, previous work on h-, r- and combined rh-adaptivity strategies is reviewed first. Then these three adaptive approaches with the MEPCM are introduced which include basic formulations for different error estimators and refinement strategies. After that, numerical implementation issues are discussed. Finally, some numerical examples including one- and two-dimensional elasticity are included to demonstrate the performance of the proposed approach.

4.2 Literature review

In this section, a literature review covering h-, r- and rh-adaptivity in the finite element method (FEM) and meshless methods is presented.

4.2.1 h-adaptivity

Error estimation

Error estimators are used to estimate the difference between the exact solution and the approximation. As the exact solution is unknown in most practical cases, the "recovered" stress has been presented, which can be approximated by a recovery technique, to replace the exact solution in error estimators. The superconvergent patch recovery technique proposed by Zienkiewicz and Zhu in [147] is one of the most-often used recovery method in the FEM. In this procedure stresses and strains are initially calculated at the superconvergent points, which are then used to calculate stresses and strain at the

nodes [148]. Error estimators can be computed in an energy norm depending on the difference between the recovered and approximated stress fields at a point or in an individual element [149]. Since the superconvergent patch recovery technique is simple to implement as explained in [150–152], the proposed error estimate based on the recovered stress in mesh-based methods have been widely employed for solving hyperbolic problems [153], two-dimensional planar elasticity problems [154] and other problems [155, 156]. After that, the idea of the "recovered" stress has been extended to a "projected" stress, which is computed in different way [157] and most often used in weak form-based meshless methods such as in the RKPM [158–160]. The projected stress values are evaluated with the same discretisation as the approximation but a reduced influence domain [161, 162]. More recently, error estimation in strong form-based meshless methods has been developed although available literature is very limited, where the errors have been estimated by the residuals of the governing equations at a set of individual points directly [163,164]. Apparently, this error estimate is simple and straightforward to implement.

Refinement strategy

In the following refinement step, new points are inserted in the problem domain and on the boundaries to reduce the distance between adjacent nodes in areas with relatively high local errors. However, in weak form-based meshless methods, regeneration of background mesh is required for numerical integration based on the newly generated points after each refinement step, which decreases the computaitonal efficiency such as using the non-conforming meshing [27]. The local refinement makes the treatment of non-conforming discretisation complicated especially for boundaries. Then refinement works with strong form-based PCMs have been developed in [163–166], which possess some advantages. The new collocation points can be inserted to local regions with relatively high errors directly. As PCMs are truly meshless methods, it is not necessary to consider numerical integration and remeshing, overcoming the difficulties mentioned above. Convergence studies on h-adaptivity in meshless collocation methods have also been provided in [166]. In contrast to weak-form based meshless methods, there is very little literature on h-adaptive methods with PCMs to date.

4.2.2 r-adaptivity

In r-adaptivity, the moving distances and directions for points or nodes need to be determined by error estimators. The residual of the material equilibrium in terms of the material force derived in [167, 168] has been used to measure the error because the material force is concerned with the energetic changes of a continuum with respect to points' locations [169–172]. The finite element method (FEM) with r-adaptivity has received much attention such as in [173–178], where the material forces were used as driving forces to relocate the mesh. Although r-adaptivity is expected to offer a better solution in the FEM, the crucial issue arising in mesh-based r-adaptivity is element distortion. The estimated errors increase in r-adaptivity process since that the movement of nodes of an element cause mesh distortion, which affects the accuracy of the solution [179–182]. Mesh optimisation has then been proposed in [183], where the movement of points is constrained to be sufficiently small by a step length parameter [184]. However this additional mesh optimisation leads to extra computational cost.

It is possible to reduce errors using r-adaptivity, but a specific accuracy may not be achievable with a fixed number of degrees of freedom. To tackle this, h-adaptivity can be used after a sequence of r-adaptivity to reduce the discretisation errors. In [185], r- and h-adaptive strategies were used in two subdomains separately without refinement on the interfaces to exploit the advantageous properties of both stategies. A comparison in terms of accuracy and convergence speed using pure and combined adaptive strategies was conducted in [186, 187] where a combined rh-adaptive approach was shown to be more efficient than pure r- or h-adaptivity alone. Combined rh-adaptivity was studied in [188, 189] for bimaterial interface problems, where discretisation errors can be reduced in succesive adaptive steps and the best sequence for combining the effectiveness of r- and h-adaption has been studied. The efficiency of using combined rh-adaptivity was compared with pure h-adaptivity in [188] and it was found that a smaller number of degrees of freedom was required in the combined strategy than in pure h-adaptivity. In relation to the present study, to author's knowledge, there is currently no literature on combined rh-adaptivity for PCMs. Therefore, the investigation of the treatment of combined rh-adaptive strategies and the comparison in terms accuracy and computational cost using

pure h-, r- and combined rh-adaptivity is the focus of this chapter.

4.3 r-adaptivity strategy in the MEPCM

As in all adaptive procedures, an error measure is required in r-adaptivity and for the case of linear elasticity, non-zero residuals of material force equilibrium (divergence of energy momentum tensor with zero body force) are used as such in [190, 191]. The idea of r-adaptivity is then applied to the MEPCM. Current approximations of solutions obtained from a given discretisation are therefore employed to estimate existing errors, which can be used to determine the moving direction and distance for collocation points in iterative r-adaptive procedure. For other PDEs, such as in Poisson problems, similar quantities can be found to act as error estimators. In this section, error estimation and point relocation in r-adaptivity with the MEPCM for linear elasticity are explained.

In this chapter, linear elastic material models with small deformations are studied. As derived in [190], the material equilibrium takes the form

$$[L]^T\{\Sigma\} = \{0\} \quad \text{in } \Omega \tag{4.1}$$

where $[L]$ is a matrix of differential operators as given in Eq. (3.3), $\{\Sigma\}$ is the Eshelby stress (or momentum tensor), $\{0\} = \{0, 0\}^T$ in two dimensions and Ω is the problem domain. The residuals of the material equilibrium are adopted as an error estimator in r-adaptivity as

$$[L]^T\{\Sigma\} = \left\{\frac{\partial W}{\partial x}\right\}_{\text{explicit}} \tag{4.2}$$

where $\left\{\frac{\partial W}{\partial x}\right\}_{\text{explicit}}$ is the explicit derivatives of the strain energy with respect to the nodal position $\{x\}$.

The MEPCM approximations $\{u^h\}$ satisfy physical equilibrium, which is expressed in terms of the Cauchy stress at each collocation point in the interior of the problem domain, but they may not fully satisfy the material equilibrium. The non-optimal locations of collocation points act in a similar way to a defect of a material as explained in Eshelby's original work and the subsequent literature on configurational mechanics for fracture. The Cauchy stress describes the deformed state with respect to displacement while the

Eshelby stress is related to the global energy change of the deformed solid with respect to nodal positions. The imbalance of the material equilibrium using the MEPCM can then be seen as a result of the discretisation. The discrete points can be argued to be defects since the translation of strain energy is broken with respect to translations between each pair of points [188]. These non-zero residuals in the divergence of the Eshelby tensor are proposed as the measure of error and r-adaptivity is accomplished by minimising these residuals in Eq. (4.1) with respect to collocation point positions.

In PCMs, the stored strain energy for linear elasticity can be expressed as

$$\begin{aligned} W &\cong \sum_{c=1}^{N_c} \frac{1}{2} \{\sigma\}_c^T \{\varepsilon\}_c V_c \\ &\cong \sum_{c=1}^{N_c} \frac{1}{2} \Big\{ [L]\{u\} \Big\}_c^T [D] \Big\{ [L]\{u\} \Big\}_c V_c \end{aligned} \tag{4.3}$$

where $\{\sigma\}$ is the Cauchy stress, $\{\varepsilon\}$ is the strain vector, V_c denotes a volume (area in two dimensions and length in one dimension) associated with a collocation point c, $[L]$ is the differential operators given in Eq. (3.3) and $[D]$ is the elastic stiffness matrix given in Eqs. (3.8) and (3.9). As the material equilibrium residual in Eq. (4.1) is non-zero in the discrete PCM formulation, the residuals can be collected as the explicit derivative of strain energy with respect to collocation point positions

$$\{R(x)\} = \left\{ \frac{\partial W}{\partial x} \right\}_c. \tag{4.4}$$

The physical equilibrium equation for elasticity problems is linearly dependent on the field variables $\{d\}$, however the material equilibrium is non-linear as non-linear terms of the field variables $\{d\}$ are included in Eq. (4.4). Therefore, the Newton-Raphson method is adopted to solve the non-linear system of equations. The positions of collocation points in the iterative step can be found by

$$\{x_{n+1}\} = \{x_n\} - [R'(x_n)]^{-1} \{R(x_n)\}, \tag{4.5}$$

where n is the Newton-Raphson iteration number, $\{x_n\}$ and $\{x_{n+1}\}$ are the estimate of positions in the previous step and the new positions in the current step. $[R'(x_n)]$

is the derivative of the residual vector $\{R(x_n)\}$ with respect to the coordinates of the collocation points. The second term on the right-hand side of Eq. (4.5) indicates the moving direction and distance for collocation points. Eq. (4.5) can be solved pointwise and the explicit form of $[R'(x)]$ is

$$[R'(x)]_c = \begin{bmatrix} \frac{\partial^2 W}{\partial x_c^2} & \frac{\partial^2 W}{\partial x_c \partial y_c} \\ \frac{\partial^2 W}{\partial x_c \partial y_c} & \frac{\partial^2 W}{\partial y_c^2} \end{bmatrix} \tag{4.6}$$

for two-dimensional problems where the second derivatives of strain energy W with respect to the current position of each collocation point are required. Since collocation points are independent of each other, the mixed second derivatives of strain energy with respect to two different collocation points are zero. Once the residual in the Newton-Raphson method is checked to satisfy the convergence criteria, the updated positions of collocation points are obtained.

In the Newton-Raphson method, the choice of convergence criteria is important, which has an effect on the accuracy and computational efficiency in the points relocation procedure. As the values of residual norms vary with problems, it is difficult to define a specific tolerance in general. Then the relative residual η_r is defined as

$$\eta_r = \frac{||\Delta R(x_n)||}{||R(x_n) + \Delta R(x_n)||} \tag{4.7}$$

in which $||R(x_n)||$ is the L_2 norm of the total material force residual of all collocation points at the nth iteration step expressed as

$$||R(x)|| = \sqrt{\sum_{c=1}^{N_c} \left(\frac{\partial W}{\partial x}\right)_c^2}, \tag{4.8}$$

and $||\Delta R(x_n)||$ is the norm of the total material force residual difference between $(n+1)$th and nth iteration steps. A value, η, is set as a measure of the tolerance and r-adaptivity continues until the relative residual η_r satisfies $\eta_r < \eta$. Typical value for η is usually set to 10^{-5}. In mesh-based methods, the relative residual norm η_r decreases initially, however η_r tends to go up in latter iterations due to progressive mesh distortion [192]. In PCMs, the variations of relative residual norm are not influenced by mesh distortion.

This convergence criterion is validated in the r-adaptive analyses presented in numerical examples section.

In the implementation of r-adaptivity with the MEPCM, the field variables $\{d\}$ are used to measure the material force residuals $\{R\}$ and form the tangent matrix $[R']$ in the current Newton-Raphson iteration step. The positions for collocation points in the current iterative step can be determined by Eq. (4.5) directly. Additional constraints are employed so that collocation points on the boundaries can only be moved on those boundaries. The vector $\{d\}$ is recalculated using the collocation points obtained in each iterative step. It is noted that in the r-adaptive MEPCM, the material force residuals are minimised with respect to collocation point coordinates since total potential energy is collected based at collocation points. Positions of source points are not changed so the max-ent basis functions constructed based at the initially distributed source points in the overall r-adaptivity analyses.

4.4 h-adaptivity strategy in the MEPCM

In addition to using r-adaptivity to improve accuracy, discretisation errors can be reduced by inserting extra collocation and source points at appropriate locations, i.e. h-adaptivity. In the proposed h-adaptivity strategy with the MEPCM, errors are measured by the residuals of the physical equilibrium at some generated calculation points in local areas and these proposed error estimators indicate the error distributions in the overall domain, while their summation estimate the global accuracy of the solution.

In order to provide an efficient way where errors can be estimated over local areas, a Delaunay triangulation associated with collocation points is generated (see Figure 4.1). The so-called calculation points in the proposed scheme are located at the Gauss quadrature points within these triangles. Arbitrary number of calculation points can be generated in each triangulation as these points are used for error estimation rather than numerical integration. In order to keep the balance of accuracy and computational cost, three calculation points are selected for each triangulation. The local error estimator is provided by calculating the residuals of the strong form-based governing equations at

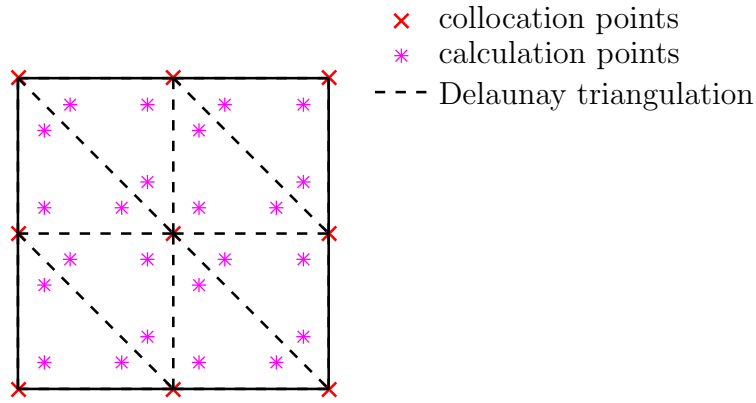

Figure 4.1: The generation of the Delaunay triangulation and calculation points in h-adaptivity.

the generated calculation points as

$$e_t = \frac{1}{3} A_t \sum_{g=1}^{3} ||\mathscr{L}\{u^h(x_g)\} - \{f^b(x_g)\}||, \tag{4.9}$$

where $\frac{1}{3}$ is the product of weight and Jacobian of Gauss quadrature, g is the number of calculation point, A_t is the area of the tth Delaunay triangle, $\{x_g\}$ is the coordinates of the gth calculation point, $\{u^h\}$ is the approximation of the solution and $||\mathscr{L}\{u^h(x_g)\} - \{f^b(x_g)\}||$ is the L_2 norm of residual of the governing equations calculated at the gth calculation point in the corresponding Delaunay triangle. e_t in Eq. (4.9) can be used as the local error estimate over the subdomain (rather than a single point). For elastic problems, the residual of the strong form governing equations in Eq. (4.9) is replaced by the physical equilibrium equation. With the description of local error in Eq. (4.9), the global error estimator can be easily obtained by

$$e_g = \frac{1}{A} \sum_{t=1}^{n_t} e_t \tag{4.10}$$

where $A = \sum_{t=1}^{n_t} A_t$ is the area of the problem domain and n_t is the total number of Delaunay triangles. The local and the global error estimators, e_t and e_g, developed for the MEPCM are used in the refinement procedure as described below.

The refinement strategy used in MEPCM h-adaptivity is based on mesh refinement ideas from weak form-based methods [193, 194] but facilitates an easier implementation without the constraints of point connectivity. The target is to reduce both local and global errors, achieving a prescribed accuracy. Here, a local refinement coefficient $k \in [0, 1]$ (uniform refinement with $k = 0$) is predefined. The permissible local error η_t is then defined as

$$\eta_t = ke_{max} \tag{4.11}$$

where e_{max} is the maximum local error. Triangles with $e_t > \eta_t$ are flagged for refinement. The selection of k is problem dependent and there is not a rule for the choice of the value of k. However, the choice of k is determined by the variation of local error estimators. A larger value of k could be chosen if local errors vary in a wide range while a smaller k is used if all local errors are close to each other.

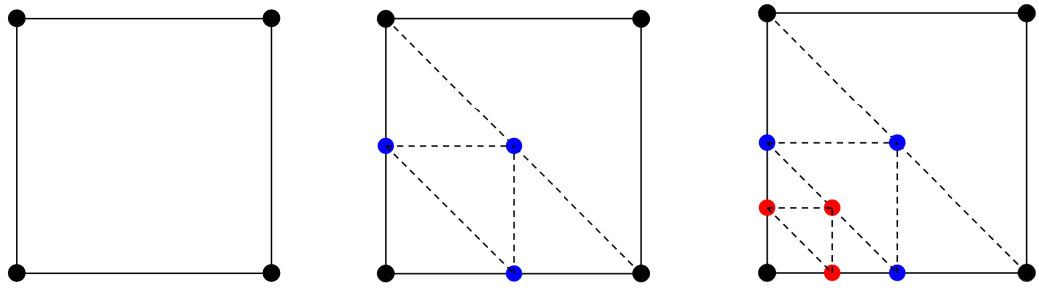

(a) Initial points distribution; (b) First refinement; (c) Second refinement.

Figure 4.2: Step by step points refinement in h-adaptivity.

Three new collocation and source points are inserted into these flagged triangles. Consider a discretisation with four points distributed as shown in Figure 4.2(a) in which two Delaunay triangles can be generated. The lower triangle is flagged for refinement so three new points are added at the centre of each two initially distributed points as presented in Figure 4.2(b). A further second refinement is given as in Figure 4.2(c). For an irregular problem domain or random distributed points, although the generated triangles are not right angled triangles, refinement is still straightforward as indicated in Figure 4.2. In each h-adaptivity step, some new points may be coincident, which have to be removed from the list of points. In the h-adaptive MEPCM, collocation points are refined in the same way as shown in Figure 4.2. The new source points are situated at

the same positions with the new collocation points. Refined source points improve the performance of the max-ent basis functions while more collocation points serve to better satisfy the governing PDEs and boundary conditions. h-adaptivity continues until the global error in Eq. (4.10) meets a prescribed value.

The effectiveness of the h-adaptive procedure can be described by an effectivity index as

$$\theta = \frac{e_g}{||e||_{L_2}} \tag{4.12}$$

where e_g is the global error estimator and $||e||_{L_2}$ is the L_2 norm of relative error. The effectivity index can be measured for those problems with analytical solutions to validate the performance of the proposed error estimator. If the effectivity index, θ keeps around a constant with an increasing number of degrees of freedom, the error estimate is efficient to indicate the actual errors. It is because the estimated error can converge at a similar rate to the actual error.

4.5 A combined rh-adaptivity approach

r- and h-adaptivity can be employed in the MEPCM separately to improve accuracy, however both have their limitations. N_c and N_s do not change in r-adaptivity and only the density of collocation points in the domain and on the boundaries is changed so in a pure r-adaptivity, an arbitrarily prescribed accuracy may not be achievable within a given number of degrees of freedom. In single h-adaptivity, although the number of points increases continuously, the positions of newly inserted points are at least partially determined by the initial distribution of points which presents a degree of inflexibility. The initial discretisation may not be the optimal distribution of points, in which the accuracy with this number of degrees of freedom can be further improved. Therefore, a combined rh-strategy is now considered in which intermittent point relocation (r-adaptivity) and h-adaptivity are both conducted. An arbitrarily defined accuracy η_g can be accomplished by an optimised point distribution within an optimal number of N_c and N_s. After the initial calculation using a given discretisation, r-adaptivity is adopted to adjust the point positions, which is followed by further h-adaptivity. As different

quantities of error estimators are used in r- and h-adaptivity respectively, it is vital to point out that the given accuracy should be achieved by the residual η_r in r-adaptivity or e_g in h-adaptivity.

4.6 Numerical implementation

All detailed formulations used in different adaptive strategies have been described in the last section. Numerical implementation using different algorithms for determining source points in the local support, is discussed in this section.

4.6.1 Algorithms for determining source points in a support

The local max-ent basis function values vary with the changes of size and shape of the local support domain of a collocation point, so compact support should be defined thereby satisfying the required property for basis functions as introduced in §3.5. Enough source points should be included in the local support domain for each collocation point to guarantee the partition of unity (PU) property of the basis functions. That is, for a given discretisation, the basis function values associated with source points inside the support domain of a collocation point are non-zero and the summation of these basis function values equals one.

In previous studies using max-ent basis functions [195, 196], the size of the support domain for each collocation point has been controlled by a scaling parameter d_{max}, so the choice of d_{max} is vital as this support region has an influence on accuracy and stability of the approximation. For a regular distribution of source and collocation points, N_s^* is the same using a fixed d_{max} for most collocation points in the interior of the problem domain and the computational cost for calculating basis functions for each collocation point in the interior of the problem domain is similar. Therefore, it is not necessary to consider this problem in Chapter 3. However, using a fixed d_{max} in a random (or unstructured) distribution of points, not only is the calculation time for constructing basis functions associated with each collocation point different because N_s^* varies but also the coefficient matrix $[K]$ may be singular since N_s^* might be zero for some collocation points. For some collocation points on boundaries, fewer source points are included in the local support. In

r-, h- and rh-adaptive processes, collocation point relocation and points refinement make the initial discretisation irregular in the following adaptive steps, therefore, additional efforts are needed to deal with this difficulty caused by the use of a fixed d_{max}.

To address this issue in the MEPCM, a method has been devised to search for the N_s^* nearest source points in the neighbourhood of each collocation point. The main idea of this algorithm is not to define a constant d_{max} but to define a minimum number of source points N_s^* in the support domain throughout the problem and these N_s^* nearest source points for each collocation point are stored for calculating the basis functions. The minimum N_s^* could be set as three in two dimensions for linear basis functions and the three nearest source points are selected. An additional check is required to ensure that the N_s^* source points are not collinear associated with the collocation point in two dimensions (similar to the issue in [197] for weak form-based meshless methods). Using this idea, the computational cost for calculating basis functions for each collocation point is similar and singular coefficient matrices $[K]$ can be avoided. If the N_s^*th and $(N_s^* + 1)$th source points have the same distances from the centred collocation point, both are included.

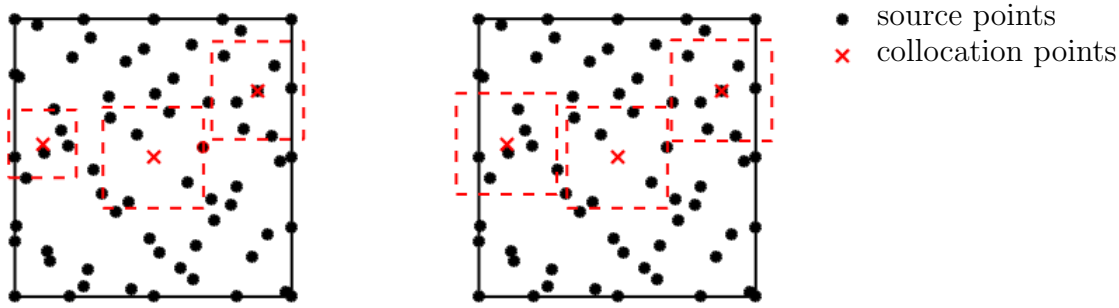

(a) Fixed N_s^* (b) Fixed size for support

Figure 4.3: Two algorithms using fixed N_s^* and d_{max} for determining N_s^*.

Determining proceeds by selection of a rectangular support domain is chosen around each colocation point and two different approaches can then be used as are shown in Figure 4.3. In Figure 4.3(a) N_s^* is set as 6 for all collocation points and it can be seen that the sizes of support domain for all collocation points are different. Since coincident source and collocation points may lead to inaccuracy of the first max-ent basis function

derivatives [114], source points that are identified in a search that are coincident with the collocation point are not counted in N_s^*. Figure 4.3(b) shows the case where the size and shape of support domain (i.e. d_{max}) is the same for all collocation points and N_s^* varies across the support domains. In the numerical examples section, the performance in terms of accuracy using fixed N_s^* and fixed d_{max} is demonstrated for comparison.

4.7 Numerical examples

In this section, some numerical examples are presented to demonstrate the performance of the proposed r-, h- and rh-adaptivity procedures. The two different algorithms for determining source points inside the support domain are implemented and compared in terms of accuracy for r- and h-adaptivity separately. The first three examples have analytical solutions so that clear L_2 norm of relative error on the displacements $||e||_{L_2}$ can be determined to show convergence rates in multiple adaptivity strategies. The effectiveness of the proposed error estimators are also validated by comparing $||e||_{L_2}$ and e_g versus degrees of freedom. The computational efficiency with respect to accuracy and computational times are also presented for each adaptivity strategy.

4.7.1 A one-dimensional bar problem

This is the same example as presented in §3.6.1, i.e. a one-dimensional linear elastic bar of unit length fixed at the point $x = 0$ is subjected to a body force $f^b(x) = x$. For this one-dimensional problem, the linear system of equations was set up in which the collocation points at the two ends satisfy the Dirichlet boundary conditions and all collocation points in the interior of the domain are enforced to satisfy the physical governing PDEs. In the small deformation case, the analytical solutions for the displacement and stress field of this problem have been given previously in Eq. (3.58). The unit length bar was discretised by a uniform distribution of collocation points and source points at the same positions.

r-adaptivity

Eleven collocation and source points are distributed uniformly in the problem domain and on the boundaries. All source points are fixed in r-adaptivity so that the max-ent basis function values stay the same in the overall analysis. Displacements at these eleven collocation points that are obtained by solving the linear system are used to measure the norm of the residual function $||R(x)||$. The residual norm $||R(x)||$ described in Eq. (4.8) in each Newton-Raphson iterative step against the iteration number is shown in Figure 4.4 (a) where the residual norm decreases in the first 7 iterative steps followed by a degradation in the last four steps, leaving $||R(x)||$ converging to a non-zero value. This is a demonstration that the discretisation errors cannot be further reduced with this given number of degrees of freedom, which is a limitation in pure r-adaptivity. The convergence characteristics of the Newton-Raphson method for this one-dimensional bar problem are shown in Figure 4.4 (b) where the gradients between pairs of steps are shown. The convergence rate is less than the theoretical convergence rate of 2.0 for the Newton-Raphson method [198, 199]. The possible reason for the lower convergence rate might be the discretisation errors from basis function values. Source points, which are used to construct basis functions, are not relocated in r-adaptivity and the same basis function values are used in the overall analysis, therefore, the errors resulting from basis functions are kept in r-adaptivity, serving to reduce the speed of error minimisation.

A comparison in terms of $||e||_{L_2}$ using uniform h-refinement and r-adaptivity with either fixed N_s^* or d_{max} is presented in Figure 4.5. It is shown that r-adaptivity with $N_s^* = 2$ has similar convergence with lower relative errors than uniform h-refinement with $N_s^* = 2$. The number of source points inside the local support N_s^* is critical to accuracy but it remains unclear how to find the optimal N_s^* theoretically [24]. As the analytical solution exists, the L_2 norm of relative error on displacements $||e||_{L_2}$ are used to study the influence of using different N_s^*. When using $d_{max} = 2.0$, the size of support domain stays the same and result in $N_s^* = 4$ for the collocation points in the interior of the problem domain using a regular discretisation. However, in the r-adaptive procedure, some collocation points are gradually moved to form an irregular distribution which may lead to deficiency in the linear system using $d_{max} = 2.0$. In the case with $d_{max} = 2.0$,

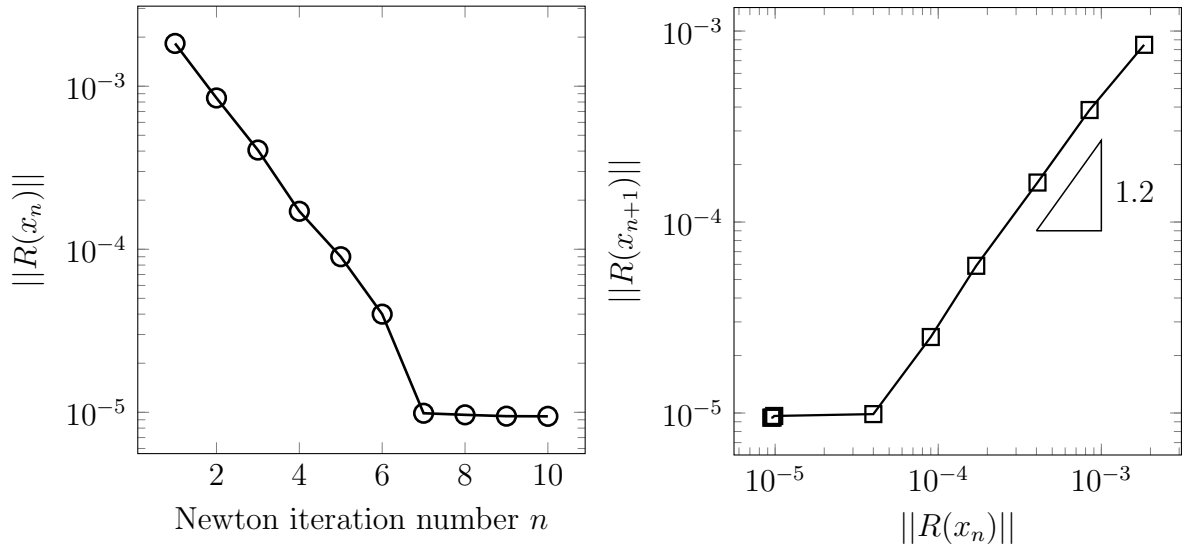

(a) $||R(x)||$ versus Newton iteration number.

(b) Convergence rate of $||R(x)||$.

Figure 4.4: Residual norms and convergence rate in the Newton-Raphson method of the one-dimensional bar problem.

the convergence rate of $||e||_{L_2}$ in the r-adaptivity analyses goes down when $N_s = 41$ as not enough source points are included in the support domain in the irregular points distribution, especially for the collocation points at two ends. When $N_s^* = 3$ and 4, 3 and 4 source points in the support domain are included to construct the basis functions. In the initially symmetric discretisations, $N_s^* = 3$ and 4 lead to the same discretisation errors for the most collocation points in the interior of the problem domain. In the latter r-adaptive steps, using $N_s^* = 4$ and $N_s^* = 3$ results in different weight function values in the irregular point distributions. From this study, using $N_s^* = 2$ appears to achieve better convergence rates than using $N_s^* = 3, 4$ and $d_{max} = 2.0$.

In order to measure the efficiency of the proposed r-adaptivity procedure, CPU times with different discretisations using uniform h-refinement and r-adaptivity were measured. With the same number of collocation points, uniform h-refinement is cheaper than r-adaptivity as the r-adaptive process takes more time to minimise the material force residuals by relocating collocation points iteratively than using uniform h-refinement. Efficiency in terms of relative errors $||e||_{L_2}$ against CPU times for uniform refinement and r-adaptivity is compared in Figure 4.6. Although for a small number of degrees of freedom (relatively high errors), r-adaptivity needs more computational time than uniform

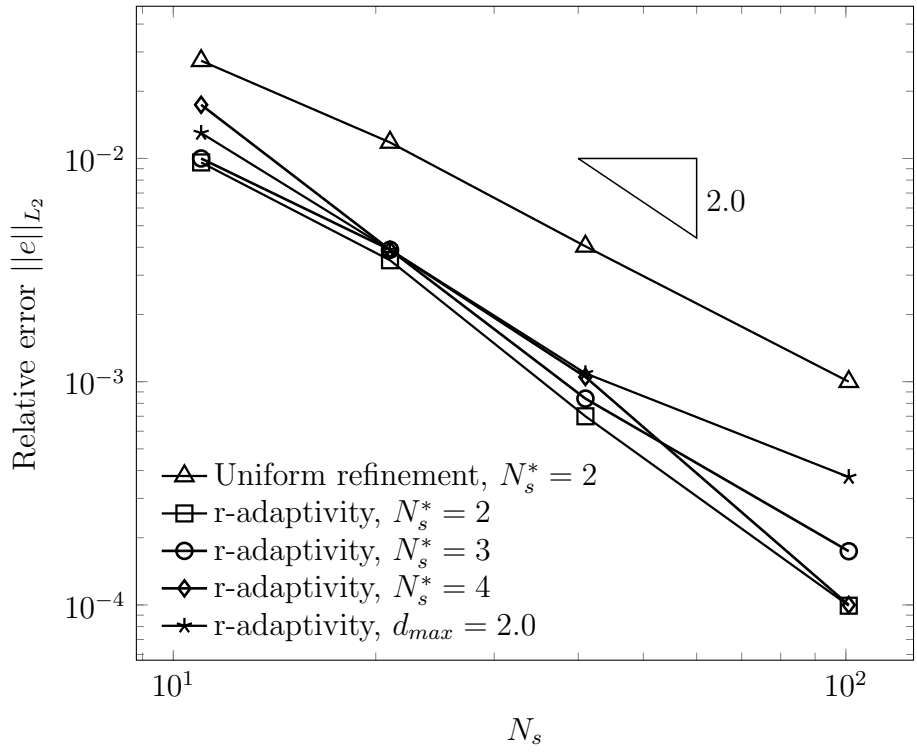

Figure 4.5: Convergence rate of $||e||_{L_2}$ of the one-dimensional bar problem using uniform refinement and r-adaptive strategy with various N_s^*.

refinement, it is observed that with an increasing number of degrees of freedom (relatively small errors), r-adaptivity is more cost effective than using uniform h-refinement. Uniform refinement cannot always improve the accuracy efficiently because the extra degrees of freedom are introduced in local regions with small errors. In this example, it is concluded that the accuracy of the MEPCM approximation can be improved through effective r-adaptivity.

h-adaptivity

The one-dimensional bar is now analysed using h-adaptivity. For initial discretisation, 6 collocation points and 6 source points were distributed in the interior of the problem domain and on the boundaries uniformly as shown in Figure 4.7(a). The governing PDEs and boundary conditions are identical to those used in the study of r-adaptivity above. The L_2 norm of relative error on displacement $||e||_{L_2}$ and the proposed global error estimator e_g in each h-adaptive step were measured. In one-dimensional analysis, the local error estimate is replaced by e_l which is estimated in each local length. In order

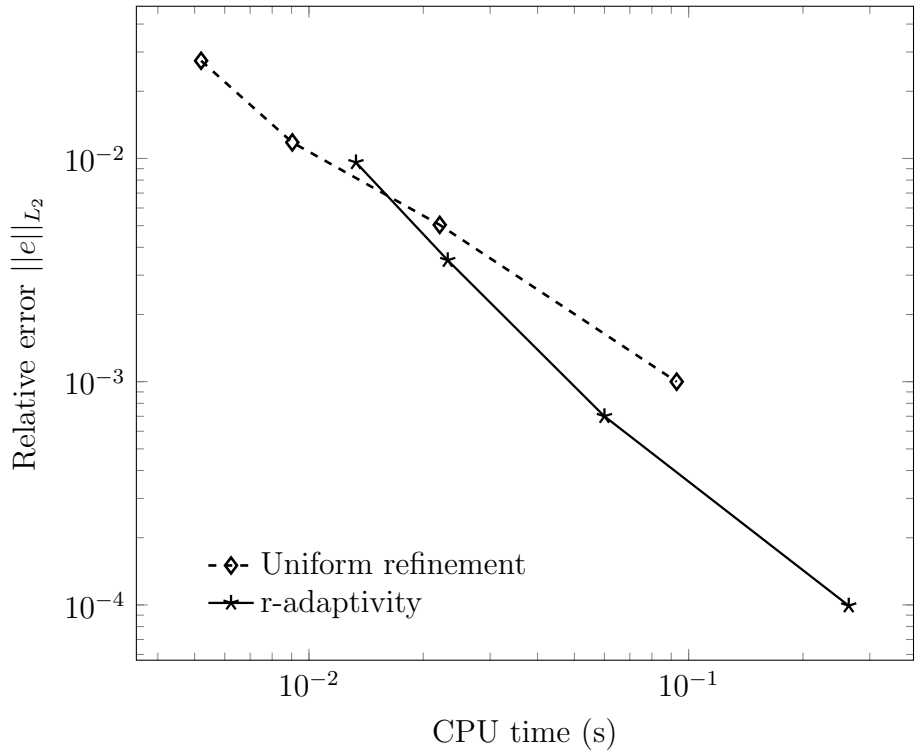

Figure 4.6: Convergence rate of $||e||_{L_2}$ against CPU time of the one-dimensional bar problem using uniform refinement and r-adaptivity with $N_s^* = 2$.

to calculate the error estimate e_l, the residuals of the strong form governing PDE were determined at the calculation points as shown in Figure 4.7(b).

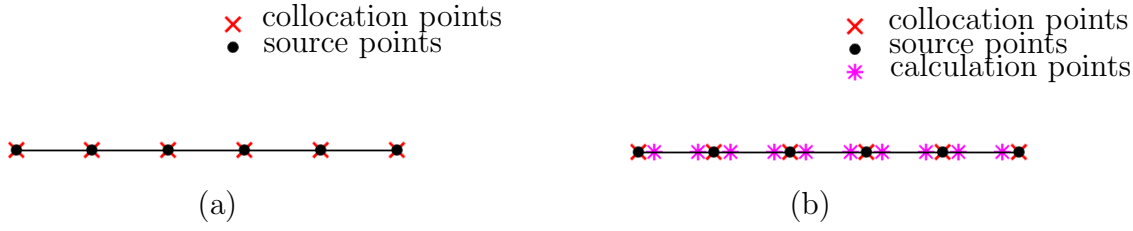

Figure 4.7: The collocation, source and calculation points generation in h-adaptivity of the one-dimensional bar problem.

The local error estimator given in Eq. (4.9) can be changed as

$$e_l = \frac{1}{2} l \sum_{g=1}^{2} ||E \frac{d^2 u_g^h}{dx_g^2} - x_g||, \tag{4.13}$$

for each local length in one-dimensional problem where l is the length between two

adjacent collocation points, x_g is the coordinate of the gth calculation point and u_g^h is the approximation at the gth calculation point. The global error is

$$e_g = \frac{1}{L}\sum_{l=1}^{n_l} e_l, \tag{4.14}$$

where L is the length of the one-dimensional problem domain and n_l is the number of individual lengths. In this example, new collocation and source points are added at the centres of local lengths as determined by the local error estimate e_l.

In this study, a comparison in terms of accuracy using fixed d_{max} and fixed N_s^* is also included. Figure 4.8 shows a plot of $||e||_{L_2}$ in the main variable u against N_s using uniform refinement and h-adaptivity with $k = 0.95$ and different sizes of support domain for the one-dimensional problem. In this figure, it can be seen that h-adaptivities with $N_s^* = 2, 3, 4$ have better convergence rates with lower errors than uniform h-refinement with $N_s^* = 2, 3, 4$. Although any choice of the support shape and size might be possible, they have an effect on the weight function and basis function values, which are critical to numerical solution. Similarly to the previous example, numerical experiments provide a way to choose an optimal N_s^* with better accuracy [24]. In the uniform h-refinement, N_s^*=2, 3, 4 are picked for comparison. It can be seen that N_s^*=2 has lower errors than the other two cases with the same discretisations. The sizes of support are different for these three different N_s^* and the maximum weight function value for N_s^*=2 is higher than the other two values. For the regular distribution of points, N_s^*=3 and 4 lead to the same support domain for the collocation points in the interior of the problem domain and consequently these approaches have similar error convergence rates, but in the adaptive process, points are added into regions with higher errors, which makes the points distribution irregular therefore N_s^*=3, 4 analyses produce different error norms. The size of support using d_{max}=2.0 is the same as N_s^*=4 for the collocation points in the interior of the problem domain, but for the boundary collocation points, N_s^*=4 has larger support. It can be observed in Figure 4.8 that the size of support domain plays a more important role in h-adaptivity as the discretisation becomes irregular. h-adaptivity with N_s^*=2 achieves a better convergence rate than using N_s^*=3, 4. In addition, this irregular points distribution also causes deficiency using $d_{max} = 2.0$ and some issues raised in §4.6

appear here, i.e. singularity problems in $[K]$ has an effect on solving the linear system and approximating the solution in the last three h-adaptive steps. From this analysis, using a fixed minimum N_s^* is more robust in h-adaptivity and N_s^*=2 is an appropriate choice in this example to achieve better accuracy.

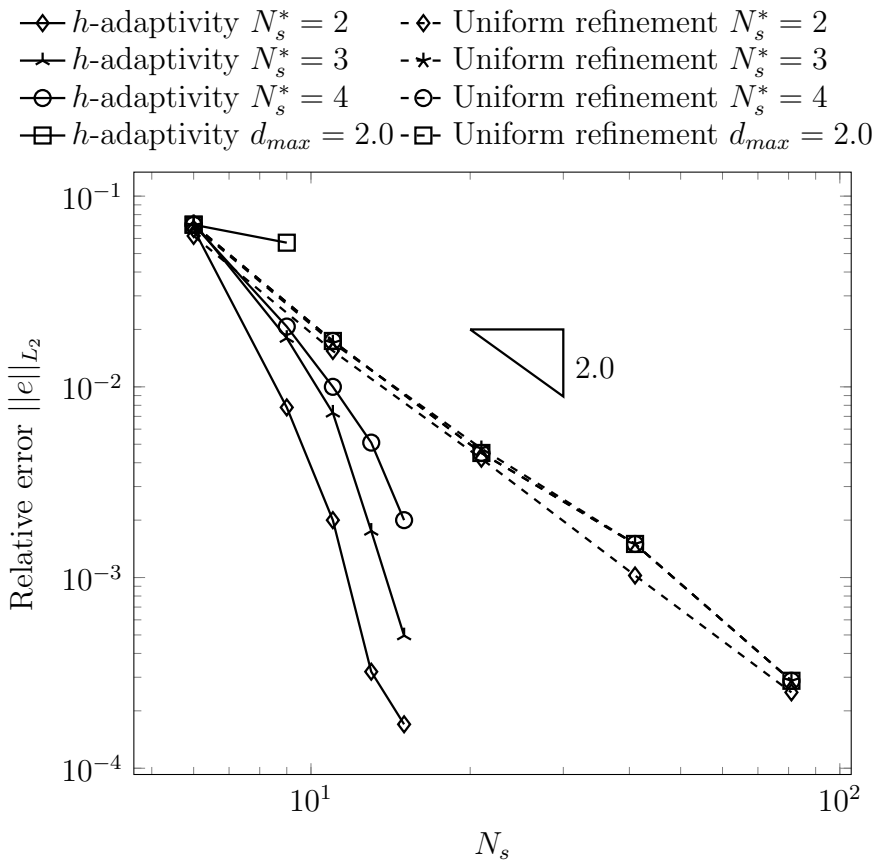

Figure 4.8: Convergence rate of $||e||_{L_2}$ of the one-dimensional bar problem using different N_s^* with $k = 0.95$.

In order to study the effect of using different values of the local refinement coefficient k on accuracy in h-adaptivity, e_g with $k = 0.9, 0.95, 0.99$ are obtained using N_s^*=2. Although there is no theoretical value for the local refinement coefficient, k, the choice of k is affected by the variation of local errors over the domain, which is discussed with the error distribution. The global error estimator e_g given in Eq. (4.10) for uniform and h-adaptivity with different k are plotted against N_s in Figure 4.9. It can be seen that the global error estimator e_g for uniform refinement decreases slower than in h-adaptivity with different k values. Using $k = 0.9$ allows more points to be added than using $k = 0.95$ and 0.99 in the adaptive steps. The convergence rate of the global error

estimator e_g using $k = 0.95$ is greater than using $k = 0.99$ and smaller than using 0.9 in the initial two steps. However, this global error estimator decreases faster than the rest two cases in the latter steps. The number of new points in the case with $k = 0.95$ makes h-adaptivity more efficient than the other two cases, achieving a better convergence with more accurate results.

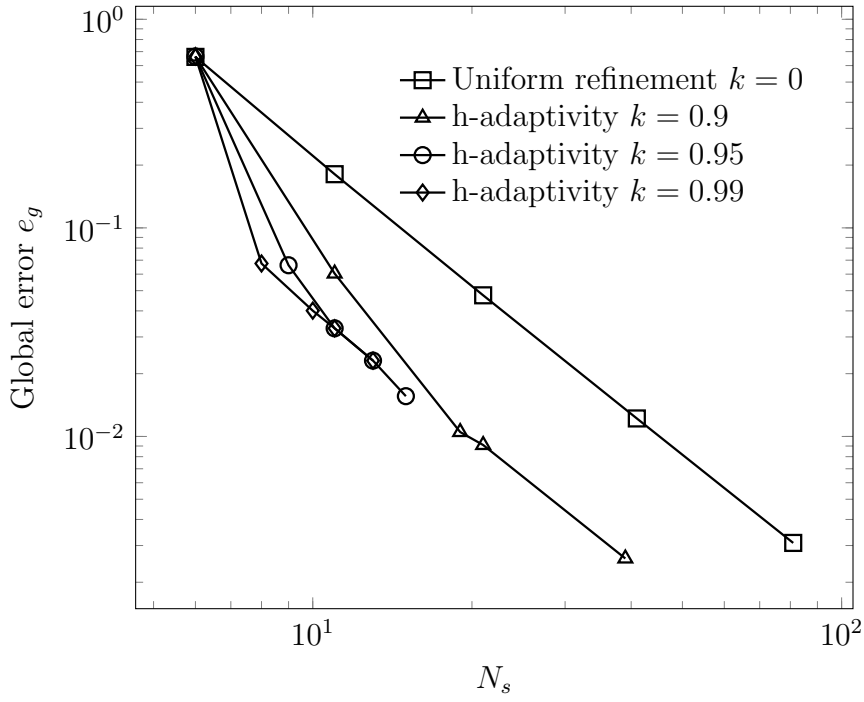

Figure 4.9: Convergence rate of e_g of the one-dimensional bar problem using different k with $N_s^* = 2$.

Figure 4.10 shows the convergence rates of $||e||_{L_2}$ in uniform refinement and h-adaptivity with different k, which is used to validate the performance of proposed e_g. It can be seen that k=0.95 performs better than using k=0.9 and 0.99 in the overall adaptive steps except for the first step. Comparing Figure 4.9 with Figure 4.10, in this one-dimensional problem with an analytical solution, a similar trend is apparent using e_g and $||e||_{L_2}$ with different k which influences the efficiency in h-adaptivity, although the magnitudes in these two figures are different.

The effectivity index θ, which is designed to show the effectiveness of the proposed error estimator in Eq. (4.9) is of use here. In Figure 4.11, the effectivity index with different k values in h-adaptivity for this one-dimensional problem is plotted. The effectivity index for $k = 0.95$ increases slightly in the continuous adaptive steps and the

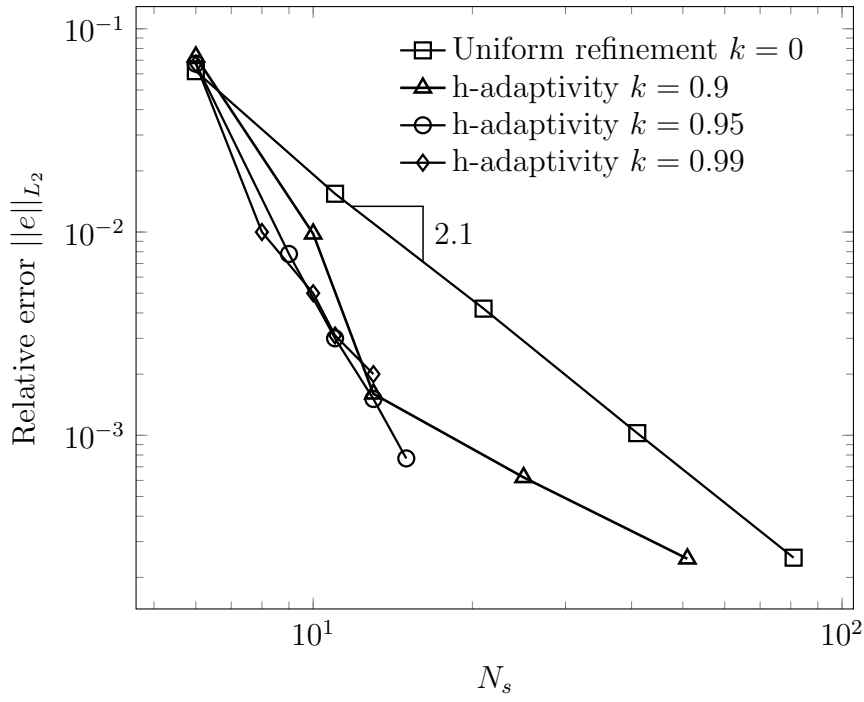

Figure 4.10: Convergence rate of $||e||_{L_2}$ of the one-dimensional bar problem using different k with $N_s^* = 2$.

gradient of θ is not a constant as the convergence rates of errors described by different error estimators have different magnitudes. The effectivity index with $k = 0.9$ shows oscillation around a value 10, which implies the ratio of the proposed error estimator and the actual error is close to a constant as discussed in §4.4. The global error estimator e_g converges at the similar rate to the actual errors.

The global error estimator e_g versus the CPU time that includes the total computational time for calculation, error estimation and point refinement for uniform refinement and h-adaptivity with different k, is shown in Figure 4.12. It can be seen that uniform refinement takes more time than h-adaptivity since in h-adaptivity fewer points are used than in uniform refinement, which makes h-adaptivity more efficient to achieve a given accuracy. Comparing the CPU times in h-adaptivity with different k, the computational cost using $k = 0.9$ is more expensive than using $k = 0.95$ and $k = 0.99$ as more new points are inserted. Less points are inserted using $k = 0.99$, but it is slower to achieve the predefined accuracy. From the above numerical results, h-adaptivity with $k = 0.95$ can achieve better accuracy with less CPU time than uniform refinement and h-adaptivity with other k values.

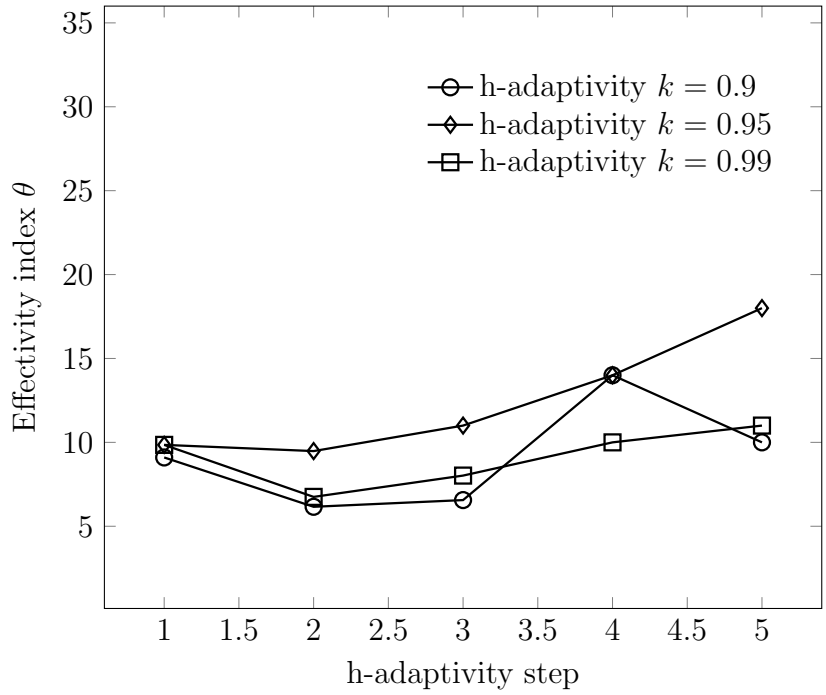

Figure 4.11: The effectivity index using h-adaptivity of a one-dimensional bar problem using different k with $N_s^* = 2$.

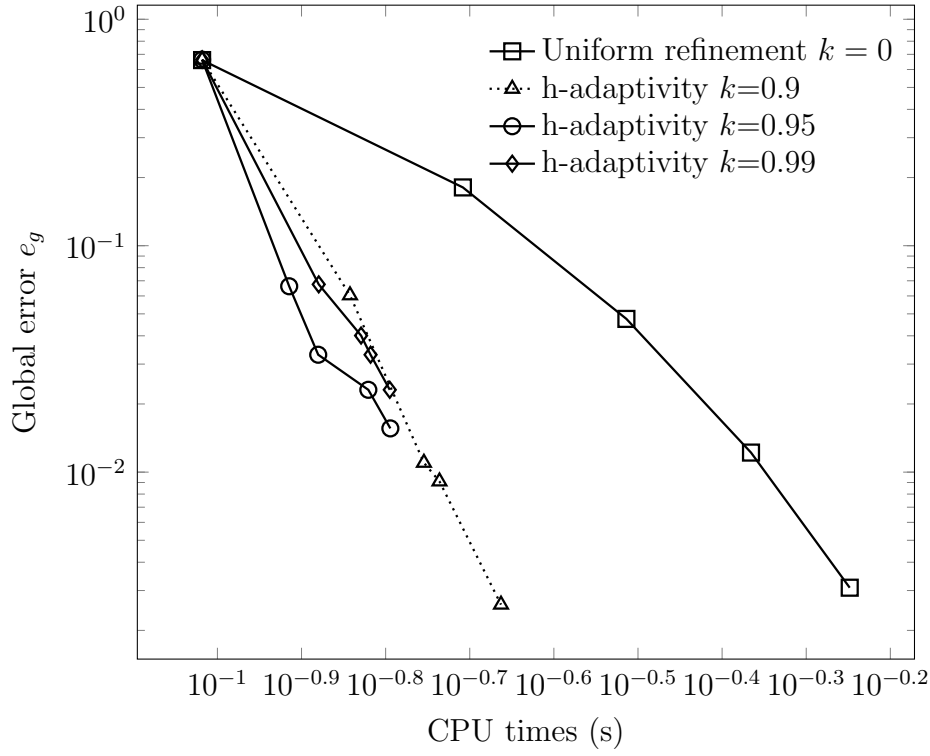

Figure 4.12: Convergence rate of e_g against CPU time of the one-dimensional bar problem using different k with $N_s^* = 2$.

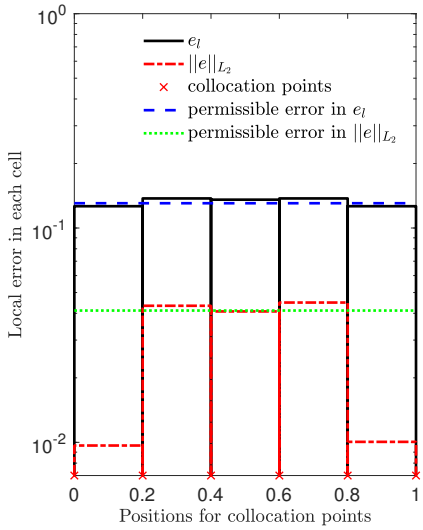

(a) The initial calculation;

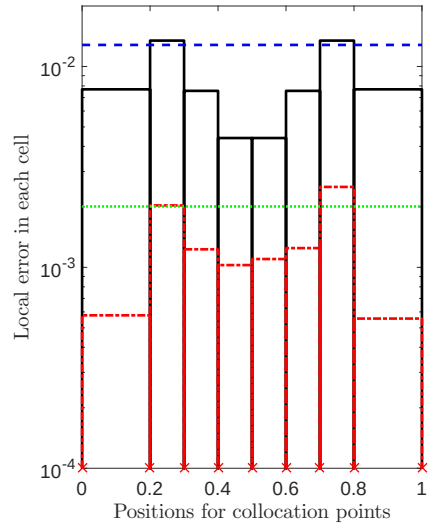

(b) The first h-adaptive step;

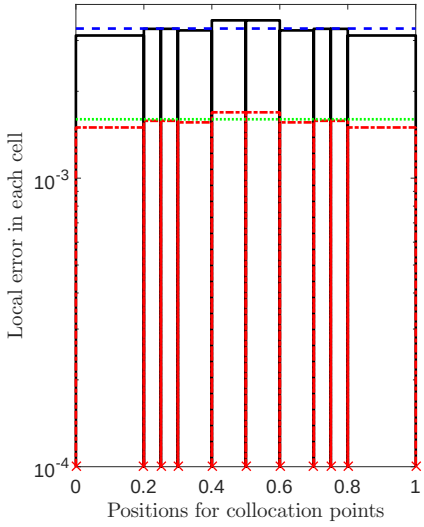

(c) The second h-adaptive step.

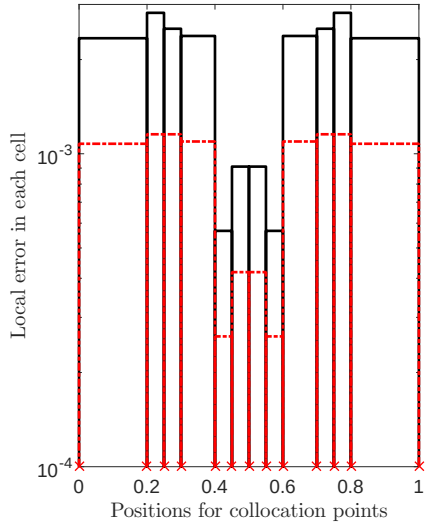

(d) The third h-adaptive step.

Figure 4.13: The collocation points and local error distributions in h-adaptivity with $k = 0.95$ of the one-dimensional bar problem.

Distributions of collocation points with local errors e_l and the L_2 norm of relative error on displacement $||e||_{L_2}$ of each local length in the step-by-step h-adaptivity with $k = 0.95$ are shown in Figure 4.13. It can be observed that the local lengths with local errors e_l and $||e||_{L_2}$ greater than the permissible errors are refined to reduce e_g in the h-adaptive process. In this figure, e_l and $||e||_{L_2}$ perform the same trend although they are measured in different ways. In Figure 4.13(b)-4.13(d), the positions for newly added collocation points can be determined by e_l or $||e||_{L_2}$. It can also be observed in Figure 4.13 that there is only a little variation in the local errors across the domain, the selections of refinement parameter k are in a small range and sensitive to the analysis. If values of k are chosen in a larger range, some choices below a value lead to the analyses which are identical with the uniform refinement ($k = 0$).

4.7.2 An infinite plate with a circular hole

In this example, an infinite plate with a circular hole with a far field stress $p = 10$ in x direction under plane stress conditions is analysed. An analytical solution exists for this problem so the proposed error estimator can be validated by comparing to the actual L_2 norms of relative errors $||e||_{L_2}$. In this example, uniform refinement, pure r-, h- and combined rh-adaptivity are compared in terms of accuracy and computational cost. As this example has already been studied in §3.6.4, the boundary conditions and analytical solution for this problem can be found there. In the entire analysis, $N_s^* = 3$ is chosen to be used. For the initial distribution, 121 collocation points are distributed in the problem domain and on the boundaries as shown in Figure 4.14(a). A total of 81 collocation points are in the domain, 4 corner points are fixed and 36 collocation points are on boundaries and can only be relocated on boundaries in one direction in pure r-adaptivity. The predefined maximum iteration number in the Newton-Raphson method was set as 20 with a tolerance number $\eta_r = 10^{-5}$ in the r-adaptive process. The global error estimator e_g is adopted to estimate the global error for overall accuracy. The local error estimator e_t for each local area is estimated at the generated calculation points as described in §3.3 and $k = 0.2$ in this example is selected to test the performance of various adaptive strategies. Unlike in the one-dimensional bar problem, the local refinement parameter k

can be defined as a small number 0.2. The variation of local errors in this example is apparent as the stress concentration effect around the circular hole area can cause a wide range of variation while the errors close to Dirichlet boundaries are getting smaller. In addition, combined rh-adaptivity is conducted and the performance in terms accuracy and computational cost of various refinement strategies is explored.

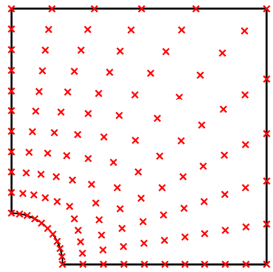

(a) A portion of the infinite plate with a circular hole with a far field stress $p = 1.0$ in x direction.

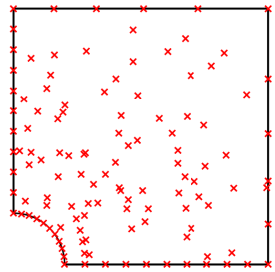

(b) Collocation points after the 1st relocation.

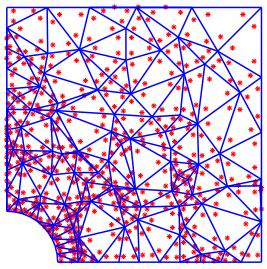

(c) The generation of triangles and calculation points.

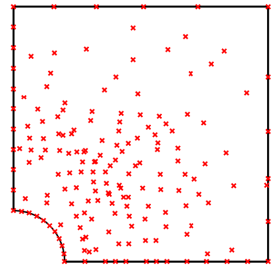

(d) Collocation points after the 1st rh-adaptivity.

Figure 4.14: The distribution of collocation points in rh-adaptivity with $k = 0.2$ of the infinite plate with a circular hole problem.

The distributions of collocation points in the first rh-adaptivity step are illustrated in Figure 4.14. After the initial calculation, collocation points moved towards the circular hole area as shown in Figure 4.14(b) because the errors close to the hole are higher than in the other local areas, considering the stress concentration effect caused by the circular hole. These updated collocation points are employed to construct the Delaunay triangulations where three calculation points are generated in each triangulation as shown in Figure 4.14(c). In the following h-adaptivity step as shown in Figure 4.14(d), most of

the newly added points are located in the area close to the hole.

The L_2 norm of relative error $||e||_{L_2}$ in terms of the displacement solutions for uniform refinement, pure h and r-adaptivity and combined rh-adaptivity are plotted in Figure 4.15. These four strategies start with the same number of degrees of freedom. The convergence rate of uniform refinement is 2.0, which agrees well with the convergence rate for the MEPCM [114]. Values of $||e||_{L_2}$ in h-adaptivity are smaller and have higher convergence rate than in uniform refinement with the same degrees of freedom. It can be observed that the convergence rate of $||e||_{L_2}$ for r-adaptivity is almost the same as the error convergence in uniform refinement as their basis functions are the same. The improvement of accuracy between uniform and r-adaptivity for different discretisations stays approximately the same. A combined rh-adaptive process is adopted five times continuously using the same initial number of degrees of freedom as in pure adaptivity. It is observed that $||e||_{L_2}$ in the combined rh-strategy exhibits a better convergence rate

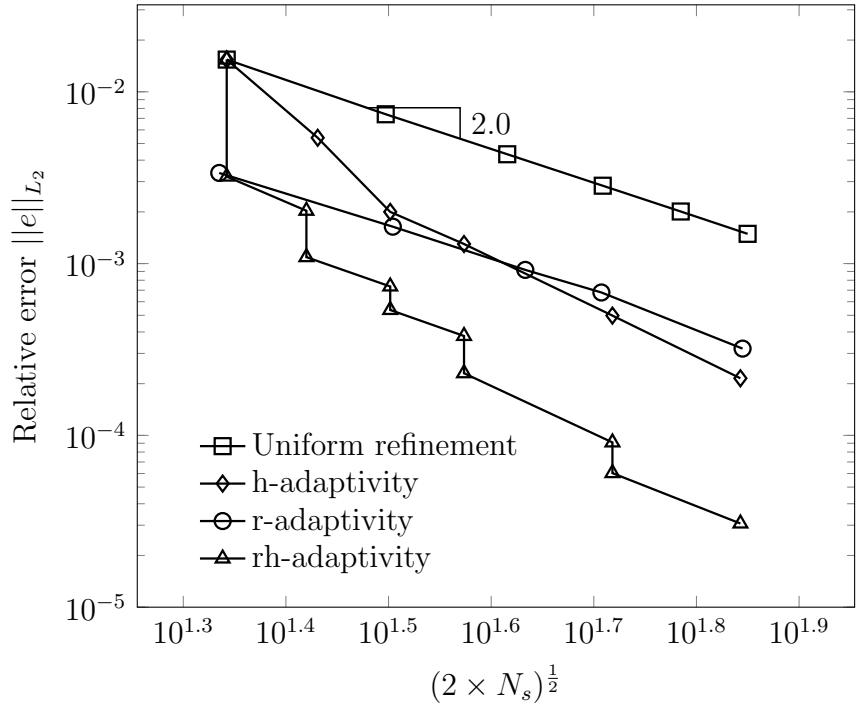

Figure 4.15: Convergence rate of $||e||_{L_2}$ of the plate with a circular hole problem with $k = 0.2$.

than uniform, r- and h-adaptivity. In rh-adaptivity, N_c and N_s increase from 121 to 1213 over five steps. After the initial calculation, the accuracy of solution can be improved in r-adaptivity where the number of degrees of freedom keeps the same indicated by the

vertical decrease in Figure 4.15. In the following h-adaptive step, the errors are reduced by increasing the number of degrees of freedom. Not only are the collocation points relocated in r-adaptivity but also additional points are refined in a combined strategy, which gives a more flexible approach with better performance in terms of accuracy than pure adaptive strategies.

In h-adaptivity and rh-adaptivity, the global error e_g is estimated in each h-adaptive refinement as shown in Figure 4.16 where e_g converges faster in rh-adaptivity than in h-adaptivity. Comparing $||e||_{L_2}$ in Figure 4.15 with e_g in Figure 4.16, although the actual values of e_g and $||e||_{L_2}$ for this example are different, they show the same changing trend and the proposed e_g can be used to predict the distributions of actual errors.

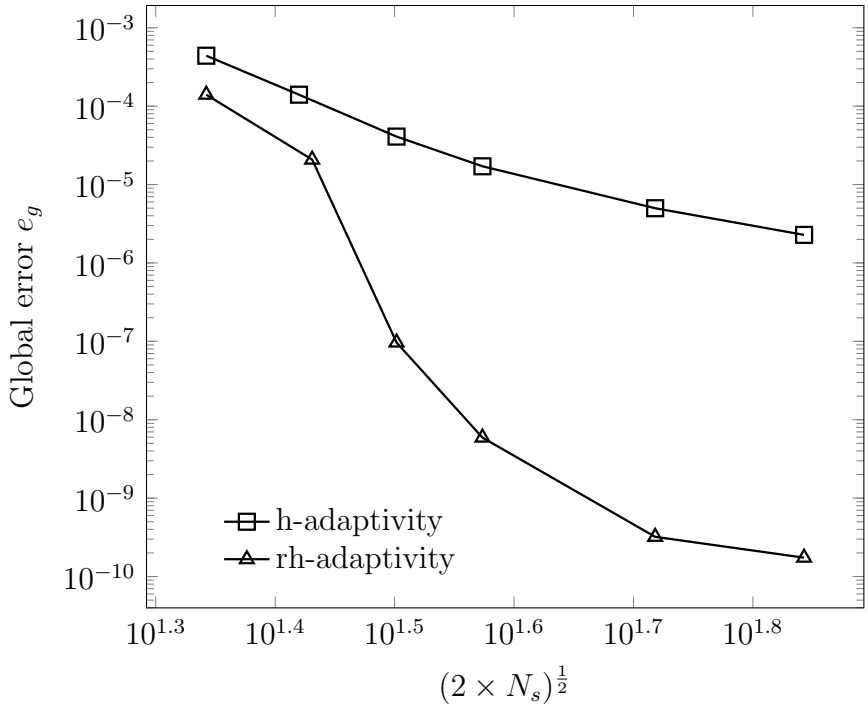

Figure 4.16: Convergence rate of e_g using h and hr-adaptivity of the plate with a circular hole problem with $k = 0.2$.

Figure 4.17 shows the material force residuals in each r step in combined rh-adaptivity. It can been seen in Figure 4.17 the minimisation of material force residual becomes more efficient from the second r-adaptive step because the refined points in the following h-adaptive step can also be used to minimise the discretisation errors.

Once again, the computational cost using these strategies are presented in Table 4.1. It is obvious that uniform refinement uses the shortest CPU time which computes the

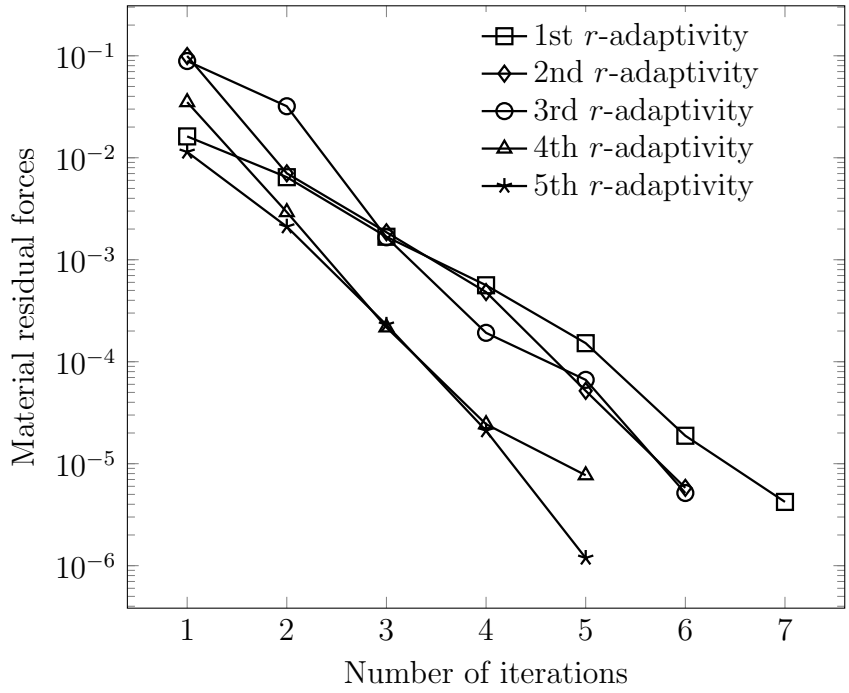

Figure 4.17: The material force residuals in the iteration process of the plate with a circular hole problem with $k = 0.2$.

	Initial N_s	Final N_s	CPU time (s)	Final $\|\|e\|\|_{L_2}$	Final e_g
Uni	1225	1225	7.76×10^1	1.49×10^{-3}	1.66×10^{-5}
h	121	1213	8.20×10^2	2.10×10^{-4}	2.28×10^{-6}
r	1225	1225	1.23×10^3	3.20×10^{-4}	3.55×10^{-6}
rh	121	1213	1.92×10^3	9.07×10^{-5}	1.74×10^{-10}

Table 4.1: Quantitative results in the infinite plate of a circular hole problem using different adaptivity approaches.

approximation of solution using the MEPCM with $N_s = 1225$. The pure h-adaptivity starts from $N_s = 121$ to $N_s = 1213$ and the CPU time for h-adaptivity includes 5 calculations using the MEPCM, 5 error measurements and 5 point refinements in total, taking 820.2s which is nearly 10 times that of using uniform refinement. The pure r-adaptivity relocates 1225 collocation points for a certain number of iterations to minimise the total potential energy. The total CPU time for this process is 15.8 times greater than uniform refinement but the error is cut by 78.5%. The total CPU time for combined rh-adaptivity is also reported. Compared to the pure h-adaptivity, the combined approach reduces 99.9% of the error but within an even longer time. After the point refinement, additional collocation point relation is conducted. This study shows that a combined rh-approach can generate more accurate approximations than r-adaptivity and h-adaptivity alone but with additional computational cost.

4.7.3 L-shaped plate under uniaxial loading

The final example presented in this chapter is that of a plane stress L-shaped plate subjected to uniform displacement on the left edge, for which the problem model and boundary conditions are shown in Figure 4.18. The right and top edge were constrained in x and y directions, respectively, and Dirichlet boundary conditions were imposed on the left edge. The other three edges were traction free. The material properties used for this example were $E = 1.0 \times 10^5$ and $\nu = 0.3$. An analytical solution is not available for this example so it is impossible to work out $||e||_{L_2}$. The proposed e_g in h-adaptivity is adopted to identify the accuracy of the local approximation in h- and rh-adaptive processes.

Again, uniform h-refinement, pure r-, h-adaptivity and combined rh-adaptivity approaches were considered for comparison in terms of accuracy and computational cost for this example. $N_s^* = 3$ is selected for entire analysis and $k = 0.3$ in h-adaptivity. As explained in last example, the local errors vary a lot in this example because of the stress singularity at point C. The total iteration number in the Newton-Raphson method for the r-adaptive process was 20 with a predefined tolerance number $\eta_r = 10^{-5}$ in r-adaptivity. At the beginning of the analysis, 96 collocation points were distributed

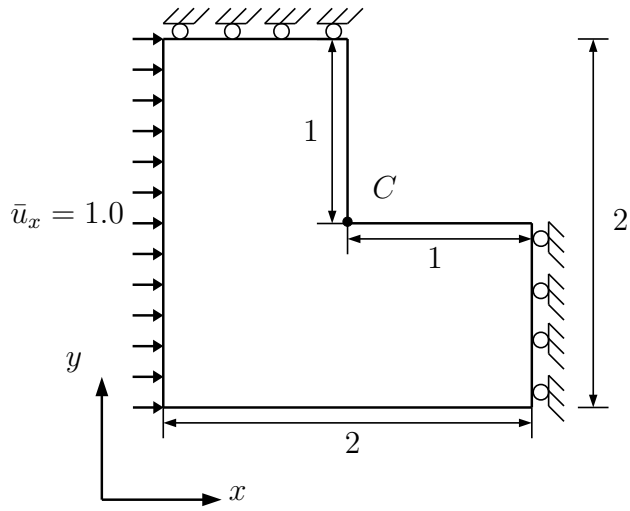

Figure 4.18: The L-shaped plate with a uniform displacement on the left edge.

regularly with the same number of source points but at slightly different positions, as shown in Figure 4.19(a). All source points inside the domain were concentrated towards point C by a scaling parameter 0.01.

As shown in 4.19(b) the collocation points relocation in the initial rh-adaptivity process leads to a distribution that concentrates a group of collocation points towards the stress singularity at C while the boundary collocation points are not moved since they fully satisfy the Dirichlet boundary conditions. Figure 4.19(c) shows the generated Delaunay triangulations associated with the updated collocation point positions in Figure 4.19(b). The generation of collocation points are illustrated in Figure 4.19(d). Figure 4.19(e) shows the collocation points distribution after the first h-adaptivity. Most new points are inserted around point C and traction free boundaries, however, the material equilibrium is not fully satisfied with these newly generated discrete points, which need further relocation as shown in Figure 4.19(f). It can be observed that although the geometry of the problem is symmetric, the points relocation and refinement are not due to the non-symmetric boundary conditions. In both the r- or h-process, collocation points are inserted near or moved towards the singularity point since the material force residual or e_t are much higher there than the rest of the domain as might be expected.

The global error e_g is also calculated to assess the accuracy of uniform refinement, r-, h- and rh-adaptivity, as shown in Figure 4.20. The global error estimator e_g in uniform

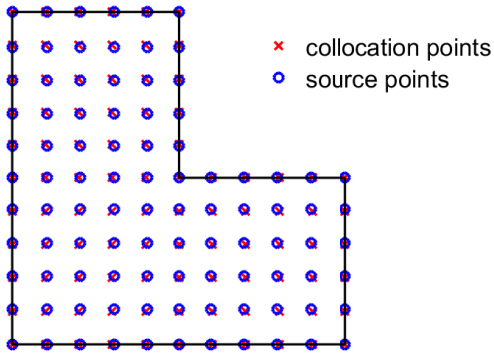

(a) Collocation and source points.

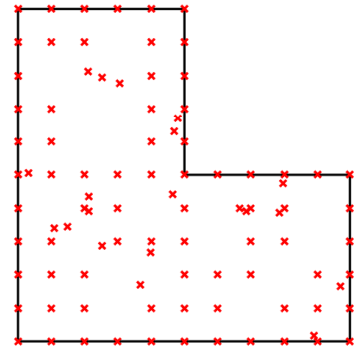

(b) Collocation points after the 1st relocation.

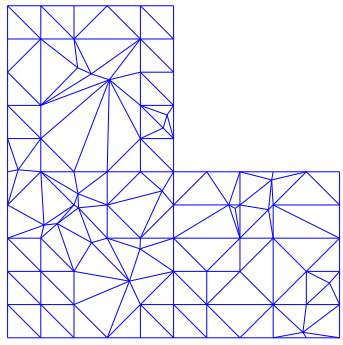

(c) The generation of triangles.

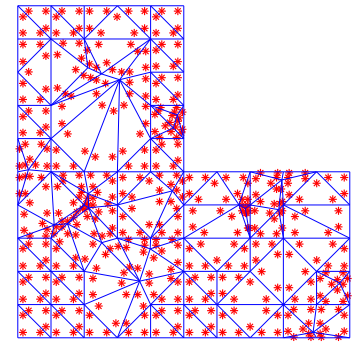

(d) The generation calculation points in triangles.

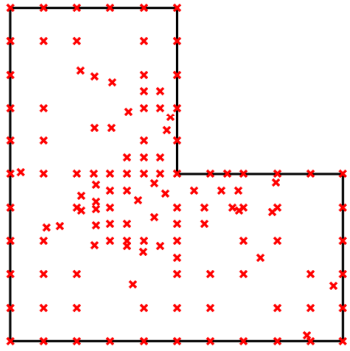

(e) Collocation points after the 1st refinement.

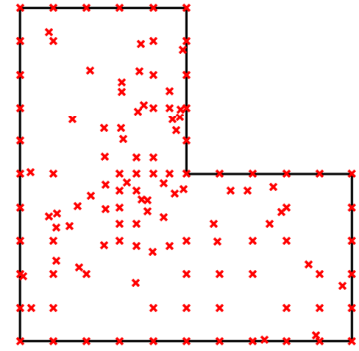

(f) Collocation points after the 2nd relocation.

Figure 4.19: The generation of points and triangulations of rh-adaptivity of the L-shaped plate.

refinement reduces more slowly than the other three methods with higher error values. h-adaptivity improves the accuracy more efficiently with a greater convergence rate than that for uniform refinement. For the same number of degrees of freedom, new collocation points are refined in the regions with higher e_t, such as near point C in this example. In uniform refinement, e_t in some regions far away point C reaches the prescribed accuracy requirement where additional collocation points are not needed. Although the material force residuals are used as residual in Newton method in r-adaptivity, e_g is also calculated after each r-process as a consistent error estimator to compare the convergence rate with the other three strategies. r-adaptivity decreases e_g within the same number of degrees of freedom and shows similar convergence rate to uniform h-refinement. Given the fact that errors have more than one source, the r-adaptive procedure can eliminate part of the discretisation errors by minimising the material force residual.

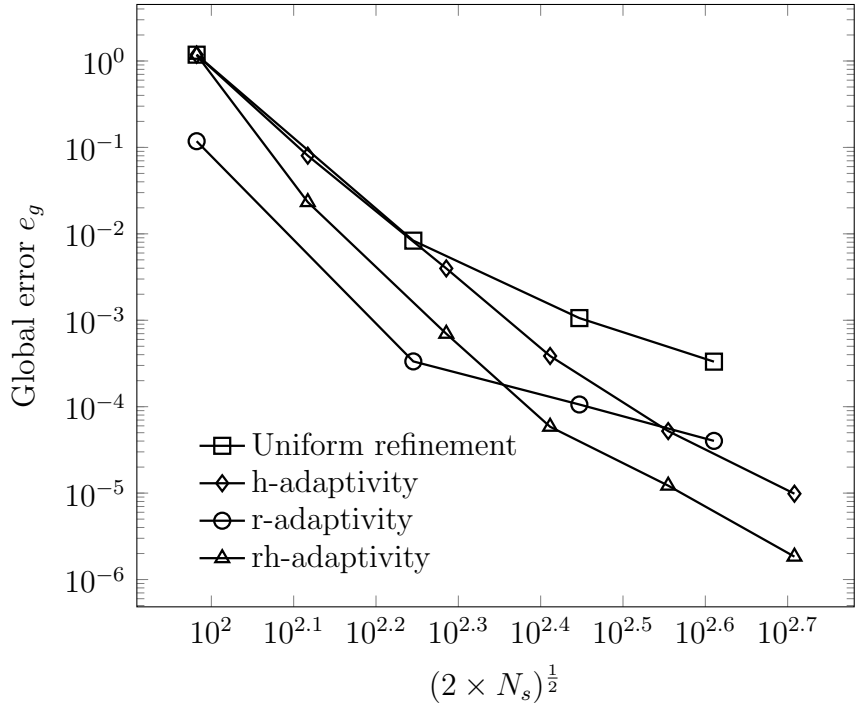

Figure 4.20: Convergence rate of e_g using different adaptivity of the L-shaped plate with $k = 0.3$.

The material force residuals measured from r-adaptive steps in a combined rh-adaptivity are shown in Figure 4.21. In the 5 r-adaptivity steps, collocation points relocations are completed within 5 iterations to achieve the prescribed requirement. The absolute value of residual in the first r-adaptivity step is higher than the rest because

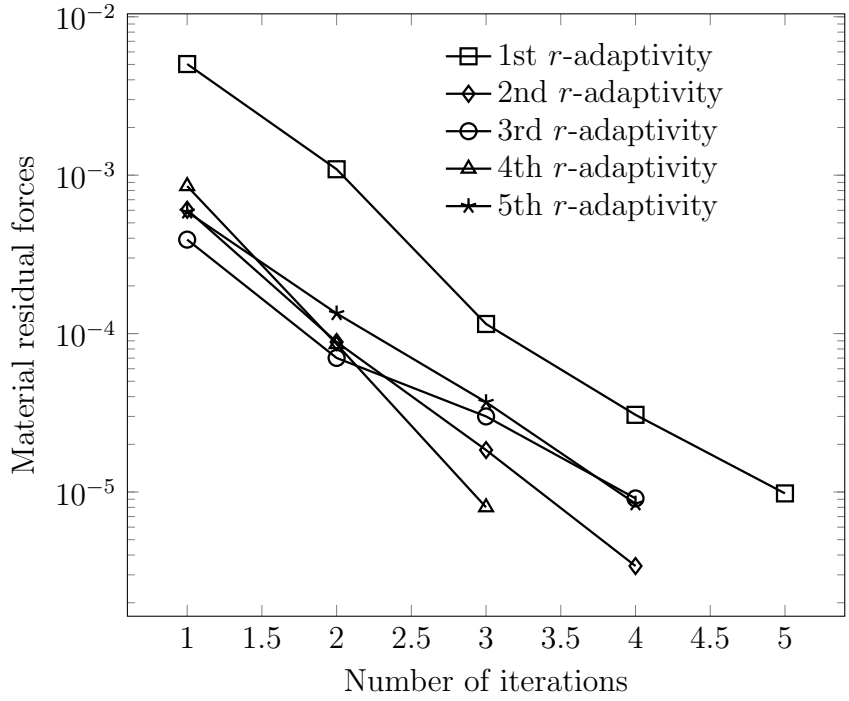

Figure 4.21: Material force residuals in the iteration process of the L-shaped plate with $k = 0.3$.

h-adaptivity is implemented after the first r-process.

For this example, Table 4.2 presents the CPU times for the different adaptive strategies. The time in h-adaptivity is counted from $N_s = 96$ to $N_s = 357$ which includes 4 MEPCM calculations, 4 error estimations and 4 point refinements. Both source and collocation points are refined in each process and basis functions and derivatives are recalculated. This repeated process costs much more CPU time (3 times) than uniform h-refinement but with an accuracy improvement. In r-adaptivity, 408 collocation points are relocated iteratively and compared to uniform refinement, an additional 184s is spent on relocation. The combined adaptive procedure is repeated 4 times which takes more time than the summation of pure h- and pure r-adaptivity since single h- and r-adaptive process are dependent to each other. The error estimation in each adaptivity step relies on the solution obtained from the previous step. However this combined method provides a more flexible way to achieve the best accuracy in contrast to the other three adaptivity processes.

	Initial N_s	Final N_s	CPU time (s)	Final e_g
Uni	408	408	9.12×10^1	3.33×10^{-4}
h	96	357	2.26×10^2	9.84×10^{-6}
r	408	408	2.75×10^2	4.02×10^{-5}
rh	96	511	5.22×10^2	1.85×10^{-6}

Table 4.2: Quantitative results of the L-shaped plate using different adaptivity approaches.

4.8 Concluding remarks

In this chapter, r-, h- and combined rh-adaptive strategies have been investigated and implemented with the MEPCM. The discrete material force residuals act as driven forces in r-adaptivity that implies the imbalance of material equilibrium equation for linear elasticity problems. r-adaptivity results in an optimal distribution of collocation points with minimum total potential energy achieved by collocation point relocation within a certain number of degrees of freedom. h-adaptivity offers a point refinement strategy to achieve better accuracy that reduces error by satisfying the physical equilibrium at more collocation points than at the original arrangement of points. Therefore, a robust error estimate based on the strong form of the governing equations residual and a clear point refinement procedure have been developed. The selection of refinement parameter k value, which has an effect on efficiency of h-adaptivity in terms of accuracy and computational cost, is not identical in h-adaptivity for different analyses. k is dependent on the requirement of prescribed accuracy in adaptivity and the problem geometry with boundary conditions and external loads. Although there is not rigorous rule to define the value of k, it can be suggested by the variation of local errors. A combined adaptive technique has been conducted in which r- and h-adaptivity are repeated in cycles to achieve a prescribed tolerance. Numerical studies are demonstrated to validate the proposed adaptivity strategies. A comparison on convergence characteristics in L_2 norm of relative error and proposed relative error norm on material force residual for the problem with analytical solution indicates that r-adaptivity is more flexible than uniform h-refinement. Meanwhile, another comparison between h-adaptivity and uniform h-refinement verifies that error estimator in h-adaptivity is stable. Both r- and h-adaptivity can achieve better accuracy with higher convergence rates than uniform re-

finement. Finally, two-dimensional problems with and without analytical solutions were examined using the combined rh-adaptivity. Discretisation errors are minimised though the satisfaction of physical and material equilibrium equations at the most points. In addition, the combined rh-adaptivity with the local MEPCM, unlike mesh-based methods, does not suffer from ill-shaped mesh and points connectivity in the updated discretisation. However, the computational cost of using combined rh-adaptivity is more expensive than single adaptive strategies and uniform refinement.

Chapter 5

Geometric non-linearity

5.1 Introduction

A large number of engineering problems are analysed under the assumption of small deformation in which a linear relationship between strains and displacements is assumed when external forces of reasonable magnitudes are applied [200]. However, this assumption may result in a less accurate approximation of the actual response when the structure undergoes large deformations [201]. For this reason, geometric non-linearity (GNL) or finite deformation becomes important, where the assumption of linearity is replaced by a non-linear relationship between strains and displacements, providing more realistic results to a variety of problems such as non-linear truss problems [202], carbon nanotube-reinforced functionally graded panels [203], crystal plasticity [204] and elastic shells [205].

Three descriptions of motion are most often used for finite deformation analyses and an appropriate choice needs to be made. In Lagrangian descriptions, motions follow the movement of each point of a body from the reference state to the current state [206, 207]. Lagrangian descriptions can be split into Total and Updated Lagrangian approaches, where the measures of strain and stress are referred to the reference and current coordinates respectively, resulting in identical results [208]. The key difference between these two formulations is that they are described in terms of different configurations, making differences in numerical efficiency [209]. In Eulerian descriptions of motion the

focus is on specific locations in the spatial coordinates at time t [206]. Co-rotational formulations use coordinate systems that can rotate with the body [210]. Lagrangian descriptions are preferable in solid mechanics because the constitutive behaviour in solids is often presented in terms of material coordinates [211]. The sequence of events in Lagrangian formulations for quasistatic problems (as covered in this thesis) is ordered by the pseudo-time. Eulerian descriptions are most appealing in fluid mechanics since all relevant quantities are referred to the position in space at time t. Co-rotational formulations are relatively less common and have been developed for the analyses of beams and shells, for instance in [210, 212].

The finite element method (FEM) has been used as a conventional way to solve large deformation problems however they are ineffective in handling extremely large deformation owing to severe mesh distortion [213,214]. The arbitrary Lagrangian-Eulerian (ALE) method attempts to circumvent these difficulties by combining the advantages of both the Lagrangian and Eulerian methods. In the method, motion is represented by a set of nodes that are allowed to move arbitrarily within the domain and mesh distortion can be better addressed by the ALE method than a pure Lagrangian or Eulerian method, but additional computational complexities are introduced in this method [215,216]. Given these problems, meshless methods have been seen as ideal tools for large deformation problems. In meshless methods, the physical domain of interest is entirely presented by scattered field points without considering meshes and elements, so the overall analyses are totally free from the issues of mesh entanglement and distortion. This attractive feature has motivated the development of this group of methods in the past 20 years, such as smooth particle hydrodynamics [217, 218], the element-free Galerkin method [219], the meshless local Petrov-Galerkin method [220], the reproducing kernel particle method [221], the meshless max-ent method [222, 223], Galerkin-based methods with max-ent basis functions [109] and the isogeometric meshless method [27, 214, 224–229].

Most meshless methods used in previous research for large deformation problems are in weak forms. Accurate and stable results can be obtained for modelling large deformation problems using these methods but they are computationally expensive because of the use of numerical integration. To challenge this, strong form-based meshless collocation methods have been suggested as they are truly meshless techniques where a

distribution of points only is required, although the literature here is tiny compared to weak form-based approaches. Strong form-based approaches have been extended to large deformation analyses such as for micromechanical structures in [230] and the collocation method of finite spheres was introduced as a meshless technique for real time simulation of surgical processes in [231].

As only a few studies using strong form-based meshless methods focus on large deformation problems, a natural development in this thesis is to apply the point collocation approach with local maximum entropy basis functions developed in Chapter 3 to problems with large deformations. In the development described here a Total Lagrangian description in terms of the reference configuration using a linear Kirchhoff stress-logarithmic strain relationship is adopted, which provides one of the most straightforward ways to implement large deformation elasticity [232]. In Chapter 4, adaptive procedures were demonstrated for the local maximum entropy point collocation method (MEPCM) but only h-adaptivity is employed for large deformation problems in this chapter. r-adaptivity is not used here for large deformation problems considering the computational cost and complexities resulting from solving two sets of non-linear systems for points relocation and recalculation of geometrically non-linear problems, respectively. An existing error estimation procedure for small deformations proposed in Chapter 4 is extended, implemented and demonstrated for large deformation in this chapter. After that, some numerical examples are presented to validate the performance of the proposed method.

5.2 Extending to geometric non-linearity

Consider a reference (undeformed) configuration in an open region Ω_0 using a Cartesian coordinate system. At time $t = 0$, a point $P \in \Omega_0$ is denoted by $\{\bar{X}\} = \{X, Y\}^T$ in two dimensions. The capital indices denote the positions in the reference configuration. As the continuum body deforms to a region Ω in the current (deformed) configuration at time t, the point P is mapped into $p \in \Omega$ at the position $\{\bar{x}\} = \{x, y\}^T$. The spatial

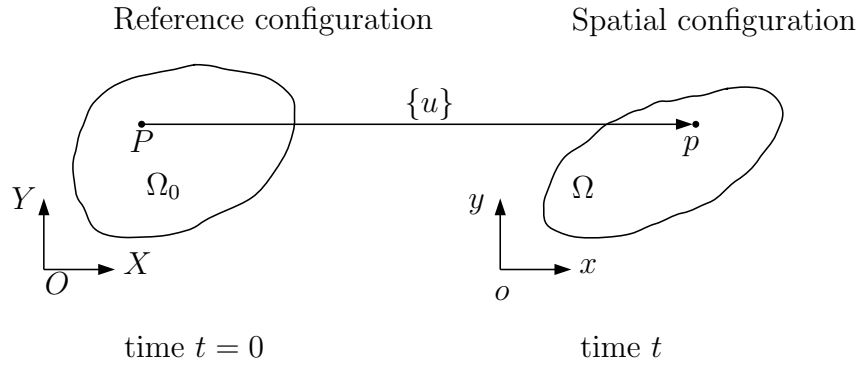

Figure 5.1: Configuration and motion of a continuum body.

position of the material point can be given as a function of pseudo-time through

$$\{\bar{x}\} = \varphi(\{\bar{X}\}, t) \tag{5.1}$$

where φ is the Lagrangian description of the motion of a body. The motion φ is a uniquely invertible function that carries the information of a material point P from the material configuration to p in the current configuration. Conversely, $\{\bar{X}\}$ can be specified uniquely by $\{\bar{x}\}$ at pseudo-time t as

$$\{\bar{X}\} = \varphi^{-1}(\{\bar{x}\}, t) \tag{5.2}$$

where φ^{-1} is the inverse motion. The displacement field of a material point is the difference between its position in the current and the reference configurations as

$$\{u(\{\bar{X}\}, t)\} = \{\bar{x}(\{\bar{X}\}, t)\} - \{\bar{X}\} \tag{5.3}$$

in terms of the reference configuration or alternatively

$$\{u(\{\bar{x}\}, t)\} = \{\bar{x}\} - \{\bar{X}(\{\bar{x}\}, t)\} \tag{5.4}$$

in terms of the current configuration. The vector of displacement in terms of the reference configuration in Eq. (5.3) is chosen in this chapter as a Total Lagrangian formulation is used.

Deformation gradient, which is used as a primary measure of deformation for a continuum body, is a crucial quantity to provide the fundamental link between the reference and current configurations as

$$[F] = \frac{\partial\{\bar{x}\}}{\partial\{\bar{X}\}} = [I] + \frac{\partial\{u\}}{\partial\{\bar{X}\}} \tag{5.5}$$

where $[I]$ is a 2×2 identity matrix in two dimensions and $\frac{\partial\{u\}}{\partial\{\bar{X}\}}$ is the partial derivatives of the displacement vector with respect to $\{\bar{X}\}$ in the reference configuration. Eq. (5.5) involves the partial derivative of an independent variable $\{\bar{x}\}$ with respect to another independent variable $\{\bar{X}\}$, which is ambiguous, so it is noted that $\{\bar{x}\}$ should refer to Eq. (5.1) whenever it appears as mentioned in [207]. Any point in the reference configuration can be mapped into the current configuration by the action of $[F]$. The volume ratio (or Jacobian determinant) J is defined as the volume change between the reference and current configurations as

$$J = \frac{dV}{dV_0} = \det([F]) > 0 \tag{5.6}$$

where dV_0 and dV denote infinitesimal volumes in the reference and current configurations respectively. $\det(\cdot)$ is the determinant of $(\cdot)$.

In geometrically non-linear analyses, multiple strain measures are available as introduced in [233]. By applying the polar decomposition to the deformation gradient, the total deformation can be split into [210, 234]

$$[F] = [R][U] = [v][R] \tag{5.7}$$

where $[U]$ and $[v]$ are, respectively, the right (material) and left (spatial) stretch tensors and $[R]$ is the orthogonal local rotation tensor with $[R]^T = [R]^{-1}$. A pure stretch is obtained when $[R]$ equals the identity matrix $[I]$. The right and left stretch tensors, which measure a change of local shape, are unique, positive definite and symmetric. Using Eq. (5.7), the right and left Cauchy-Green strain tensors, $[C]$ and $[b]$, can be obtained directly from the deformation gradient as

$$[C] = [F]^T[F] = [U]^2, \tag{5.8}$$

and

$$[b] = [F][F]^T = [v]^2, \tag{5.9}$$

respectively, which describe the deformation without rigid body rotation. Although there are many options for strain and stress measures, the logarithmic strain and Kirchhoff stress are chosen in finite deformation analyses throughout this thesis, which extends the use of the small deformation constitutive model to large deformation problems without modification. These strain and stress measures can also provide constitutive models with the same framework for other material behaviour for instance material non-linearity. The logarithmic strain based on the left stretch is defined as

$$[\varepsilon] = \frac{1}{2}\ln([b]) \tag{5.10}$$

in which $[\varepsilon]$ is the spatial logarithmic strain measure. The symmetric Kirchhoff stress $\{\tau\}$ for linear elastic materials can be obtained from the logarithmic strain via a linear relationship as

$$\{\tau\} = [D]\{\varepsilon\} \tag{5.11}$$

where $[D]$ is the conventional linear elastic isotropic material stiffness tensor introduced in Eq. (3.9). As the vector form $\{\varepsilon\}$ is required in Eq. (5.11), four components in the matrix form $[\varepsilon]$ in Eq. (5.10) can be written in a 3×1 vector with a relationship $\varepsilon_{xy} = \varepsilon_{yx}$.

In large deformation problems, stress measures can be defined in terms of the reference and current configurations, corresponding to Total and Updated Lagrangian formulations. As shown in Figure 5.2, the first Piola-Kirchhoff stress component P_{11} is calculated from the undeformed area A_0 and the current area A is used to obtain the Cauchy stress component σ_{11}. The Cauchy stress can also be given by making use of the Kirchhoff stress $[\tau]$, as

$$[\sigma] = \frac{[\tau]}{J} \tag{5.12}$$

with the volume ratio J given in Eq. (5.6). As the matrix form of the Kirchhoff stress is required in Eq. (5.12), all components in Eq. (5.11) τ_{xx}, τ_{yy} and τ_{xy} with a relationship $\tau_{xy} = \tau_{yx}$ in the vector form of the Kirchhoff stress can be written in a matrix form. As

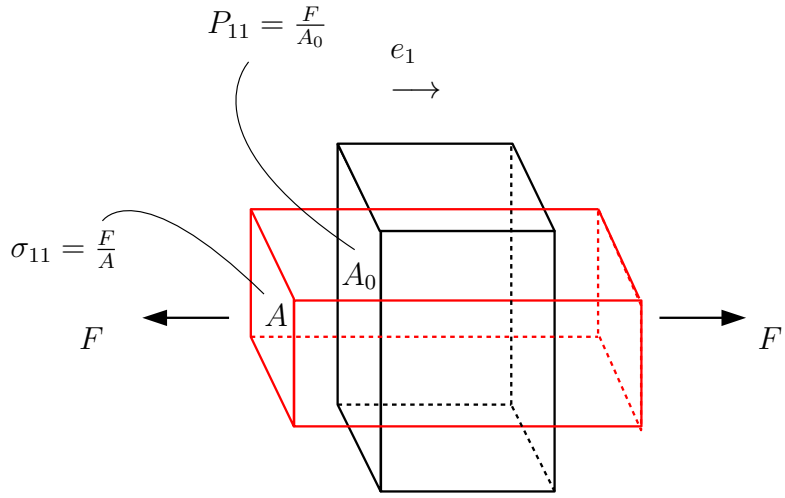

Figure 5.2: Stress components referred to the reference and current configurations.

mentioned in §5.1, the Total and Updated Lagrangian formulations can be transformed to each other, so the two corresponding stress measures can be related by the volume ratio J and the deformation gradient $[F]$ as

$$[P] = J[\sigma][F]^{-T}. \tag{5.13}$$

Although the Cauchy stress is symmetric, it is noted that the first Piola-Kirchhoff stress is, in general, non-symmetric because the deformation gradient is a non-symmetric matrix.

As the Total Lagrangian formulation is selected for large deformation analyses, the first Piola-Kirchhoff stress $[P]$ will be used in the governing PDEs, which will be described in the next section.

5.3 Geometric non-linearity with the local max-ent point collocation method

In this section, the MEPCM with a Total Lagrangian formulation will be detailed for geometrically non-linear problems, named geometrically non-linear MEPCM.

The Total Lagrangian formulation is used for large deformation problems throughout this thesis as the basis functions and their derivatives calculated based on the reference configuration can be reused throughout the analysis. Therefore, the continuous readjustment of basis functions required in the Updated Lagrangian formulation can be avoided here, improving the computational efficiency [212, 235].

The governing PDEs and boundary conditions in terms of the reference configuration are therefore expressed as

$$[L^{NL}]^T\{P\} = \{f^b\} \qquad \text{in } \Omega^0 \tag{5.14}$$

and

$$\{u\} = \{\bar{u}^0\} \ \text{ on } \Gamma_u^0 \ \text{ and } \ [n^0]^T\{P\} = \{\bar{t}^0\} \ \text{ on } \Gamma_t^0. \tag{5.15}$$

where Ω^0 is problem domain in the reference configuration, and Γ_u^0 and Γ_t^0 are the Dirichlet and Neumann boundaries in terms of the reference configuration, respectively. In Eq. (5.14), $[L^{NL}]$ is a matrix of differential operators for two-dimensional large deformation problems

$$[L^{NL}] = \begin{bmatrix} \frac{\partial}{\partial x} & 0 \\ 0 & \frac{\partial}{\partial y} \\ \frac{\partial}{\partial y} & \frac{\partial}{\partial x} \\ \frac{\partial}{\partial x} & \frac{\partial}{\partial y} \end{bmatrix} \tag{5.16}$$

which is different from the differential operators for small deformation problems in Eq. (3.3) because the first Piola-Kirchhoff stress is non-symmetric in general and four components of $[P]$ given in Eq. (5.13) are included in the vector form, i.e. $\{P\} = \{P_{xx}, P_{yy}, P_{xy}, P_{yx}\}^T$. In Eq. (5.14), $\{f^b\}$ is a vector of body forces, $\{u\}$ is a vector of displacements, $\{\bar{u}^0\}$ and $\{\bar{t}^0\}$ are the prescribed displacements and tractions and $[n^0]$ is

the normal matrix to the boundary Γ_t^0 in the reference configuration as

$$[n^0] = \begin{bmatrix} n_x & 0 \\ 0 & n_y \\ n_y & n_x \\ n_x & n_y \end{bmatrix}. \tag{5.17}$$

The superscript zero in Eqs. (5.14) and (5.15) denotes that the variables are defined over the undeformed configuration. Compared with the governing equations and boundary conditions for small deformation analyses, the Cauchy stress is here replaced by the first Piola-Kirchhoff stress in the Total Lagrangian formulation. In the following, the MEPCM will be used to discretise the formulations in Eqs. (5.14) and (5.15) for geometrically non-linear problems.

In PCMs, the governing equations in Eq. (5.14) are applied to all collocation points in the interior of the problem domain and the corresponding boundary conditions in Eq. (5.15) are imposed at the boundary collocation points, leading to a discrete set of equations, as set out in Eq. (3.15). Since three different conditions (governing equations, Dirichlet and Neumann boundary conditions) are applied to collocation points in the interior of the problem domain and on boundaries respectively, three different components which are included in the overall collection of collocation point equations, are rewritten in terms of the exact solution as

$$\{G\} = \{\{G_1\}^T, \{G_2\}^T, \{G_3\}^T\} = \{0\}, \tag{5.18}$$

which is size $2N_c \times 1$ in two dimensions. The three individual components are

$$\{G_1\} = \left\{ \; [L^{NL}]^T\{P\} - \{f^b\} \; \right\}_i \quad i = 1, ..., l \tag{5.19a}$$

$$\{G_2\} = \left\{ \; \{u\} - \{\bar{u}^0\} \; \right\}_j \quad j = 1, ..., m \tag{5.19b}$$

$$\{G_3\} = \left\{ \; [n^0]^T\{P\} - \{\bar{t}^0\} \; \right\}_k \quad k = 1, ..., n \tag{5.19c}$$

respectively, where the variables in each component represent the same meanings as in Eqs. (5.14) and (5.15). Similarly to small deformation analyses presented in Chapter

3, l is the number of collocation points in the interior of the domain, m and n are the remaining numbers of collocation points on boundaries carrying Dirichlet and Neumann boundary conditions. The total number of collocation points covering the domain is $l+m+n=N_c$. All components in the non-linear system $\{G\}$ equal zero with the exact solution. However, the vector of displacements at source points $\{d\}$ cannot always fully satisfy the equation system $\{G\}$, resulting in a non-zero residual vector $\{R\}$ in terms of the displacements at source points $\{d\}$. Similarly to $\{G\}$, there are three components in $\{R\}$. The non-linear relationship between strains and displacements in finite deformation analyses for solid mechanics leads to a non-linear system of equations in terms of the unknown displacements at source points, which cannot be determined directly, therefore a suitable solver is needed.

A Newton-Raphson method is adopted here to linearise the non-linear system and provide the approximations of the solutions to these problems with geometrically non-linearity. Unlike the use of the Newton-Raphson method for r-adaptivity in Chapter 4, it is difficult to obtain a converged solution if the entire load (which could be a traction or a prescribed displacement) is imposed over one step for a large deformation analysis, so the external load is split into load steps. A number of iterations are required over each load step. The vector of incremental displacements at source points $\{\Delta d_{p+1}\}$ over the $(p+1)$th load step is obtained by the summation of the iterative displacements of all iteration steps used in this load step as

$$\{\Delta d_{p+1}\}=\sum_{q=1}^{n^{NR}}\{\delta d^q\} \tag{5.20}$$

where n^{NR} is the total number of iterations to find convergence in the $(p+1)$th load step and $\{\delta d^q\}$ is the vector of iterative displacements in the current qth iteration step. In the $(p+1)$th load step, the unknown iterative displacements in the $(q+1)$th iterative step can be calculated by reducing the problem to a linear system of equations as

$$\{\delta d^{q+1}\}=-[\{R^q_{p+1}\}']^{-1}\{R^q_{p+1}\} \tag{5.21}$$

where $\{R^q_{p+1}\}$ is the residual vector at the previous qth iterative step and $[\{R^q_{p+1}\}']$ is

Jacobian of the residual vector $\{R^q_{p+1}\}$ with respect to the displacements in the qth iterative step $\{d^q_{p+1}\}$ as

$$[\{R^q_{p+1}\}'] = \frac{\partial\{R^q_{p+1}\}}{\partial\{d^q_{p+1}\}}. \tag{5.22}$$

The displacements at source points in the $(p+1)$th load step $\{d_{p+1}\}$ with the incremental displacements in this load step are

$$\{d_{p+1}\} = \{d_p\} + \{\Delta d_{p+1}\} \tag{5.23}$$

where $\{d_p\}$ is the vector of displacements at source points in the pth load step. In Eq. (5.22), the gradients of $\{R_2\}$ and $\{R_3\}$ can be derived easily. The detailed derivation of the gradient of $\{R_1\}$ is given in Appendix B.

A vital component of the Newton-Raphson method is the stopping criterion. The choice of the stopping criterion to signal that enough iterations have been undertaken over each load step of the Newton-Raphson method, has an effect on the accuracy and computational efficiency of this method. In finite deformation analyses with the MEPCM, the terms in the residual vector $\{R\}$ arise from different sources and hence may have significantly different dimensions and significance. Therefore, the choice of stopping criterion must take account of the different sources of residual. For the l collocation points in the interior of the problem domain, at which the governing PDEs must be satisfied, the norm of the residual which is used to set the stopping criterion at each individual collocation point, can be expressed as

$$||R_1|| = \sqrt{\sum_{i=1}^{l}([L^{NL}]^T\{P\} - \{f^b\})_i^2}. \tag{5.24}$$

The residual norms at collocation points on the Dirichlet and Neumann boundaries are given as

$$||R_2|| = \sqrt{\sum_{j=1}^{m}(\{u\} - \{\bar{u}^0\})_j^2} \tag{5.25}$$

and

$$||R_3|| = \sqrt{\sum_{k=1}^{n}([n^0]^T\{P\} - \{\bar{t}^0\})_k^2} \tag{5.26}$$

respectively. As the mixed nature of the sources in the residual norms, the normalised residual is used. In the $(p+1)$th load step, the residual norm for the whole problem in the qth iterative step $||R||_{p+1}^q$ can be obtained as

$$||R||_{p+1}^q = \frac{||R_1||_{p+1}^q}{||R_1||_{p+1}^1} + \frac{||R_2||_{p+1}^q}{||R_2||_{p+1}^1} + \frac{||R_3||_{p+1}^q}{||R_3||_{p+1}^1}. \tag{5.27}$$

In Eq. (5.27), three components of residual norms in the qth iteration step are normalised by the corresponding residual norm in the first iterative step of the same load step. The total residual norm is the summation of the normalised residual norm components. In the Newton-Raphson method, the stopping criterion is defined as

$$||R||_{p+1}^q \leq \eta \tag{5.28}$$

where η is the user-defined tolerance number. The choice of a stopping criterion and the associated user-defined tolerance number η must be done with great care. A typical value of the prescribed tolerance η is set to 10^{-5}.

The performance of the proposed stopping criterion in the Newton-Raphson method will be validated in the numerical examples section.

5.4 h-adaptivity with geometric non-linearity

The idea of h-adaptivity for large deformation analyses can be identical to those small deformation analyses ideally, but they have some differences since load steps are introduced in large deformation analyses and different stress measures are used for problems with geometric non-linearity. The error estimator proposed for small deformations in §4.4 is here extended to large deformations with necessary modifications.

For large deformation problems, h-adaptivity is applied after the initial calculation using all load steps. Error estimators are employed to estimate the local and global errors existed in the solution obtained from the last load step of previous calculation.

The following points refinement is determined by the local error estimators and the global error estimator is used to describe the overall accuracy of the problem. The problem needs to be recalculated from the first load step after the points refinement of h-adaptivity, where the basis functions are constructed based on the refined points distribution.

The local error estimator E_t for large deformation problems is given as

$$E_t = \frac{1}{3} A_t \sum_{g=1}^{3} ||[L^{NL}]^T\{P\} - \{f^b\}||_g \tag{5.29}$$

where $\frac{1}{3}$ is the product of weight and Jacobian of Gauss quadrature, A_t is the area of the tth Delaunay triangulation, $||[L^{NL}]^T\{P\} - \{f^b\}||$ is the L_2 norm of the residual of the strong form-based governing equations described by the Total Lagrangian formulation in terms of the reference configuration in Eq. (5.14) and g is the gth calculation point in the corresponding Delaunay triangulation. The residuals in Eq. (5.29) are evaluated as opposed to the Cauchy stress for the small deformation case (refer back to a previous §4.4). Similarly to small deformation cases, three calculation points are generated in each Delaunay triangulation associated with collocation points. As the calculation points are not used for integration purpose, the choice of the number of calculation points in each Delaunay triangulation can be arbitrary for error estimation. In order to keep balance between effectiveness and computational cost, three calculation points are selected here. The global error estimator E_g is then defined as

$$E_g = \sum_{t=1}^{nt} E_t, \tag{5.30}$$

where t is the index of Delaunay triangulation, nt is the total number of Delaunay triangulations and E_t is the local error estimator given in Eq. (5.29).

The refinement strategy is also the same as that used for small deformation problems. Three new collocation and source points are inserted in each triangulation. Using h-adaptivity in large deformations, basis functions have to be recalculated after the refinement in each h-adaptive step and the nearest points searching is required, which is time-consuming. Compared with weak-form meshless methods, remeshing and numerical

integration are not required in h-adaptive MEPCM for large deformation problems. The efficiency of h-adaptivity for large deformation will be studied in the following numerical examples section.

5.5 Numerical examples

The basic formulation including the kinematics and stress measures for the analysis of large deformation problems using the Total Lagrangian approach in terms of the reference configuration with the MEPCM has been developed in previous sections of this chapter. In this section, some numerical examples that have analytical solutions are analysed to demonstrate the performance of the proposed method. h-adaptivity for large deformation is validated for some of the problems.

5.5.1 One-dimensional bar with h-adaptivity

A one-dimensional bar of unit length ($l_0 = 1$) was modelled as the first example in this section as shown in Figure 5.3(a). The bar was fixed at one end, i.e. $\bar{u}_{x(X=0)} = 0$ and a large deformation prescribed Dirichlet boundary condition was applied to the other end, i.e. $\bar{u}_{x(X=1)} = 1$. The material property was Young's modulus $E = 1000$. According to Eqs. (5.5), (5.9) and (5.10), the analytical solutions for the deformation gradient, left Cauchy-Green strain and logarithmic strain are, respectively

$$F = 1 + \frac{\bar{u}_x}{l_0}, \quad b = (1 + \frac{\bar{u}_x}{l_0})^2, \quad \varepsilon = \ln(1 + \frac{\bar{u}_x}{l_0}) \tag{5.31}$$

where $\bar{u}_x$ is the prescribed displacement at the end of the bar and l_0 is the original length of the bar. Substituting Eqs. (5.11) and (5.12) to (5.13), the first Piola-Kirchhoff stress can be determined using the expression of the deformation gradient in Eq. (5.31) as

$$P_{xx} = E\frac{\ln(1 + \frac{\bar{u}_x}{l_0})}{1 + \frac{\bar{u}_x}{l_0}} \tag{5.32}$$

which can be used to compare with the numerical results.

The geometrically non-linear MEPCM was employed to solve the problem and the

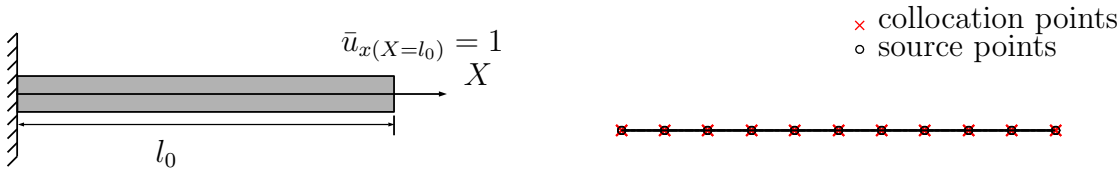

(a) The geometry model. (b) Points distribution.

Figure 5.3: The geometry model and points distributions of the one-dimensional bar problem.

problem domain and boundaries were discretised by 11 collocation and source points placed uniformly as shown in Figure 5.3(b). For each collocation point, the minimum number of source points inside the support domain N_s^* was set as 2 and the local max-ent formulation was used to construct basis functions and derivatives. Nine collocation points inside the domain were set to satisfy the governing PDEs in Eq. (5.14) and the two collocation points at the ends, were set to satisfy the Dirichlet boundary conditions as given in Eq. (5.15). The formed non-linear system of equations was solved by the Newton-Raphson method using 10 load steps with a predefined tolerance number of $\eta = 10^{-5}$. The maximum number of iterations used in each load step was 10. In order to find the iterative displacements in the current iterative step as described in Eq. (5.21), the Jacobian matrix $[R']$ has to be calculated by the derivative of the residual vector $\{R\}$ with respect to the displacements in the previous iterative step. In the formulation of $[R']$ (see Appendix B), all basis functions and derivatives are constructed referred to the reference configuration. As discussed in §5.3, the recalculation of basis functions and derivatives are not required in the overall analysis because the Total Lagrangian formulation is used where all variables are obtained referred to the reference configuration.

For comparison, the analytical and numerical (obtained by the MEPCM with a geometrically non-linear framework) first Piola-Kirchhoff stress P_{xx} in each load step are plotted against displacement u_x in Figure 5.4. It can be seen that both analytical and numerical results follow an almost identical non-linear path. The residual norms in all iterative steps of the first three load steps in the Newton-Raphson method are presented in Table 5.1 where the residual norms $||R||$ calculated by Eq. (5.27) keeps decreasing in each load step until the stopping criterion in Eq. (5.28) is satisfied. Four iterative steps

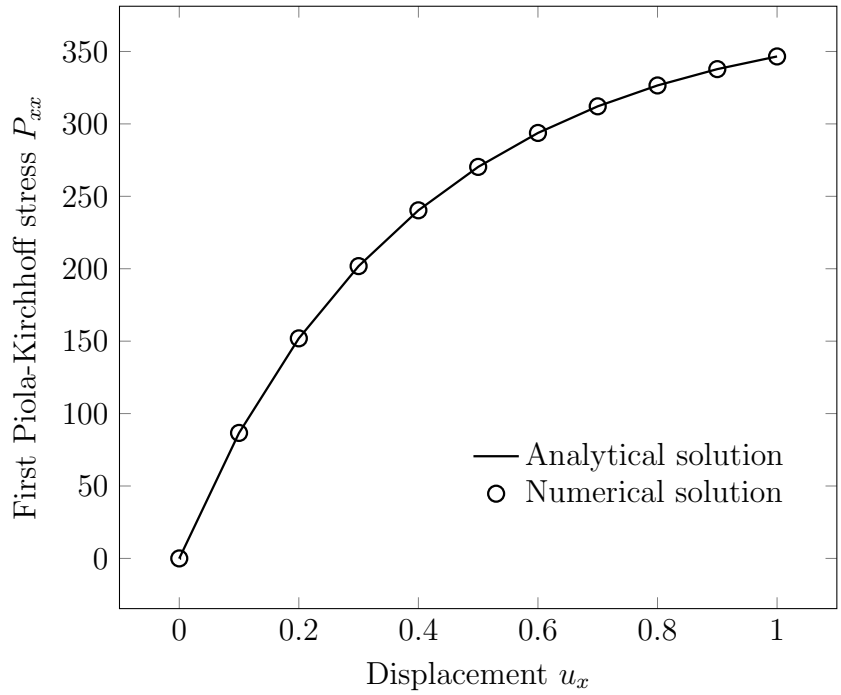

Figure 5.4: First Piola-Kirchhoff stress P_{xx} against displacement u_x of the one-dimensional bar problem.

are required in the first load step and three iterations are needed in the latter two load steps. These residual norms in different load steps show the convergence rate close to 2.0 which is the theoretically optimum value [199].

	Load step		
Iteration	1	2	3
1	2.000×10^{0}	2.000×10^{0}	2.000×10^{0}
2	1.458×10^{-1}	3.907×10^{-2}	2.440×10^{-4}
3	1.132×10^{-3}	3.009×10^{-6}	1.778×10^{-11}
4	9.047×10^{-6}	–	–

Table 5.1: Residual norms of the Newton-Raphson method showing near asymptotic quadratic convergence of the one-dimensional bar problem.

After the initial calculation, h-adaptivity with different values of the local refinement coefficient $k = 0, 0.6, 0.7$ and 0.8 is studied to improve the accuracy of the approximation. Since an analytical solution exists for this problem, the L_2 norm of relative error on displacement $||e||_{L_2}$ with different discretisations are calculated to show the convergence performance of using the geometrically nonlinear MEPCM (as shown in Figure 5.5(a)). The convergence rate for uniform refinement is close to 2.5, which is identical to the convergence rate for linear elasticity using the MEPCM in [114]. In this figure, $||e||_{L_2}$ for

analyses using h-adaptivity, with different values of $k = 0.6, 0.7, 0.8$, are plotted against the degrees of freedom N_s. It can be seen that h-adaptivity with $k = 0.6, 0.7, 0.8$ achieves better convergence rates with lower errors than uniform h-refinement. In the case with $k = 0.6$, more local regions are refined where more new collocation and source points are inserted than in the cases with $k = 0.7$ and 0.8, but $||e||_{L_2}$ using $k = 0.6$ converges slower than using $k = 0.7$ and 0.8 as some of the newly added points are not critical for the convergence. The relative error $||e||_{L_2}$ in the analysis with $k = 0.8$ decreases faster in the first adaptive step but there is degradation in the latter steps. This is likely to be due to not enough new points being added to reduce the discretisation errors from the second step, which makes the adaptivity less efficient. It can be observed that $k = 0.7$ is more efficient in the overall h-adaptivity analysis than the other two choices of the local refinement coefficient k. The global error estimator E_g given in Eq. (5.30) is used to describe the overall accuracy for general problems with or without analytical solutions and here E_g for the analyses with different values of k is plotted against N_s (see Figure 5.5(b)). Similar convergence rates to those plotted for $||e||_{L_2}$ in Figure 5.5(a) are evident although they are measured in different ways.

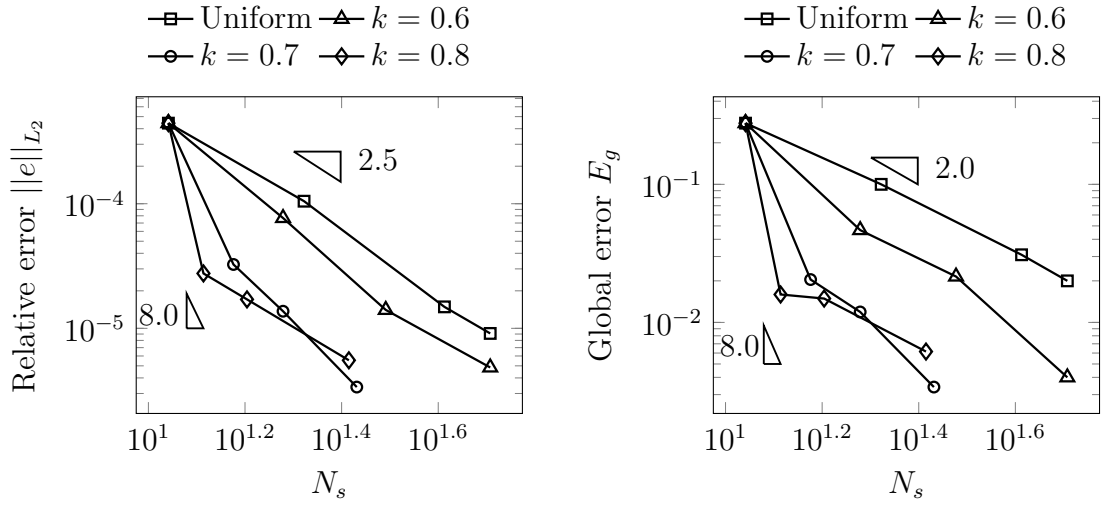

(a) Convergence rate of $||e||_{L_2}$.

(b) Convergence rate of E_g.

Figure 5.5: Convergence rates of $||e||_{L_2}$ and E_g of the one-dimensional bar problem for the analyses with different k.

In order to study the effectiveness of the proposed global error estimator E_g, the

effectivity indices θ (as introduced in §4.4) of using different k values are plotted in Figure 5.6. The effectivity index θ for the analysis with uniform refinement ($k = 0$) keeps increasing in four steps. When $k = 0.6$, the value of θ increases in the third step while θ oscillates around a constant value in other three steps. The values of effectivity indices θ for analyses with $k = 0.7$ and $k = 0.8$ are very close to each other. They are close to a constant in the first two h-adaptive steps and slightly increase in the latter two steps. As it has been discussed in §4.4, the effectivity index θ is expected to oscillate around a constant so that the relative error $||e||_{L_2}$ has the similar convergence rate to the proposed global error estimator E_g. Here it can be analysed that θ in the analyses of using $k = 0.7$ and 0.8 shows oscillations. The proposed global error estimator E_g and the L_2 norm of relative error on displacements $||e||_{L_2}$ show similar convergence rates in adaptive steps.

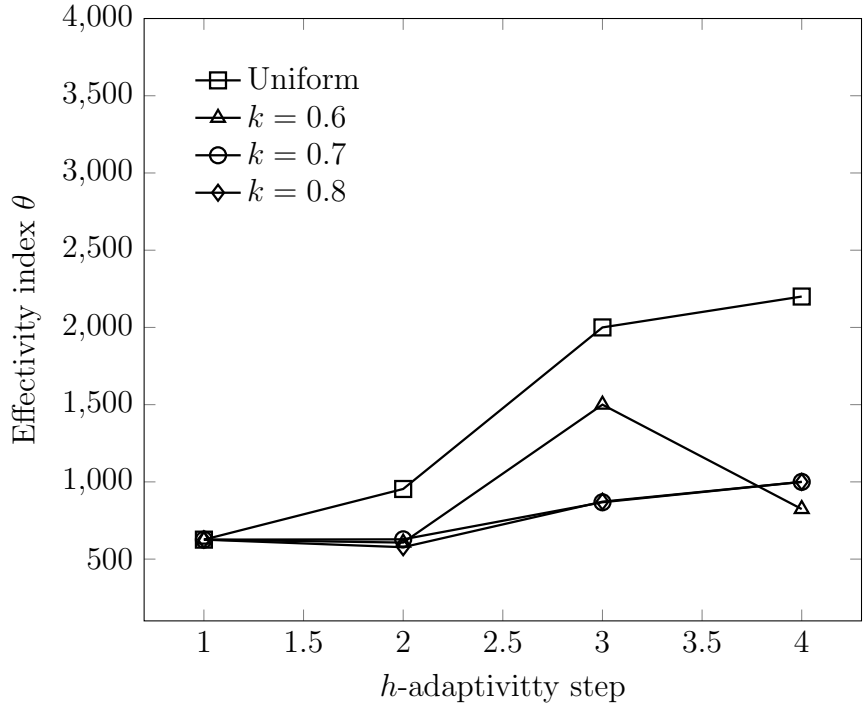

Figure 5.6: The effectivity index θ using h-adaptivity of the one-dimensional bar problem for the analyses with different k.

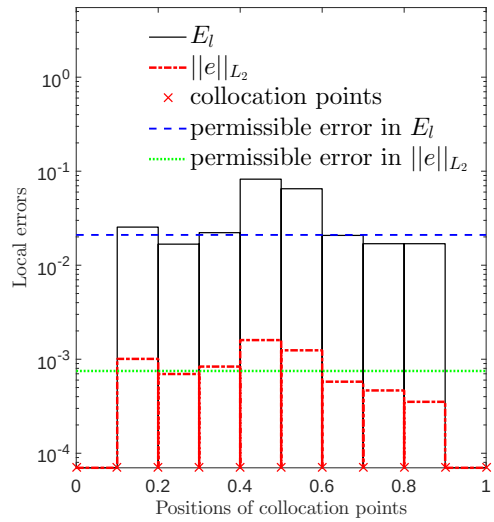

(a) The initial calculation.

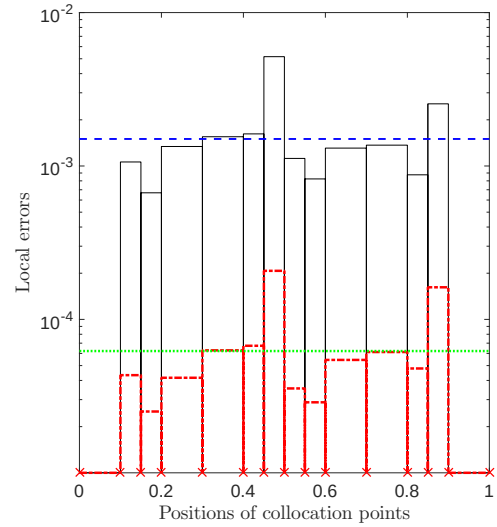

(b) The first h-adaptive step.

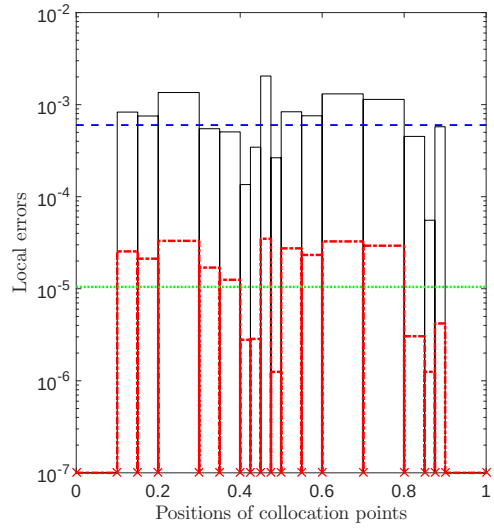

(c) The second h-adaptive step.

Figure 5.7: The collocation points and local error distributions in h-adaptivity with $k = 0.7$ of the one-dimensional bar problem.

It is useful to compare the distributions of the local errors measured by E_l with the L_2 norm of relative error $||e||_{L_2}$ in this simple problem with analytical solution because this comparison can show the performance of the proposed error estimator. The discrete local error distributions of both $||e||_{L_2}$ and E_l in h-adaptivity analysis with $k = 0.7$ are plotted in Figure 5.7. The local lengths in which the local errors are greater than their

permissible errors require further refinement in the following adaptive steps. Figure 5.7 shows that the same local lengths are selected for refinement even though different error measures are used. It is seen that the proposed local error estimator E_l is efficient as the actual error distribution can be estimated by E_l. In the continuous adaptivity steps, the distribution of collocation points become irregular from a uniform distribution in the initial calculation. Although there is not a direct method for choosing an appropriate value of the local refinement parameter k to make h-adaptivity more efficient, it has been analysed in §4.7.1 that the choice of k is based on the variation of the local error estimator across the problem. When k is below a specific value, the same points refinement can be given. For example, the variation of the local error in this example is not apparent, small values of k can lead to the same refinements.

5.5.2 Two-dimensional square domain problems

Two two-dimensional square domain problems are now analysed to validate the performance of the geometrically non-linear MEPCM in two dimensions.

Tension of a square domain

This example is the one-dimensional tension of a two-dimensional plane strain square domain as shown in Figure 5.8(a). The original side length of the square domain was $L_0 = 1$. The material properties used in this example were Young's modulus, E of 1000 and Poisson's ratio, ν of 0.3. Three sides of the square domain were subjected to roller boundary conditions and a prescribed displacement of $\bar{u}_x = 1$ was imposed perpendicular to the fourth edge.

This problem has an analytical solution where the deformation gradient can be simplified into two dimensions with the plane strain condition as

$$[F] = \begin{bmatrix} \frac{L}{L_0} & 0 \\ 0 & 1 \end{bmatrix} \tag{5.33}$$

where L_0 is the original side length and L is the current side length of the two-dimensional domain in x direction. The left Cauchy-Green strain and the logarithmic strain can

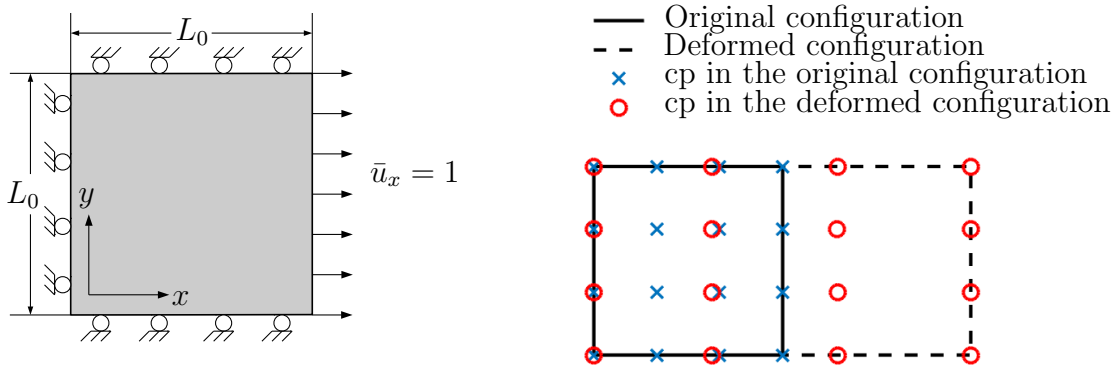

(a) Problem geometry. (b) Original and current configurations.

Figure 5.8: Tension of a two-dimensional square domain: geometry and configurations.

consequently be determined by

$$[b] = \begin{bmatrix} (\frac{L}{L_0})^2 & 0 \\ 0 & 1 \end{bmatrix} \quad \text{and} \quad [\varepsilon] = \begin{bmatrix} \ln(\frac{L}{L_0}) & 0 \\ 0 & 0 \end{bmatrix} \tag{5.34}$$

respectively. A linear elastic constitutive relationship in Eq. (5.11) is employed to obtain the Kirchhoff stress as

$$\{\tau\} = \frac{E(\ln(L) - \ln(L_0))}{(1+\nu)(1-2\nu)} \begin{Bmatrix} (1-\nu) & \nu & 0 \end{Bmatrix}^T \tag{5.35}$$

in a vector form as explained in §5.2 and the first Piola-Kirchhoff stress, which is derived with respect to the reference configuration is given as

$$\{P\} = \frac{E(\ln(L) - \ln(L_0))}{(1+\nu)(1-2\nu)} \begin{Bmatrix} (1-\nu) & \nu\dfrac{L}{L_0} & 0 & 0 \end{Bmatrix}^T. \tag{5.36}$$

There are four components in $\{P\}$ as $P_{xy} \neq P_{yx}$ in general. The shear components in the first Piola-Kirchhoff stress are zero as the prescribed displacement, $\bar{u}_x$ perpendicular to the edge of the square domain is a constant.

Using the geometrically non-linear MEPCM to analyse this large deformation problem, 16 source and collocation points were distributed in the domain and on the boundaries uniformly as shown in Figure 5.8(b). The prescribed displacement boundary condition $\bar{u}_x = 1$ was applied in 10 load steps. The maximum iteration number in each load

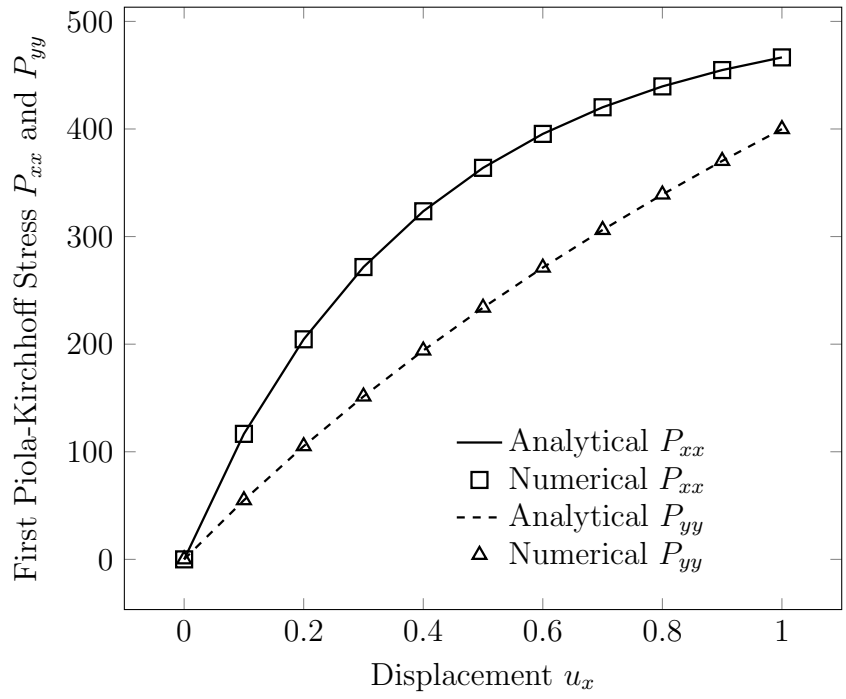

Figure 5.9: Tension of a two-dimensional square domain: first Piola-Kirchhoff stress components P_{xx} and P_{yy} against displacement in x direction u_x.

step was predefined as 10 and the prescribed tolerance number η was 10^{-5}. The deformed configuration for the final load step is shown in Figure 5.8(b). The approximations of the normal components of the first Piola-Kirchhoff stress P_{xx} and P_{yy} are plotted against the displacement in x direction in Figure 5.9. It can be seen that both P_{xx} and P_{yy} show non-linear relationship with displacement and the numerical and analytical results agree even for this very coarse discretisation where P_{xx} shows greater non-linearity because the prescribed displacement was applied in x direction.

To examine the overall performances across the domain (instead of at one point as above) the L_2 norms of relative errors on displacement $||e||_{L_2}$ against an increasing number of degrees of freedom by uniform refinement are shown in Figure 5.10. It can be observed that the order of convergence is greater than 2.0, which agrees with the convergence rate of the MEPCM for small deformations (as indicated in Chapter3).

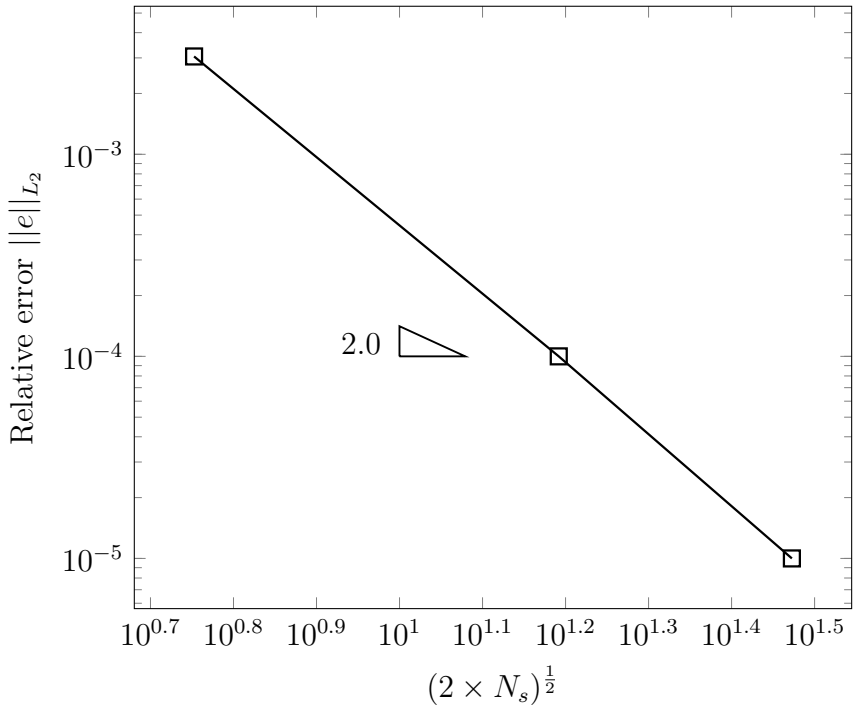

Figure 5.10: Tension of a two-dimensional square domain: convergence rate of $||e||_{L_2}$ with uniform refinement.

A two-dimensional square domain under simple shear with h-adaptivity

This example is a two-dimensional plane strain square domain under simple shear as shown in Figure 5.11. The original side length of the square domain was $L_0 = 1$. The material properties used in this problem were Young's modulus, E of 1000 and a Poisson's ratio, ν of 0.3. The bottom edge was fixed and a roller boundary condition was applied to the top edge. It is noted that the displacement constraints are required for left and right edges since the reference configuration does not deform as expected without any external traction or prescribed displacement. For plane strain analysis, the deformation in the out-of-plane direction is zero, so the current configuration in two dimensions is given as

$$x = X + \frac{\Delta L}{L_0} Y \tag{5.37a}$$

$$y = Y \tag{5.37b}$$

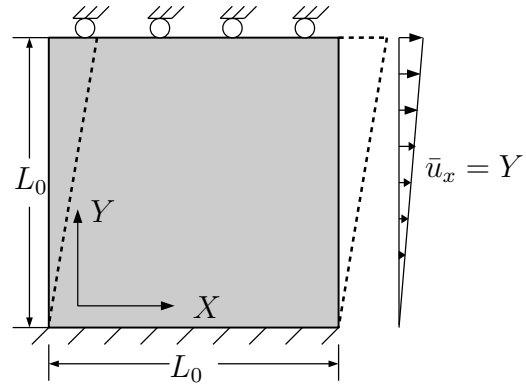

Figure 5.11: Geometry of a two-dimensional square domain under simple shear.

where L_0 is the original side length of the square domain, ΔL is the sheared distance on the top side and is predefined as 25 in this example. The deformation gradient and the left Cauchy-Green strain can be determined as

$$[F] = \begin{bmatrix} 1 & \frac{\Delta L}{L_0} \\ 0 & 1 \end{bmatrix} \quad \text{and} \quad [b] = \begin{bmatrix} 1 + (\frac{\Delta L}{L_0})^2 & \frac{\Delta L}{L_0} \\ \frac{\Delta L}{L_0} & 1 \end{bmatrix} \tag{5.38}$$

respectively and the principal logarithmic strains derived from the left Cauchy-Green strain are

$$\{\hat{\varepsilon}\} = \frac{1}{2}\Big\{ \ln\Big(1 + \frac{(\Delta L)^2}{2} + \Delta L\sqrt{\frac{(\Delta L)^2}{4} + 1}\Big) \quad \ln\Big(1 + \frac{(\Delta L)^2}{2} - \Delta L\sqrt{\frac{(\Delta L)^2}{4} + 1}\Big) \quad 0\Big\}^T. \tag{5.39}$$

In this example, the Cauchy stress equals the Kirchhoff stress due to $J = 1$. With the given value of ΔL, the analytical solution of Cauchy stress can be obtained by using Eqs. (5.10) and (5.11).

The problem was initially modelled using 16 source and collocation points distributed uniformly in the domain and on the boundaries. The prescribed shear deformation (to the top edge) was imposed over 40 load steps, the maximum number of iterations in each load step was set as 10 and a tolerance number, $\eta = 10^{-5}$ was used in the Newton-Raphson method. The analytical and numerical MEPCM results for the Cauchy stress components σ_{xx} and σ_{xy} are plotted against displacement in x direction u_x in Figure 5.12(a) where the non-linear stress-displacement relationship can be clearly observed.

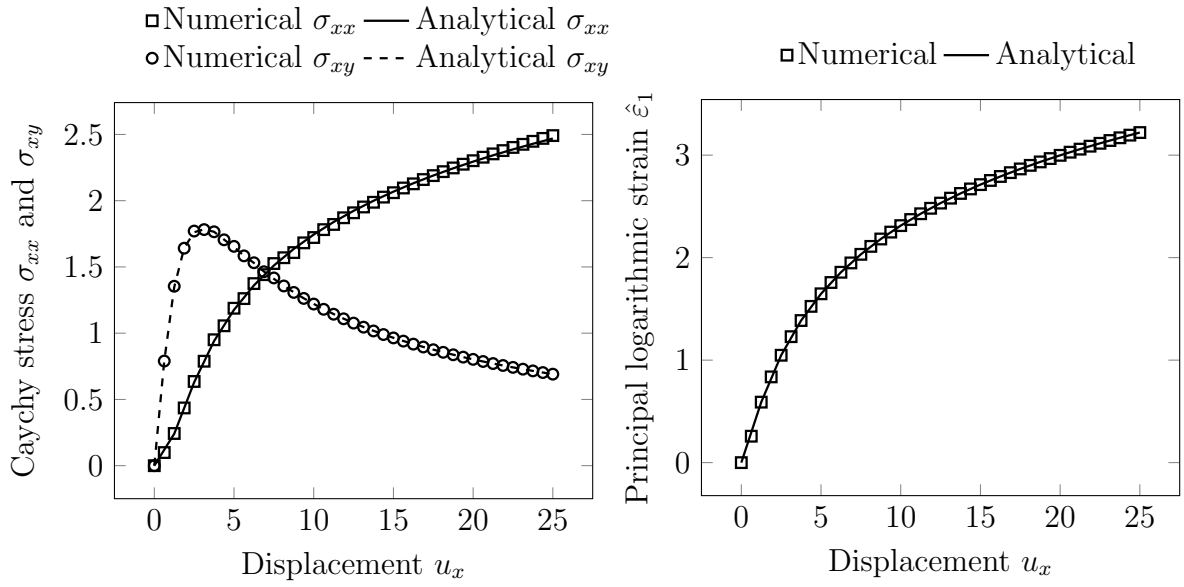

(a) Cauchy stress components σ_{xx} and σ_{xy} against displacement in x direction u_x.

(b) Principal logarithmic strain component $\hat{\varepsilon}_1$ plotted against displacement in x direction, u_x.

Figure 5.12: Cauchy stress and principal logarithmic strain components against displacement of the top boundary in x direction, u_x of the two-dimensional square domain under simple shear.

The shear component of the Cauchy stress, σ_{xy} increases initially before reaching a maximum and then decreases gradually, the explanation being that the change of cross section area has an effect on the values of σ_{xy}. It is observed that the numerical results show in general good agreement with the analytical solution components. In Figure 5.12(b), the numerical and analytical principal strains are plotted against displacement in x direction, in which the geometrically non-linear behaviour is clear. The MEPCM results again show good agreement with the analytical solution.

The reference configuration and the current configuration for the first load step with discretisations are shown in Figure 5.13(a). As the shear component of the Cauchy stress σ_{xy} shows greater non-linearity, the relative error e_σ of the Cauchy stress component σ_{xy} is measured by

$$e_\sigma = \left| \frac{\sigma^h_{xy} - \sigma^e_{xy}}{\sigma^e_{xy}} \right| \tag{5.40}$$

where σ^h_{xy} and σ^e_{xy} are the approximated and exact solution respectively. A plot of e_σ using the same discretisation as in Figure 5.13(a) is shown in Figure 5.13(b) where the

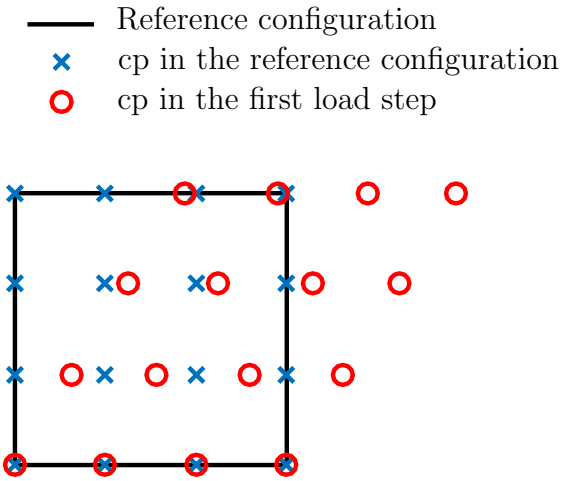

(a) The reference and current configurations.

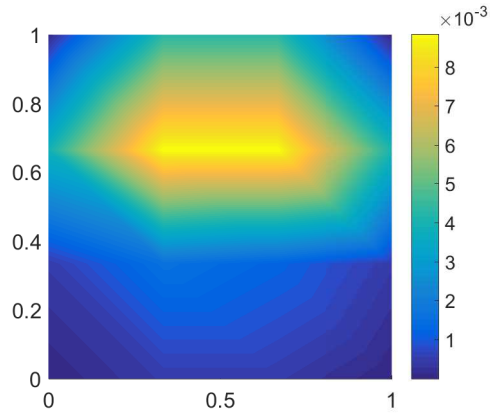

(b) The relative error of the Cauchy stress component σ_{xy}.

Figure 5.13: Configurations and relative error of Cauchy stress error component σ_{xy} of the two-dimensional square domain under simple shear.

errors on boundaries are lower than that of the problem domain because three sides are restrained by Dirichlet boundary conditions and the other side is restrained in Y direction. Although the stress field is a constant over the domain and on the boundaries of this two-dimensional square domain under simple shear, the relative error of Cauchy stress component σ_{xy} is not uniformly distributed. The highest relative error is around 8 times of the error on boundaries. The governing PDEs are only enforced at individual collocation points to formulate the linear system in terms of the displacement at source points. The different discretisation errors at these source points give different distributions of stress error.

Figure 5.14 shows the L_2 norm of relative error on displacement $||e||_{L_2}$ for overall problem at the last iterative step of each load step against the displacement of the top boundary, where staggered decreases of $||e||_{L_2}$ can be seen with an increasing displacement in the first 20 load steps. It seems that some oscillations occur in the numerical solution. The satisfaction of the stopping criterion could be a possible reason. The residual norm $||R||_p^{n^{NR}}$ of the last iteration step at each load step is plotted in this figure where all residual norms converge to the prescribed tolerance number $\eta = 10^{-5}$ but in different order of magnitude. It is observed that in the first 20 load steps, the values of $||e||_{L_2}$ at odd load steps are higher than the values at their next steps (even steps). The

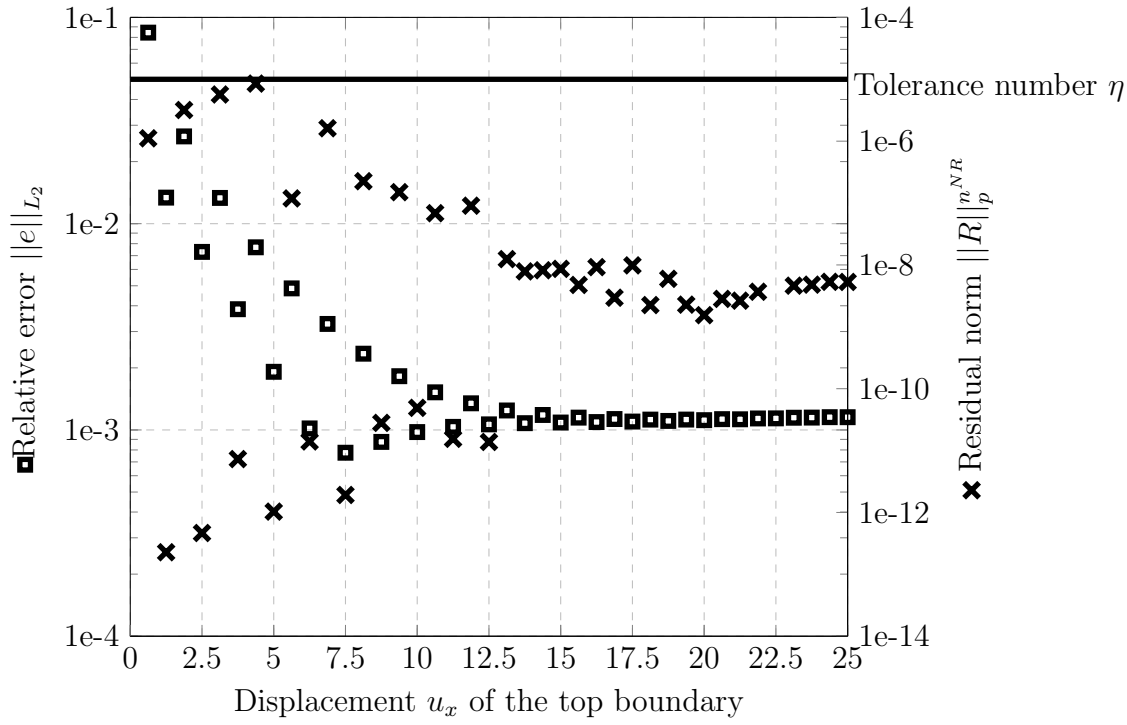

Figure 5.14: L_2 norm of relative error $||e||_{L_2}$ and the residual norm $||R||_p^{n^{NR}}$ in each load step of the Newton-Raphson method against displacement of the top boundary of the two-dimensional square domain under simple shear.

corresponding values of residual norms at these odd load steps are in the range between 10^{-8} and 10^{-5} while those at even load steps between 10^{-13} and 10^{-10}. It is explained that a smaller error norm can be obtained if the residual norm is much lower than the prescribed tolerance number in the stopping criterion. Although there is not a strict value for tolerance number, it is obvious that a smaller η gives more accurate results with higher computational cost. Tolerance number should be chosen considering the balance between accuracy and computational cost. In the following 20 load steps, $||e||_{L_2}$ stays around a constant value, where the oscillations disappear. The residual norms in the latter 20 load steps do not converge to a constant, but their oscillation is reduced to a small range, leading to similar accuracy in these load steps. It is summarised that the value of the residual norm indicates the accuracy at corresponding load step.

The non-zero residual norms at all iterative steps in the Newton-Raphson method for the first 3 load steps are selected here to show the convergence behaviour (see Table 6.1). The stopping criterion proposed in §5.4 is adopted. The asymptotically quadratic convergence exhibited here indicates a correct implementation. In order to validate the

performance of the proposed stopping criterion in the Newton-Raphson method, the residual norms $||R||$ at boundaries, in the interior of the problem domain only and for the overall problem are plotted separately for comparison as shown in Figure 5.15. It can be seen that the normalised residuals on the boundary and in the interior of the problem domain only converge at a rate of 2.0, which is the same with the convergence rate for overall problem.

	Load step		
Iteration	1	2	3
1	2.000×10^{0}	2.000×10^{0}	2.000×10^{0}
2	1.193×10^{-2}	5.436×10^{-1}	9.941×10^{-2}
3	1.112×10^{-6}	3.565×10^{-5}	6.189×10^{-6}
4	–	2.276×10^{-13}	–

Table 5.2: Residual norms of the Newton-Raphson method showing near asymptotic quadratic convergence of the two-dimensional square domain under simple shear.

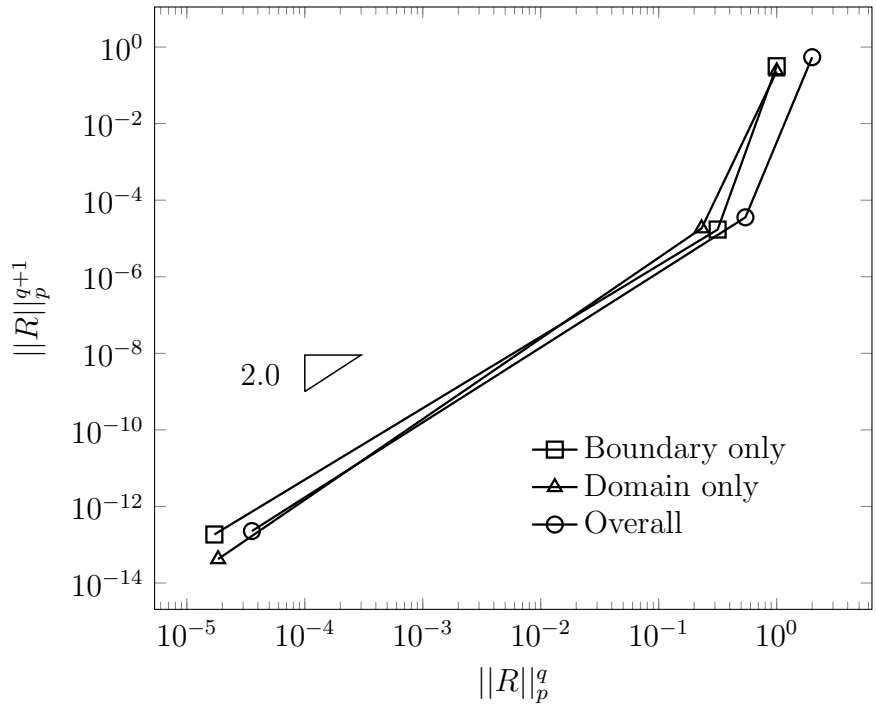

Figure 5.15: Convergence rate of residual norms in the second load step of the Newton-Raphson method of the two-dimensional square domain under simple shear.

To examine the convergence behaviour of h-adaptivity for this two-dimensional square domain under simple shear, the L_2 norm of relative error on displacement $||e||_{L_2}$ against an increasing number of degrees of freedom for uniform refinement and h-adaptivity with

various local refinement coefficient k=0.25, 0.4, 0.5 and 0.6 is presented in Figure 5.16(a). The convergence rate of $||e||_{L_2}$ using uniform refinement ($k = 0$) is close to 2.0 and it is observed that h-adaptivity with k=0.25, 0.4, 0.5 and 0.6 gives better convergence rates with lower errors than using uniform refinement (the case with k=0). As the numbers of newly added points in the first adaptive step are the same for all k values, $||e||_{L_2}$ values are the same in this adaptive step. However, in the latter adaptive steps performances diverge and k=0.5 achieves better efficiency than the other cases. The global error estimate E_g of this problem using the same values of k as in Figure 5.16(a) is plotted in Figure 5.16(b). It can be seen that the global error estimator E_g converges at the same rate as the $||e||_{L_2}$. In this example, the value k=0.5 is chosen as a more efficient local refinement parameter than using the other values in h-adaptivity, which is different from the optimal k value for the one-dimensional bar problem, as the variations of local errors in these two problems are not identical. A smaller k value used in this example than in the one-dimensional bar problem, which indicates that the variation of the local errors across the problem domain in this example is in a wide range.

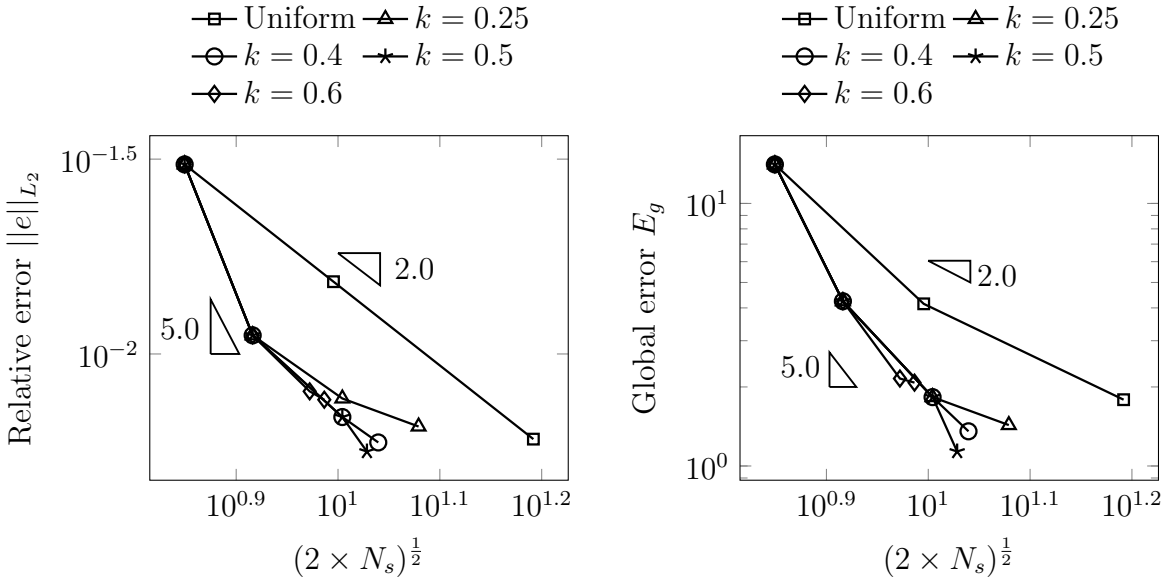

(a) Convergence rate of $||e||_{L_2}$.

(b) Convergence rate of E_g.

Figure 5.16: Convergence rate of $||e||_{L_2}$ and E_g of the two-dimensional square domain under simple shear for the analyses with different k.

Figure 5.17 shows the distributions of collocation points in the successive h-adaptive steps. The regular distribution of collocation points becomes irregular as some new

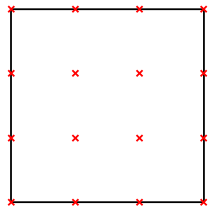

(a) The initial distribution.

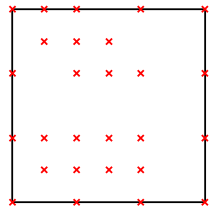

(b) The first h-adaptive step.

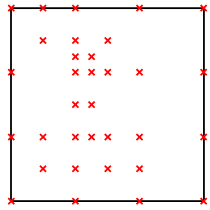

(c) The second h-adaptive step.

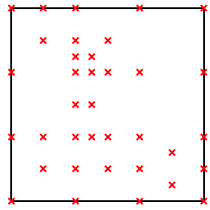

(d) The third h-adaptive step.

Figure 5.17: The collocation point distributions using h-adaptivity with $k = 0.5$ of the two-dimensional square domain under simple shear.

collocation points are inserted into local regions with relatively high errors. It can be seen, the newly added points are mainly located in the interior of the two-dimensional square domain away from boundaries as the errors on boundaries are relatively small. The distributions of collocation points gradually become non-symmetric as the error distributions are non-symmetric caused by the prescribed displacement. In the first h-adaptive step, new collocation points are added near top and bottom edges, which have shear displacement and zero displacement respectively. In the following second and third adaptive steps, some local regions near the top edge are refined again, where the relative error in the Cauchy stress component is higher than the other areas by recalling Figure 5.13(b). The differences of stress distributions in this example are not significant, so it is not clearly measurable to determine the areas that need more points.

5.5.3 Plate and beam problems with large deformation

Plate and beam problems with finite deformation are classical problems for numerical validation, for which some analytical solutions are available (e.g. those available in [236]).

Compared with the examples studied above, the resulting shear stress distributions for plate and beam problems show singularities at the constraint end, leading to a significant adaptive refinement in this area. Here, they are used to further demonstrate the performance of the geometrically non-linear MEPCM with h-adaptivity.

Uniformly distributed load and fully fixed ends

This is effectively a plane strain plate subjected to a uniformly distributed load q and fully fixed at two ends. Since the structure is symmetric, only half of the plate was simulated. Figure 5.18 shows the geometry with the boundary conditions of this problem, where dimensions were length $L = 10$ and thickness $H = 0.2$. Since this is plane strain, the width of the plate out of the plane of the diagram, was taken as being unity. The elastic material properties were Young's modulus, $E = 1 \times 10^7$ and Poisson's ratio, $\nu = 0.2$ and the uniformly distributed load, $q = 40$. The half of the plane strain plate was fully fixed at the centre point of left-hand end and above and below the centre point at this end were restrained by roller boundary conditions. At the truncation end, roller boundary conditions were applied. This plane strain plate problem has previously been used to validate the performance of the FEM using an Updated Lagrangian formulation and the max-ent basis fucntion-based method in [237] and [136], respectively. The analytical solution for the deflection can be found in [237].

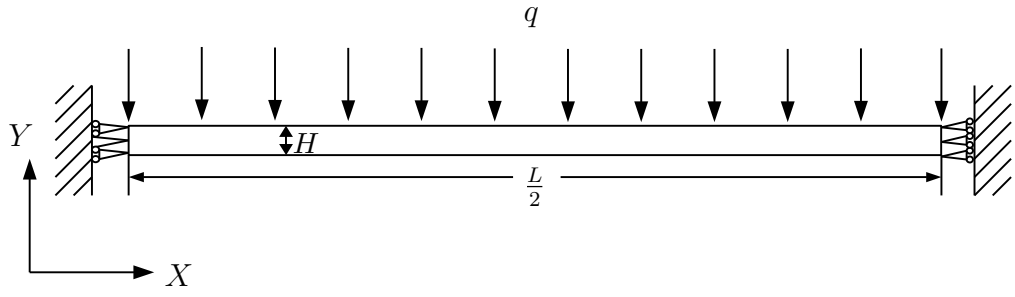

Figure 5.18: Geometry and boundary conditions of the plate with uniformly distributed load, q and fixed at two ends.

To solve this problem, 63 (21×3) source and collocation points were distributed in the problem domain and on the boundaries. The centre collocation point at the left-hand end was subjected to zero displacement boundary condition in both x and y directions.

Roller boundary conditions were applied to the other two collocation points at this end and the three collocation points at the truncation end. The uniform pressure q was applied over 20 equal load steps. In the Newton-Raphson method the maximum iteration number was 10 and the tolerance η was set as 10^{-5}. The initially undeformed and the final deformed configurations with collocation point distributions are shown in Figure 5.19. As the displacement in y direction, u_y is much larger than the deformation in x direction, the color in this figure shows the displacement, u_y of this plate with uniformly distributed load, q, and fixed at two ends. The positive direction is defined in Figure 5.18, so u_y for this problem is negative as indicated by the colourbar where the scale of displacement is the same as the geometry. It can be seen that the maximum deflection at the right-hand side end is near -0.12 , which is over the half of the thickness of the plate. The deformation at the left-hand side is zero.

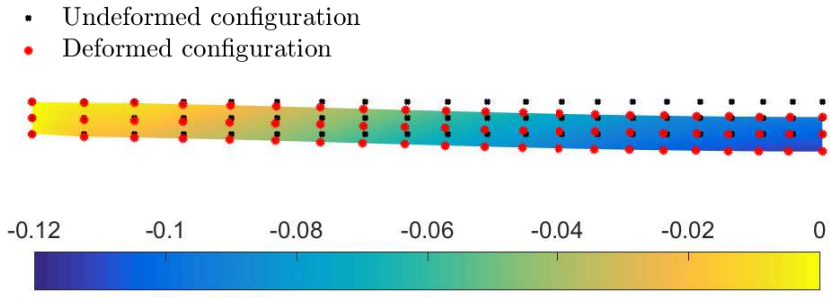

Figure 5.19: The reference and current configurations with displacement u_y of the plate with uniformly distributed load, q, and fixed at two ends.

Comparison of the uniformly distributed pressure, q versus the normalised displacement, $\frac{u_y}{H}$ relationship between analytical and numerical solutions is given in Figure 5.20. The non-linear relationship between the uniformly distributed load and normalised displacement can be observed in Figure 5.20 and the numerical results are in agreement with the analytical solution.

The residual norms of the Newton-Raphson method in three selected load steps are presented in Table 5.3 where the quadratic convergence rates indicate the correct imple-

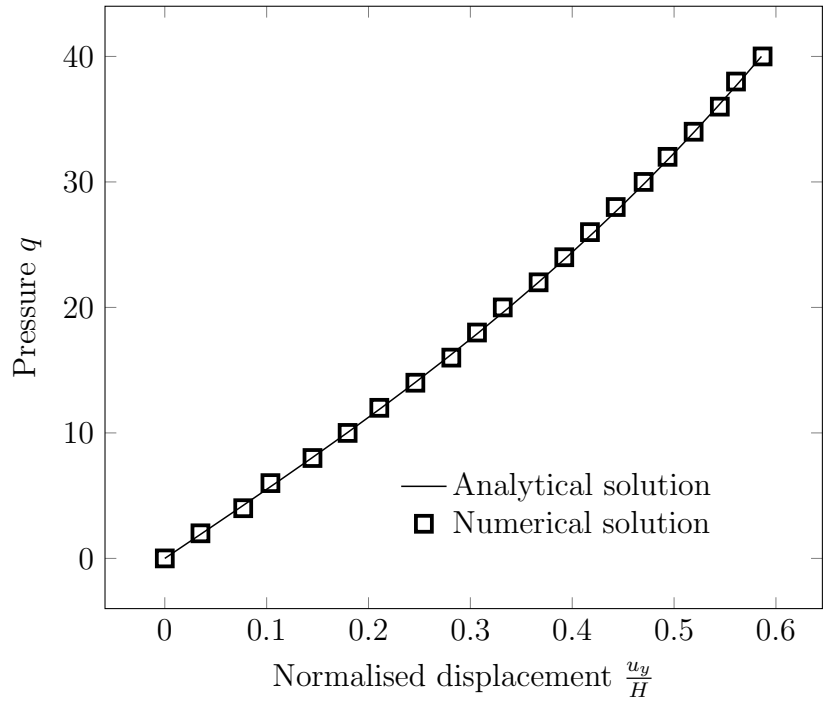

Figure 5.20: Pressure versus normalised displacement of the plate with uniformly distributed load, q, and fixed at two ends

mentation of the non-linear solver. The stopping criterion proposed in §5.4 are adopted and the residual norms in the iterative steps of the Newton-Raphson method satisfy the stopping criterion within three or four iterative steps in all load steps. As three conditions (governing equations and two different boundary conditions) are employed in this example, the normalised residual norm in the first iterative step is 3.0.

	Load step		
Iteration	1	10	20
1	3.000×10^{0}	3.000×10^{0}	3.000×10^{0}
2	3.536×10^{-1}	9.803×10^{-2}	4.011×10^{-2}
3	3.483×10^{-3}	9.393×10^{-6}	5.965×10^{-6}
4	5.819×10^{-7}	–	

Table 5.3: Residual norms in the Newton-Raphson method showing near asymptotic quadratic convergence of the plate with uniformly distributed load, q, and fixed at two ends.

Uniformly distributed load and simple supported ends

The plane strain plate subjected to a uniformly distributed load q with simple supports is analysed. Similarly to the previous example, one-half was taken for simulation. The

problem geometry and the boundary conditions are shown in Figure 5.21. The same dimensions and material properties as used in the last example were used but different boundary conditions were applied on this plate problem with uniformly distributed load and simple supported ends. The centre point at the left-hand side was fully fixed and roller boundary conditions were applied to the right-hand side. The analytical solution of the deflection of this plate problem can be found in [237].

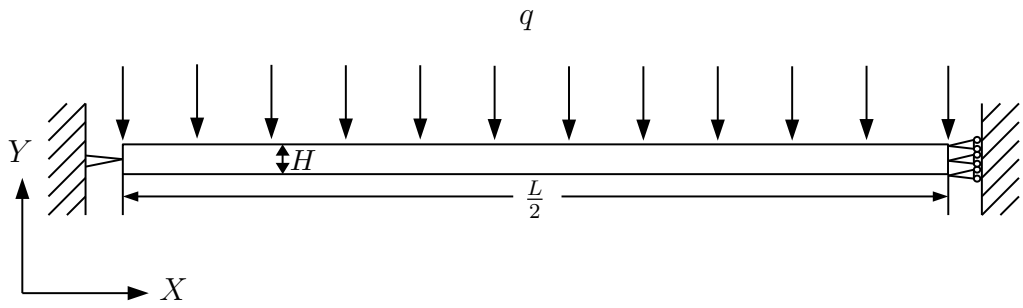

Figure 5.21: Geometry of the plate with uniformly distributed load, q, and simple supported ends

The total number of 153 (51×3) source and collocation points were distributed in the problem domain and on the boundaries. The boundary conditions were imposed at the collocation points at the ends and the uniform pressure q was applied over 20 equal load steps. The maximum number of iterations in the Newton-Raphson method was 10 and the predefined tolerance η was 10^{-5}. The undeformed and deformed configurations with collocation point distributions are shown in Figure 5.22. Similarly to the plate problem with fully fixed ends, the colour in this figure indicates the displacement in y direction, u_y. The colourbar provides the value of displacement with the same scale as the geometry. The maximum deflection at the right-hand side of this simply supported plate is around -0.2, which is the thickness of the plate. Compared with the last example, the deformation for in this problem is larger as the plate with fixed ends has more constraints on boundaries.

Comparison of the uniformly distributed pressure, q versus the normalised displacement, $\frac{u_y}{H}$ relationship between analytical and numerical solutions is given in Figure 5.23. The non-linear relationship between the uniformly distributed load and normalised displacement can be observed in Figure 5.23 and the numerical results once again there is

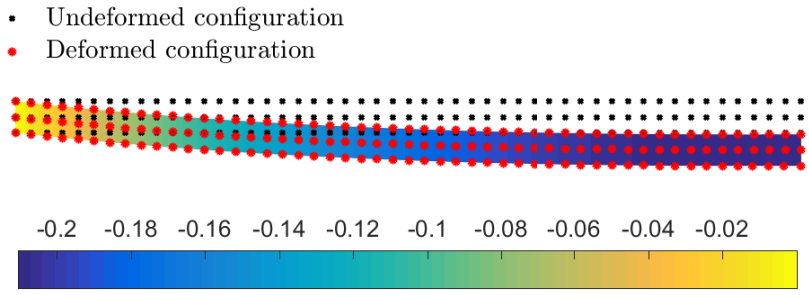

Figure 5.22: The reference and current configurations with displacement u_y of the plate with uniformly distributed load, q, and simple supported ends.

excellent agreement with the analytical solution. With the same externally applied load, it can be seen that the deflection in this figure is more pronounced than in Figure 5.20.

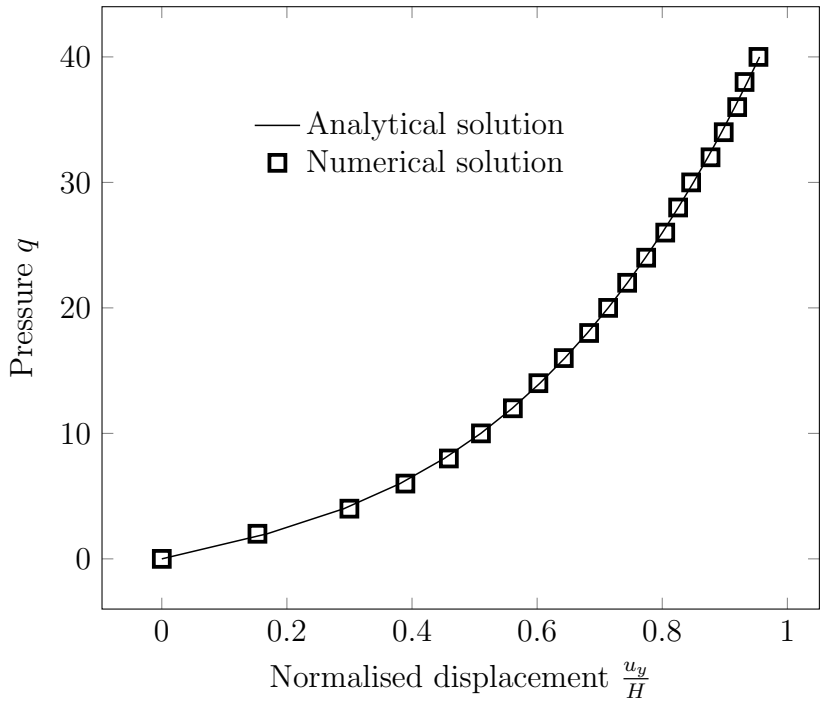

Figure 5.23: Pressure versus normalised displacement of the plate with uniformly distributed load, q, and simple supported ends.

Beam bending with large deformation and h-adaptivity

While it is important to take account of geometric non-linearity in the two beam bending problems above the displacement is not extremely large compared to the thickness of the

plane strain beams. In order to thoroughly test the geometrically non-linear MEPCM, a cantilever beam bending under uniformly distributed load with very large displacement is studied, and here h-adaptivity is used to improve the accuracy of the solution efficiently. The problem model with the boundary conditions is shown in Figure 5.24. The problem was solved with $L = 10$, $B = 1$, $H = 1$, Young's modulus $E = 12000$ and Poisson's ratio $\nu = 0.2$. A load, $q = 10$ was applied on the top edge of the beam. Note that throughout the analysis, this uniformly distributed load, does not change its direction and magnitude, and is independent of the deformation. The centre point of the left-hand side was fully fixed and roller boundary conditions were applied to points above and below the centre point. The right-hand side of this beam was free. The analytical solution for this problem starts from the Euler-Bernoulli bending theory and was derived in [238].

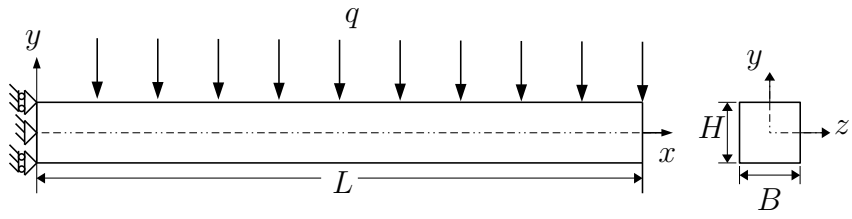

Figure 5.24: Geometry of the elastic cantilever beam problem with uniformly distributed load.

In the analysis, 3×33 collocation and source points were distributed uniformly in the domain and on the boundaries. The middle collocation point at the fixed end was fully fixed and roller boundary conditions were applied to the other two collocation points at this end. Define a load parameter to convert the external load dimensionless as

$$K = \frac{qL^3}{EI} \tag{5.41}$$

where I is the moment of inertia of the cross section

$$I = \frac{BH^3}{12}. \tag{5.42}$$

The total pressure was applied in 50 load steps. The prescribed tolerance, η was set

as 10^{-5}. The uniform pressure was applied to collocation points on the top edge. As mentioned in §5.3, the basis functions and derivatives associated with source points, which are used throughout the analysis, are constructed based on the initial distribution of points because that all variables in the Total Lagrangian formulation are referred back to the reference configuration.

The undeformed configuration at the beginning of the simulation and deformed configuration of the beam at the end of the analysis are shown in Figure 5.25 where a clear large deformation can be observed. Again, the colours in this figure shows the displacement in y direction, u_y. The colourbar indicates the value of displacement with the same scale as the geometry. Compared with the last two beam problems, the deformation for this beam bending problem is significant.

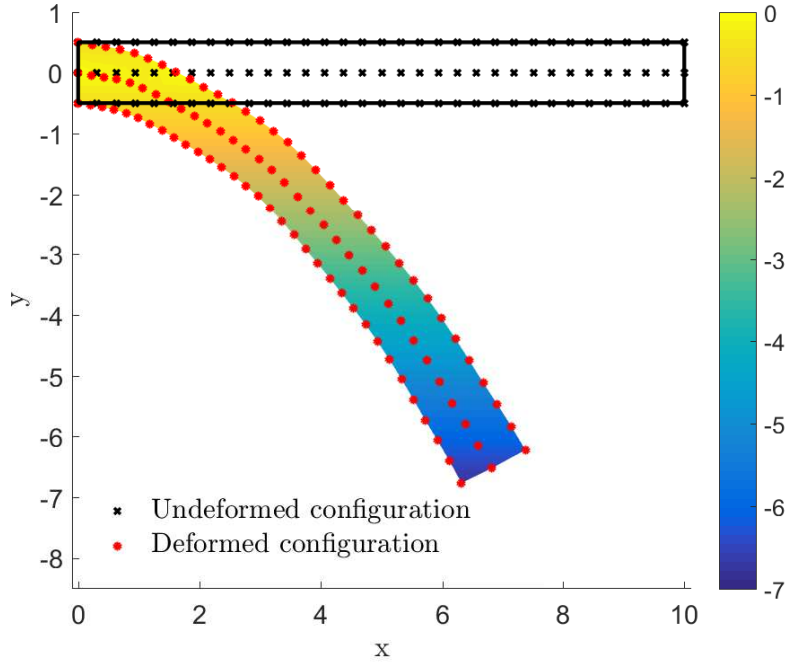

Figure 5.25: The reference and current configurations with displacement u_y of the elastic cantilever beam problem with uniformly distributed load.

The residual norms in selected load steps are presented to show the convergence performance of the Newton-Raphson method in Table 5.4. In these selected load steps, the stopping criterion are satisfied within three steps and the convergence rate of error norms is close to 2.0, which is the theoretical value.

	Load step		
Iteration	1	26	50
1	3×10^{-0}	3×10^{0}	3×10^{0}
2	5.793×10^{-2}	3.713×10^{-2}	4.707×10^{-2}
3	3.597×10^{-6}	8.582×10^{-6}	2.968×10^{-6}

Table 5.4: Residual norms in the Newton-Raphson method showing near asymptotic quadratic convergence of the elastic cantilever beam problem with uniformly distributed load.

Figure 5.26 shows the load parameter K against the honrizotal and vertical displacements at the middle point of the free end normalised by the length of the beam. The analytical solution provided in [238] is also given for comparison. It can be seen that the load parameter and the normalised displacement have a non-linear relationship and the MEPCM results agree well with the analytical solution.

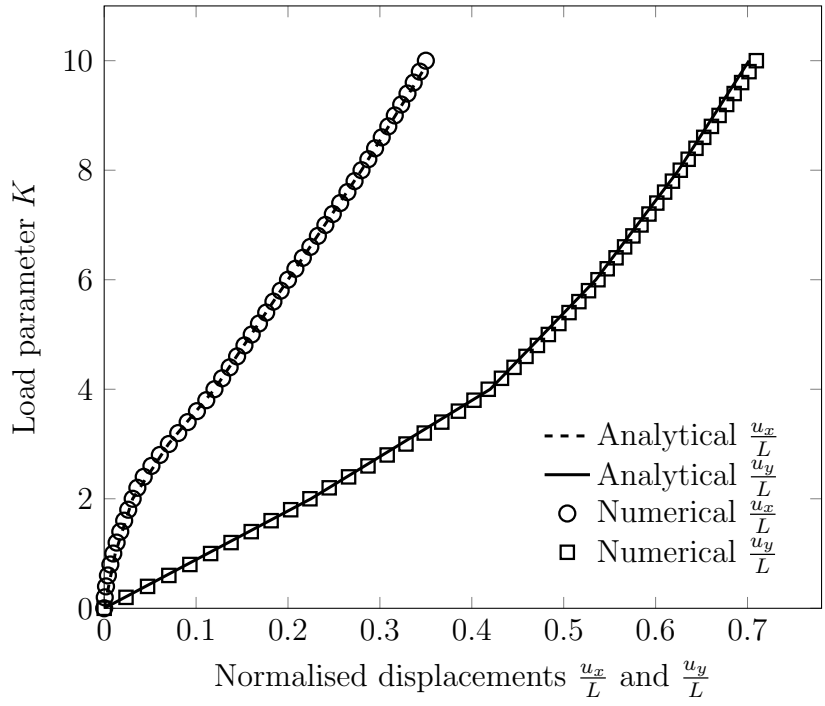

Figure 5.26: The load parameter K against normalised displacements, $\frac{u_x}{L}$ and $\frac{u_y}{L}$, at the mid-depth point at the end of beam of the elastic cantilever beam problem with uniformly distributed load.

Finally, h-adaptivity is applied after all load steps of the initial calculation for this beam bending problem and the local refinement parameter $k = 0.5$ is chosen. The local error estimator E_t is used to estimate the local error in each Delaunay triangulation, which is constructed based at originally distributed collocation points as shown in Figure

5.27(a). Three calculation points are generated in each triangle given in Figure 5.27(b) to estimate the local error estimators, which are used in the following points refinement. The problem needs to be recalculated using the new discretisation from the first load step. The distributions of collocation points in the first and second h-adaptive steps are shown in Figure 5.27(c)-5.27(d) where new collocation points are added close to the fixed end as expected. In Figure 5.27(c), all new collocation points are inserted close to the fixed end of the beam. In the second step (see Figure 5.27(d)), although all new points are added close to the fixed end, most of them are located near the two corners where the singularities occur. The global error estimator E_g is presented to

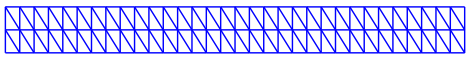

(a) The generation of Delaunay triangulations after the initial calculation.

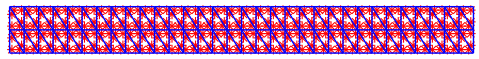

(b) The generation of calculation points in Delaunay triangulations for error estimation in the first h-adaptivity.

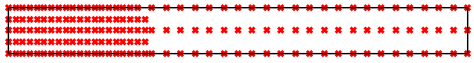

(c) The distribution of collocation points after the first h-adaptive step.

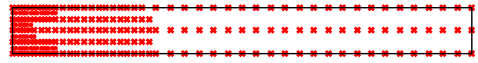

(d) The distribution of collocation points after the second h-adaptive step.

Figure 5.27: h-adaptivity of the elastic cantilever beam problem with uniformly distributed load with $k = 0.5$.

show the discretisation error for the whole beam problem using uniform refinement and h-adaptivity with $k = 0.5$ in Figure 5.28, where h-adaptivity achieves better convergence rate with lower error than uniform refinement. As discussed in Chapter 4, the choice of the local refinement parameter is affected by the variation of the local errors. It is apparent that the shear stress at the fixed end varies a lot, so the local errors for this beam problem vary in a large range and a smaller value of k can be selected.

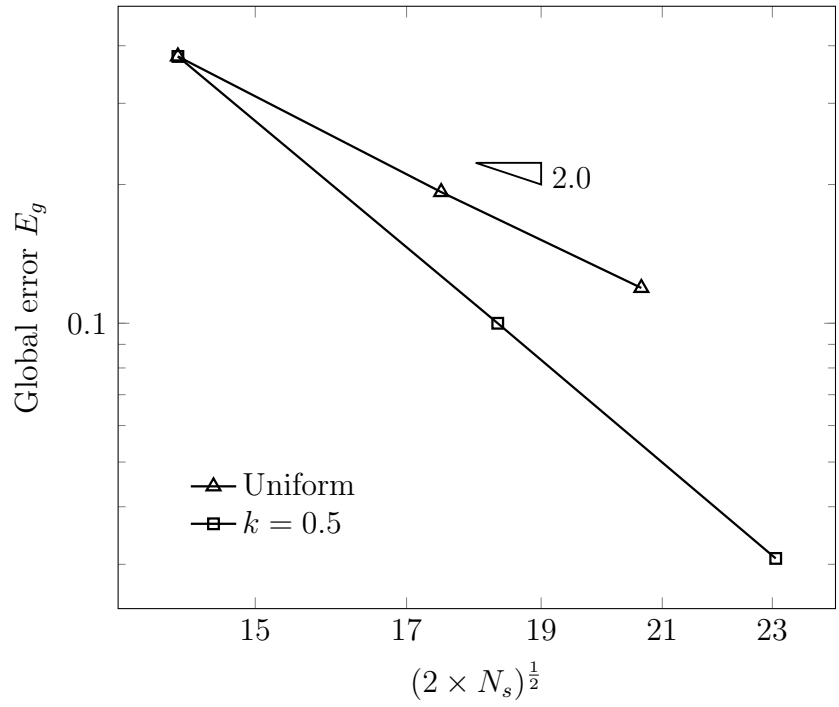

Figure 5.28: Convergence rate of E_g in h-adaptivity of the elastic cantilever beam problem with uniformly distributed load with $k = 0.5$.

5.6 Concluding remarks

In this chapter, the MEPCM has been developed for modelling problems subjected to geometric non-linearity, where a non-linear strain-displacement relationship is included. The basic kinematics and strain measures used in large deformation problems have been reviewed. A Total Lagrangian approach is employed in this chapter in which stress measures correspond to this description are referred to the reference configuration. The entire load is applied over load steps for large deformations and the Newton-Raphson method has been used to solve the formed non-linear system, in which the stopping criterion has been discussed. h-adaptivity strategy used for small deformations earlier in the thesis has been extended to large deformation analyses and some differences between large and small deformations have been pointed out. In large deformation problems, h-adaptivity is adopted after the initial calculation of all load steps. The local error estimator for small formation problems is extended here but the Cauchy stress in strong form governing equations is replaced by the first Piola-Kirchhoff stress referred to the reference configuration for large formation problems. The problem requires to be recalcu-

lated after each refinement therefore basis functions and derivatives have to be computed based on the newly generated points. Some numerical examples, in both one and two dimensions have been analysed to validate the performance of the proposed approach. The L_2 norm of the residual on displacement $||e||_{L_2}$ and proposed error estimators using various discretisations have been calculated to show the convergence performance. The proposed h-adaptive strategy has been implemented in selected numerical examples and its efficiency with different values of the local refinement parameter, k has been compared. This chapter shows that the MEPCM appears to be a robust way to model large deformation problems, given that it is a strong form-based meshless method.

Chapter 6

Membrane problems

6.1 Introduction

Membranes are widely used in engineering structures such as roofs, airbags, aircrafts and parachutes as they typically possess high performance in resisting external loads with much lower weight than traditional structures, reducing the cost and environmental impact of structures [239–241]. As shown in Figure 6.1, a membrane is a thin structure where the ratios between thickness and other dimensions are very small. The external pressure p_z is applied to the out-of-plane direction, leading to in-plane stress σ and corresponding deformation, u_z. A review of the literature on the behaviour of membranes, with emphasis in practical applications, can be found in [242].

Membrane theory which describes the mechanical behaviour of membranes, is extracted from the far more complex, classical shell theory, although computational membrane formulations are not always absolutely identical to the relevant parts of shell theory [243–248]. Bending stiffness is taken into account in shell theory, whereas it is completely neglected in membrane theory [249]. It is computationally challenging to model membrane problems as they are geometrically non-linear structures that can undergo large displacements and large strains [250, 251]. In order to describe the mechanical behaviour of real membrane structures accurately, membrane problems are often modelled using hyperelastic materials, where the constitutive laws are derived from the free-energy functions [252]. The most widely used hyperelastic material models for mem-

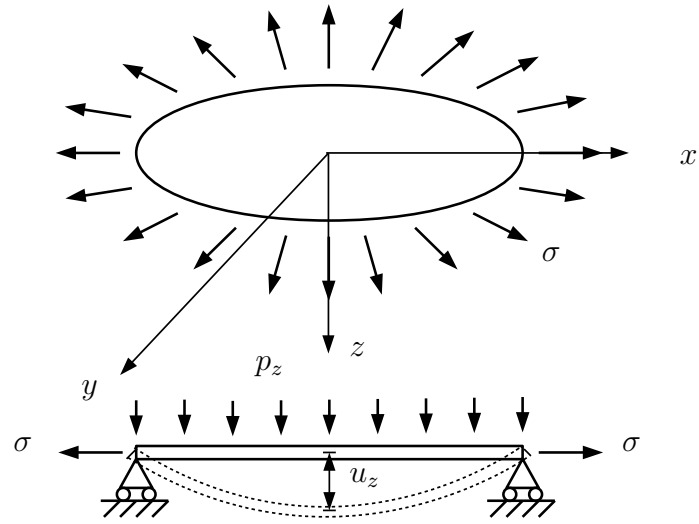

Figure 6.1: Membrane structure (given in [1]).

brane problems are the neo-Hookean [234], Mooney-Rivlin [253] and Ogden models [254]. An extensive review of constitutive models for hyperelasticity can be found in [255]. An important characteristic of rubber-like membrane is the instability when they undergo large deformations. The geometry of membranes can be complex and their configurations under external loads may result in instability phenomena. The external load increases sharply first until an unstable condition with the maximum external load is reached. Then this load declines and re-rises finally with an increasing deformation. The maximum and minimum external loads, which appear on the equilibrium path, are corresponding instability points. The instability analysis of tubular and spherical balloons using the Gent material model has been presented from theoretical and experimental views [256]. The unstable status has been illustrated by analysing the relationship between the external pressure and the variation of energy [257]. As the instability is complicated to analyse, no doubt the instability study remains to be discovered.

For membrane problems, the out-of-plane deformations result from in-plane stresses rather than using full three-dimensional constitutive theory. The stiffness of a membrane problem is zero at the start of deformation. A prestress or a prestretch can be, therefore, applied to the undeformed membrane structures by either prescribed displacements or

tractions acting along the boundary to avoid zero stiffness [258]. As shown in Figure 6.2(a), a cylindrical membrane with a length L_0 is prestretched in z direction to a length L (see Figure 6.2(b)). The prestretch leads to negative radial expansions at all height sections except the top and bottom surfaces. The external load is then applied to this prestretched membrane in Figure 6.2(b).

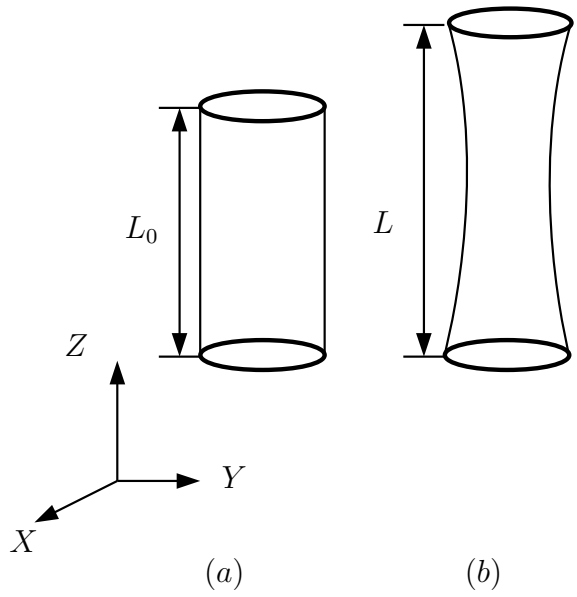

Figure 6.2: Prestretched cylindrical membrane.

Analytical solutions are only available for a few membrane problems such as the inflation of spherical rubber balloons [259], thus the numerical study of geometrically nonlinear membrane problems is of great importance. The finite element method (FEM) has been widely used in early numerical analysis of membrane problems [260–264], where membranes with various loading and boundary conditions have been modelled, such as the inflation of a flat circular membrane without a prestretch [265, 266] and the deformation of an initially tensioned membrane under uniform pressure with analytical solutions [267]. The initial configuration with a prestress has been introduced for the air supported membranes and further used in membranes with more complex geometries [268, 269]. The analog equation method has been applied to flat and non-flat membranes with arbitrary shapes, in which the governing PDEs for membrane problems are replaced by Poisson's equations [270]. More recently, a point collocation finite element method has been proposed to analyse the prestressed membrane problems where the gov-

erning equations described in the Cartesian coordinates are applied to collocation points directly and the basis functions are constructed based on a mesh [271]. As compared to the methods used above, the strong form based MEPCM can be applied to analyse membrane problems due to they have some attractive features, which is the aim of this chapter.

As the local maximum entropy point collocation method (MEPCM) proposed in Chapter 3 has been applied to large deformation analyses in Chapter 5, demonstrating some advantages due to the lack of a mesh, it seems natural to extend this strong form-based method to geometrically non-linear membrane analyses, presented for the first time in this thesis. However, the MEPCM cannot be applied to membranes directly since the use of a prestress (or a prestretch) introduces an additional configuration and the governing equation component in the out-of-plane direction has to be included. The kinematics and stress measures for both linear elastic and large strain hyperelastic materials are introduced first followed by the basic theory for membrane problems including the governing equations and boundary conditions described by a Total Lagrangian formulation with the MEPCM. Since the instability occurs at the equilibrium path of hyperelasticity, a Newton-Raphson arc-length method is introduced to capture the snap-through behaviour. Some numerical examples of membrane problems using different material models are analysed to demonstrate the performance of the proposed novel method under prestretches and external loads.

6.2 Kinematics

In this section, the basic kinematics for flat membrane structures with a prestretch is introduced. As mentioned in the last section, an in-plane prestretch, which is used for membrane problems to obtain a non-zero stiffness at the start of deformation, can be applied independently before external loads. In order to apply a prestretch to a membrane, a prescribed displacement vector $\{u^{pre}\} = \{u_x^{pre}, u_y^{pre}\}^T$ can be imposed on boundaries of a membrane in the reference configuration, resulting in a new configuration, referred to the initial configuration. In the prestretch vector, u_x^{pre} and u_y^{pre} are the values of the prestretch components in X and Y directions. Therefore kinematics for

flat membrane problems with a prestretch includes a description of three successive configurations, the reference (undeformed), initial (prestretched) and current (deformed) configurations, as shown in Figure 6.3.

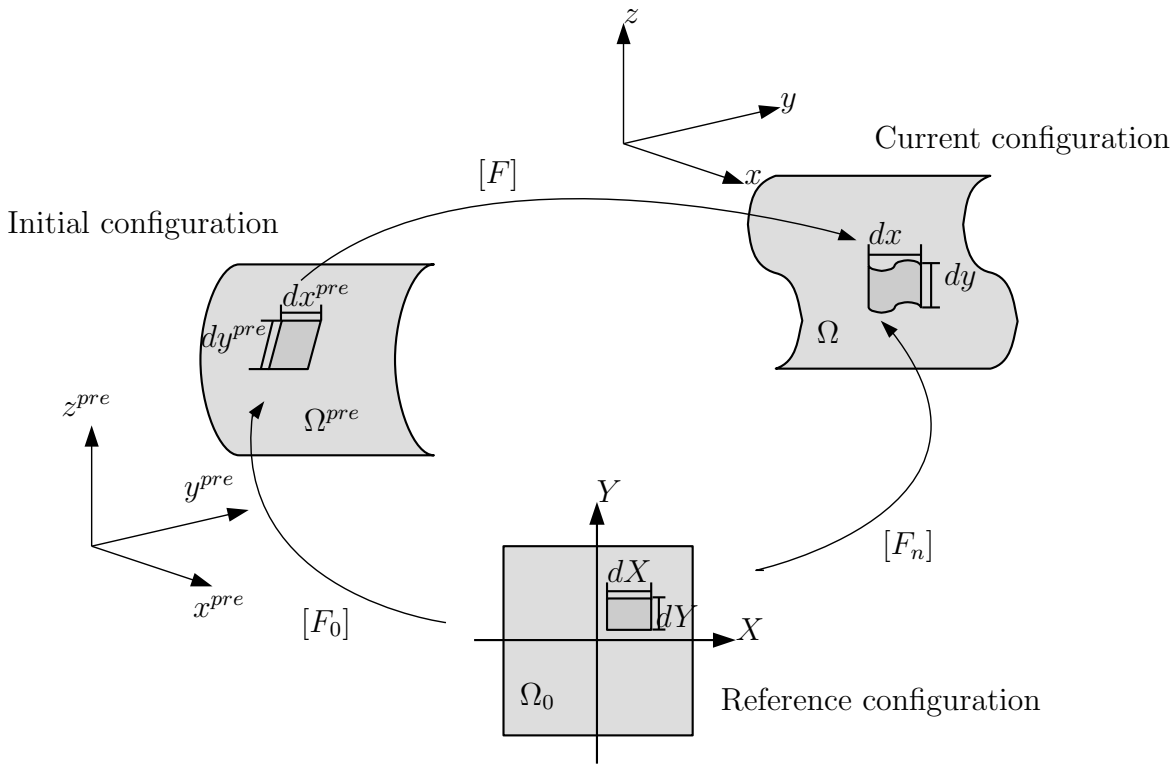

Figure 6.3: The reference, initial and current configurations of membranes.

A point on the membrane surface in the two-dimensional reference configuration Ω_0 is given by $\{\bar{X}\} = \{X, Y\}^T$. The coordinate $\{\bar{x}^{pre}\} = \{x^{pre}, y^{pre}, z^{pre}\}^T$ is defined in the initial configuration Ω^{pre} with a prestretch and the coordinate $\{\bar{x}\} = \{x, y, z\}^T$ describes the position of a point in the corresponding current configuration Ω. The position vectors in both the initial and current configurations, $\{\bar{x}^{pre}\}$ and $\{\bar{x}\}$, have three components, which can refer to the two-dimensional reference coordinate $\{\bar{X}\}$. Mappings between these three configurations can be given as

$$\{\bar{x}^{pre}\} = \varphi_{x^{pre}}(\{\bar{X}\}), \quad \{\bar{x}\} = \varphi(\{\bar{x}^{pre}\}, t) \quad \text{and} \quad \{\bar{x}\} = \varphi_x(\{\bar{X}\}, t). \tag{6.1}$$

The function $\varphi_{x^{pre}}$ is the Lagrangian description of the motion which can map a point

from the reference configuration Ω_0 to the initial configuration Ω^{pre}, φ is used to map a point from the initial configuration Ω^{pre} to the current configuration Ω and a point in the reference configuration Ω_0 can be mapped into the current configuration Ω by φ_x directly. The corresponding deformation gradients can be expressed in terms of these three different configurations as

$$[F_0] = \frac{\partial\{\bar{x}^{pre}\}}{\partial\{\bar{X}\}}, \quad [F] = \frac{\partial\{\bar{x}\}}{\partial\{\bar{x}^{pre}\}} \quad \text{and} \quad [F_n] = \frac{\partial\{\bar{x}\}}{\partial\{\bar{X}\}} \tag{6.2}$$

where $[F_0]$ describes the deformation from the reference to the initial configurations caused by the prestretch, $[F]$ measures the deformation resulting from the external load without the prestretch and $[F_n]$ gives the total deformation referred back to the reference configuration.

Similarly to large deformation analyses in Chapter 5, a Total Lagrangian formulation is used for membrane problems as the initially calculated basis functions and the derivatives can be reused throughout the analysis. However, as the deformation is caused by the external load without a prestretch, all variables used in the Total Lagrangian formulation can refer to both the reference and the initial configurations (see [269, 272]). The Total Lagrangian formulation in terms of the reference configuration is used in this chapter as the reference configuration is given directly and mappings between the reference and the initial configurations are not required. The deformation gradient $[F_n]$ is used in the following strain and stress measures as it refers to the reference configuration.

In order to find the relationship between these expressions of deformation gradients, $[F_0]$, $[F]$ and $[F_n]$, the vector of the infinitesimal lengths in the initial configuration $\{d\bar{x}^{pre}\}$ can be given in terms of the reference configuration, and the vector of the infinitesimal lengths in the current configuration $\{d\bar{x}\}$ can be described in terms of the reference and the initial configurations, by using the corresponding deformation gradients as

$$\{d\bar{x}^{pre}\} = [F_0]\{d\bar{X}\}, \quad \{d\bar{x}\} = [F]\{d\bar{x}^{pre}\} \quad \text{and} \quad \{d\bar{x}\} = [F_n]\{d\bar{X}\} \tag{6.3}$$

where $\{d\bar{X}\}$ is the vector of the infinitesimal lengths in the reference configuration. Eq.

(6.3) can be rearranged to obtain the following relationship

$$[F_n] = [F][F_0]. \tag{6.4}$$

Three corresponding right and left Cauchy-Green strains (given in Eqs. (5.8) and (5.9)) in terms of the different configurations are given as

$$[C_0] = [F_0]^T[F_0], \quad [C] = [F]^T[F] \quad \text{and} \quad [C_n] = [F_n]^T[F_n] \tag{6.5}$$

and

$$[b_0] = [F_0][F_0]^T, \quad [b] = [F][F]^T \quad \text{and} \quad [b_n] = [F_n][F_n]^T \tag{6.6}$$

in which $[C_0]$ and $[b_0]$ describe the strains resulting from the a prestretch, $[C]$ and $[b]$ are used to measure the strains caused by the external load, and $[C_n]$ and $[b_n]$ represent the total strains. Substituting Eq. (6.4) into Eq. (6.5), $[C_n]$ can be written as a function of deformation gradients $[F_0]$ and $[F_n]$ as

$$[C_n] = [F_n]^T[F_n] = [F_0]^T[F]^T[F][F_0] = [F_0]^T[C][F_0]. \tag{6.7}$$

Again, various strain measures are available in large deformation membrane problems. The logarithmic strain, which has a linear relationship with the Kirchhoff stress, is used for linear elastic membranes, as explained in §5.2 the constitutive model for small deformation can be used for large deformation problems without modification. The logarithmic strain in terms of the reference configuration $[\varepsilon_n]$ is given as

$$[\varepsilon_n] = \frac{1}{2}\ln([b_n]). \tag{6.8}$$

Another strain measure, the Green-Lagrangian strain, which is adopted for hyperelastic material models, is defined in terms of the reference configuration as

$$[E_n] = \frac{1}{2}\left(2\frac{\partial\{u\}}{\partial\{\bar{X}\}} + \frac{\partial\{u\}}{\partial\{\bar{X}\}}\frac{\partial\{u\}}{\partial\{\bar{X}\}}\right) = \frac{1}{2}([C_n] - [I]) \tag{6.9}$$

where $\{u\} = \{u_x, u_y, u_z\}^T$ is the vector of displacement for membrane problems in terms

of the reference configuration and the non-linear term $\frac{\partial\{u\}}{\partial\{\bar{X}\}}\frac{\partial\{u\}}{\partial\{\bar{X}\}}$ is the source of the geometric non-linearity.

Comparing with large deformation analyses in Chapter 5, an initial configuration is introduced for membrane problems. Kinematics and two strain measures in terms of the reference configuration have been given in this section, which will be employed to obtain stress measures for different material models in the next section.

6.3 Stress measures

In this section, stress measures for both linear elastic and hyperelastic material models are provided associated with the membrane kinematics introduced in the last section.

6.3.1 Linear elastic membranes

For linear elastic membrane problems with geometric non-linearity, a linear Kirchhoff stress-logarithmic strain relationship is used as

$$\{\tau_n\} = [D]\{\varepsilon_n\} \tag{6.10}$$

for the same reasons as mentioned in §6.2. In Eq. (6.10), $[D]$ is the elastic material stiffness matrix given in Eq. (3.9) and $\{\varepsilon_n\}$ is the logarithmic strain with respect to the reference configuration. Four components in the 2×2 matrix of $[\varepsilon_n]$ in Eq. (6.8) can be written into a 3×1 vector form of $\{\varepsilon_n\}$ with $\varepsilon_{xy} = \varepsilon_{yx}$. The first Piola-Kirchhoff stress in terms of the reference configuration can then be expressed as

$$[P_n] = [\tau_n][F_n]^{-T} \tag{6.11}$$

where the symmetric Kirchhoff stress $[\tau_n]$ can be rearranged from $\{\tau_n\}$ in Eq. (6.10) with $\tau_{xy} = \tau_{yx}$. In the analysis of membrane problems, the symmetric second Piola-Kirchhoff stress with respect to the reference configuration is introduced as

$$[S_n] = [F_n]^{-T}[\tau_n][F_n]^{-T} = [F_n]^{-1}[P_n] \tag{6.12}$$

which has no direct physical meaning but is used in the following section for hyperelastic materials. It should be noted that using the Total Lagrangian formulation, all stress measures used in the governing PDEs and corresponding boundary conditions for membranes, need to refer to the reference configuration.

6.3.2 Hyperelastic membranes

As hyperelastic materials are most often used in membrane problems, some basic concepts of hyperelasticity are now reviewed. The formulation of stress measures for the hyperelastic membrane problems, for one particular case (the Ogden [273] material model) is described.

Basic theory

A brief introduction to hyperelasticity is included here (based on [234, 274]). In contrast to linear elasticity, hyperelastic materials are characterised by the existence of a free-energy function ψ which is dependent on the deformation, so stress measures are obtained based on the free-energy function, i.e. the second Piola-Kirchhoff stress used for membrane problems can be obtained from the free-energy function ψ with respect to the Green-Lagrangian strain or the right Cauchy-Green strain. Although ψ is usually given in terms of different variables, such as the principal stretches and invariants, for different material models, they can be converted to the function in terms of the Green-Lagrangian strain or the right Cauchy-Green strain. The principal stretches $\lambda_1, \lambda_2, \lambda_3$, which are the principal values of the right and left stretches, $[U]$ and $[v]$ (given in §5.2), are the square root of principal values of the right Cauchy-Green strain $[C]$. The relationship between the right Cauchy-Green strain $[C]$ and the invariants I_1, I_2 and I_3 is given as

$$I_1([C]) = \mathrm{tr}([C]) \tag{6.13a}$$

$$I_2([C]) = \frac{1}{2}\left[(\mathrm{tr}([C]))^2 - \mathrm{tr}([C]^2)\right] \tag{6.13b}$$

$$I_3([C]) = \det([C]) \tag{6.13c}$$

where $\mathrm{tr}([C]) = C_{11} + C_{22} + C_{33}$. As the right Cauchy-Green strain can be obtained from deformation gradient by Eq. (6.5) in terms of the different configurations, the free-energy function can be expressed as a function of the deformation gradient $[F]$, the right Cauchy-Green strain $[C]$, the invariants I_1, I_2 and I_3, and the principal stretches $\lambda_1, \lambda_2, \lambda_3$ as

$$\psi([F]) = \tilde{\psi}([C]) = \bar{\psi}(I_1([C]), I_2([C]), I_3([C])) = \hat{\psi}(\lambda_1, \lambda_2, \lambda_3). \tag{6.14}$$

For some hyperelastic materials which are assumed to have incompressibility, very little volumetric change is observed with very large deformations. In such cases, the invariant I_3 as given in Eq. (6.13c), is unity, so the free-energy function in Eq. (6.14) is only dependent on I_1 and I_2 as $\bar{\psi}(I_1([C]), I_2([C]))$.

In order to obtain the second Piola-Kirchhoff stress from the free-energy function, the principal stretches and invariants in Eq. (6.14) have to be replaced by the right Cauchy-Green strain, which is described in the following.

Hyperelastic membranes

The stress measures for hyperelastic membranes with respect to the reference configuration are introduced here. This derivation follows the idea in [268]. Using the Total Lagrangian formulation in terms of the reference configuration, the second Piola-Kirchhoff stress is given as

$$[S_n] = 2\frac{\partial \tilde{\psi}([\bar{C}])}{\partial [C_n]} \tag{6.15}$$

where $[S_n]$ is the second Piola-Kirchhoff stress in terms of the reference configuration, $\tilde{\psi}([\bar{C}])$ is the free-energy function of the right Cauchy-Green strain caused by the external load and $[\bar{C}]$ is the in-plane strain resulting from the external load. Using the chain rule, the second Piola-Kirchhoff stress in Eq. (6.15) can be written as

$$[S_n] = 2\frac{\partial \tilde{\psi}([\bar{C}])}{\partial [\bar{C}]}\frac{\partial [\bar{C}]}{\partial [C_n]}. \tag{6.16}$$

It is noted that the deformation caused by the prestretch is not included in the free-energy function as the prestretch is used to avoid zero stiffness. For membrane problems,

transverse shear strains in $[\bar{C}]$ vanish and the thickness strain in the out-of-plane direction is dependent on the in-plane strain components as indicated in the incompressibility condition. Two components C_{11} and C_{22} are the principal values of $[\bar{C}]$. The in-plane principal stretches λ_1 and λ_2 can be expressed by the in-plane right Cauchy-Green strain components as

$$\lambda_1^2 = C_{11} \quad \text{and} \quad \lambda_2^2 = C_{22}. \tag{6.17}$$

The right Cauchy-Green strain in terms of the initial configuration $[C]$ can be rearranged as

$$[C] = \begin{bmatrix} [\bar{C}] & 0 \\ 0 & C_{33} \end{bmatrix} \tag{6.18}$$

where the in-plane strain $[\bar{C}]$ is

$$[\bar{C}] = \begin{bmatrix} C_{11} & 0 \\ 0 & C_{22} \end{bmatrix} \tag{6.19}$$

and each component of $[\bar{C}]$ can be found in the expression of $[C]$. The current thickness of the membrane varies in the deformation process, and is obtained by using the incompressibility condition so that

$$h = \lambda_3 h^{pre} = (C_{33})^{\frac{1}{2}} h^{pre} \tag{6.20}$$

in which the thickness in the initial configuration h^{pre} caused by a prestretch can be obtained via

$$h^{pre} = (\lambda_0)_3 h_0. \tag{6.21}$$

In Eq. (6.21), $(\lambda_0)_3$ is the principal stretch in terms of the reference configuration. Considering incompressibility, $(\lambda_0)_3$ can be given by $(\lambda_0)_3 = (C_0)_{11}^{-1}(C_0)_{22}^{-1}$ where $(C_0)_{11}$ and $(C_0)_{22}$ can be found in Eq. (1.5a). The thickness value h^{pre} is used in the initial configuration and the thickness h is used in the current configuration.

The Ogden material model

The Ogden [273] material model is considered in this chapter to provide a capability for very large strains as the Neo-Hookean [234] and Mooney-Rivlin [253] models fail to represent the behaviour of rubbery materials with very large strains [275]. The free-energy function, ψ, based on the principal stretches has been proposed by Ogden [276–278]. Its form is given by

$$\hat{\psi}(\lambda_1, \lambda_2, \lambda_3) = \sum_{p=1}^{N} \frac{\mu_p}{\alpha_p}(\lambda_1^{\alpha_p} + \lambda_2^{\alpha_p} + \lambda_3^{\alpha_p} - 3) \tag{6.22}$$

in which N is the total number of terms in the series ($N = 3$ is used in the following examples), α_p ($p = 1, ..., N$) and μ_p are corresponding material constants. The values of these material constants are selected appropriately to fit the experimental results. Using the relationship in Eq. (6.17) and the chain rule, the second Piola-Kirchhoff stress (which will be used in next section) in Eq. (6.16) can be derived as

$$\begin{aligned} [S_n] &= 2\frac{\partial \hat{\psi}(\lambda_k)}{\partial [C_n]} \\ &= 2\frac{\partial \hat{\psi}(\lambda_k)}{\partial \lambda_k}\frac{\partial \lambda_k}{\partial [\bar{C}]}\frac{\partial [\bar{C}]}{\partial [C_n]} \end{aligned} \tag{6.23}$$

where

$$\frac{\partial \hat{\psi}(\lambda_1, \lambda_2)}{\partial \lambda_k} = \sum_{p=1}^{N} \mu_p \lambda_k^{\alpha_p - 1}, \tag{6.24}$$

$\frac{\partial \lambda_k}{\partial [\bar{C}]}$ and $\frac{\partial [\bar{C}]}{\partial [C_n]}$ can be calculated from Eqs. (6.17) and (6.7).

In this section, the stress measures required for linear elastic and the hyperelastic Ogden material models for membrane problems have been provided, and will next be introduced to the equilibrium theory for membranes.

6.4 Equilibrium of membranes

The governing PDEs based on the stress measures introduced in the previous section, for geometrically non-linear membranes, are given in [279, 280] as

$$\frac{\partial N_{xx}}{\partial X} + \frac{\partial N_{xy}}{\partial Y} = p_x \tag{6.25a}$$

$$\frac{\partial N_{xy}}{\partial X} + \frac{\partial N_{yy}}{\partial Y} = p_y \tag{6.25b}$$

$$\frac{\partial}{\partial X}\Big(N_{xx}\frac{\partial u_z}{\partial X} + N_{xy}\frac{\partial u_z}{\partial Y}\Big) + \frac{\partial}{\partial Y}\Big(N_{yy}\frac{\partial u_z}{\partial Y} + N_{xy}\frac{\partial u_z}{\partial X}\Big) = p_z \tag{6.25c}$$

in terms of the reference configuration over the domain Ω^0 where u_z is the out-of-plane displacement in the vector of $\{u\} = \{u_x, u_y, u_z\}^T$ and p_x, p_y and p_z are the external pressure components in

$$\{\bar{p}\} = \{p_x, p_y, p_z\}^T. \tag{6.26}$$

In Eq. (6.25), N_{xx}, N_{yy} and N_{xy} are in-plane resultant forces (integrated forces or membrane forces) in terms of the reference configuration. These components of resultant forces can be written in a matrix form as

$$[N] = \begin{bmatrix} N_{xx} & N_{xy} \\ N_{xy} & N_{yy} \end{bmatrix}. \tag{6.27}$$

In membrane problems, membrane forces are often employed in the governing PDEs as they vary with thickness. Membrane force matrix $[N]$ is obtained from the second Piola-Kirchhoff stress in terms of the reference configuration $[S_n]$ and the current thickness h as

$$[N] = h(\{u\})[S_n]. \tag{6.28}$$

It is noted that the membrane thickness $h(\{u\})$ is a function of the displacement $\{u\}$, which is updated with the deformation of membranes in the current configuration. The expression of the second Piola-Kirchhoff stress in terms of the reference configuration $[S_n]$ can be found in Eqs. (6.12) and (6.23) for linear elastic and the hyperelastic Ogden materials, respectively.

Dirichlet and Neumann boundary conditions for membrane problems are given as

$$u_x = \bar{u}_x^0 \quad u_y = \bar{u}_y^0 \quad \text{and} \quad u_z = \bar{u}_z^0 \tag{6.29}$$

on Dirichlet boundaries Γ_u and

$$t_x = N_{xx} n_x^0 + N_{xy} n_y^0 = \bar{t}_x^0 \tag{6.30a}$$

$$t_y = N_{xy} n_x^0 + N_{yy} n_y^0 = \bar{t}_y^0 \tag{6.30b}$$

$$t_z = (N_{xx} n_x^0 + N_{xy} n_y^0)\frac{\partial u_z}{\partial X} + (N_{yy} n_y^0 + N_{xy} n_y^0)\frac{\partial u_z}{\partial Y} = \bar{t}_z^0 \tag{6.30c}$$

on Neumann boundaries Γ_t where the prescribed displacement vector is given as $\{\bar{u}^0\} = \{\bar{u}_x^0, \bar{u}_y^0, \bar{u}_z^0\}^T$, the prescribed traction vector is given as $\{\bar{t}^0\} = \{\bar{t}_x^0, \bar{t}_y^0, \bar{t}_z^0\}^T$ and n_x^0, n_y^0 and n_z^0 are the components of the unit normal matrix to the membrane surface in the reference configuration

$$[n_m^0] = \begin{bmatrix} n_x^0 & 0 \\ 0 & n_y^0 \\ n_y^0 & n_x^0 \end{bmatrix}. \tag{6.31}$$

Compared to the governing equations and boundary conditions used for two-dimensional geometrically non-linear problems in Eqs. (5.14) and (5.15), here the third component in the out-of-plane direction is included in Eqs. (6.25), (6.29) and (6.30) and the non-symmetric first Piola-Kirchhoff stress is replaced by the symmetric resultant force. Therefore, the 4×2 unit normal matrix in Eq. (5.17) becomes the 3×2 unit normal matrix in Eq. (6.31). The derivatives of the out-of-plane displacement terms are included in the component of Neumann boundary conditions given in Eq. (6.30).

To analyse the membrane problem using the MEPCM, an appropriate condition from Eqs. (6.25), (6.29) and (6.30) is imposed at each collocation point in the interior of the membrane surface and on boundaries, leading to a non-linear system of equations in terms of a vector of the displacement at source points, similar to the systems developed earlier in the thesis for different problems, i.e.

$$\{G\} = \{\{G_1\}^T, \{G_2\}^T, \{G_3\}^T\} = \{F_p^{int}\}^T - \{F_p^{ext}\}^T = \{0\} \tag{6.32}$$

where three different components are

$$\{G_1\} = \left\{ \begin{array}{c} \frac{\partial N_{xx}}{\partial X} + \frac{\partial N_{xy}}{\partial Y} - p_x \\ \frac{\partial N_{xy}}{\partial X} + \frac{\partial N_{yy}}{\partial Y} - p_y \\ \frac{\partial}{\partial X}\left(N_{xx}\frac{\partial u_z}{\partial X} + N_{xy}\frac{\partial u_z}{\partial Y}\right) + \frac{\partial}{\partial Y}\left(N_{yy}\frac{\partial u_z}{\partial Y} + N_{xy}\frac{\partial u_z}{\partial X}\right) - p_z \end{array} \right\}_i \quad i = 1, ..., l \quad (6.33)$$

$$\{G_2\} = \left\{ \begin{array}{c} u_x - \bar{u}_x^0 \\ u_y - \bar{u}_y^0 \\ u_z - \bar{u}_z^0 \end{array} \right\}_j \quad j = 1, ..., m \quad (6.34)$$

and

$$\{G_3\} = \left\{ \begin{array}{c} t_x - \bar{t}_x^0 \\ t_y - \bar{t}_y^0 \\ t_z - \bar{t}_z^0 \end{array} \right\}_k \quad k = 1, ..., n. \quad (6.35)$$

In the above equations, l is the number of collocation points in the interior of the domain where the collocation is to the governing equations, m and n are the remaining numbers of collocation points on boundaries carrying Dirichlet and Neumann boundary conditions respectively. The total number of collocation points covering the domain is $l + m + n = N_c$. $\{F_p^{int}\}$ is a vector of the internal variables and $\{F_p^{ext}\}$ is a vector of the external variables. All terms at the right-hand side of Eqs. (6.25), Eqs. (6.29) and Eqs. (6.30) are put in $\{F_p^{int}\}$ and the known variables including the out-of-plane pressures, prescribed displacements and external tractions are independently put in the external variables $\{F_p^{ext}\}$. The internal $\{F_p^{int}\}$ and external variables $\{F_p^{ext}\}$ are introduced here as they are used in the non-linear solver in the following. The non-linear system of equations in Eq. (6.32) should equal a zero vector with the vector of the exact displacements. However the exact solution is unknown and the non-linear system $\{G\}$ in Eq. (6.32) has a non-zero residual vector $\{R\}$ in terms of the unknown vector of displacements at source points $\{d\} = \{d_x, d_y, d_z\}^T$. The solution can be found by minimising the non-zero residual vector

$$\{R\} = \{\{R_1\}^T, \{R_2\}^T, \{R_3\}^T\} = \{F_p^{int}\}^T - \{F_p^{ext}\}^T \quad (6.36)$$

which can be expressed by three corresponding residual components.

For linear elastic membrane problems, the Newton-Raphson method introduced in §5.3 can be adopted to linearise the non-linear system and obtain a vector of displacements at source points $\{d\}$ incrementally. In the Newton-Raphson method, Jacobian of the residual vector is formed by linearising the non-linear system of residual in Eq. (6.36) with respect to the displacement at source points $\{d\}$ as

$$[R'] = \begin{bmatrix} \left[\frac{\partial R_1}{\partial d_x}\right] & \left[\frac{\partial R_1}{\partial d_y}\right] & \left[\frac{\partial R_1}{\partial d_z}\right] \\ \left[\frac{\partial R_2}{\partial d_x}\right] & \left[\frac{\partial R_2}{\partial d_y}\right] & \left[\frac{\partial R_2}{\partial d_z}\right] \\ \left[\frac{\partial R_3}{\partial d_x}\right] & \left[\frac{\partial R_3}{\partial d_y}\right] & \left[\frac{\partial R_3}{\partial d_z}\right] \end{bmatrix}. \tag{6.37}$$

Eq. (5.22) can be used to calculate the iterative displacement vector and the Newton-Raphson method continues until the stopping criterion in Eq. (5.28) are satisfied. Compared with the residual norms $||R_1||$, $||R_2||$ and $||R_3||$ for the other large deformation problems in Chapter 5, one more component at each collocation point is included in Eqs. (5.24), (5.25) and (5.26) for membrane problems. For hyperelastic materials, instability can occur on the equilibrium path, therefore an appropriate method is required to find a solution for the non-linear system, which is described in the following.

The Newton-Raphson method is usually ideal for the solution of sets of non-linear equations resulting from numerical methods used in solid mechanics due to fast convergence and robustness, however, they have some limitations. The method is able to solve any load-controlled non-linear system efficiently, where the equilibrium path can be captured by increasing the load field in $\{F_p^{ext}\}$ and the increment between any two load steps can be user-defined. The displacement-controlled equilibrium path can also be tracked using the Newton-Raphson method by increasing the vector of displacements $\{d\}$. However, the Newton-Raphson method fails to accurately follow the equilibrium path which is not load- and displacement-controlled (with more complex unstable equilibrium). As reviewed in §6.1, the instability happens when the external load does not change monotonically and the external load in the next load step needs to be determined automatically. A limit point appears on the equilibrium path to show a local maximum or minimum value (defined as a snap-through or a snap-back behaviour) [281, 282]).

Typical equilibrium paths associated with a snap-through or a snap-back behaviour are illustrated in Figure 6.4 in which λ_m is a load factor to determine the external load in the next load step. The Newton-Raphson method is unable to track the equilibrium path accurately when the limit point A is reached.

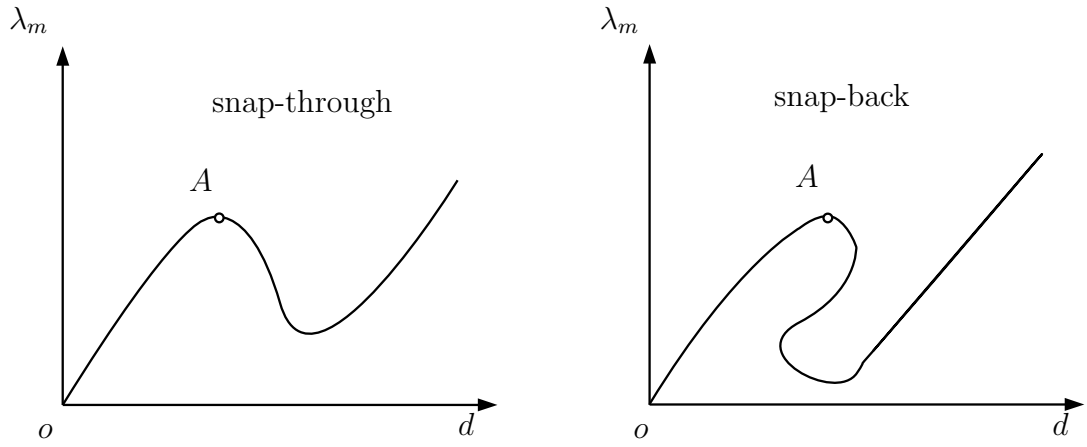

Figure 6.4: Unstable equilibrium: Snap-through and snap-back behaviour.

To address these issues, the Newton-Raphson approach can be complemented by an "arc-length" method [283] which provides an efficient way to trace the equilibrium path beyond the limit point A. An equilibrium path is controlled by a load factor λ_m and displacement pairs as $\{\lambda_m, \{d\}\}$ (see Figure 6.4). An extra constraint with an additional unknown λ_m is added to the residual vector $\{R\}$ to find the solution. The arc-length method is grouped into spherical and cylindrical arc-length methods because they have different constraint equations

$$\{\Delta u\}^T\{\Delta u\} + \Delta\lambda_m^2\psi_{arc}^2\{F_p^{int}\}^T\{F_p^{int}\} - l^2 = 0 \tag{6.38}$$

and

$$\{\Delta u\}^T\{\Delta u\} = l^2 \tag{6.39}$$

respectively, where $\Delta\{u\}$ is the incremental displacement and $\Delta\lambda_m$ is the incremental load factor, ψ_{arc} is a prescribed scaling parameter, $\{F_p^{int}\}$ is a vector of internal variables and l is a prescribed incremental solution length. In this chapter, the cylindrical

arc-length method is combined with the Newton-Raphson method to find the solution of the non-linear system for membrane problems with hyperelastic materials since the prescribed scaling parameter ψ_{arc} is zero in Eq. (6.39) which simplifies the constraint equation. The stopping criterion in Eq. (5.28) are adopted here with some differences. Similarly to the stopping criterion used for linear elastic membrane problems above, three components at each collocation points are included to calculate the residual norms. The detailed formulations of the Newton-Raphson arc-length method are provided in Appendix D [211, 283–290].

The vector of displacements at source points $\{d\}$ in terms of the reference configuration for linear elastic and hyperelastic membrane problems can be calculated by the Newton-Raphson and the Newton-Raphson arc-length methods, respectively. The approximation of displacement including the prestretch at any point can be approximated by basis function values and $\{d\}$ associated with the source points inside the support domain using Eq. (3.17). However, compared to the previous two-dimensional problems, the matrix of basis function values associated with each source point is 3×3 and the vector of displacement at each source point is 3×1 as the out-of-plane displacement exists for membrane problems.

6.5 Numerical examples

The detailed formulation for the analysis of membrane problems using the Total Lagrangian approach in term of the reference configuration with the geometrically non-linear MEPCM have been discussed in previous sections of this chapter. In this section, some numerical examples using both linear elastic and the hyperelastic Ogden materials are analysed to demonstrate the performance of the proposed method.

6.5.1 Inflation of a linear elastic membrane

The first example is the analysis of an initially flat rectangular membrane loaded with a uniform pressure on the membrane surface as shown in Figure 6.5. This linear elastic membrane problem has been studied in a reference [270], where the geometry and material properties were used here with side length $a = 5.0$ m, aspect ratios $a/b = 1$

and 7/5, thickness $h_0 = 0.004$ m, uniform pressure $p_z = 5$ kPa, Young's Modulus of linear elasticity, E=1.1×10^5 kN/m^2, and Poisson's ratio, ν=0.3. The four edges of the membrane were fully fixed.

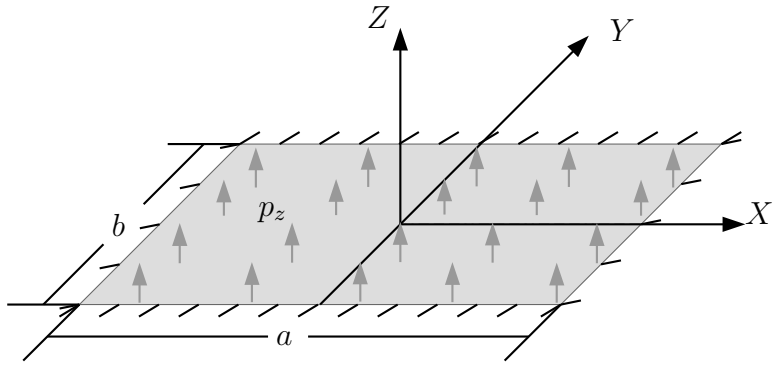

Figure 6.5: An initially flat linear elastic membrane model subjected to a uniform pressure.

A square membrane with $a/b = 1$ is studied first. Using the MEPCM to analyse this problem, 21×21 collocation and source points were distributed uniformly in the interior of the problem domain and on boundaries. The change of the thickness is ignored in this linear elastic membrane as the deformation caused by the given uniform pressure has little effect on the current thickness. The prescribed uniform pressure p_z was applied at collocation points in the interior of the problem domain. A zero displacement boundary condition was imposed at each collocation point on boundaries in the initial configuration. As the non-linear strain-displacement relationship has been used in this geometrically non-linear membrane problem, a non-linear system of equations is formed in terms of the unknown displacements at source points $\{d\}$. For a linear elastic membrane, the equilibrium path is monotonic and the problem can be solved by the Newton-Raphson method. The out-of-plane pressure p_z was normalised by $\bar{p}_z = p_z(1-\nu^2)/Eh_0$ and applied over 10 load steps. The maximum number of iterations was set as 10 and the tolerance number, η set as 10^{-5}.

Figure 6.6 displays the deformed configurations of the linear elastic square membrane under a uniform pressure at the first, second, fourth and tenth load steps, respectively, which presents the total deformation of the membrane caused by the successively increased out-of-plane pressure. These four configurations in Figure 6.6 are mapped from

the reference configuration by using the vector of displacements at all collocation points. The colours in Figure 6.6 indicate the out-of-plane displacements, u_z at all collocation points over different load steps and the colours are illustrated by the colourbar in each subfigure next to the configuration with the same unit as the dimensions of the geometry. As expected, the maximum deflection occurs at the central point of the membrane surface. The out-of-plane deformation becomes apparent with an increasing value of the pressure. The differences between Figure 6.6(a)-(d) are caused by the different values of the external pressure p_z over all these load steps.

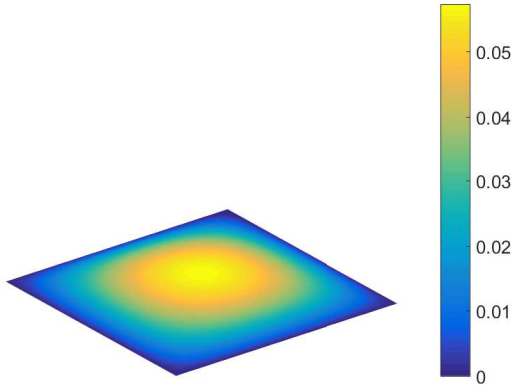

(a) The first load step.

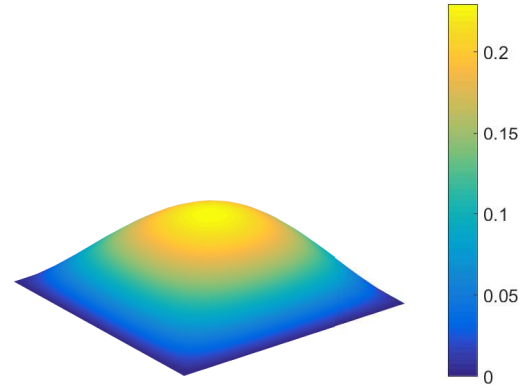

(b) The second load step.

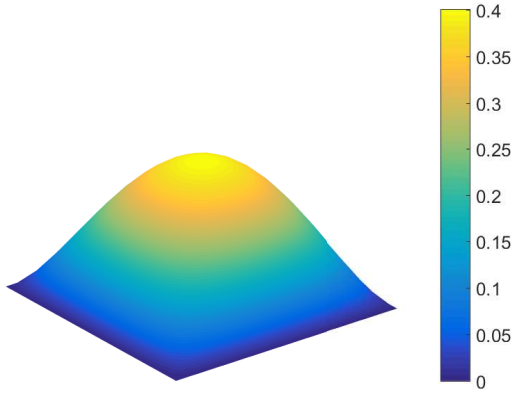

(c) The fourth load step.

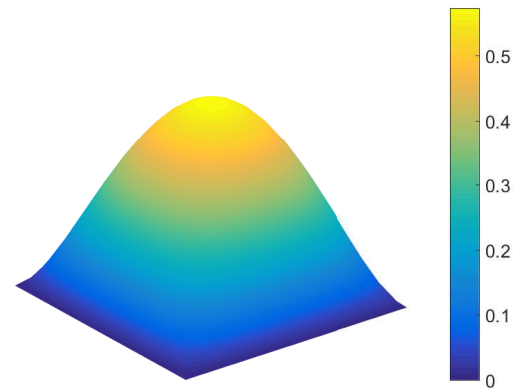

(d) The tenth load step.

Figure 6.6: The deformed configurations with the out-of-plane displacement, u_z (m) at different load steps of the initially flat linear elastic membrane problem subjected to a uniform pressure.

The deflection u_z at $Y = 0$ against the position in X direction at four different load

steps are presented in Figure 6.7 to show the deformation throughout selected load steps. It can be observed that the in-plane displacements are smaller than the out-of-plane displacement at each of these four load steps. The overall out-of-plane displacement, u_z of this linear elastic membrane problem under the given uniform pressure is slightly less than fifteen times of its original thickness, h_0.

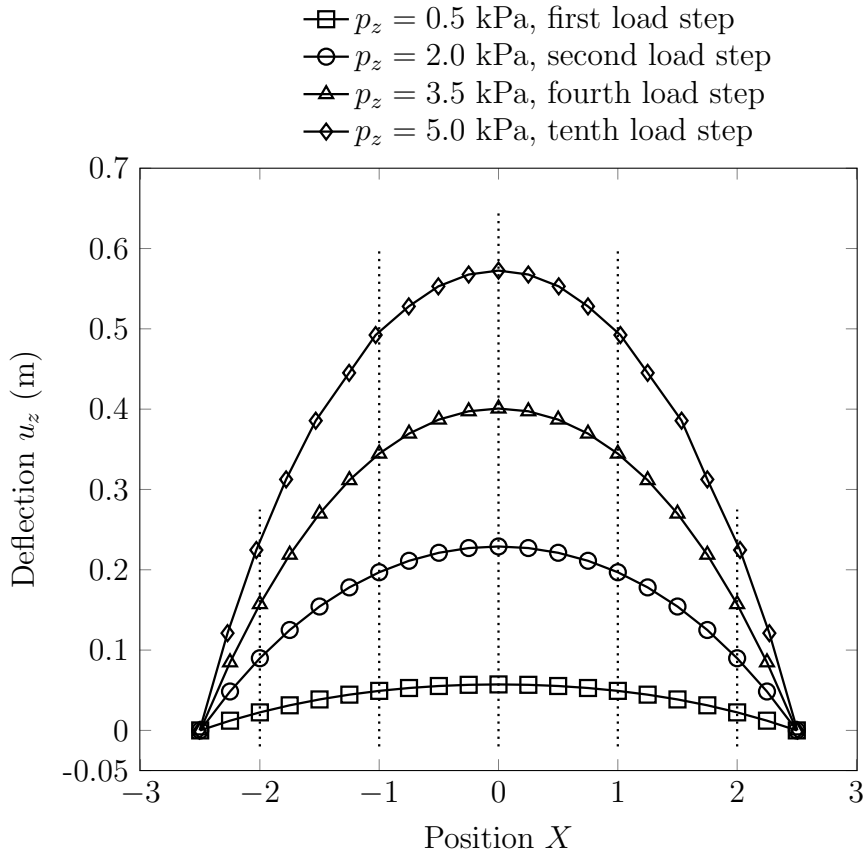

Figure 6.7: The deflections u_z (m) at $Y = 0$ over different load steps of the initially flat linear elastic membrane problem subjected to a uniform pressure.

Figure 6.8 shows the relationship between the normalised pressure $\bar{p}_z$ and the normalised out-of-plane deflection u_z/a at the centre point of the membrane surface over all load steps, in which a non-linear relationship can be clearly observed by comparing with the linear indicator in this figure. For this linear elastic membrane problem, it can be seen that the external pressure goes up with an increasing displacement, u_z, therefore, the equilibrium path without instability can be captured by using the Newton-Raphson method. The increment between each two load steps can be predefined. Here, a constant increment is employed.

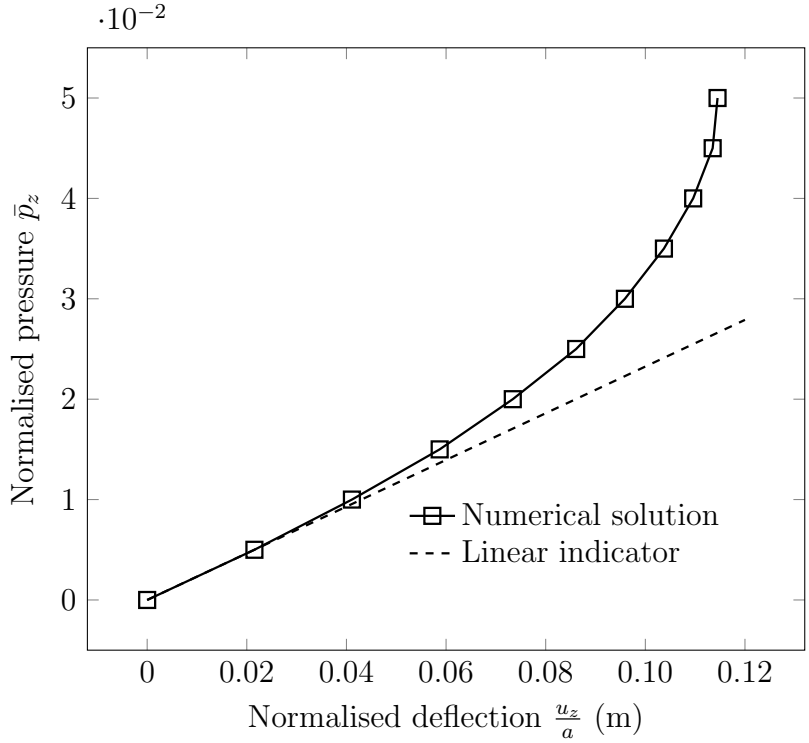

Figure 6.8: The normalised pressure $\bar{p}_z$ at the centre point of the membrane surface against normalised deflection $\frac{u_z}{a}$ of the initially flat linear elastic membrane problem subjected to a uniform pressure.

	Load step		
Iteration	1	2	3
1	2.000×10^{0}	2.000×10^{0}	2.000×10^{0}
2	2.097×10^{-1}	9.704×10^{-2}	1.673×10^{-2}
3	8.512×10^{-3}	1.683×10^{-6}	1.513×10^{-6}
4	4.307×10^{-8}	–	–
Iteration	8	9	10
1	2.000×10^{0}	2.000×10^{0}	2.000×10^{0}
2	9.274×10^{-2}	4.412×10^{-2}	1.273×10^{-2}
3	9.926×10^{-6}	4.389×10^{-6}	4.315×10^{-6}

Table 6.1: Residual norms in the Newton-Raphson method of the initially flat linear elastic membrane problem subjected to a uniform pressure.

The residual norms of the non-linear system of equations at each iteration step over the first and the last three load steps of the Newton-Raphson method are given in Table 6.1 where the stopping criterion described in Eq. (5.28) is satisfied using four iteration steps for the first load step and using three iteration steps over the other five load steps. Compared with the residual vector for large deformation analyses in Chapter 5, three components for each collocation point are included in the residual vector for membrane problems. However, the convergence rates of residual norms in these selected load steps are close to 2.0, which is the theoretical value. The convergence rate of the Newton-Raphson method is not affected by the number of components in the residual vector.

The study above demonstrates the MEPCM to deliver apparently physically reasonable results. However to properly validate, further studies of the rectangular linear elastic membrane were then carried out. In addition to the square membrane ($a/b = 1$), a rectangular membrane with $a/b = 7/5$ was studied and various discretisations were applied to both problems. The reference results of the normalised maximum deflections u_z/a at the central point of the rectangular membranes with different aspect ratios are given in Table 6.2 where the reference results collected in [270] are listed for comparison without further citations of the original publications. These reference results are obtained by different approximated solutions and the solution given by Storakers is seen the closest to the exact solution. In this table, N_c represents the number of nodes in mesh-based methods instead of the number of collocation points in the MEPCM. When $a/b = 1$, the MEPCM result is close to reference results and the percentage difference of the normalised out-of-plane displacement u_z/a between the MEPCM and the Storakers's results is 0.78%. The numerical result using the MEPCM is larger than Hencky's and Kao and Perrone's results. When the ratio a/b is greater than one, the maximum deflection is smaller than that of square membranes as the side length b is shorter than a, in which the change of geometry restricts the inflation of the rectangular membrane. The normalised deflection obtained by the MEPCM is greater than most results in Table 6.2 but it is still lower than Foppl's and Storakers's results. The percentage differences between the MEPCM and Storakers's solution is 2.42% .

	$a/b = 1$		$a/b = 7/5$	
Methods	N_c	u_z/a	N_c	u_z/a
Foppl (1920)	–	0.1208	–	0.0909
Hencky (1921)	–	0.1080	–	–
Borg (1953)	–	–	–	0.0833
Kao and Perrone (1972)	–	0.1090	–	0.0810
Storakers (1983b)	–	0.1156	–	0.0869
FEM	149	0.1142	189	0.0843
AEM (2001)	149	0.1082	189	0.0801
MEPCM	41×41	0.1147	43×31	0.0848

Table 6.2: Normalised central deflection $\frac{u_z}{a}$ with different aspect ratios and discretisations of the initially flat linear elastic membrane problem subjected to a uniform pressure.

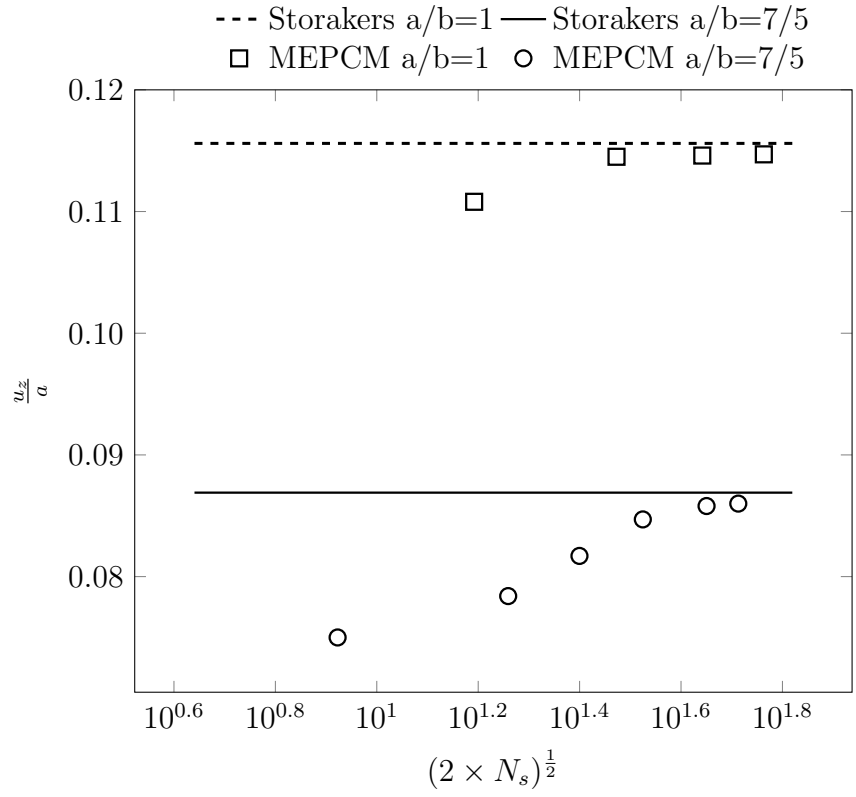

Figure 6.9: The normalised deflection u_z/a at the centre point against the number of degrees of freedom of the initially flat linear elastic membrane problem subjected to a uniform pressure.

Figure 6.9 shows the normalised deflection u_z/a at the centre point against the number of degrees of freedom of the initially flat linear elastic membrane problem subjected to a uniform pressure. With an increasing number of degrees of freedom, the normalised deflections for both square and rectangular membranes using the MEPCM is getting closer to Storakers's results. The maximum deflection u_z increases with a uniformly refined discretisation. As the out-of-plane displacements for this linear elastic membrane problem are not very large, the membrane problems using the large strain hyperelastic Ogden material model are presented in the following.

6.5.2 Inflation of a square hyperelastic membrane

In this example, the inflation of a square membrane using the hyperelastic Ogden material model with an initial prestretch and clamped boundary conditions is analysed. The simulation of this square membrane problem has already been carried out in [291], which provides the reference results to this problem for comparison.

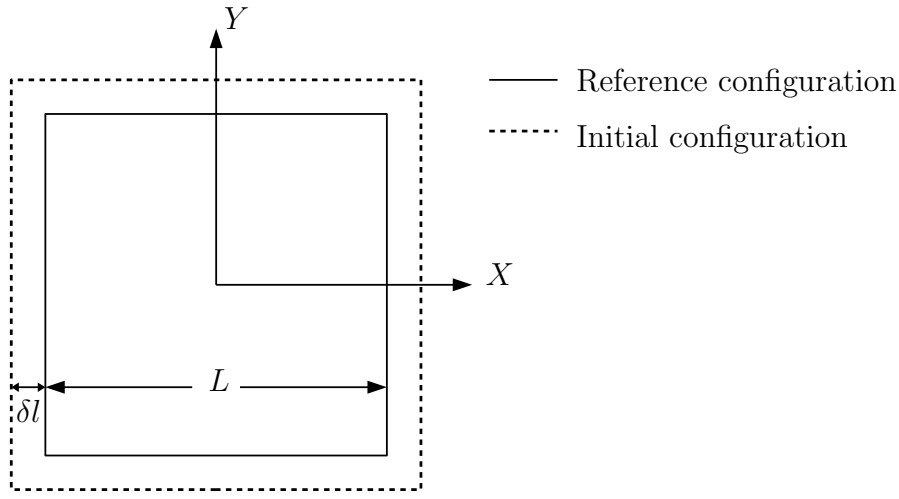

Figure 6.10: The reference and initial configurations of the square hyperelastic membrane problem subjected to a uniform pressure.

The reference and initial configurations of this membrane problem are shown in Figure 6.10, where the side length in the reference configuration, $L = 20$ cm and the original thickness of the thin membrane, $h_0 = 0.1$ cm. The initial external pressure was $p_0 = 0.98$ kPa. All boundaries were fully fixed. As the rotation stiffness for membrane problems is

zero, clamped boundary conditions can be simplified as fully fixed boundary conditions. In order to avoid numerical issues arising from the zero tangent stiffness of this flat membrane without any load (as has been discussed in §6.1), the square membrane in the reference configuration was prestretched by applying an in-plane prescribed prestretch vector $\{u^{pre}\}$ to boundaries before the external load was applied, resulting in the initial configuration (see Figure 6.10). As the exact value of prestretch is not given in the reference [291]. The in-plane prestretch components in $\{u^{pre}\}$ were chosen to be $\delta l = u_x^{pre} = u_y^{pre} = 0.05$ cm and the external load comprised a uniform pressure applied to the membrane surface.

This example is studied to show the effectiveness of the geometrically non-linear MEPCM for large strain hyperelastic material models. The rubber behaviour of this square membrane is described by the incompressible Ogden material model where the free-energy function has been given in Eq. (6.22) and using the material parameters (which can be found in [273, 292])

$$\alpha_1 = 1.3, \quad \alpha_2 = 5.0, \qquad \alpha_3 = -2.0, \tag{6.40a}$$

$$\mu_1 = 6.3, \quad \mu_2 = 0.012, \quad \mu_3 = -0.1\text{kg/cm}^2. \tag{6.40b}$$

As the equilibrium path of this problem using the hyperelastic Ogden material model shows instability, which cannot be traced by the Newton-Raphson method, a combined Newton-Raphson arc-length method is employed to capture the snap-through behaviour. The details of this method have been discussed in §6.4 and given in Appendix D. The external load in the current load step is obtained by multiplying the load factor λ_m in this load step with the initial pressure of $p_0 = 0.98$ kPa. The maximum number of load steps and iterations were predefined as 150 and 10 respectively, and the tolerance number was set as η=10^{-5}. To study this square membrane example, 21×21 collocation and source points were distributed uniformly in the interior of the problem domain and on boundaries.

Figure 6.11 depicts the evolution of the deformed geometry of the square membrane over four different load steps. The total deformation results from the initially applied prestretch and the external pressure. The out-of-plane displacements at all collocation

points in each subfigure are indicated by different colours and the corresponding values of different colours are given by the colourbar in each subfigure with the same unit as the dimensions of the geometry. The initially flat membrane inflates from Figure 6.11(a)-(d), corresponding to central deflections, u_z=4.39 cm to u_z=21.49 cm, respectively. The deflection, u_z in Figure 6.11(d) is over 20 cm which is the side length of the square membrane in the reference configuration. Both the in-plane tension and the out-of-plane deflection are clearly significant as compared to the original dimensions of the square membrane.

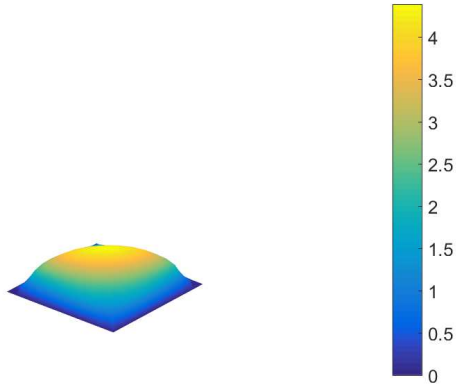

(a) $u_z(0,0) = 4.39cm.$

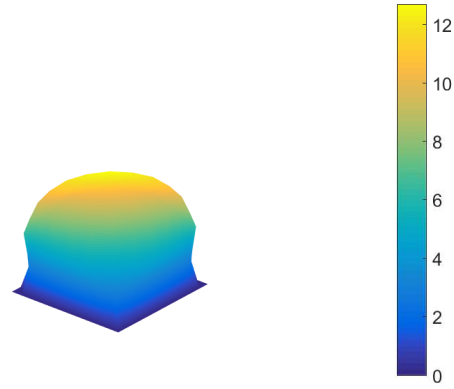

(b) $u_z(0,0) = 12.68cm.$

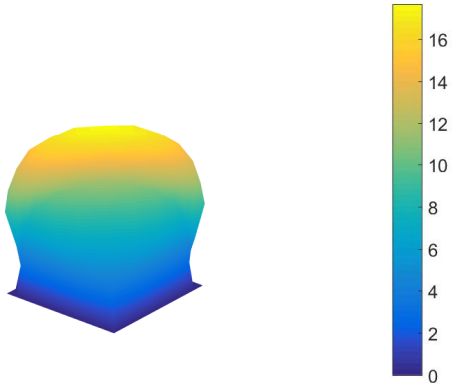

(c) $u_z(0,0) = 17.64cm.$

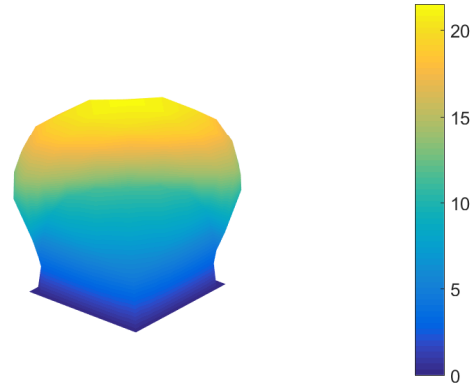

(d) $u_z(0,0) = 21.49cm.$

Figure 6.11: The deformed configurations with the out-of-plane displacement, u_z (cm) at different load steps of the square hyperelastic membrane problem subjected to a uniform pressure.

To examine the pressure-deflection relationship and the effect of prestretch values on

the equilibrium path in this membrane problem, the uniform pressure against deflection u_z at the central point of the square membrane surface with four different prestretch values is given in Figure 6.12. This equilibrium path is captured using the Newton-Raphson arc-length method and the reference results [291] are also plotted in this figure for comparison. It can be seen that the snap-through behaviour using different prestretch values is captured clearly and the pressure-deflection curves for this square membrane problem exhibit similar trends with the reference results in general. In the analyses using different prestretch values and reference results, the pressure increases sharply at the beginning of the deformation until it reaches a limit point with the maximum pressure (an instability point) which corresponds to the deformed state shown in Figure 6.11(b). After that, an apparent drop of the pressure is followed by a monotonic increase. The membrane keeps inflating with an non-monotonically increasing external pressure.

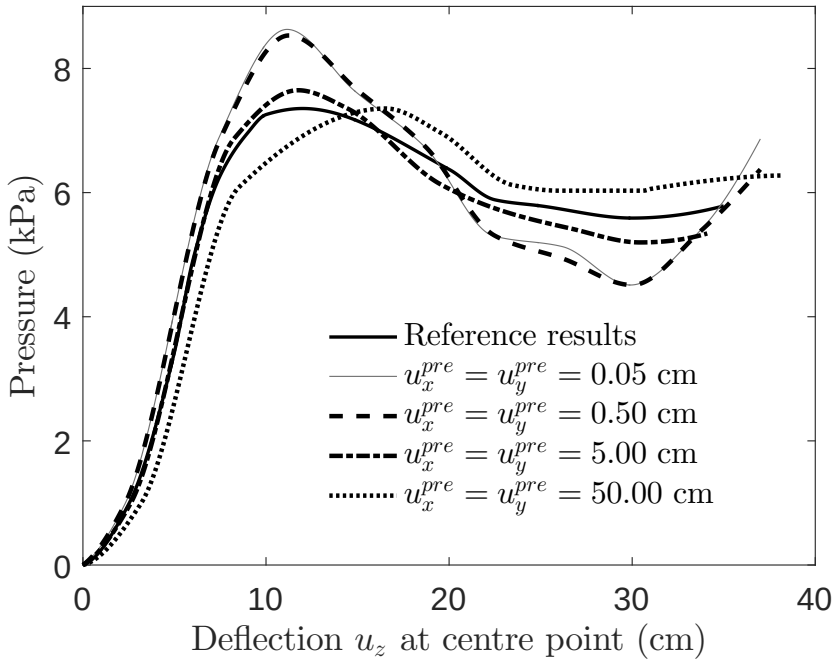

Figure 6.12: Pressure versus deflection at central point of the square hyperelastic membrane problem subjected to a uniform pressure.

Also clear in Figure 6.12 is the fact that the prestretch value $\{u^{pre}\}$ adopted in the reference configuration has a clear effect on the pressure-deflection relationship, perhaps not a surprise. The analyses with $\{u^{pre}\} = \{0.05, 0.05\}^T$ and $\{u^{pre}\} = \{0.50, 0.50\}^T$ (cm) show very close numerical results except the slightly different maximum pressures. At the

start of the equilibrium path using these two prestretch values, the membrane is stiffer to inflate and the pressure increases faster than using the other values, reaching the maximum pressure which is higher than using the other cases. Then the pressure decreases to reach the local minimum pressure value followed by a re-rise. After these two instability points, the equilibrium paths with $\{u^{pre}\} = \{0.05, 0.05\}^T$ and $\{u^{pre}\} = \{0.50, 0.50\}^T$ (cm) are still close to each other. When the prestretch values are 5.00 cm and 50.00 cm, the square membrane becomes easier to inflate than in the other cases with smaller gradients at the beginning of the path and a smaller peak pressure value. For the same pressure value, the analysis with the largest value of the prestretch, $\{u^{pre}\} = \{50.00, 50.00\}^T$ (cm) results in the largest central deflection u_z. In this analysis, it is observed that the maximum pressure decreases as the prestretch increases. The larger prestretch value can affect the instability behaviour, i.e. the equilibrium path using $\{u^{pre}\} = \{0.05, 0.05\}^T$ (cm) shows stronger instability than using $\{u^{pre}\} = \{50.00, 50.00\}^T$ (cm). The use of prestretch can also lower the maximum pressure.

It can be seen that the analysis with $\{u^{pre}\} = \{5.00, 5.00\}^T$ (cm) gives the closest results with the reference results but there are still some differences. Their equilibrium paths at the beginning are nearly overlapped but show some differences from the pressure value of about 6 kPa. The membrane in the reference results is softer to inflate. Then the difference can be seen at the peak pressure value, at which the peak pressure in the reference results is a lower than the numerical result with $\{u^{pre}\} = \{5.00, 5.00\}^T$ (cm). After the peak pressure, the reference results are still softer than using $\{u^{pre}\} = \{5.00, 5.00\}^T$ (cm). Therefore, the prestretch values used in [291] is analysed between 0.50-5.00 (cm). The numerical and reference results of this membrane problem were obtained by different methods and discretisations. Different prestretch values were applied to the reference configuration in the numerical and reference results, which results in different initial configurations. However, the snap-through behaviour is obtained using the MEPCM and the equilibrium path using $\{u^{pre}\} = \{5.00, 5.00\}^T$ (cm) generally agree well with the reference results.

In order to investigate the influence of the value of a prestretch, some formulations introduced in previous sections need to be recalled. The resultant forces used in the governing PDEs for geometrically non-linear membrane problems (as given in Eqs. (6.25)),

are calculated using the second Piola-Kirchhoff stress $[S_n]$ in terms of the reference configuration, and the current thickness of the membrane, h as described in Eq. (6.28). Since the same uniform pressures are applied to all analyses with different values of the prestretch, $[S_n]$ is identical with different values of the prestretch. It is presented in Eq. (6.21) that the thickness of the membrane in the initial configuration h^{pre} is affected by prestretch. To measure this influence, the membrane thicknesses in the initial configuration h^{pre} and the maximum pressures at the first limit points of pressure-deflection curves $(p_z)_{max}$ using four different prestretch values are given in Table 6.3. It is clear that a larger value of the prestretch leads naturally to a thinner membrane in the initial configuration, achieving a lower limit point on the pressure-deflection curve. When the prestretch $u_x^{pre} = u_y^{pre} = 50$ cm, the gradient of the equilibrium path at the start indicates a softer response and the instability behaviour is less obvious than the other cases. The reference result of the maximum pressure in the equilibrium path is closer to the results using prestretch values 50.00 cm than 5.00 cm but the equilibrium path generally agrees better with the case using 5.00 cm.

u_x^{pre} (cm)	u_y^{pre} (cm)	h_0(cm)	h^{pre}(cm)	$(p_z)_{max}$(kPa)
0.05	0.05	0.1	0.0990	8.6294
0.50	0.50	0.1	0.0907	8.5314
5.00	5.00	0.1	0.0444	7.6490
50.00	50.00	0.1	0.0028	7.3451
Reference	–	0.1	–	7.3550

Table 6.3: The thicknesses and the maximum pressures of the square hyperelastic membrane problem subjected to a uniform pressure.

The residual norms in the non-linear system of equations over the first three load steps and another three load steps after the first instability point of the Newton-Raphson arc-length method are given in Table 6.4. It can be seen that, near asymptotic quadratic convergence using the Newton-Raphson arc-length method is reached using three or four iteration steps before satisfying the stopping criterion given in Eq. (5.28). The convergence rate in the Newton-Raphson arc-length method is not affected by the instability of the equilibrium path.

A half diagonal of the flat square membrane was taken for analysis as a portion of the full geometry where one end (the corner point of the square membrane) was fully

	Load step		
Iteration	1	2	3
1	2.000×10^{0}	2.000×10^{0}	2.000×10^{0}
2	9.000×10^{-2}	1.950×10^{-1}	9.326×10^{-2}
3	3.990×10^{-3}	9.582×10^{-3}	8.141×10^{-6}
4	3.036×10^{-7}	9.053×10^{-7}	–
Iteration	60	61	62
1	2.000×10^{0}	2.000×10^{0}	2.000×10^{0}
2	1.832×10^{-1}	4.239×10^{-2}	1.842×10^{-1}
3	5.360×10^{-3}	9.723×10^{-6}	4.674×10^{-3}
4	1.116×10^{-7}	–	6.589×10^{-7}

Table 6.4: Residual norms in the arc-length Newton-Raphson method of the square hyperelastic membrane problem subjected to a uniform pressure.

fixed and the roller boundary condition was applied to another end (centre point of the square membrane). The maximum number of iterations in the arc-length Newton-Raphson method was set the same as the analysis for the full geometry. The numerical results of the deformed configurations at four different load steps are shown in Figure 6.13, in which the similar changing trend is observed to the full geometry as shown in Figure 6.11.

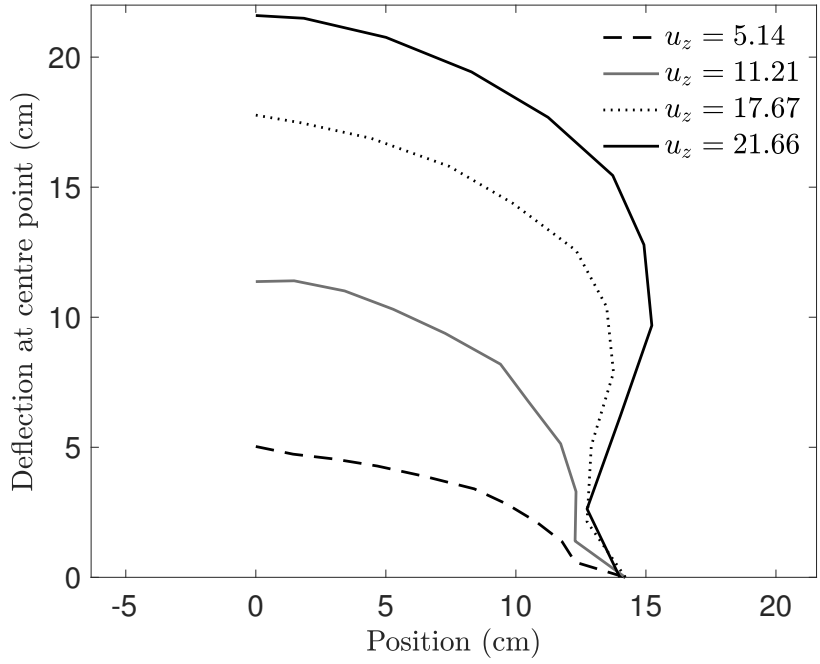

Figure 6.13: The deformed configurations with the out-of-plane displacement, u_z (cm) at different load steps of the half diagonal of the square hyperelastic membrane problem subjected to a uniform pressure.

6.5.3 Inflation of a circular membrane with hyperelasticity

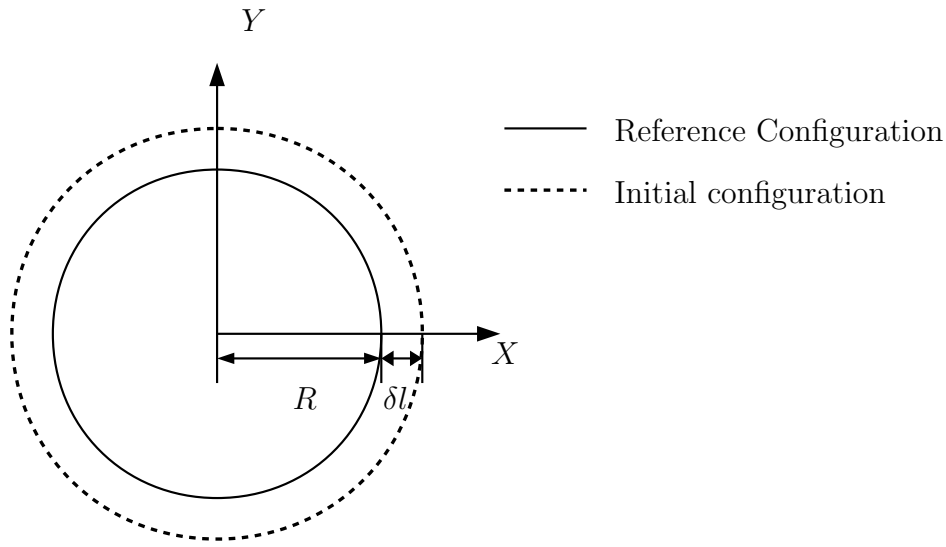

Figure 6.14: The reference and initial configurations of the circular hyperelastic membrane subjected to a uniform pressure.

The final example is the inflation of a circular membrane with an initially applied prestretch, which has been modelled in [291, 293] using the FEM. The reference and the initial configurations of the circular membrane are shown in Figure 6.14 where the radius and the original thickness of the circular membrane were $R = 10$ cm and $h_0 = 0.1$ cm, respectively. All material parameters used for the hyperelastic Ogden material model, the external pressure at the first load step and boundary conditions of the circular membrane were the same as in the previous square membrane problem. The same prestretch value $u_x^{pre} = u_y^{pre}$=0.50 cm was used in this example. Again, the Newton-Raphson arc-length method was employed to solve the non-linear system of equations, where the maximum number of load steps and iterations were set as 150 and 10, respectively, and the predefined tolerance number η was 10^{-5}. Using the MEPCM to analyse this initially flat circular problem, a total number of 361 collocation and source points, i.e. 10 collocation points in the radial direction, 36 collocation points in the axial direction and 1 collocation point at the central of the circular membrane, were distributed.

The evolution of this circular membrane using the hyperelastic Ogden material model obtained at different load steps in this simulation is plotted in Figure 6.15. The colours

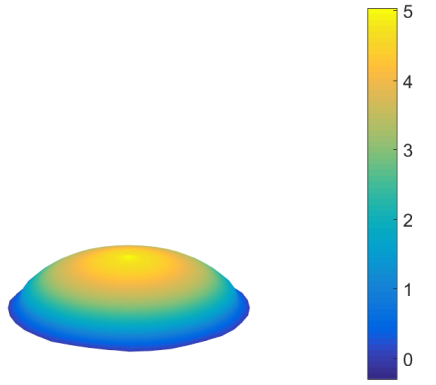

(a) $u_z(0,0) = 5.02$ cm.

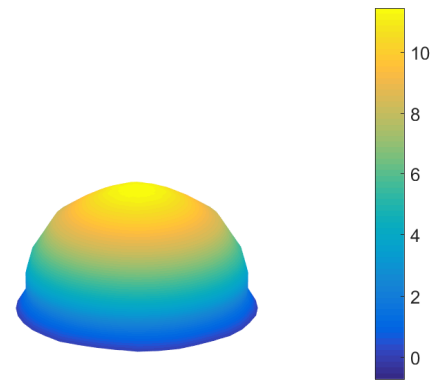

(b) $u_z(0,0) = 11.37$ cm.

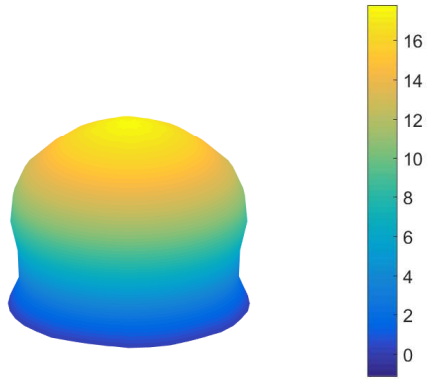

(c) $u_z(0,0) = 17.77$ cm.

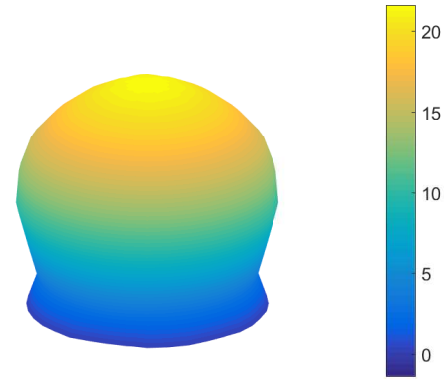

(d) $u_z(0,0) = 21.60$ cm.

Figure 6.15: The deformed configurations with the out-of-plane displacement, u_z (cm) at different load steps of the circular hyperelastic membrane subjected to a uniform pressure.

in each subfigure represent the out-of-plane deflections at all collocation points of each deformed configuration with a colourbar next to the configuration which indicates the scale of the out-of-plane deformation. The deformation of the circular membrane can be seen to be very similar to the previous example, although here a spherical form is approached. The in-plane tension and out-of-plane deflection can be observed clearly.

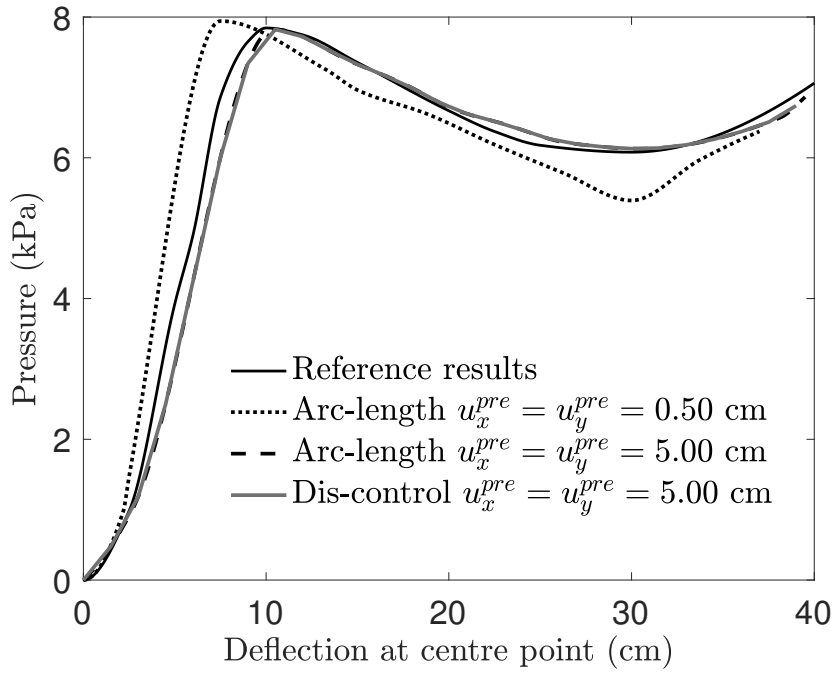

Figure 6.16: Pressure versus deflection at central point of the square hyperelastic membrane problem subjected to a uniform pressure.

Similarly to the last example of the square membrane, the pressure-deflection curves at the central point of the circular membrane with two different values of prestrtch, 0.50 cm and 5.00 cm are presented in Figure 6.16. The reference results for this circular membrane are also plotted in this figure for comparison. The snap-through behaviour observed in the last example is also detected for the present circular membrane problem. As shown in this figure, the circular membrane with a prestretch is inflating under the uniform pressure until the pressure reaches a limit point with the maximum pressure. Then, a decrease of the pressure occurs followed by a monotonic increase. The configuration corresponding to the maximum pressure is shown in Figure 6.15(b). It can be seen from Figure 6.15(c)-(d) and Figure 6.16 that the circular membrane keeps inflating after the first instability point although the pressure value goes down.

Again, two different values of the prestretch are chosen in the simulation, which gives the similar trends for pressure against deflection curves. Comparing these two curves using different prestretches, the smaller prestretch value $u_x^{pre} = u_y^{pre}$=0.50 cm makes it difficult to inflate the initially flat circular membrane therefore a higher maximum pressure is required than the other case. After the first instability point, the pressures with two different prestretch values decrease at a similar rate, but the deflection u_z is larger using a larger prestretch than another one with the same pressure value. In this example, the equilibrium path with a prestretch value of 5.00 cm is closer to the reference results but with some differences at the start of the deformation. The membrane in the reference is stiffer to inflate at the beginning stage before the instability point than using $u_x^{pre} = u_y^{pre}$=5.00 cm but their maximum pressure values are very similar. The pressure-deflection relationship at the central point of the circular membrane in the reference [291] shows the similar trend as the numerical results. As discussed above, the differences between the reference and numerical results could be caused by the same reasons, i.e. different methods and discretisations, and the use of different prestretch values in numerical and reference results. The differences in the analyses with different values of the prestretch may be caused by the membrane thickness, where the larger prestretch value, i.e. 5.00 cm, makes the membrane thickness in the initial configuration thinner, leading to a larger deformation than the case using a prestretch of 0.50 cm with the same pressure value as shown in Table 6.5. Comparing the maximum pressure $(p_z)_{max}$ between the square membrane in last example and a circular membrane in this example, a higher pressure value is required for the circular membrane to reach the instability point in the reference results, resulting from the differences of geometry. The numerical results using the MEPCM with $u_x^{pre} = u_y^{pre}$=5.00 cm give higher maximum pressure for circular membrane than the square membrane. The circular membrane is axisymmetric geometry and the discretisations for the square and circular membranes are different but as shown in Table 6.5 the initial thickness values are the same in both the square and circular membranes. Since there is no snap-back behaviour for this example, the displacement-controlled Newton-Raphson method is employed to solve this example for comparison, in which the total out-of-plane displacement at the centre point was 40 cm and applied by 160 steps. The pressure-deflection curve using the displacement-

controlled Newton-Raphson method is given in Figure 6.16. It can be observed that the displacement-controlled Newton-Raphson method presents very similar results to the results obtained by the arc-length Newton-Raphson method with the same value of prestretch. However, in this figure, slight differences can be seen around the first instability point as the increment of the externally applied displacement at each step using the displacement-controlled Newton-Raphson method is a constant, making it less accurate to capture the equilibrium path around the instability point than using the arc-length Newton-Raphson method. The increment of the externally applied load in the arc-length Newton-Raphson method varies at each load step, which is determined by the incremental variables in the last load step.

For both square and circular hyperelastic Ogden membranes studied in this section, the numerical results using the MEPCM in terms of their inflation process over four load steps (one step before the first instability point, one load step at the first instability and two loads after the first instability points) have been presented. The equilibrium paths with snap-through behaviour have been traced and the configurations correspond to the maximum pressure values on the load-deflection curves have been analysed. The equilibrium paths of both square and circular membranes with different prestretch values have been presented, which are compared with the reference results. They show similar trend with two instability points and the MEPCM results show generally good agreement with the reference results when $u_x^{pre} = u_y^{pre}$=5.00 cm. It has been analysed that the values of prestretch have an effect on the equilibrium curve including the positions and the values of the instability points. Both of these two examples show that a larger prestretch can lead to a thinner membrane in the initial configuration, which makes the membrane softer to inflate. It has been seen from the numerical results that a large value of the prestretch can reduce the instability.

u_x^{pre} (cm)	u_y^{pre} (cm)	h_0(cm)	h^{pre}(cm)	$(p_z)_{max}$(kPa)
0.50	0.50	0.1	0.0907	7.9433
5.00	5.00	0.1	0.0444	7.8257
Reference	–	0.1	–	7.8453

Table 6.5: The thicknesses and the maximum pressures of the circular hyperelastic membrane problem subjected to a uniform pressure.

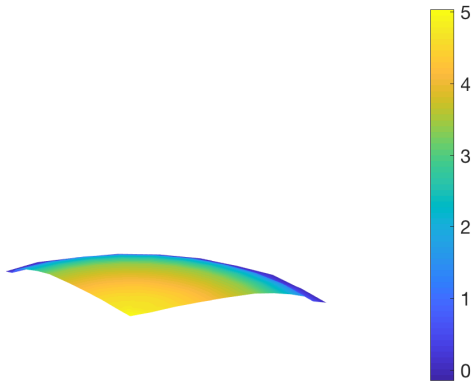

(a) $u_z(0,0) = 5.26$ cm.

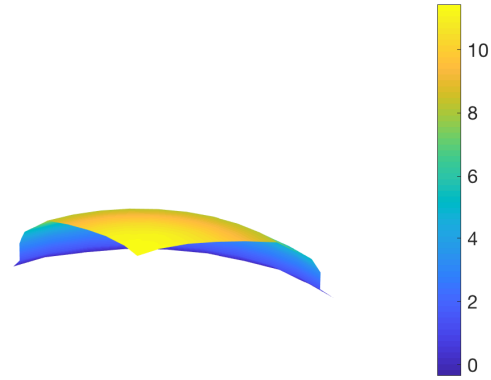

(b) $u_z(0,0) = 10.52$ cm.

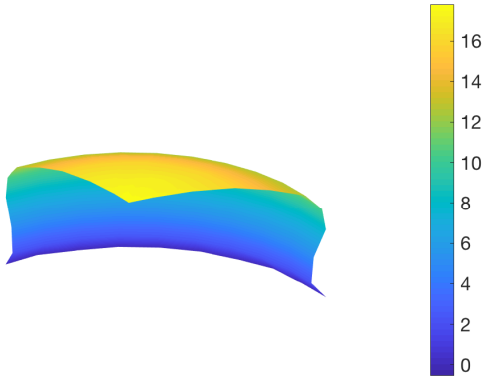

(c) $u_z(0,0) = 17.98$ cm.

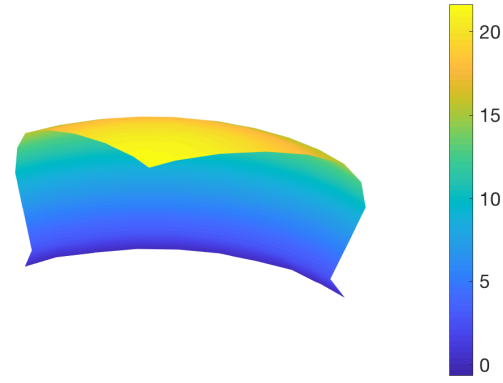

(d) $u_z(0,0) = 20.78$ cm.

Figure 6.17: The deformed configurations with the out-of-plane displacement, u_z (cm) at different load steps of quarter of the circular hyperelastic membrane subjected to a uniform pressure.

Due to symmetry, quarter of the circular membrane was taken for analysis. Roller boundary conditions were applied at the symmetric boundaries. The deformed configurations with the out-of-plane displacement, u_z at different load steps of quarter of the circular hyperelastic membrane with prestretch 0.50 cm are given in Figure 6.17, which shows the similar inflation procedure to the full geometry.

6.6 Concluding remarks

In this chapter, an application of the geometrically non-linear MEPCM to membrane problems has been investigated. The initial configuration results from an initially applied prestress or prestretch has been introduced therefore three configurations are included for membrane problems. Stress measures for linear elastic and hyperelastic materials have been presented. The governing PDEs, which include the in-plane and the out-of-plane components, have been described by the Total Lagrangian formulation in terms of the reference configuration, where all variables referred to the reference configuration have been used and the out-of-plane deformation is characterised by in-plane stresses and strains. The proposed formulation can accommodate both linear elastic and large strain hyperelastic material models, resulting in a non-linear system of equations. A Newton-Raphson arc-length method has been employed to capture the snap-through behaviour in the equilibrium path of hyperelastic membranes involving very large deformations. Some numerical examples using both linear elastic and the hyperelastic Ogden model with a prestretch have been analysed to validate the capabilities of the proposed method. The inflation process and the non-linear load-displacement relationship have been observed for the linear elastic membrane problem. Comparisons in terms of the central deflection with various aspect ratios and discretisations between the reference results and the numerical results using the MEPCM have been conducted, in which a good agreement has been observed. For the hyperelastic square and circular membranes, the proposed geometrically non-linear MEPCM has been employed to obtain their evolution process. The differences of their equilibrium paths using various prestretch values have been discussed and one of those prestretch values gives generally good agreement with the reference results although the prestretch value is not given in the reference. In

addition, it has been analysed that the thickness in the initial configuration is affected by the prestretch, which has further influence on the equilibrium path and deformation.

Chapter 7

Conclusions and recommendations for future work

7.1 Conclusions

Numerical modelling of solid mechanics problems with geometric non-linearity remains challenging due to their complicated mechanical behaviour and high computational cost. A variety of numerical methods have been reviewed, however, it is still an ongoing research topic in the field of computational mechanics to develop accurate and efficient numerical methods that can accommodate these problems. Weak form-based meshless methods become attractive in some ways to provide solutions but they are restricted by their high computational cost caused by numerical integration. In this thesis, a strong form-based meshless method with local maximum entropy basis functions has been proposed as a novel numerical model, which has been applied to solve geometrically non-linear problems.

The overview and motivation of this thesis have been introduced in Chapter 1. Chapter 2 has presented the background of meshless methods. Some properties of meshless basis functions have been discussed followed by four representatives of meshless basis functions. After that, the development together with the classification of meshless methods have been discussed. The remaining research challenges have been listed at the end of Chapter 2. The main contributions of this thesis are contained from Chapter 3 to

Chapter 6. In the following, important points and main conclusions of each contributing chapter are summarised one by one.

The local maximum entropy point collocation method

In Chapter 3, the local maximum entropy point collocation method (MEPCM) has been proposed for solving Poisson and linear elastic problems. The conventional PCM with RK basis functions has been implemented first, however, the imposition of Dirichlet boundary conditions is inaccurate as the RK basis function does not satisfy the Kronecker delta property and the calculation of the second basis function derivatives is computationally expensive. The local maximum entropy (max-ent) basis function has, therefore, been employed in a PCM, where those issues in the conventional RK-based point collocation method have been addressed. Local max-ent basis functions possess the weak Kronecker-delta property on boundaries, which allows the direct imposition of Dirichlet boundary conditions. Some variables used in max-ent basis functions can be reused in their derivative expressions, which reduces the computational cost for the overall analysis using the MEPCM. Two-dimensional Poisson and one- and two-dimensional linear elastic examples have been presented using both methods. The comparison in terms of accuracy, CPU times and flops has been studied, where the MEPCM performs better than the RK-based point collocation method as the MEPCM results are more accurate with higher rate of convergence and lower flops than the other.

Error estimation and adaptive strategies

In Chapter 4, r-, h- and combined rh-adaptive strategies have been developed in the PCM with local max-ent basis functions for linear elasticity problems. r-adaptivity using the MEPCM has been proposed first where the discretisation errors are minimised by points relocation, preserving the same number of degrees of freedom. The errors are estimated by the material equilibrium residuals, which provide the moving distances and directions to relocate collocation points. h-adaptive MEPCM has then been presented, in which the residuals of strong form-based governing PDEs at three calculation points in each Delaunay triangulation has been used as the local error estimate. A refinement strategy based on the discretisation of collocation points has been adopted. As the pre-

scribed accuracy cannot be achieved by a pure adaptivity efficiently, r- and h-adaptivity have been combined to rh-adaptivity which can reduce the discretisation errors with limited number and optimal positions of points. Compared with adaptivity in weak form-based meshless methods, the implementation of adaptivity in the MEPCM is more straightforward without considering the remeshing for numerical integration and mesh distortion. After the discussion of numerical issues, linear elasticity problems have been analysed to demonstrate the performance of the proposed adaptive strategies. The comparison using different adaptive strategies in terms of accuracy and computational cost has been conducted, in which the combined rh-adaptivity achieves better accuracy with less number of degrees of freedom than pure strategies but with much computational cost.

Geometrically non-linear analysis

In Chapter 5, the MEPCM with h-adaptivity has been developed for solving geometrically non-linear problems. Completed formulations including the kinematics and stress measures in terms of different configurations have been given. The governing PDEs and boundary conditions have been described using the Total Lagrangian formulation referred to the reference configuration. As the non-linear system of equations in terms of the field variables at source points has been formulated, the Newton-Raphson method has been employed to linearise the non-linear system, where the stopping criterion have been discussed. After the initial calculation, h-adaptivity for small deformations has been extended to large deformations, in which the local error estimator is replaced by the governing PDEs in terms of the first Piola-Kirchhoff stress. The problem needs to be recalculated after each h-adaptive step. A variety of numerical examples subjected to large deformations have been presented to demonstrate the performance of the proposed method, where a non-linear strain-displacement relationship has been observed. h-adaptivity has been employed in selected examples, which can improve the accuracy more efficiently than using the uniform refinement.

Analysis of membrane problems

In Chapter 6, the MEPCM for geometrically non-linear problems has been extended to the analysis of membrane problems. Three different configurations including the reference, initial and current configurations have been introduced as a prestretch is used to avoid the non-zero stiffness matrix. The kinematics and stress measures for linear elastic and hyperelstic materials have been given. After that, the governing PDEs and boundary conditions have been described using the Total Lagrangian formulation in terms of the reference configuration. The Newton-Raphson method has been used for solving linear elastic membrane problems. As the instability occurs at the equilibrium path of hyperelastic materials with large deformations, the Newton-Raphson arc-length method has been employed to find the snap-through equilibrium path. Some numerical examples including linear elastic and hyperelastic Ogden materials have been analysed to validate the proposed methods. The effect of prestrestch values on the equilibrium path have been discussed. As all examples do not have analytical solutions, reference results have been used for comparison.

7.2 Recommendations for future work

Based on the work undertaken in this thesis, there are a number of areas which present themselves as clear opportunities for future research and development. Some of those points are listed as below:

- Geometric non-linearity has been modelled using the proposed MEPCM in many problems in this thesis, which gives the structural response under extremely large external loads or low stiffness. The proposed MEPCM can be further applied to material non-linearity where the linear Kirchhoff stress-logarithmic strain relationship can be used.

- The modelling of membrane problems using the hyperelastic Ogden material model has been provided in this thesis and it would be clearly interesting to see the performance using the other hyperelastic material models such as the neo-Hookean, Mooney-Rivlin, and Hencky models for membrane problems. Different expressions

for the free energy functions would be used to find the corresponding equilibrium paths.

- All numerical examples demonstrated in this thesis have two-dimensional geometries although membrane problems have out-of-plane displacements. Extending the numerical analyses using the MEPCM to three dimensions is more realistic and challenging. The representation of boundaries and the construction of basis functions with an appropriate choice of the size of support domain for each collocation point need to be further explored.

- Strong form-based point collocation methods are relatively easy to implement, but in use they often suffer from instabilities and lower accuracy. One of the possible reasons is that the governing partial differential equations and corresponding boundary conditions are applied only at a limited number of individual collocation points. These conditions are neglected at the other points. There is always a set of points at which the approximations are more accurate than at the other points, however, no theoretical "best" distribution is available for the number and locations of collocation points. Some special techniques have to be investigated to improve the quality of a discretisation.

- All the examples presented in this thesis have been chosen with boundaries which are aligned with the collocation points. There is a lack of well-developed method for tracking boundaries when the geometry boundaries do not align with distributed points. Some recent work on this topic has been proposed such as the use of B-splines but there are still some distances from a method which can be extended for all types of arbitrary boundaries.

- The local error estimator used in h-adaptivity for the point collocation method in this thesis, takes into account the error residuals at some generated calculation points that are distributed in domain area. In further study, the error residuals at boundaries could be considered and the errors result from boundaries can be reduced using the following h-refinement strategy.

- Basis functions in the current PCM are obtained by the local maximum entropy

approximation, which shows some advantages. However, some other types some basis functions could also be considered to make a comparison in terms of the accuracy and computational cost, such as using the radial basis function.

Appendix A

The second derivatives of a local maximum entropy basis function

This appendix presents the derivation of the second derivatives of a local maximum entropy basis function. The expression of the local max-ent basis function at a single point is

$$\phi_i = \frac{Z_i}{Z} = \frac{w_i e^{f_i(\{x\},\{\lambda\})}}{\sum_{j=1}^{N_s^*} w_j e^{f_j(\{x\},\{\lambda\})}}, \tag{A.1}$$

where

$$f_i(\{x\},\{\lambda\}) = -\{\lambda\}^T \cdot (\{x_i\} - \{x\}) \tag{A.2}$$

and $\{\lambda\}$ is the function of $\{x\}$. The gradient of Z_i and Z can be written as

$$\{Z_{i,k}\} = \{w_{i,k}\}e^{f_i} + w_i e^{f_i}\{f_{i,k}\}, \tag{A.3}$$

$$[Z_{i,kl}] = [w_{i,kl}]e^{f_i} + \{w_{i,l}\}e^{f_i}\{f_{i,k}\} + \{w_{i,l}\}e^{f_i}\{f_{i,k}\} + w_i e^{f_i}\{f_{i,k}\}\{f_{i,l}\} + w_i e^{f_i}[f_{i,kl}], \tag{A.4}$$

and

$$\{Z_{,k}\} = \sum_{j=1}^{N_s^*}\{w_{j,k}\}e^{f_j} + \sum_{j=1}^{N_s^*} w_j e^{f_j}\{f_{j,k}\}, \tag{A.5}$$

$$[Z_{,kl}] = \sum_{j=1}^{N_s^*}\Big([w_{j,kl}]e^{f_j} + \{w_{j,k}\}e^{f_j}\{f_{j,l}\} + \{w_{j,l}\}e^{f_j}\{f_{j,k}\} + w_j e^{f_j}\{f_{j,k}\}\{f_{j,l}\} + w_j e^{f_j}[f_{j,kl}]\Big), \tag{A.6}$$

where the gradient of $f_i(\{x\},\{\lambda\})$ is

$$\{f_{i,k}\} = \frac{\partial f_i}{\partial\{x\}} + \frac{\partial f_i}{\partial\{\lambda\}}[D\lambda] = \{\lambda\} - (\{x_i\} - \{x\})[D\lambda], \tag{A.7}$$

$$[f_{i,kl}] = 2[D\lambda] - (\{x_i\} - \{x\})[D\lambda]\cdot[D\lambda], \tag{A.8}$$

Define $\{r(\{x\},\{\lambda\})\}$ is a function on $\{x\}$ and $\{\lambda\}$ as

$$\{r(\{x\},\{\lambda\})\} = \sum_{j=1}^{N_s^*} -\phi_j\cdot(\{x_j\} - \{x\}) \tag{A.9}$$

and $\{r(\{x\},\{\lambda\})\}$ is exactly zero because of the reproducing conditions. The derivatives of $\{r(\{x\},\{\lambda\})\}$ is

$$[r(\{x\},\{\lambda\})_{,k}] = \left[\frac{\partial r}{\partial x}\right] + \left[\frac{\partial r}{\partial\lambda}\right][D\lambda] = 0, \tag{A.10}$$

where

$$\left[\frac{\partial r}{\partial x}\right] = 1 - \sum_{j=1}^{n}\phi_j(\{x_j\} - \{x\})\frac{\{w_{j,k}\}}{w_j} \tag{A.11}$$

obtained from Eq. (A.9) and

$$\begin{aligned}[J(\{x\},\{\lambda\})] = \left[\frac{\partial r}{\partial\lambda}\right] &= \sum_{j=1}^{N_s^*}\phi_j(\{x\},\{\lambda\})(\{x_j\} - \{x\})\otimes(\{x_j\} - \{x\}) \\ &- \{r(\{x\},\{\lambda\})\}\otimes\{r(\{x\},\{\lambda\})\}.\end{aligned} \tag{A.12}$$

Then $[D\lambda]$ is solved as

$$[D\lambda] = -[J]^{-1} + [J]^{-1}\sum_{j=1}^{N_s^*}\phi_j(\{x_j\} - \{x\})\frac{\{w_{j,k}\}}{w_j}. \tag{A.13}$$

The second derivatives of the basis function is

$$[\phi_{i,kl}] = \frac{[Z_{i,kl}]}{Z} - \frac{\{Z_{i,k}\}\{Z_{,l}\}}{Z^2} - \frac{\{Z_{i,l}\}\{Z_{,k}\}}{Z^2} - \frac{Z_i\{Z_{,kl}\}}{Z^2} + \frac{Z_i(\{Z_{,k}\})^2}{Z^3} + \frac{Z_i(\{Z_{,l}\})^2}{Z^3}. \tag{A.14}$$

Substitute the Eq. (A.3)-(A.6) into Eq. (A.14) then the expression of the second derivatives of the basis functions are obtained.

Appendix B

Tangent stiffness matrix for large deformation analysis

In this appendix the derivation of the tangent stiffness matrix for large deformation analysis is presented. The first Piola-Kirchhoff stress can be written as

$$P_{ij} = \tau_{ik} F^{-T}_{kj}. \tag{B.1}$$

The governing PDE using the total Lagrangian formulation is

$$\frac{\partial P_{ij}}{\partial X_j} = \frac{\partial \tau_{ik}}{\partial X_j}(F^{-1})_{jk} + \tau_{ik}\frac{\partial (F^{-1})_{jk}}{\partial X_j} \tag{B.2}$$

Using the chain rule,

$$\frac{\partial \tau_{ik}}{\partial X_j} = \frac{\partial \tau_{ik}}{\partial \varepsilon_{ab}}\frac{\partial \varepsilon_{ab}}{\partial b_{cd}}\frac{\partial b_{cd}}{\partial F_{ef}}\frac{\partial F_{ef}}{\partial X_j} \tag{B.3}$$

where

$$\frac{\partial \tau_{ik}}{\partial \varepsilon_{ab}} = D_{ikab}, \tag{B.4}$$

$$\frac{\partial \varepsilon_{ab}}{\partial b_{cd}} = \frac{1}{2}\frac{\partial \log(b_{ab})}{\partial b_{cd}}, \tag{B.5}$$

$$\begin{aligned}\frac{\partial b_{cd}}{\partial F_{ef}} &= \frac{\partial F_{cm}}{\partial F_{ef}}F^T_{md} + F_{cm}\frac{\partial F^T_{md}}{\partial F_{ef}} \\ &= \delta_{ce}F_{df} + F_{cf}\delta_{de}\end{aligned} \tag{B.6}$$

and

$$\frac{\partial F_{ef}}{\partial X_j} = \frac{\partial}{\partial X_j}\Big(\frac{\partial x_e}{\partial X_f}\Big). \tag{B.7}$$

Using the chain rule,

$$\frac{\partial (F^{-1})_{jk}}{\partial X_j} = \frac{\partial (F^{-1})_{jk}}{\partial F_{ef}}\frac{\partial F_{ef}}{\partial X_j}. \tag{B.8}$$

The tangent matrix which is the gradient of the governing PDEs with respect to the displacement at source points as

$$\frac{\partial}{\partial d_g}\Big(\frac{\partial P_{ij}}{\partial X_j}\Big) = \frac{\partial}{\partial d_g}\Big(\frac{\partial \tau_{ik}}{\partial X_j}\Big)(F^{-1})_{jk} + \frac{\partial \tau_{ik}}{\partial X_j}\frac{\partial (F^{-1})_{jk}}{\partial d_g} + \frac{\partial \tau_{ik}}{\partial d_g}\frac{\partial (F^{-1})_{jk}}{\partial X_j} + \tau_{ik}\frac{\partial}{\partial d_g}\Big(\frac{\partial (F^{-1})_{jk}}{\partial X_j}\Big) \tag{B.9}$$

where

$$\frac{\partial}{\partial d_g}\Big(\frac{\partial \tau_{ik}}{\partial X_j}\Big) = \frac{\partial \tau_{ik}}{\partial \varepsilon_{ab}}\frac{\partial \varepsilon_{ab}}{\partial b_{cd}}\frac{\partial b_{cd}}{\partial F_{ef}}\frac{\partial}{\partial d_g}\Big(\frac{\partial F_{ef}}{\partial X_j}\Big), \tag{B.10}$$

$$\frac{\partial (F^{-1})_{jk}}{\partial d_g} = \frac{\partial (F^{-1})_{jk}}{\partial F_{ef}}\frac{\partial F_{ef}}{\partial d_g}, \tag{B.11}$$

$$\frac{\partial \tau_{ik}}{\partial d_g} = \frac{\partial \tau_{ik}}{\partial \varepsilon_{ab}}\frac{\partial \varepsilon_{ab}}{\partial b_{cd}}\frac{\partial b_{cd}}{\partial F_{ef}}\frac{\partial F_{ef}}{\partial d_g} \tag{B.12}$$

and

$$\frac{\partial}{\partial d_g}\Big(\frac{\partial (F^{-1})_{jk}}{\partial X_j}\Big) = \frac{\partial (F^{-1})_{jk}}{\partial F_{ef}}\frac{\partial}{\partial d_g}\Big(\frac{\partial F_{ef}}{\partial X_j}\Big). \tag{B.13}$$

Appendix C

The tangent matrix for linear elastic membranes

The membrane force for linear elastic materials is

$$N_{ij} = h_0 (F^{-1})_{ik} P_{kj} \tag{C.1}$$

The first two components R_1 and R_2 in the governing PDE are

$$\frac{\partial N_{ij}}{\partial X_j} = h_0 \Big[\frac{\partial (F^{-1})_{ik}}{\partial X_j} P_{kj} + (F^{-1})_{ik} \frac{\partial P_{kj}}{\partial X_j} \Big] \tag{C.2}$$

where

$$\frac{\partial (F^{-1})_{ik}}{\partial X_j} = \frac{\partial (F^{-1})_{ik}}{\partial F_{ab}} \frac{\partial F_{ab}}{\partial X_j} \tag{C.3}$$

and $\frac{\partial P_{kj}}{\partial X_j}$ is given in Eq. (B.2). The gradient of $\{R_1\}$ and $\{R_2\}$ with respect to d_g is

$$\begin{aligned} \frac{\partial}{\partial d_g} \Big(\frac{\partial N_{ij}}{\partial X_j} \Big) = h_0 \Big[& \frac{\partial}{\partial d_g} \Big(\frac{\partial (F^{-1})_{ik}}{\partial X_j} \Big) P_{kj} + \frac{\partial (F^{-1})_{ik}}{\partial X_j} \frac{\partial P_{kj}}{\partial d_g} \\ & + \frac{\partial (F^{-1})_{ik}}{\partial d_g} \frac{\partial P_{kj}}{\partial X_j} + (F^{-1})_{ik} \frac{\partial}{\partial d_g} \Big(\frac{\partial P_{kj}}{\partial X_j} \Big) \Big] \end{aligned} \tag{C.4}$$

where

$$\frac{\partial}{\partial d_g} \Big(\frac{\partial (F^{-1})_{ik}}{\partial X_j} \Big) = \frac{\partial (F^{-1})_{ik}}{\partial F_{ab}} \frac{\partial}{\partial d_g} \Big(\frac{\partial F_{ab}}{\partial X_j} \Big), \tag{C.5}$$

$$\frac{\partial (F^{-1})_{ik}}{\partial X_j} = \frac{\partial (F^{-1})_{ik}}{\partial F_{ab}} \frac{\partial F_{ab}}{\partial X_j}, \tag{C.6}$$

$$\frac{\partial (F^{-1})_{ik}}{\partial d_g} = \frac{\partial (F^{-1})_{ik}}{\partial F_{ab}} \frac{\partial F_{ab}}{\partial d_g} \tag{C.7}$$

and $\frac{\partial}{\partial d_g}\left(\frac{\partial P_{kj}}{\partial X_j}\right)$ is given in Eq. (B.9).

The third component in the governing PDE is

$$R_3 = N_{11}\frac{\partial^2 d_3}{\partial X_1^2} + 2N_{12}\frac{\partial^2 d_3}{\partial X_1 \partial X_2} + N_{22}\frac{\partial^2 d_3}{\partial X_2^2} + f_z^b, \tag{C.8}$$

. The derivatives of R_3 with respect to d_g are

$$\frac{\partial R_3}{\partial d_g} = \frac{\partial N_{11}}{\partial d_g}\frac{\partial^2 d_3}{\partial X_1^2} + 2\frac{\partial N_{12}}{\partial d_g}\frac{\partial^2 d_3}{\partial X_1 \partial X_2} + \frac{\partial N_{22}}{\partial d_g}\frac{\partial^2 d_3}{\partial X_2^2} \tag{C.9}$$

where

$$\begin{aligned} \frac{\partial N_{ij}}{\partial d_g} &= h_0\Big[\frac{\partial (F^{-1})_{ik}}{\partial d_g} P_{kj} + (F^{-1})_{ik}\frac{\partial P_{kj}}{\partial d_g}\Big] \\ &= h_0\Big\{\frac{\partial (F^{-1})_{ik}}{\partial d_g} P_{kj} + (F^{-1})_{ik}\Big[\frac{\partial \tau_{kl}}{\partial d_g}(F^{-1})_{jl} + \tau_{kl}\frac{\partial (F^{-1})_{jl}}{\partial d_g}\Big]\Big\}. \end{aligned} \tag{C.10}$$

Appendix D

Newton-Raphson arc-length method

The detailed formulations for the Newton-Raphson arc-length method are given in this Appendix, where the vector $\{u\}$ denote to the $\{d\}$ in Chapter 6. The non-linear system of equations is given as

$$\{F_p^{int}(\{u\})\} - \{(F_p^{ext})\} = \{0\} \quad \text{or} \quad \{F_p^{int}(\{u\})\} - \lambda\{F_{p0}^{ext}\} = \{0\} \tag{D.1}$$

with the exact solution $\{u\}$. It is supposed that the point $(\lambda, \{u\})$ satisfies the system of equations and thus follows the equilibrium path. Unlike the Newton-Raphson method, the arc-length method postulates in both the displacement increments $\{\Delta u\}$ and load parameter increment $\Delta\lambda$. The incremental load factor within load step is updated by

$$\lambda_{n+1} = \lambda_n + \Delta\lambda \tag{D.2}$$

which is used to find the external load in the incremental load step. Both $\{\Delta u\}$ and $\Delta\lambda$ are unknowns in contrast to the Newton-Raphson method where $\Delta\lambda$ is given and $\{\Delta u\}$ needs to be solved iteratively. At $(n+1)$th load step, the solution $(\lambda_{n+1}, \{u_{n+1}\})$ is used to measure the residual as

$$\begin{aligned} \{R\} &= \{F_p^{int}(\{u_{n+1}\})\} - \lambda_{n+1}\{F_{p0}^{ext}\} \\ &= \{F_p^{int}(\{u_n\} + \{\Delta u\} + \{\delta u\})\} - (\lambda_n + \Delta\lambda + \delta\lambda)\{F_{p0}^{ext}\} \end{aligned} \tag{D.3}$$

$\{\delta u\}$ and $\delta\lambda$ are the displacement and load parameter increment in the current iteration step within $(n+1)$th load step and $\{\Delta u\}$ is the displacement increment in the current load step. The residual from in Eq. (D.3) can be written as a form using Taylor series with linear term as

$$\begin{aligned} &\{F_p^{int}(\{u_n\}+\{\Delta u\})\}+ \\ &\Big[\frac{\partial\{F_p^{int}(\{u\})\}}{\partial\{u\}}\Big]_{\{u_n\}+\{\Delta u\}}\cdot\{\delta u\}- \\ &(\lambda_n+\Delta\lambda+\delta\lambda)\{F_{p0}^{ext}\}=\{0\} \end{aligned} \tag{D.4}$$

where the derivatives of the internal variables with respect to the field variable $\{u\}$ $[\partial\{F^{int}(u)\}/\partial\{u\}]$ is replaced by the quantity $[R']$, leading to

$$[R']_{\{u_n\}+\{\Delta u\}}\cdot\{\delta u\}-\delta\lambda\{F_{p0}^{ext}\}=-\{F_p^{int}(\{u_n\}+\{\Delta u\})\}+(\lambda+\Delta\lambda)\{F_{p0}^{ext}\}. \tag{D.5}$$

In order to solve $\{\delta u\}$ and one more unknown value $\delta\lambda$, the number of equations in Eq. (D.5) is not sufficient to determine $\{\delta u\}$ and $\delta\lambda$. The supplementary equation that completes the non-linear system is the arc-length equation. The cylindrical arc-length constraint can be defined as

$$(\{\Delta u\}+\{\delta u\})^T(\{\Delta u\}+\{\delta u\})=l^2 \tag{D.6}$$

where l is the defined arc length. A graphical representation is shown in Figure D.1 which illustrates a system with two degrees of freedom. The value of l decides the position of next point on equilibrium path. The equilibrium solution at the end of the increment is determined by an intersection A and B between the solution path and a ball of radius l in the space of nodal displacements (a cylinder in the $\lambda-u$ space) centred at the equilibrium configuration u_n of the beginning in this load step. The non-consistent method is implemented to solve the coupled system to obtain the unknowns $\{\delta u\}$ and

$\delta\lambda$ as

$$\begin{aligned}\{\delta u\} = -[R']^{-1}_{\{u_n\}+\{\Delta u\}} \cdot [\{F_p^{int}(\{u_n\}+\{\Delta u\})\} \\ - (\lambda_n + \Delta\lambda)\{F_{p0}^{ext}\}] \\ + \delta\lambda([R']^{-1}_{\{u_n\}+\{\Delta u\}}\{F_{p0}^{ext}\}).\end{aligned} \tag{D.7}$$

Introducing $\{\delta u^N\}$ and $\{\delta u^A\}$ to Eq. (D.7), it is obtained

$$\{\delta u\} = \{\delta u^N\} + \delta\lambda\{\delta u^A\} \tag{D.8}$$

where

$$\{\delta u^N\} = -[R']^{-1}_{\{u_n\}+\{\Delta u\}} \cdot [\{F_p^{int}(\{u_n\}+\{\Delta u\})\} - (\lambda_n + \Delta\lambda)\{F_{p0}^{ext}\}] \tag{D.9(a))}$$

$$\{\delta u^A\} = ([R']^{-1}_{\{u_n\}+\{\Delta u\}}\{F_{p0}^{ext}\}). \tag{D.9(b))}$$

Eq. (D.8) is substituted into the arc-length constraint in Eq. (D.6), leading to a quadratic equation for $\delta\lambda$

$$\begin{aligned}(\{\delta u^A\}^T\{\delta u^A\})\delta\lambda^2 + \\ 2\{\delta u^A\}^T\Big\{\{\Delta u^{k-1}\} + \{\delta u^N\}\Big\}\delta\lambda + \\ \Big\{\{\Delta u^{k-1}\} + \{\delta u^N\}\Big\}^T\Big\{\{\Delta u^{k-1}\} + \{\delta u^N\}\Big\} - l^2 = 0\end{aligned} \tag{D.10}$$

Once $\delta\lambda$ is solved, it can be substituted into Eq. (D.8) to update the displacement variation and complete the iteration. The possible intersections are associated with $\delta\lambda_1$ and $\delta\lambda_2$. The projections (dot products) of the increment in current and previous iteration step are calculated to select the proper $\delta\lambda$ as

$$\max\Big\{\delta\lambda_{1,2}(\{\Delta u^{k-1}\} + \{\delta u^N\} + \delta\lambda\{\delta u^A\})^T\{\Delta u^{k-1}\}\Big\} \tag{D.11}$$

or

$$\max\Big\{\delta\lambda_{1,2}\{\Delta u^{k-1}\}^T\{\Delta u^A\}\Big\}.$$

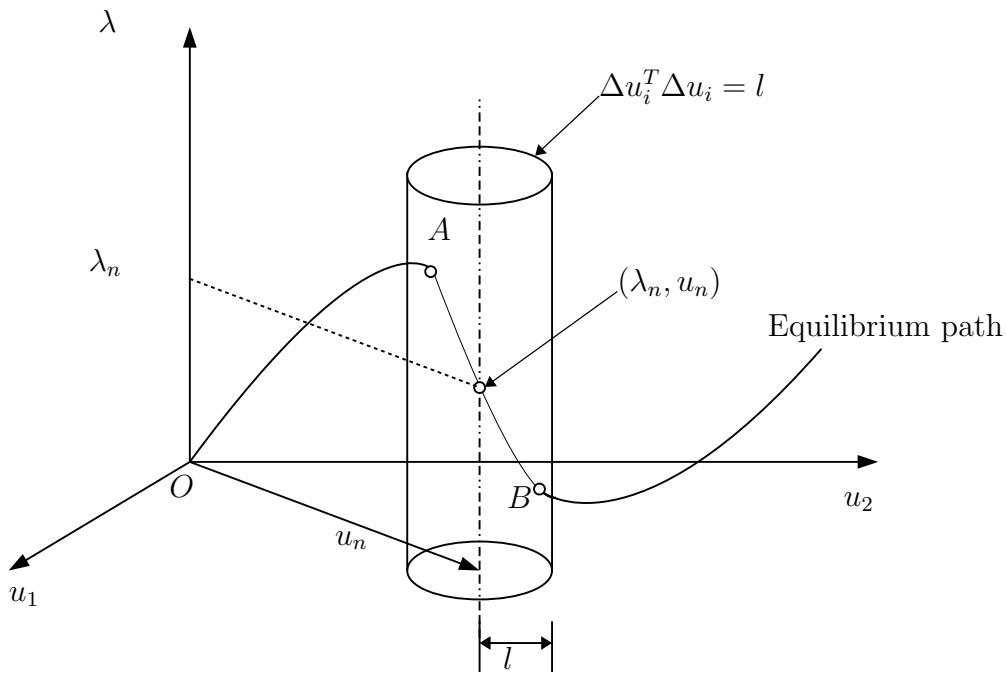

Figure D.1: The cylindrical arc-length method.

Application of this rule leads to a robust selection of a appropriate $\delta\lambda$ in each iteration but is again associated with yet another drawback. Since the increments in the first load step are zero, it fails to find a proper $\delta\lambda$ using Eq. (D.11) as the corresponding dot products are zero for both solutions. One way to initiate the method at the beginning of every increment has been proposed that for the first iteration step in every load step, the load factor is computed as

$$\delta\lambda = sign\Big(\{\Delta u_n\}^T \{\delta u\}^A\Big) \times \frac{l}{\sqrt{\{\delta u^A\}^T \{\delta u^A\}}} \tag{D.12}$$

instead of using Eq. (D.11).

The combined Newton-Raphson arc-length scheme is explained as follows.

(i) For the first load step $n = 1$, the Newton-Raphson method is employed to obtain the increment and update the initial displacement $\{u_0\}$ as

$$\{u_1\} = \{u_0\} + \{\Delta u^{k-1}\} + \{\delta u\} \tag{D.13}$$

where

$$\{\delta u\} = -[R']^{-1}\{F_p^{int}(\{u_0\} + \{\Delta u^{k-1}\})\} \tag{D.14}$$

(ii) At nth ($n > 1$) load step, when $k = 1$, and set initial field variable and incremental load factor

$$\{u_n^0\} = \{u_{n-1}\}, \quad \lambda_n^0 = \lambda_{n-1}, \quad \{R^0\} = \{F_p^{int}(\{u_n\})\} - \lambda_n\{F_{p0}^{ext}\} \tag{D.15}$$

Use Eq. (D.9) to solve the incremental displacement $\{\delta u^N\}$ and $\{\delta u^A\}$ and Eq. (D.12) to initialise the load factor $\delta\lambda^1$. (iii) Set $k = k + 1$ and solve the linear system for $\{\delta u^N\}$ and $\{\delta u^A\}$. (v) Find the appropriate iterative load factor $\delta\lambda$ by solving Eq. (D.10) and choose the proper direction by Eq. (D.10). (vi) Update the displacement

$$\{\delta u\} = \{\delta u^N\} + \delta\lambda\{\delta u^A\} \tag{D.16}$$

and

$$\{\Delta u^k\} = \{\Delta u^{k-1}\} + \{\delta u\} \tag{D.17}$$

(vii) Update the incremental load factor

$$\lambda_{n+1}^k = \lambda_{n+1}^{k-1} + \delta\lambda^k \tag{D.18}$$

and the incremental displacements

$$\{u_{n+1}^k\} = \{u_{n+1}^{k-1}\} + \delta\{u^k\} \quad \text{and} \quad \{\Delta u_{n+1}^k\} = \{\Delta u_{n+1}^{k-1}\} + \{\delta u^k\} \tag{D.19}$$

(viii) Update residual

(ix) Check the stopping criterion

References

[1] C. D. Coman and A. P. Bassom, "On the nonlinear membrane approximation and edge-wrinkling," *International Journal of Solids and Structures*, vol. 82, pp. 85–94, 2016.

[2] O. C. Zienkiewicz, R. L. Taylor, and R. L. Taylor, *The finite element method: solid mechanics*, vol. 2. Butterworth-Heinemann, 2000.

[3] N. Newmark, "Numerical methods of analysis of bars, plates, and elastic bodies," in *Selected Papers By Nathan M. Newmark: Civil Engineering Classics*, pp. 313–344, ASCE, 1949.

[4] K.-J. Bathe and E. L. Wilson, *Numerical methods in finite element analysis*. Prentice-Hall, 1976.

[5] R. W. Clough, "The finite element in plane stress analysis," *Proceeding 2nd ASCE Conference On Electric Computation, 1960*, 1960.

[6] O. C. Zienkiewicz and Y. K. Cheung, "The finite element method for analysis of elastic isotropic and orthotropic slabs.," *Proceedings of the Institution of Civil Engineers*, vol. 28, no. 4, pp. 471–488, 1964.

[7] O. Zienkiewicz, "Origins, milestones and directions of the finite element method a personal view," *Handbook of Numerical Analysis*, vol. 4, pp. 3–67, 1996.

[8] V. Gupta, C. A. Duarte, I. Babuška, and U. Banerjee, "A stable and optimally convergent generalized FEM (sgfem) for linear elastic fracture mechanics," *Computer Methods in Applied Mechanics and Engineering*, vol. 266, pp. 23–39, 2013.

[9] T. Nguyen-Thoi, T. Bui-Xuan, P. Phung-Van, H. Nguyen-Xuan, and P. Ngo-Thanh, "Static, free vibration and buckling analyses of stiffened plates by CS-FEM-DSG3 using triangular elements," *Computers & Structures*, vol. 125, pp. 100–113, 2013.

[10] E. Stein, "Fundamentals: Introduction and Survey," *Encyclopedia of Computational Mechanics*, 2004.

[11] W. M. Coombs and R. S. Crouch, "Non-associated Reuleaux plasticity: analytical stress integration and consistent tangent for finite deformation mechanics," *Computer Methods in Applied Mechanics and Engineering*, vol. 200, no. 9-12, pp. 1021–1037, 2011.

[12] R. D. Wood and O. Zienkiewicz, "Geometrically nonlinear finite element analysis of beams, frames, arches and axisymmetric shells," *Computers & Structures*, vol. 7, no. 6, pp. 725–735, 1977.

[13] K. N. Chau, K. N. Chau, T. Ngo, K. Hackl, and H. Nguyen-Xuan, "A polytree-based adaptive polygonal finite element method for multi-material topology optimization," *Computer Methods in Applied Mechanics and Engineering*, vol. 332, pp. 712–739, 2018.

[14] R. Huiskes and E. Chao, "A survey of finite element analysis in orthopedic biomechanics: the first decade," *Journal of Biomechanics*, vol. 16, no. 6, pp. 385–409, 1983.

[15] M. Griebel and M. A. Schweitzer, "A particle-partition of unity method for the solution of elliptic, parabolic, and hyperbolic pdes," *SIAM Journal on Scientific Computing*, vol. 22, no. 3, pp. 853–890, 2000.

[16] L. F. Richardson, "IX. the approximate arithmetical solution by finite differences of physical problems involving differential equations, with an application to the stresses in a masonry dam," *Philosophical Transactions of the Royal Society of London. Series A, Containing Papers of a Mathematical or Physical Character*, vol. 210, no. 459-470, pp. 307–357, 1911.

[17] T. A. Cruse and F. J. Rizzo, "A direct formulation and numerical solution of the general transient elastodynamic problem. I," *Journal of Mathematical Analysis and Applications*, vol. 22, no. 1, pp. 244–259, 1968.

[18] P. K. Banerjee and R. Butterfield, *Boundary element methods in engineering science*, vol. 17. McGraw-Hill London, 1981.

[19] G. Hattori, I. A. Alatawi, and J. Trevelyan, "An extended boundary element method formulation for the direct calculation of the stress intensity factors in fully anisotropic materials," *International Journal for Numerical Methods in Engineering*, vol. 109, no. 7, pp. 965–981, 2017.

[20] T. J. Hughes, J. A. Cottrell, and Y. Bazilevs, "Isogeometric analysis: CAD, finite elements, NURBS, exact geometry and mesh refinement," *Computer Methods in Applied Mechanics and Engineering*, vol. 194, no. 39-41, pp. 4135–4195, 2005.

[21] A. Huerta, T. Belytschko, S. Fernández-Méndez, T. Rabczuk, X. Zhuang, and M. Arroyo, "Meshfree methods," *Encyclopedia of Computational Mechanics Second Edition*, pp. 1–38, 2018.

[22] T. Belytschko, Y. Y. Lu, and L. Gu, "Element-free Galerkin methods," *International Journal for Numerical Methods in Engineering*, vol. 37, no. 2, pp. 229–256, 1994.

[23] T. Belytschko, D. Organ, and C. Gerlach, "Element-free Galerkin methods for dynamic fracture in concrete," *Computer Methods in Applied Mechanics and Engineering*, vol. 187, no. 3-4, pp. 385–399, 2000.

[24] T.-P. Fries and H. G. Matthies, "Classification and overview of meshfree methods," *Department of Mathematics and Computer Science, Technical University of Braunschweig*, 2003.

[25] C. A. Duarte and J. Oden, *A review of some meshless methods to solve partial differential equations*. Texas Institute for Computational and Applied Mathematics Austin, TX, 1995.

[26] V. P. Nguyen, T. Rabczuk, S. Bordas, and M. Duflot, "Meshless methods: a review and computer implementation aspects," *Mathematics and Computers in Simulation*, vol. 79, no. 3, pp. 763–813, 2008.

[27] J.-S. Chen, M. Hillman, and S.-W. Chi, "Meshfree methods: progress made after 20 years," *Journal of Engineering Mechanics*, vol. 143, no. 4, p. 04017001, 2017.

[28] T. Belytschko, Y. Krongauz, D. Organ, M. Fleming, and P. Krysl, "Meshless methods: an overview and recent developments," *Computer Methods in Applied Mechanics and Engineering*, vol. 139, no. 1-4, pp. 3–47, 1996.

[29] G.-R. Liu and Y.-T. Gu, *An introduction to meshfree methods and their programming*. Springer Science & Business Media, 2005.

[30] Y. Gu, "Meshfree methods and their comparisons," *International Journal of Computational Methods*, vol. 2, no. 4, pp. 477–515, 2005.

[31] G. Liu, "An overview on meshfree methods: for computational solid mechanics," *International Journal of Computational Methods*, vol. 13, no. 05, p. 1630001, 2016.

[32] G.-R. Liu and Y. Gu, "A point interpolation method for two-dimensional solids," *International Journal for Numerical Methods in Engineering*, vol. 50, no. 4, pp. 937–951, 2001.

[33] G.-R. Liu, *Mesh free methods: moving beyond the finite element method*. CRC press, 2002.

[34] R. A. Gingold and J. J. Monaghan, "Smoothed particle hydrodynamics: theory and application to non-spherical stars," *Monthly Notices of the Royal Astronomical Society*, vol. 181, no. 3, pp. 375–389, 1977.

[35] L. B. Lucy, "A numerical approach to the testing of the fission hypothesis," *The Astronomical Journal*, vol. 82, pp. 1013–1024, 1977.

[36] G.-R. Liu and M. B. Liu, *Smoothed particle hydrodynamics: a meshfree particle method*. World Scientific, 2003.

[37] M. Liu and G. Liu, "Smoothed particle hydrodynamics (SPH): an overview and recent developments," *Archives of Computational Methods in Engineering*, vol. 17, no. 1, pp. 25–76, 2010.

[38] A. M. Tartakovsky and P. Meakin, "Pore scale modeling of immiscible and miscible fluid flows using smoothed particle hydrodynamics," *Advances in Water Resources*, vol. 29, no. 10, pp. 1464–1478, 2006.

[39] J. Jeong, M. Jhon, J. Halow, and J. Van Osdol, "Smoothed particle hydrodynamics: Applications to heat conduction," *Computer Physics Communications*, vol. 153, no. 1, pp. 71–84, 2003.

[40] J. Swegle, D. Hicks, and S. Attaway, "Smoothed particle hydrodynamics stability analysis," *Journal of Computational Physics*, vol. 116, no. 1, pp. 123–134, 1995.

[41] J. J. Monaghan, "Why particle methods work," *SIAM Journal on Scientific and Statistical Computing*, vol. 3, no. 4, pp. 422–433, 1982.

[42] J. J. Monaghan, "An introduction to SPH," *Computer Physics Communications*, vol. 48, no. 1, pp. 89–96, 1988.

[43] S. Li and W. K. Liu, "Meshfree and particle methods and their applications," *Applied Mechanics Reviews*, vol. 55, no. 1, pp. 1–34, 2002.

[44] J. Bonet and S. Kulasegaram, "Correction and stabilization of smooth particle hydrodynamics methods with applications in metal forming simulations," *International Journal for Numerical Methods in Engineering*, vol. 47, no. 6, pp. 1189–1214, 2000.

[45] G. A. Dilts, "Moving-least-squares-particle hydrodynamics I. consistency and stability," *International Journal for Numerical Methods in Engineering*, vol. 44, no. 8, pp. 1115–1155, 1999.

[46] Y. Lu, T. Belytschko, and L. Gu, "A new implementation of the element free Galerkin method," *Computer Methods in Applied Mechanics and Engineering*, vol. 113, no. 3-4, pp. 397–414, 1994.

[47] C. A. Duarte and J. T. Oden, "An hp adaptive method using clouds," *Computer Methods in Applied Mechanics and Engineering*, vol. 139, no. 1-4, pp. 237–262, 1996.

[48] J. M. Melenk and I. Babuška, "The partition of unity finite element method: basic theory and applications," *Computer Methods in Applied Mechanics and Engineering*, vol. 139, no. 1-4, pp. 289–314, 1996.

[49] T. Belytschko, J. Fish, and A. Bayliss, "The spectral overlay on finite elements for problems with high gradients," *Computer Methods in Applied Mechanics and Engineering*, vol. 81, no. 1, pp. 71–89, 1990.

[50] P. Lancaster and K. Salkauskas, "Surfaces generated by moving least squares methods," *Mathematics of Computation*, vol. 37, no. 155, pp. 141–158, 1981.

[51] T. Belytschko, Y. Lu, and L. Gu, "Crack propagation by element-free Galerkin methods," *Engineering Fracture Mechanics*, vol. 51, no. 2, pp. 295–315, 1995.

[52] W. K. Liu, S. Jun, and Y. F. Zhang, "Reproducing kernel particle methods," *International Journal for Numerical Methods in Fluids*, vol. 20, no. 8-9, pp. 1081–1106, 1995.

[53] S. Atluri and T.-L. Zhu, "The meshless local Petrov-Galerkin (MLPG) approach for solving problems in elasto-statics," *Computational Mechanics*, vol. 25, no. 2-3, pp. 169–179, 2000.

[54] T. Rabczuk and T. Belytschko, "Cracking particles: a simplified meshfree method for arbitrary evolving cracks," *International Journal for Numerical Methods in Engineering*, vol. 61, no. 13, pp. 2316–2343, 2004.

[55] W. Ai and C. E. Augarde, "An adaptive cracking particle method for 2D crack propagation," *International Journal for Numerical Methods in Engineering*, vol. 108, no. 13, pp. 1626–1648, 2016.

[56] M. Arroyo and M. Ortiz, "Local maximum-entropy approximation schemes: a seamless bridge between finite elements and meshfree methods," *International*

Journal for Numerical Methods in Engineering, vol. 65, no. 13, pp. 2167–2202, 2006.

[57] B. Nayroles, G. Touzot, and P. Villon, "Generalizing the finite element method: diffuse approximation and diffuse elements," *Computational Mechanics*, vol. 10, no. 5, pp. 307–318, 1992.

[58] T. Belytschko, Y. Lu, L. Gu, and M. Tabbara, "Element-free Galerkin methods for static and dynamic fracture," *International Journal of Solids and Structures*, vol. 32, no. 17-18, pp. 2547–2570, 1995.

[59] S. N. Atluri and T. Zhu, "A new meshless local Petrov-Galerkin (MLPG) approach in computational mechanics," *Computational Mechanics*, vol. 22, no. 2, pp. 117–127, 1998.

[60] S. N. Atluri, *The meshless method (MLPG) for domain & BIE discretizations*, vol. 677. Tech Science Press Forsyth, 2004.

[61] A. Mazzia, M. Ferronato, G. Pini, and G. Gambolati, "A comparison of numerical integration rules for the meshless local Petrov–Galerkin method," *Numerical Algorithms*, vol. 45, no. 1-4, pp. 61–74, 2007.

[62] E. Shivanian, "A new spectral meshless radial point interpolation (SMRPI) method: a well-behaved alternative to the meshless weak forms," *Engineering Analysis with Boundary Elements*, vol. 54, pp. 1–12, 2015.

[63] J. Dolbow and T. Belytschko, "Numerical integration of the galerkin weak form in meshfree methods," *Computational mechanics*, vol. 23, no. 3, pp. 219–230, 1999.

[64] J.-S. Chen, C.-T. Wu, S. Yoon, and Y. You, "A stabilized conforming nodal integration for Galerkin mesh-free methods," *International Journal for Numerical Methods in Engineering*, vol. 50, no. 2, pp. 435–466, 2001.

[65] M. Hillman and J.-S. Chen, "Nodally integrated implicit gradient reproducing kernel particle method for convection dominated problems," *Computer Methods in Applied Mechanics and Engineering*, vol. 299, pp. 381–400, 2016.

[66] Y.-M. Guo and G. Yagawa, "A meshless method with conforming and nonconforming sub-domains," *International Journal for Numerical Methods in Engineering*, vol. 110, no. 9, pp. 826–841, 2017.

[67] E. J. Kansa, "Multiquadrics: A scattered data approximation scheme with applications to computational fluid-dynamics: I surface approximations and partial derivative estimates," *Computers & Mathematics with Applications*, vol. 19, no. 8-9, pp. 127–145, 1990.

[68] E. J. Kansa, "Multiquadrics: A scattered data approximation scheme with applications to computational fluid-dynamics: II solutions to parabolic, hyperbolic and elliptic partial differential equations," *Computers & Mathematics with Applications*, vol. 19, no. 8, pp. 147–161, 1990.

[69] M. A. Jankowska, A. Karageorghis, and C.-S. Chen, "Improved Kansa RBF method for the solution of nonlinear boundary value problems," *Engineering Analysis with Boundary Elements*, vol. 87, pp. 173–183, 2018.

[70] G. Yao, C.-S. Chen, and H. Zheng, "A modified method of approximate particular solutions for solving linear and nonlinear pdes," *Numerical Methods for Partial Differential Equations*, vol. 33, no. 6, pp. 1839–1858, 2017.

[71] L. Wang, J.-S. Chen, and H.-Y. Hu, "Subdomain radial basis collocation method for fracture mechanics," *International journal for numerical methods in engineering*, vol. 83, no. 7, pp. 851–876, 2010.

[72] X. Zhang, X.-H. Liu, K.-Z. Song, and M.-W. Lu, "Least-squares collocation meshless method," *International Journal for Numerical Methods in Engineering*, vol. 51, no. 9, pp. 1089–1100, 2001.

[73] G. E. Fasshauer, "Solving partial differential equations by collocation with radial basis functions," *Vanderbilt University Press Nashville, TN*, pp. 131–138, 1997.

[74] N. R. Aluru, "A point collocation method based on reproducing kernel approximations," *International Journal for Numerical Methods in Engineering*, vol. 47, no. 6, pp. 1083–1121, 2000.

[75] C. Coleman, "On the use of radial basis functions in the solution of elliptic boundary value problems," *Computational Mechanics*, vol. 17, no. 6, pp. 418–422, 1996.

[76] H.-Y. Hu, J.-S. Chen, and W. Hu, "Error analysis of collocation method based on reproducing kernel approximation," *Numerical Methods for Partial Differential Equations*, vol. 27, no. 3, pp. 554–580, 2011.

[77] E. Oñate and S. Idelsohn, "A mesh-free finite point method for advective-diffusive transport and fluid flow problems," *Computational Mechanics*, vol. 21, no. 4-5, pp. 283–292, 1998.

[78] E. Oñate, S. Idelsohn, O. Zienkiewicz, and R. Taylor, "A finite point method in computational mechanics. Applications to convective transport and fluid flow," *International Journal for Numerical Methods in Engineering*, vol. 39, no. 22, pp. 3839–3866, 1996.

[79] B. Boroomand, A. Tabatabaei, and E. Oñate, "Simple modifications for stabilization of the finite point method," *International Journal for Numerical Methods in Engineering*, vol. 63, no. 3, pp. 351–379, 2005.

[80] K. Balakrishnan and A. P. Ramachandran, "Osculatory interpolation in the method of fundamental solution for nonlinear poisson problems," *Journal of Computational Physics*, vol. 172, pp. 1–18, 2001.

[81] G. Liu and Y. Gu, "A meshfree method: meshfree weak–strong (MWS) form method, for 2-D solids," *Computational Mechanics*, vol. 33, no. 1, pp. 2–14, 2003.

[82] M. Dehghan and A. Ghesmati, "Combination of meshless local weak and strong (MLWS) forms to solve the two dimensional hyperbolic telegraph equation," *Engineering Analysis with Boundary Elements*, vol. 34, no. 4, pp. 324–336, 2010.

[83] G. Liu, Y. Wu, and H. Ding, "Meshfree weak–strong (MWS) form method and its application to incompressible flow problems," *International Journal for Numerical Methods in Fluids*, vol. 46, no. 10, pp. 1025–1047, 2004.

[84] J.-S. Chen, L. Wang, H.-Y. Hu, and S.-W. Chi, "Subdomain radial basis collocation method for heterogeneous media," *International Journal for Numerical Methods in Engineering*, vol. 80, no. 2, pp. 163–190, 2009.

[85] S.-W. Chi, J.-S. Chen, and H.-Y. Hu, "A weighted collocation on the strong form with mixed radial basis approximations for incompressible linear elasticity," *Computational Mechanics*, vol. 53, no. 2, pp. 309–324, 2014.

[86] C. Anitescu, Y. Jia, Y. J. Zhang, and T. Rabczuk, "An isogeometric collocation method using superconvergent points," *Computer Methods in Applied Mechanics and Engineering*, vol. 284, pp. 1073–1097, 2015.

[87] D. Wang, J. Wang, and J. Wu, "Superconvergent gradient smoothing meshfree collocation method," *Computer Methods in Applied Mechanics and Engineering*, vol. 340, pp. 728–766, 2018.

[88] X.-W. Gao, L.-F. Gao, Y. Zhang, M. Cui, and J. Lv, "Free element collocation method: A new method combining advantages of finite element and mesh free methods," *Computers & Structures*, 2019.

[89] S.-W. Chi, J.-S. Chen, H.-Y. Hu, and J. P. Yang, "A gradient reproducing kernel collocation method for boundary value problems," *International Journal for Numerical Methods in Engineering*, vol. 93, no. 13, pp. 1381–1402, 2013.

[90] S. Fernández-Méndez and A. Huerta, "Imposing essential boundary conditions in mesh-free methods," *Computer Methods in Applied Mechanics and Engineering*, vol. 193, no. 12-14, pp. 1257–1275, 2004.

[91] T. Belytschko, D. Organ, and Y. Krongauz, "A coupled finite element-element-free Galerkin method," *Computational Mechanics*, vol. 17, no. 3, pp. 186–195, 1995.

[92] A. Shedbale, I. Singh, B. Mishra, and K. Sharma, "Ductile failure modeling and simulations using coupled FE–EFG approach," *International Journal of Fracture*, vol. 203, no. 1-2, pp. 183–209, 2017.

[93] S. Fernández-Méndez, P. Díez, and A. Huerta, "Convergence of finite elements enriched with mesh-less methods," *Numerische Mathematik*, vol. 96, no. 1, pp. 43–59, 2003.

[94] S. Fernández-Méndez and A. Huerta, "Coupling finite elements and particles for adaptivity: An application to consistently stabilized convection-diffusion," in *Meshfree Methods for partial differential equations*, pp. 117–129, Springer, 2003.

[95] A. Huerta, S. Fernández-Méndez, and W. K. Liu, "A comparison of two formulations to blend finite elements and mesh-free methods," *Computer Methods in Applied Mechanics and Engineering*, vol. 193, no. 12-14, pp. 1105–1117, 2004.

[96] C. E. Shannon, "A mathematical theory of communication," *Bell system technical journal*, vol. 27, no. 3, pp. 379–423, 1948.

[97] E. T. Jaynes, "Information theory and statistical mechanics," *Physical Review*, vol. 106, no. 4, p. 620, 1957.

[98] M. Arroyo, "Maximum-entropy meshfree coordinates in computational mechanics," in *Generalized Barycentric Coordinates in Computer Graphics and Computational Mechanics*, pp. 229–243, CRC Press, 2017.

[99] D. Millán, N. Sukumar, and M. Arroyo, "Cell-based maximum-entropy approximants," *Computer Methods in Applied Mechanics and Engineering*, vol. 284, pp. 712–731, 2015.

[100] F. Amiri, C. Anitescu, M. Arroyo, S. P. A. Bordas, and T. Rabczuk, "XLME interpolants, a seamless bridge between XFEM and enriched meshless methods," *Computational Mechanics*, vol. 53, no. 1, pp. 45–57, 2014.

[101] C. J. Cyron, M. Arroyo, and M. Ortiz, "Smooth, second order, non-negative meshfree approximants selected by maximum entropy," *International Journal for Numerical Methods in Engineering*, vol. 79, no. 13, pp. 1605–1632, 2009.

[102] D. González, E. Cueto, and M. Doblaré, "A higher order method based on local maximum entropy approximation," *International Journal for Numerical Methods in Engineering*, vol. 83, no. 6, pp. 741–764, 2010.

[103] A. Ortiz, M. Puso, and N. Sukumar, "Maximum-entropy meshfree method for incompressible media problems," *Finite Elements in Analysis and Design*, vol. 47, no. 6, pp. 572–585, 2011.

[104] O. Kardani, M. Nazem, M. Kardani, and S. Sloan, "On the application of the maximum entropy meshfree method for elastoplastic geotechnical analysis," *Computers and Geotechnics*, vol. 84, pp. 68–77, 2017.

[105] F. Amiri, D. Millán, M. Arroyo, M. Silani, and T. Rabczuk, "Fourth order phase-field model for local max-ent approximants applied to crack propagation," *Computer Methods in Applied Mechanics and Engineering*, vol. 312, pp. 254–275, 2016.

[106] A. L. Gain, G. H. Paulino, L. S. Duarte, and I. F. Menezes, "Topology optimization using polytopes," *Computer Methods in Applied Mechanics and Engineering*, vol. 293, pp. 411–430, 2015.

[107] M. Nazem, M. Kardani, B. Bienen, and M. Cassidy, "A stable Maximum-Entropy Meshless method for analysis of porous media," *Computers and Geotechnics*, vol. 80, pp. 248–260, 2016.

[108] F. Greco, L. Coox, and W. Desmet, "Maximum-entropy methods for time-harmonic acoustics," *Computer Methods in Applied Mechanics and Engineering*, vol. 306, pp. 1–18, 2016.

[109] C. Peco, D. Millán, A. Rosolen, and M. Arroyo, "Efficient implementation of Galerkin meshfree methods for large-scale problems with an emphasis on maximum entropy approximants," *Computers & Structures*, vol. 150, pp. 52–62, 2015.

[110] F. Greco, L. Coox, F. Maurin, and W. Desmet, "NURBS-enhanced maximum-entropy schemes," *Computer Methods in Applied Mechanics and Engineering*, vol. 317, pp. 580–597, 2017.

[111] M. Foca, *On a Local Maximum Entropy interpolation approach for simulation of coupled thermo-mechanical problems. Application to the Rotary Frictional Welding process.* PhD thesis, Ecole Centrale de Nantes (ECN), 2015.

[112] F. Greco, L. Filice, C. Peco, and M. Arroyo, "A stabilized formulation with maximum entropy meshfree approximants for viscoplastic flow simulation in metal forming," *International Journal of Material Forming*, vol. 8, no. 3, pp. 341–353, 2015.

[113] A. Rosolen, C. Peco, and M. Arroyo, "An adaptive meshfree method for phase-field models of biomembranes. Part I: Approximation with maximum-entropy basis functions," *Journal of Computational Physics*, vol. 249, pp. 303–319, 2013.

[114] L. Fan, W. M. Coombs, and C. E. Augarde, "The point collocation method with a local maximum entropy approach," *Computers & Structures*, vol. 201, pp. 1–14, 2018.

[115] A. S. Saada, *Elasticity: theory and applications*, vol. 16. Elsevier, 2013.

[116] R. L. Hardy, "Multiquadric equations of topography and other irregular surfaces," *Journal of geophysical research*, vol. 76, no. 8, pp. 1905–1915, 1971.

[117] H.-Y. Hu, Z.-C. Li, and A. H.-D. Cheng, "Radial basis collocation methods for elliptic boundary value problems," *Computers & Mathematics with Applications*, vol. 50, no. 1-2, pp. 289–320, 2005.

[118] J. Li, "Mixed methods for fourth-order elliptic and parabolic problems using radial basis functions," *Advances in Computational Mathematics*, vol. 23, no. 1-2, pp. 21–30, 2005.

[119] C. Franke and R. Schaback, "Solving partial differential equations by collocation using radial basis functions," *Applied Mathematics and Computation*, vol. 93, no. 1, pp. 73–82, 1998.

[120] J. Wang and G. Liu, "On the optimal shape parameters of radial basis functions used for 2-D meshless methods," *Computer Methods in Applied Mechanics and Engineering*, vol. 191, no. 23-24, pp. 2611–2630, 2002.

[121] E. Kansa and Y. Hon, "Circumventing the ill-conditioning problem with multiquadric radial basis functions: applications to elliptic partial differential equations," *Computers and Mathematics with Applications*, vol. 39, no. 7-8, pp. 123–138, 2000.

[122] A. Wong, Y. Hon, T. Li, S. Chung, and E. Kansa, "Multizone decomposition for simulation of time-dependent problems using the multiquadric scheme," *Computers & Mathematics with Applications*, vol. 37, no. 8, pp. 23–43, 1999.

[123] G. Liu and Y. Gu, "A local radial point interpolation method (LRPIM) for free vibration analyses of 2-D solids," *Journal of Sound and Vibration*, vol. 246, no. 1, pp. 29–46, 2001.

[124] X. Zhang, K. Z. Song, M. W. Lu, and X. Liu, "Meshless methods based on collocation with radial basis functions," *Computational Mechanics*, vol. 26, no. 4, pp. 333–343, 2000.

[125] J.-S. Chen, C. Pan, C.-T. Wu, and W. K. Liu, "Reproducing kernel particle methods for large deformation analysis of non-linear structures," *Computer Methods in Applied Mechanics and Engineering*, vol. 139, no. 1-4, pp. 195–227, 1996.

[126] W. K. Liu and Y. Chen, "Wavelet and multiple scale reproducing kernel methods," *International Journal for Numerical Methods in Fluids*, vol. 21, no. 10, pp. 901–931, 1995.

[127] H. J. Choe, D. Kim, H. Kim, and Y. Kim, "Meshless method for the stationary incompressible Navier-Stokes equations," *Discrete and Continuous Dynamical Systems Series B*, vol. 1, no. 4, pp. 495–526, 2001.

[128] W.-K. Liu, S. Li, and T. Belytschko, "Moving least-square reproducing kernel methods (I) methodology and convergence," *Computer Methods in Applied Mechanics and Engineering*, vol. 143, no. 1, pp. 113–154, 1997.

[129] J.-S. Chen, C. Pan, and C.-T. Wu, "Large deformation analysis of rubber based on a reproducing kernel particle method," *Computational Mechanics*, vol. 19, no. 3, pp. 211–227, 1997.

[130] W. Han and X. Meng, "Error analysis of the reproducing kernel particle method," *Computer Methods in Applied Mechanics and Engineering*, vol. 190, no. 46-47, pp. 6157–6181, 2001.

[131] J. Dolbow and T. Belytschko, "An introduction to programming the meshless element free Galerkin method," *Archives of Computational Methods in Engineering*, vol. 5, no. 3, pp. 207–241, 1998.

[132] A. Huerta and S. Fernández-Méndez, "Coupling element free Galerkin and finite element methods," in *Proceedings of the European Congress on Computational Methods in Applied Sciences and Engineering (ECCOMAS 2000)*, pp. 11–14, 2000.

[133] N. Sukumar, "Construction of polygonal interpolants: a maximum entropy approach," *International Journal for Numerical Methods in Engineering*, vol. 61, no. 12, pp. 2159–2181, 2004.

[134] A. Rosolen, D. Millán, and M. Arroyo, "On the optimum support size in meshfree methods: A variational adaptivity approach with maximum-entropy approximants," *International Journal for Numerical Methods in Engineering*, vol. 82, no. 7, pp. 868–895, 2010.

[135] A. Rosolen, D. Millán, and M. Arroyo, "Second-order convex maximum entropy approximants with applications to high-order PDE," *International Journal for Numerical Methods in Engineering*, vol. 94, no. 2, pp. 150–182, 2013.

[136] Z. Ullah, *Nonlinear solid mechanics analysis using the parallel selective element-free Galerkin method*. PhD thesis, Durham University, 2013.

[137] F. Greco and N. Sukumar, "Derivatives of maximum-entropy basis functions on the boundary: Theory and computations," *International Journal for Numerical Methods in Engineering*, vol. 94, no. 12, pp. 1123–1149, 2013.

[138] S. P. Timoshenko and J. N. Goodier, *Theory of elasticity*. McGraw-Hill New York, 1970.

[139] O. C. Zienkiewicz and J. Z. Zhu, "A simple error estimator and adaptive procedure for practical engineerng analysis," *International Journal for Numerical Methods in Engineering*, vol. 24, no. 2, pp. 337–357, 1987.

[140] Y. Cai, P. Sun, H. Zhu, and T. Rabczuk, "A mixed cover meshless method for elasticity and fracture problems," *Theoretical and Applied Fracture Mechanics*, vol. 95, pp. 73–103, 2018.

[141] A. R. Díaz, N. Kikuchi, and J. E. Taylor, "A method of grid optimization for finite element methods," *Computer Methods in Applied Mechanics and Engineering*, vol. 41, no. 1, pp. 29–45, 1983.

[142] V. Darrigrand, Á. Rodríguez-Rozas, I. Muga, D. Pardo, A. Romkes, and S. Prudhomme, "Goal-oriented adaptivity using unconventional error representations for the multidimensional Helmholtz equation," *International Journal for Numerical Methods in Engineering*, vol. 113, no. 1, pp. 22–42, 2018.

[143] T. van Opstal, P. Bauman, S. Prudhomme, and E. van Brummelen, "Goal-oriented model adaptivity for viscous incompressible flows," *Computational Mechanics*, vol. 55, no. 6, pp. 1181–1190, 2015.

[144] F. Barros, S. Proença, and C. de Barcellos, "On error estimator and p-adaptivity in the generalized finite element method," *International Journal for Numerical Methods in Engineering*, vol. 60, no. 14, pp. 2373–2398, 2004.

[145] P. Solin, K. Segeth, and I. Dolezel, *Higher-order finite element methods*. Chapman and Hall/CRC, 2003.

[146] P. Šolın and L. Demkowicz, "Goal-oriented hp-adaptivity for elliptic problems," *Computer Methods in Applied Mechanics and Engineering*, vol. 193, no. 6-8, pp. 449–468, 2004.

[147] J. Zhu and O. Zienkiewicz, "Superconvergence recovery technique and a posteriori error estimators," *International Journal for Numerical Methods in Engineering*, vol. 30, no. 7, pp. 1321–1339, 1990.

[148] O. Zienkiewicz and J. Zhu, "Adaptivity and mesh generation," *International Journal for Numerical Methods in Engineering*, vol. 32, no. 4, pp. 783–810, 1991.

[149] M. Kumar, T. Kvamsdal, and K. A. Johannessen, "Superconvergent patch recovery and a posteriori error estimation technique in adaptive isogeometric analysis," *Computer Methods in Applied Mechanics and Engineering*, vol. 316, pp. 1086–1156, 2017.

[150] I. Babuška and W. Reinhbolt, "A-posteriori analysis for adaptive finite element computations," *SIAM Journal on Numerical Analysis*, vol. 15, pp. 736–754, 1978.

[151] I. Babuška, "The self adaptive approach in the finite element method," *The Mathematics of Finite Elements and Applications II, MAFELAP*, pp. 125–142, 1975.

[152] O. C. Zienkiewicz and J. Z. Zhu, "The superconvergent patch recovery and a posteriori error estimates. Part 1: The recovery technique," *International Journal for Numerical Methods in Engineering*, vol. 33, no. 7, pp. 1331–1364, 1992.

[153] M. H. Afshar and A. R. Firoozjaee, "Adaptive simulation of two dimensional hyperbolic problems by collocated discrete least squares meshless method," *Computers & Fluids*, vol. 39, no. 10, pp. 2030–2039, 2010.

[154] M. Afshar, M. Naisipour, and J. Amani, "Node moving adaptive refinement strategy for planar elasticity problems using discrete least squares meshless method," *Finite Elements in Analysis and Design*, vol. 47, no. 12, pp. 1315–1325, 2011.

[155] E. Rabizadeh, A. S. Bagherzadeh, and T. Rabczuk, "Goal-oriented error estimation and adaptive mesh refinement in dynamic coupled thermoelasticity," *Computers & Structures*, vol. 173, pp. 187–211, 2016.

[156] Z. Zhang and J. Zhu, "Analysis of the superconvergent patch recovery technique and a posteriori error estimator in the finite element method (I)," *Computer Methods in Applied Mechanics and Engineering*, vol. 123, no. 1-4, pp. 173–187, 1995.

[157] H.-J. Chung and T. Belytschko, "An error estimate in the EFG method," *Computational Mechanics*, vol. 21, no. 2, pp. 91–100, 1998.

[158] T. Belytschko, W. K. Liu, and M. Singer, "On adaptivity and error criteria for meshfree methods," *Studies in Applied Mechanics*, vol. 47, pp. 217–230, 1998.

[159] W. K. Liu, R. A. Uras, and Y. Chen, "Enrichment of the finite element method with the reproducing kernel particle method," *Journal of Applied Mechanics*, vol. 64, no. 4, pp. 861–870, 1997.

[160] H. Lu and J. Chen, "Adaptive meshfree particle method," *Lecture Notes in Computational Science and Engineering*, vol. 26, pp. 251–267, 2002.

[161] C. K. Lee and C. Zhou, "On error estimation and adaptive refinement for element free Galerkin method: Part I: stress recovery and a posteriori error estimation," *Computers & Structures*, vol. 82, no. 4, pp. 413–428, 2004.

[162] C. K. Lee and Y. Shuai, "An automatic adaptive refinement procedure for the reproducing kernel particle method. Part II: Adaptive refinement," *Computational Mechanics*, vol. 40, no. 3, pp. 415–427, 2007.

[163] B. B. T. Kee, G. Liu, and C. Lu, "A least-square radial point collocation method for adaptive analysis in linear elasticity," *Engineering Analysis with Boundary Elements*, vol. 32, no. 6, pp. 440–460, 2008.

[164] Q. Tang, K. Wei, G. Zhang, and X. Sun, "A fully automatic h-adaptive analysis procedure using the edge-based smoothed point interpolation method," *International Journal of Computational Methods*, p. 1845001, 2018.

[165] G. R. Liu, B. B. T. Kee, and L. Chun, "A stabilized least-squares radial point collocation method (LS-RPCM) for adaptive analysis," *Computer Methods in Applied Mechanics and Engineering*, vol. 195, no. 37-40, pp. 4843–4861, 2006.

[166] K. C. Cheung and L. Ling, "Convergence studies for an adaptive meshless least-squares collocation method," *International Journal of Computational Methods and Experimental Measurements*, vol. 5, no. 3, pp. 377–386, 2017.

[167] J. D. Eshelby, "The force on an elastic singularity," *Philosophical Transactions of the Royal Society of London A*, vol. 244, no. 877, pp. 87–112, 1951.

[168] J. Eshelby, "Energy relations and the energy-momentum tensor in continuum mechanics," in *Fundamental contributions to the continuum theory of evolving phase interfaces in solids*, pp. 82–119, Springer, 1999.

[169] N. Kikuchi, "Adaptive grid-design methods for finite element analysis," *Computer Methods in Applied Mechanics and Engineering*, vol. 55, no. 1-2, pp. 129–160, 1986.

[170] R. Radovitzky and M. Ortiz, "Error estimation and adaptive meshing in strongly nonlinear dynamic problems," *Computer Methods in Applied Mechanics and Engineering*, vol. 172, no. 1-4, pp. 203–240, 1999.

[171] M. Braun, "Configurational forces induced by finite-element discretization," *Proceeding of Estonian Academy of Science. Physics. Mathematics*, vol. 46, no. 1/2, pp. 24–31, 1997.

[172] C. J. Budd, W. Huang, and R. D. Russell, "Adaptivity with moving grids," *Acta Numerica*, vol. 18, pp. 111–241, 2009.

[173] R. Mueller and G. Maugin, "On material forces and finite element discretizations," *Computational Mechanics*, vol. 29, no. 1, pp. 52–60, 2002.

[174] E. Kuhl, H. Askes, and P. Steinmann, "An ALE formulation based on spatial and material settings of continuum mechanics. Part 1: Generic hyperelastic formulation," *Computer Methods in Applied Mechanics and Engineering*, vol. 193, no. 39, pp. 4207–4222, 2004.

[175] D. S. McRae, "R-refinement grid adaptation algorithms and issues," *Computer Methods in Applied Mechanics and Engineering*, vol. 189, no. 4, pp. 1161–1182, 2000.

[176] P. Béal, J. Koko, and R. Touzani, "Mesh r-adaptation for unilateral contact problems," *International Journal of Applied Mathematics and Computer Science*, vol. 12, pp. No–1, 2001.

[177] D. Materna and F.-J. Barthold, "Configurational variations for the primal and dual problem in elasticity," *ZAMM-Journal of Applied Mathematics and Mechanics/Zeitschrift für Angewandte Mathematik und Mechanik*, vol. 89, no. 8, pp. 666–676, 2009.

[178] R. Mueller, D. Gross, and G. Maugin, "Use of material forces in adaptive finite element methods," *Computational Mechanics*, vol. 33, no. 6, pp. 421–434, 2004.

[179] A. Rajagopal and S. Sivakumar, "Optimality of finite element grids based on material forces and error assessment," *Computer Assisted Methods in Engineering and Science*, vol. 12, pp. 1–21, 2006.

[180] P. Thoutireddy and M. Ortiz, "A variational r-adaption and shape-optimization method for finite-deformation elasticity," *International Journal for Numerical Methods in Engineering*, vol. 61, no. 1, pp. 1–21, 2004.

[181] S. Riehl and P. Steinmann, "On structural shape optimization using an embedding domain discretization technique," *International Journal for Numerical Methods in Engineering*, vol. 109, no. 9, pp. 1315–1343, 2017.

[182] H. Askes, E. Kuhl, and P. Steinmann, "An ALE formulation based on spatial and material settings of continuum mechanics. Part 2: Classification and applications," *Computer Methods in Applied Mechanics and Engineering*, vol. 193, no. 39, pp. 4223–4245, 2004.

[183] C. Pain, A. Umpleby, C. De Oliveira, and A. Goddard, "Tetrahedral mesh optimisation and adaptivity for steady-state and transient finite element calculations," *Computer Methods in Applied Mechanics and Engineering*, vol. 190, no. 29-30, pp. 3771–3796, 2001.

[184] R. Mueller, S. Kolling, and D. Gross, "On configurational forces in the context of the finite element method," *International Journal for Numerical Methods in Engineering*, vol. 53, no. 7, pp. 1557–1574, 2002.

[185] H. Askes and A. Rodríguez-Ferran, "A combined rh-adaptive scheme based on domain subdivision. Formulation and linear examples," *International Journal for Numerical Methods in Engineering*, vol. 51, no. 3, pp. 253–273, 2001.

[186] D. Materna and F.-J. Barthold, "Goal-oriented r-adaptivity based on variational arguments in the physical and material spaces," *Computer Methods in Applied Mechanics and Engineering*, vol. 198, no. 41, pp. 3335–3351, 2009.

[187] U. Basappa, A. Rajagopal, and J. Reddy, "Adaptive isogeometric analysis based on a combined r-h strategy," *International Journal for Computational Methods in Engineering Science and Mechanics*, vol. 17, no. 2, pp. 73–92, 2016.

[188] A. Rajagopal and S. Sivakumar, "A combined rh adaptive strategy based on material forces and error assessment for plane problems and bimaterial interfaces," *Computational Mechanics*, vol. 41, no. 1, pp. 49–72, 2007.

[189] S. Riehl and P. Steinmann, "An integrated approach to shape optimization and mesh adaptivity based on material residual forces," *Computer Methods in Applied Mechanics and Engineering*, vol. 278, pp. 640–663, 2014.

[190] J. Eshelby, "The elastic energy-momentum tensor," *Journal of Elasticity*, vol. 5, no. 3-4, pp. 321–335, 1975.

[191] E. Kuhl and P. Steinmann, "Material forces in open system mechanics," *Computer Methods in Applied Mechanics and Engineering*, vol. 193, no. 23-26, pp. 2357–2381, 2004.

[192] R. Gangadharan, A. Rajagopal, and S. Sivakumar, "An rh adaptive strategy based on material forces and error assessment," *CMC-Tech Science Press-*, vol. 1, pp. 229–244, 2004.

[193] T. Rabczuk and T. Belytschko, "Adaptivity for structured meshfree particle methods in 2D and 3D," *International Journal for Numerical Methods in Engineering*, vol. 63, no. 11, pp. 1559–1582, 2005.

[194] Z. Ullah and C. Augarde, "Finite deformation elasto-plastic modelling using an adaptive meshless method," *Computers & Structures*, vol. 118, pp. 39–52, 2013.

[195] Z. Ullah, W. Coombs, and C. Augarde, "An adaptive finite element/meshless coupled method based on local maximum entropy shape functions for linear and nonlinear problems," *Computer Methods in Applied Mechanics and Engineering*, vol. 267, pp. 111–132, 2013.

[196] Z. Ullah, C. E. Augarde, R. S. Crouch, and W. M. Coombs, "FE-EFGM coupling using maximum entropy shape functions and its application to small and finite deformation," in *19th UK Conference of the Association for Computational Mechanics in Engineering (ACME), Heriot-Watt University, Edinburgh, UK*, pp. 277–280, 2011.

[197] X. Zhuang, C. Heaney, and C. Augarde, "On error control in the element-free Galerkin method," *Engineering Analysis with Boundary Elements*, vol. 36, no. 3, pp. 351–360, 2012.

[198] C. T. Kelley, *Solving nonlinear equations with Newton's method*, vol. 1. Siam, 2003.

[199] C. Kelley, "Iterative methods for linear and nonlinear equations," *Frontiers in Applied Mathematics*, vol. 16, pp. 575–601, 1995.

[200] A. J. M. Spencer, *Continuum mechanics*. Dover, New York, 2004.

[201] K. Imai and D. M. Frangopol, "Geometrically nonlinear finite element reliability analysis of structural systems. I: theory," *Computers & Structures*, vol. 77, no. 6, pp. 677–691, 2000.

[202] D. M. Frangopol and K. Imai, "Geometrically nonlinear finite element reliability analysis of structural systems. II: applications," *Computers & Structures*, vol. 77, no. 6, pp. 693–709, 2000.

[203] L. Zhang, Z. Lei, K. Liew, and J. Yu, "Large deflection geometrically nonlinear analysis of carbon nanotube-reinforced functionally graded cylindrical panels," *Computer Methods in Applied Mechanics and Engineering*, vol. 273, pp. 1–18, 2014.

[204] A. Alipour, S. Wulfinghoff, H. R. Bayat, S. Reese, and B. Svendsen, "The concept of control points in hybrid discontinuous Galerkin methodsapplication to geometrically nonlinear crystal plasticity," *International Journal for Numerical Methods in Engineering*, vol. 114, no. 5, pp. 557–579, 2018.

[205] L. Leonetti, F. Liguori, D. Magisano, and G. Garcea, "An efficient isogeometric solid-shell formulation for geometrically nonlinear analysis of elastic shells," *Computer Methods in Applied Mechanics and Engineering*, vol. 331, pp. 159–183, 2018.

[206] P. Wriggers, *Nonlinear finite element methods*. Springer Science & Business Media, 2008.

[207] T. Belytschko, W. K. Liu, B. Moran, and K. Elkhodary, *Nonlinear finite elements for continua and structures*. John wiley & sons, 2013.

[208] K.-J. Bathe, *Finite element procedures*. Prentice Hall, Pearson Education, Inc, 2006.

[209] K.-J. Bathe and S. Bolourchi, "Large displacement analysis of three-dimensional beam structures," *International Journal for Numerical Methods in Engineering*, vol. 14, no. 7, pp. 961–986, 1979.

[210] G. A. Holzapfel, *Nonlinear solid mechanics: a continuum approach for engineering science*. John Wiley & Sons, Ltd, 2000.

[211] M. A. Crisfield, *Non-linear finite element analysis of solids and structures*, vol. 1. Wiley New York, 1991.

[212] C. C. Huang, F. Fujii, and K. M. Hsiao, "An explicit algorithm for geometrically nonlinear transient analysis of spatial beams using a corotational total Lagrangian finite element formulation," *Computers & Structures*, vol. 200, pp. 68–85, 2018.

[213] R. de Borst, M. A. Crisfield, J. J. Remmers, and C. V. Verhoosel, *Nonlinear finite element analysis of solids and structures*. John Wiley & Sons, 2012.

[214] W. Li, N. Nguyen-Thanh, and K. Zhou, "Geometrically nonlinear analysis of thin-shell structures based on an isogeometric-meshfree coupling approach," *Computer Methods in Applied Mechanics and Engineering*, vol. 336, pp. 111–134, 2018.

[215] W. K. Liu, C. Herman, C. Jiun-Shyan, and B. Ted, "Arbitrary Lagrangian-Eulerian Petrov-Galerkin finite elements for nonlinear continua," *Computer Methods in Applied Mechanics and Engineering*, vol. 68, no. 3, pp. 259–310, 1988.

[216] W. K. Liu, J.-S. Chen, T. Belytschko, and Y. F. Zhang, "Adaptive ALE finite elements with particular reference to external work rate on frictional interface," *Computer Methods in Applied Mechanics and Engineering*, vol. 93, no. 2, pp. 189–216, 1991.

[217] L. D. Libersky, A. G. Petschek, T. C. Carney, J. R. Hipp, and F. A. Allahdadi, "High strain Lagrangian hydrodynamics: a three-dimensional SPH code for dynamic material response," *Journal of Computational Physics*, vol. 109, no. 1, pp. 67–75, 1993.

[218] S. Yashiro and T. Okabe, "Smoothed particle hydrodynamics in a generalized coordinate system with a finite-deformation constitutive model," *International Journal for Numerical Methods in Engineering*, vol. 103, no. 11, pp. 781–797, 2015.

[219] G. Li and T. Belytschko, "Element-free Galerkin method for contact problems in metal forming analysis," *Engineering Computations*, vol. 18, no. 1/2, pp. 62–78, 2001.

[220] Z. Han, A. Rajendran, and S. Atluri, "Meshless local petrov-galerkin (MLPG) approaches for solving nonlinear problems with large deformations and rotations," *Computer Modeling in Engineering and Sciences*, vol. 10, no. 1, p. 1, 2005.

[221] K. Liew, T. Ng, and Y. Wu, "Meshfree method for large deformation analysis–a reproducing kernel particle approach," *Engineering Structures*, vol. 24, no. 5, pp. 543–551, 2002.

[222] N. Zakrzewski, M. Nazem, S. Sloan, and M. Cassidy, "On application of the maximum entropy meshless method for large deformation analysis of geotechnical problems," in *Applied Mechanics and Materials*, vol. 846, pp. 331–335, Trans Tech Publications, 2016.

[223] S. Kumar, K. Danas, and D. M. Kochmann, "Enhanced local maximum-entropy approximation for stable meshfree simulations," *Computer Methods in Applied Mechanics and Engineering*, vol. 344, pp. 858–886, 2019.

[224] F. Maurin, F. Greco, S. Dedoncker, and W. Desmet, "Isogeometric analysis for nonlinear planar Kirchhoff rods: weighted residual formulation and collocation of the strong form," *Computer Methods in Applied Mechanics and Engineering*, 2018.

[225] R. Kruse, N. Nguyen-Thanh, L. de Lorenzis, and T. J. Hughes, "Isogeometric collocation for large deformation elasticity and frictional contact problems," *Computer Methods in Applied Mechanics and Engineering*, vol. 296, pp. 73–112, 2015.

[226] Z. Han and S. Atluri, "On the (Meshless Local Petrov-Galerkin) MLPG-Eshelby Method in Computational Finite Deformation Solid Mechanics-Part II," *Computer Modelling Engineering Science*, vol. 97, pp. 199–237, 2014.

[227] A. Shojaei, T. Mudric, M. Zaccariotto, and U. Galvanetto, "A coupled meshless finite point/Peridynamic method for 2D dynamic fracture analysis," *International Journal of Mechanical Sciences*, vol. 119, pp. 419–431, 2016.

[228] P. Krysl and T. Belytschko, "Analysis of thin shells by the element-free Galerkin method," *International Journal of Solids and Structures*, vol. 33, no. 20-22, pp. 3057–3080, 1996.

[229] D. Levin, "The approximation power of moving least-squares," *Mathematics of Computation of the American Mathematical Society*, vol. 67, no. 224, pp. 1517–1531, 1998.

[230] G. Li and N. Aluru, "Linear, nonlinear and mixed-regime analysis of electrostatic MEMS," *Sensors and Actuators A: Physical*, vol. 91, no. 3, pp. 278–291, 2001.

[231] Y.-J. Lim and S. De, "Real time simulation of nonlinear tissue response in virtual surgery using the point collocation-based method of finite spheres," *Computer Methods in Applied Mechanics and Engineering*, vol. 196, no. 31-32, pp. 3011–3024, 2007.

[232] W. Coombs, *Finite deformation of particulate geomaterials: frictional and anisotropic Critical State elasto-plasticity*. PhD thesis, Durham University, 2011.

[233] J. Bonet and R. D. Wood, *Nonlinear continuum mechanics for finite element analysis*. Cambridge university press, 1997.

[234] E. A. de Souza Neto, D. Perić, and D. R. Owen, *Computational methods for plasticity: theory and applications*. John Wiley & Sons, 2011.

[235] J. Mäkinen, "Total Lagrangian Reissner's geometrically exact beam element without singularities," *International Journal for Numerical Methods in Engineering*, vol. 70, no. 9, pp. 1009–1048, 2007.

[236] S. P. Timoshenko and S. Woinowsky-Krieger, *Theory of plates and shells*. McGraw-hill, 1959.

[237] T. K. Molstad, "Finite deformation analysis using the finite element method," Master's thesis, University of British Columbia, 1977.

[238] J. Holden, "On the finite deflections of thin beams," *International Journal of Solids and Structures*, vol. 8, no. 8, pp. 1051–1055, 1972.

[239] Y. Lian, W. Shyy, D. Viieru, and B. Zhang, "Membrane wing aerodynamics for micro air vehicles," *Progress in Aerospace Sciences*, vol. 39, no. 6-7, pp. 425–465, 2003.

[240] R. Amini, C. E. Eckert, K. Koomalsingh, J. McGarvey, M. Minakawa, J. H. Gorman, R. C. Gorman, and M. S. Sacks, "On the in vivo deformation of the mitral valve anterior leaflet: effects of annular geometry and referential configuration," *Annals of Biomedical Engineering*, vol. 40, no. 7, pp. 1455–1467, 2012.

[241] A. Patil, A. DasGupta, and A. Eriksson, "Contact mechanics of a circular membrane inflated against a deformable substrate," *International Journal of Solids and Structures*, vol. 67, pp. 250–262, 2015.

[242] C. H. Jenkins and J. W. Leonard, "Nonlinear dynamic response of membranes: state of the art," *Applied Mechanics Reviews*, vol. 44, no. 7, pp. 319–328, 1991.

[243] T. Belytschko, H. Stolarski, W. K. Liu, N. Carpenter, and J. S. Ong, "Stress projection for membrane and shear locking in shell finite elements," *Computer Methods in Applied Mechanics and Engineering*, vol. 51, no. 1-3, pp. 221–258, 1985.

[244] V. Prot, B. Skallerud, and G. Holzapfel, "Transversely isotropic membrane shells with application to mitral valve mechanics. Constitutive modelling and finite element implementation," *International Journal for Numerical Methods in Engineering*, vol. 71, no. 8, pp. 987–1008, 2007.

[245] M. K. Rausch, F. A. Tibayan, D. C. Miller, and E. Kuhl, "Evidence of adaptive mitral leaflet growth," *Journal of the Mechanical Behavior of Biomedical Materials*, vol. 15, pp. 208–217, 2012.

[246] J. Simo, D. Fox, and M. Rifai, "On a stress resultant geometrically exact shell model. Part II: The linear theory; computational aspects," *Computer Methods in Applied Mechanics and Engineering*, vol. 73, no. 1, pp. 53–92, 1989.

[247] J. C. Simo and D. D. Fox, "On a stress resultant geometrically exact shell model. Part I: Formulation and optimal parametrization," *Computer Methods in Applied Mechanics and Engineering*, vol. 72, no. 3, pp. 267–304, 1989.

[248] G. Wempner and D. Talaslidis, *Mechanics of solids and shells: theories and approximations*. CRC press, 2002.

[249] C. H. Jenkins, *Progress in astronautics and aeronautics: gossamer spacecraft: membrane and inflatable structures technology for space applications*, vol. 191. AIAA, 2001.

[250] K. Weinberg and P. Neff, "A geometrically exact thin membrane model investigation of large deformations and wrinkling," *International Journal for Numerical Methods in Engineering*, vol. 74, no. 6, pp. 871–893, 2008.

[251] P. B. Ryzhakov and E. Oñate, "A finite element model for fluid–structure interaction problems involving closed membranes, internal and external fluids," *Computer Methods in Applied Mechanics and Engineering*, vol. 326, pp. 422–445, 2017.

[252] L. Chen, N. Nguyen-Thanh, H. Nguyen-Xuan, T. Rabczuk, S. P. A. Bordas, and G. Limbert, "Explicit finite deformation analysis of isogeometric membranes," *Computer Methods in Applied Mechanics and Engineering*, vol. 277, pp. 104–130, 2014.

[253] A. E. Green and W. Zerna, *Theoretical elasticity*. Dover, New York, 1992.

[254] R. W. Ogden, *Non-linear elastic deformations*. Courier Corporation, 1997.

[255] A. Selvadurai, "Deflections of a rubber membrane," *Journal of the Mechanics and Physics of Solids*, vol. 54, no. 6, pp. 1093–1119, 2006.

[256] A. Gent, "Elastic instabilities in rubber," *International Journal of Non-Linear Mechanics*, vol. 40, no. 2-3, pp. 165–175, 2005.

[257] Y. Fu and Y. Xie, "Stability of localized bulging in inflated membrane tubes under volume control," *International Journal of Engineering Science*, vol. 48, no. 11, pp. 1242–1252, 2010.

[258] R. A. Sauer, T. X. Duong, and C. J. Corbett, "A computational formulation for constrained solid and liquid membranes considering isogeometric finite elements," *Computer Methods in Applied Mechanics and Engineering*, vol. 271, pp. 48–68, 2014.

[259] A. Needleman, "Inflation of spherical rubber balloons," *International Journal of Solids and Structures*, vol. 13, no. 5, pp. 409–421, 1977.

[260] J. Oden and T. Sato, "Finite strains and displacements of elastic membranes by the finite element method," *International Journal of Solids and Structures*, vol. 3, no. 4, pp. 471–488, 1967.

[261] I. Fried, "Finite element computation of large rubber membrane deformations," *International Journal for Numerical Methods in Engineering*, vol. 18, no. 5, pp. 653–660, 1982.

[262] S. Tang, "Large strain analysis of an inflating membrane," *Computers & Structures*, vol. 15, no. 1, pp. 71–78, 1982.

[263] T. Rumpel and K. Schweizerhof, "Volume-dependent pressure loading and its influence on the stability of structures," *International Journal for Numerical Methods in Engineering*, vol. 56, no. 2, pp. 211–238, 2003.

[264] M. Stanuszek, "Fe analysis of large deformations of membranes with wrinkling," *Finite Elements in Analysis and Design*, vol. 39, no. 7, pp. 599–618, 2003.

[265] R. S. Rivlin and D. Saunders, "Large elastic deformations of isotropic materials VII. Experiments on the deformation of rubber," *Philosophical Transactions of the Royal Society of London. Series A, Mathematical and Physical Sciences*, vol. 243, no. 865, pp. 251–288, 1951.

[266] W. Yang and W. Feng, "On axisymmetrical deformations of nonlinear membranes," *Journal of Applied Mechanics*, vol. 37, no. 4, pp. 1002–1011, 1970.

[267] J. Campbell, "On the theory of initially tensioned circular membranes subjected to uniform pressure," *The Quarterly Journal of Mechanics and Applied Mathematics*, vol. 9, no. 1, pp. 84–93, 1956.

[268] J. Bonet, R. Wood, J. Mahaney, and P. Heywood, "Finite element analysis of air supported membrane structures," *Computer Methods in Applied Mechanics and Engineering*, vol. 190, no. 5-7, pp. 579–595, 2000.

[269] A. J. Gil and J. Bonet, "Finite element analysis of prestressed structural membranes," *Finite Elements in Analysis and Design*, vol. 42, no. 8-9, pp. 683–697, 2006.

[270] J. Katsikadelis, M. Nerantzaki, and G. Tsiatas, "The analog equation method for large deflection analysis of membranes. A boundary-only solution," *Computational Mechanics*, vol. 27, no. 6, pp. 513–523, 2001.

[271] K. F. Kolsti and D. L. Kunz, "A point collocation method for geometrically nonlinear membranes," *International Journal of Solids and Structures*, vol. 50, no. 2, pp. 288–296, 2013.

[272] S. Kumar, K. Danas, and D. M. Kochmann, "Enhanced local maximum-entropy approximation for stable meshfree simulations," *Computer Methods in Applied Mechanics and Engineering*, 2018.

[273] R. W. Ogden, "Large deformation isotropic elasticity–on the correlation of theory and experiment for incompressible rubberlike solids," *Proceeding of the Royal Society of London A*, vol. 326, no. 1567, pp. 565–584, 1972.

[274] M. K. Rausch and E. Kuhl, "On the mechanics of growing thin biological membranes," *Journal of the Mechanics and Physics of Solids*, vol. 63, pp. 128–140, 2014.

[275] J. T. Oden, *Finite elements of nonlinear continua*. Dover, New York, 2006.

[276] R. Ogden, G. Saccomandi, and I. Sgura, "Fitting hyperelastic models to experimental data," *Computational Mechanics*, vol. 34, no. 6, pp. 484–502, 2004.

[277] B. Kim, S. B. Lee, J. Lee, S. Cho, H. Park, S. Yeom, and S. H. Park, "A comparison among Neo-Hookean model, Mooney-Rivlin model, and Ogden model for chloroprene rubber," *International Journal of Precision Engineering and Manufacturing*, vol. 13, no. 5, pp. 759–764, 2012.

[278] M. M. Attard and G. W. Hunt, "Hyperelastic constitutive modeling under finite strain," *International Journal of Solids and Structures*, vol. 41, no. 18-19, pp. 5327–5350, 2004.

[279] C. H. Jenkins, "Nonlinear dynamic response of membranes: State of the art-Update," *Applied Mechanics Reviews*, vol. 49, no. 10S, pp. S41–S48, 1996.

[280] J. N. Reddy, *Theory and analysis of elastic plates and shells*. CRC Press, 2006.

[281] M. Rezaiee-Pajand and R. Naserian, "Geometrical nonlinear analysis based on optimization technique," *Applied Mathematical Modelling*, vol. 53, pp. 32–48, 2018.

[282] K. S. Lee, S. E. Han, and T. Park, "A simple explicit arc-length method using the dynamic relaxation method with kinetic damping," *Computers & Structures*, vol. 89, no. 1-2, pp. 216–233, 2011.

[283] Y. Feng, D. Perić, and D. Owen, "Determination of travel directions in path-following methods," *Mathematical and Computer Modelling*, vol. 21, no. 7, pp. 43–59, 1995.

[284] M. Crisfield, "A fast incremental/iterative solution procedure that handles snap-through," in *Computational Methods in Nonlinear Structural and Solid Mechanics*, pp. 55–62, Elsevier, 1981.

[285] M. Crisfield, "An arc-length method including line searches and accelerations," *International Journal for Numerical Methods in Engineering*, vol. 19, no. 9, pp. 1269–1289, 1983.

[286] E. A. de Souza Neto and Y. Feng, "On the determination of the path direction for arc-length methods in the presence of bifurcations and snap-backs'," *Computer Methods in Applied Mechanics and Engineering*, vol. 179, no. 1-2, pp. 81–89, 1999.

[287] E. Riks, "An incremental approach to the solution of snapping and buckling problems," *International Journal of Solids and Structures*, vol. 15, no. 7, pp. 529–551, 1979.

[288] Y. Feng, D. Owen, and D. Perić, "On the sign of the determinant of the structural stiffness matrix for determination of loading increment in arc-length algorithms," *Communications in Numerical Methods in Engineering*, vol. 13, no. 1, pp. 47–49, 1997.

[289] Y. Feng, D. Perić, and D. Owen, "A new criterion for determination of initial loading parameter in arc-length methods," *Computers & Structures*, vol. 58, no. 3, pp. 479–485, 1996.

[290] A. Eriksson and A. Nordmark, "Instability of hyper-elastic balloon-shaped space membranes under pressure loads," *Computer Methods in Applied Mechanics and Engineering*, vol. 237, pp. 118–129, 2012.

[291] E. A. de Souza Neto, D. Perić, and D. Owen, "Finite elasticity in spatial description: Linearization aspects with 3-D membrane applications," *International Journal for Numerical Methods in Engineering*, vol. 38, no. 20, pp. 3365–3381, 1995.

[292] L. Treloar, "Stress-strain data for vulcanized rubber under various types of deformation," *Rubber Chemistry and Technology*, vol. 17, no. 4, pp. 813–825, 1944.

[293] P. Wriggers and R. Taylor, "A fully non-linear axisymmetrical membrane element for rubber-like materials," *Engineering Computations*, vol. 7, no. 4, pp. 303–310, 1990.